A MULTI-LEVEL UPSCALING AND VALIDATION FRAMEWORK FOR UNCERTAINTY QUANTIFICATION IN ADDITIVELY MANUFACTURED LATTICE STRUCTURES

A Dissertation
Presented to
The Academic Faculty

by

Recep Muhammet Gorguluarslan

In Partial Fulfillment
of the Requirements for the Degree
Doctor of Philosophy in Mechanical Engineering

Georgia Institute of Technology
December 2016

A MULTI-LEVEL UPSCALING AND VALIDATION FRAMEWORK FOR UNCERTAINTY QUANTIFICATION IN ADDITIVELY MANUFACTURED LATTICE STRUCTURES

Approved by:

Dr. Seung-Kyum Choi, Chair
Mechanical Engineering
Georgia Institute of Technology

Dr. David W. Rosen
Mechanical Engineering
Georgia Institute of Technology

Dr. David L. McDowell
Mechanical Engineering
Georgia Institute of Technology

Dr. Christopher J. Saldana
Mechanical Engineering
Georgia Institute of Technology

Dr. Rafi L. Muhanna
Civil and Environmental Engineering
Georgia Institute of Technology

Date Approved: November 2, 2016

ACKNOWLEDGEMENTS

First of all, I would like to express my sincere gratitude to my advisor Dr. Seung-Kyum Choi for his guidance, support, and encouragement over the years. He has always emphasized high-quality results in my research, presentations, and written documents as well as in my graduate course work. He has always encouraged me to put in my best in everything and expect the best results in the end. I could not have grown immensely as a researcher and individual over the last few years without his support and understanding.

I would also like to thank other members of my dissertation reading committee, Dr. David W. Rosen (ME), Dr. Christopher J. Saldana (ME), Dr. David L. McDowell (ME), and Dr. Rafi L. Muhanna (CEE), for taking the time to peruse my dissertation and suggest necessary improvements.

This doctoral dissertation would not have been possible without the help and support of the kind people around me and the excellent research facilities that Georgia Institute of Technology provides. I would like to thank all the students, past and present, who always volunteered to help me in times of need and encouraged/pushed/directed me in the right direction whenever I hit a wall. I would especially like to thank Mahmoud Al-Zahrani and Sang-in Park who has many times contributed to the success of this dissertation indirectly by their technical help, advice on this work, challenging and insightful discussions. My discussions with Thomas Stone, Sungkun Hwang, Jiten Patel and Yitaou Liu have also been very helpful.

I am thankful to Dr. Umesh N. Gandhi for guiding and encouraging me to learn and develop my software skills in design optimization and finite element modeling during my internship at Toyota Research Institute North America. I also thank Dr. Mehmet Ali Guler from TOBB

University of Economics and Technology for teaching me the core fundamentals of finite element analysis during my undergraduate years, which form a critical part of this dissertation.

Last but not least I would like to thank my parents and brothers for their unconditional love, wishes, patience and faith without which I would not have made it this far. They have inculcated me with the virtues of hard work, dedication, and perseverance since my early days. I exist because of them. I especially thank my lovely wife Esra Gorguluarslan for tolerating my excessive working time and constantly providing me with the best possible diversions from any difficulty; her ever-lasting love, patience, and encouragement has made this dissertation possible.

TABLE OF CONTENTS

LIST OF TABLES

LIST OF FIGURES

GLOSSARY

2D	=	Two dimensional
3D	=	Three dimensional
A-D	=	Anderson-Darling
AM	=	Additive manufacturing
AIC	=	Akaike information criterion
BIC	=	Bayesian information criterion
CDF	=	Cumulative distribution function
COV	=	Coefficient of variation
CLS	=	Cellular lattice structure
CLT	=	Central limit theorem
CT	=	Computer tomography
EBM	=	Electron beam melting
ECDF	=	Empirical cumulative distribution function
FE	=	Finite element
FDM	=	Fused deposition modeling
GA	=	Genetic algorithm
GEV	=	Generalized extreme value
GOF	=	Goodness-of-fit

K-S	=	Kolmogorov-Smirnov
KUBC	=	Kinematic uniform boundary condition
LHS	=	Latin hypercube sampling
LM	=	Levenberg-Marquardt
MAE	=	Mean absolute error
MAV	=	Micro-aerial vehicle
MCS	=	Monte Carlo sampling
MLE	=	Maximum likelihood estimation
MSE	=	Mean squared error
MUBC	=	Mixed uniform boundary condition
PBC	=	Periodic boundary conditions (PBC)
PCE	=	Polynomial chaos expansion
PCHIP	=	Piecewise cubic Hermite interpolating polynomial
PDF	=	Probability density function
PIT	=	Probability integral transformation
PSO	=	Particle swarm optimization
RBDO	=	Reliability-based design optimization
RDM	=	Relative density mapping
RVE	=	Representative volume Element

SA	=	Simulated annealing
SC	=	Simple cubic
SIMP	=	Solid Isotropic Material with Penalization
SLA	=	Selective laser Annealing
SLM	=	Selective laser melting
SLS	=	Selective laser sintering
SMS	=	Size matching and scaling
SRVE	=	Stochastic representative volume element
SUBC	=	Static uniform boundary condition
SUD	=	Standard uniform distribution
UQ	=	Uncertainty quantification
V&V	=	Verification and validation

LIST OF SYMBOLS

A	=	cross-sectional area
b	=	PCE coefficients
d_{KS}	=	maximum distance between two cumulative density functions
D	=	diameter
D	=	distribution model
e	=	error
E	=	elastic modulus
$F_X(.)$	=	cumulative density function of random variable X
F	=	force
$G(.)$	=	limit state function
H	=	hypothesis
K	=	global stiffness matrix
IL	=	information loss value
L	=	lattice cell size
L	=	likelihood function
M_r	=	r-th statistical moment
k	=	number of statistical parameters
n	=	number of samples

P	=	number of PCE coefficients
$p(.)$	=	probability density function
u	=	cumulative distribution function value of a sample
ν	=	Poisson's ratio
V	=	volume
U	=	global displacement vector
X	=	random input variable
Y	=	random response or output variable
α	=	significance level
μ_X	=	mean of random variable X
σ_X	=	standard deviation of random variable X
σ	=	stress
Φ	=	orthogonal polynomials
θ	=	statistical parameters of a distribution model
Ω	=	material medium
ε	=	strain
ρ	=	density of the lattice cell
γ	=	porosity
ξ	=	random variables in orthogonal polynomials

δ_S	=	difference between target and fabricated diameter
$\boldsymbol{\Xi}$	=	mapping between the design variables and PCE coefficients.
Γ	=	boundary condition

SUMMARY

Multiscale modeling techniques are playing an ever increasing role in the effective design of complex engineering systems including aircraft, automobiles, etc. Lightweight cellular lattice structures (CLSs) gained interest recently since their complex structure, composed of a network of interconnected strut members, can be fabricated by additive manufacturing (AM). However, uncertainties in the fabricated strut members of CLSs are introduced by the layer-by-layer manufacturing process. These fine scale uncertainties influence the overall product performance resulting in inaccurate predictions of reality and increased complexity in simulations. In this research, a multi-level upscaling and validation framework is established that will enable accurate estimation of the performance of AM-fabricated CLSs under uncertainties. An improved stochastic upscaling method based on Polynomial Chaos Expansion (PCE) is employed to quantify and propagate the uncertainties across multiple levels efficiently. The upscaling method is integrated with a hierarchical validation approach to ensure that accurate predictions are made with the homogenized models. The u-pooling method is incorporated with the Kolmogorov-Smirnov test as the validation metric to efficiently use the limited experimental data during validation. The framework is applied to representative examples to demonstrate its efficacy in accurately characterizing the elastic properties of CLSs under uncertainties. The framework is also used to show its applicability in designing CLSs under uncertainties without the use of expensive simulations and optimization processes. The proposed framework is generalized to apply to any complex engineering structure that incorporates computationally intensive simulations and/or expensive experiments associated with fine scale uncertainties.

CHAPTER 1. INTRODUCTION

The main goal of this dissertation is to establish approaches for efficient uncertainty quantification and propagation across multiple scale levels for realistic modeling of cellular lattice structures (CLSs) fabricated by additive manufacturing (AM). In this chapter, CLSs, design approaches, multiscale modeling methods, uncertainty effects, and verification and validation (V&V) concepts are introduced to identify the research question and formulate corresponding hypotheses.

Advances in science and engineering have enabled more complex research efforts regarding the computational modeling and design of complex engineering materials and structures. It is even possible to investigate the effects of details at very small scales (e.g. atomistic scale, nanoscale, microscale etc.) on the overall performance of the engineering systems. With the rapid advances in computational power and capabilities, the current surge of interest is to utilize the computational models efficiently to design complex microstructural materials that can satisfy the design requirements of the engineering structures or systems, which would not be possible with the traditional materials selection approach [1]. CLSs are one of these complex microstructural materials that gained interest in the design of lightweight and high strength engineering applications. Recent advancements in AM techniques made it possible to fabricate their complex structures which consist of a network of interconnected strut members.

However, the introduction of the fine scale details and uncertainties into the modeling process is rapidly increasing the complexity of the computational models of engineering systems or structures. Furthermore, uncertainties in material properties, geometry, manufacturing processes and operational environments are critical at all scales [2]. In AM-fabricated lattice structures, there exist increased uncertainties in fabricated material properties and geometry at

microscopic levels due to the layer-by-layer manufacturing process which will eventually effect all scale levels. The common challenge, which hinders the use of computational models that incorporate the microscopic level details and uncertainties, is the huge computational expense associated with the analysis of the heterogeneous material behavior to evaluate the final structure responses. Hence, traditional one-scale physics-based models are neither feasible nor efficient for modeling and simulation of such complex structures due to the increased computational complexity when fine scale uncertainties are involved. To overcome the complexity issue and to simplify the computational models used for predicting reality, multiscale modeling techniques are implemented for the design of materials, products, and systems. Moreover, there is a trade-off between the simplicity of the computational models and the prediction accuracy, which necessitates the use of V&V approaches along with the multiscale modeling techniques to evaluate the prediction accuracy. Hence, the increased demand for developing computational models that account for small scale level uncertainties will require designers to develop efficient multi-level uncertainty quantification and validation methodologies to predict reality accurately.

The organization of this chapter starts with an introduction to CLSs, which can be fabricated in a range from nanoscale to macroscale using AM techniques in Section 1.1. In Section 1.2, computational design approaches that utilize topology optimization and multiscale modeling processes for cellular lattice structures are described. An introduction and literature review to multiscale modeling techniques, which have been extensively used in the last few decades to simplify the computational complexity in modeling and designing materials and structures at various scale levels, is provided in Section 1.3. In Section 1.4, a literature review and a discussion are presented about the issue of uncertainties in the lattice structures fabricated by AM. In Section 1.5, V&V definitions are introduced, and general approaches used in literature to evaluate model

predictions are reviewed. Based on these introductions, the research questions are identified, and hypotheses are formulated in Section 1.6. This chapter is completed by discussing how the following chapters in the dissertation relate to the research questions in Section 1.7.

1.1. Cellular Lattice Structures (CLSs)

Nature presents highly efficient materials and systems for handling any condition in its environment. Natural materials and structures such as human and animal bone and wood are strong enough to withstand the environmental conditions and have minimum weight to allow any necessary movement. When the internal structure of bone (Figure 1.1(a)) or tree (Figure 1.1(b)) is analyzed, it is seen that nature produces a porous cellular structure, which includes material only in the important regions of the part to attain a lightweight but still strong structure.

(a) (b)

(a) Bone cellular structure. (b) Bamboo tree cellular structure.

Figure 1.1. Natural materials.

Cellular structures or materials, which mimic these natural structures, have long been investigated and shown to possess unique combinations of low weight, high stiffness, and strength, and substantial energy absorption [3]. These materials have been promising potential in engineering applications since light weight, and strong structures are of interest for a variety of industries, including biomedical, automotive and aerospace [4]. Also, when designed properly, open gaps in

the material structure can be exploited for active cooling or energy storage, providing unique opportunities for multi-functionality [5].

The concept of cellular structures used in engineering applications can be divided into two categories as (1) stochastic cellular structures and (2) non-stochastic cellular structures [4]. Stochastic cellular structures are also known as stochastic foams, which have random variations in the size of cells and therefore cannot be characterized by a single unit cell as shown in Figure 1.2(a). Non-stochastic cellular structures, on the other hand, are characterized by a unit cell that is repeated throughout the structure. Those with a unit cell that is repeated in two directions are known as prismatic structures such as honeycombs (Figure 1.2(b)) while those with a unit cell that is repeated in three directions are referred to cellular lattice structures (CLSs) (Figure 1.2(c)). CLSs are also known as micro-truss materials or mesostructured materials in the literature.

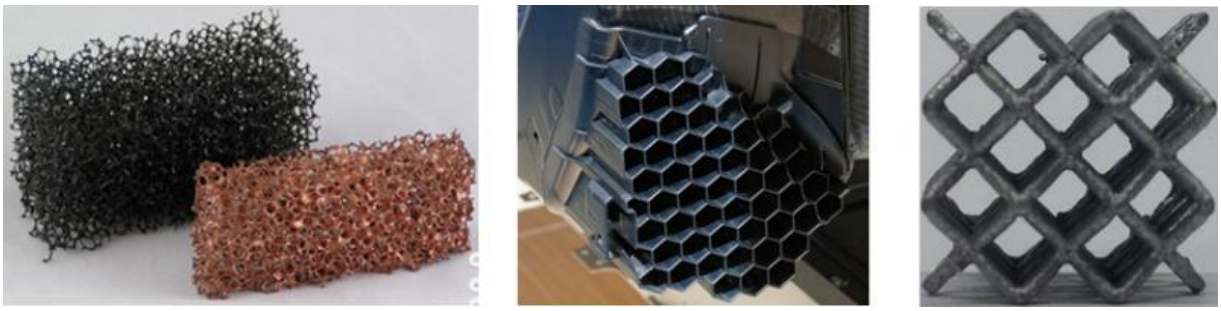

(a) (b) (c)

(a) Stochastic foam, (b) Honeycomb structure (c) Cellular lattice structure

Figure 1.2. Types of lightweight cellular structures

Among these cellular structures, CLSs offer inherent advantages over foams due to their ability to provide lighter and stronger structures [6], [7]. Stochastic foams, which have random cellular architectures, possess some beneficial properties such as specific surface area but the inefficient distribution of the constituent results in low mechanical properties such as stiffness, strength, and energy absorption [3]. Introducing order as in CLSs can substantially improve material utilization

and resultant mechanical properties. CLSs can be fabricated using conventional manufacturing techniques such as casting, forming and textile techniques [8]. Unfortunately, the complexity of these cellular CLSs is a big issue for these conventional manufacturing techniques since they involve very complex nodal geometry (e.g. fillet, radii, and thickness variations). The available CLSs are either cast in multiple steps or built using a tooled approach, which makes only a small number of cells per unit of time possible for production [9].

AM techniques have gained attention recently since they enable the fabrication of complex structures. AM, which is also known as 3D printing, is a layer-based manufacturing process where the parts are fabricated by adding material [10]. AM-fabricated parts were used as nonfunctional prototypes for years, produced primarily for visual purposes in initial product development. Recent developments in AM allow parts of high complexity, such as CLSs, to be built in relatively short time-scales. As technology has advanced, AM has seen vast improvements in its potential ability to serve more and more industrial customers. The quality of the parts produced by AM techniques has also started to be on par with or better than that of conventional methods for parts with high complexity [11]. For instance, the selective laser melting (SLM) process fabricates lattice-based structures with enhanced quality that conventional manufacturing techniques cannot provide [12]. Hence, AM techniques are now being used to fabricate parts that satisfy real world applications or production requirements [13]. Complex and lightweight structures such as air ducts used in military jet fighters can be designed as a single component using AM techniques, instead of being assembled with multiple parts fabricated by conventional techniques [14]. Cellular components with tailored microstructures can also be additively manufactured with a high level of quality for bone replacement implants [15], [16]. Thus, improvements in AM technology have also enabled the fabrication of custom CLS designs with complex shapes for industrial applications [17].

There exist several different printing processes in AM area. Therefore, the fabricated CLSs can have a characteristic cell length in the range of nanoscales to millimeter scales depending on the AM technique used. For instance, material extrusion processes (e.g. Fused Deposition Modeling (FDM)) and Selective Laser Sintering (SLS) processes can produce CLSs in millimeter to centimeter scale due to their limited resolution. Selective Laser Annealing (SLA) can make millimeter scale lattice cells with the high surface quality compared the processes mentioned above. These AM techniques use plastic-based materials in the fabrication of the structures. Metal-based AM techniques also exist such as SLM and Electron Beam Melting (EBM) processes which can fabricate CLSs at micrometer and millimeter scales. Since metal parts have highs strength, an extensive literature exist on the investigation of metal CLSs [13]. Recent advancements have also enabled the fabrication of the nanoscale and microscale CLSs. Some of the techniques are the technique of self-propagating photopolymer waveguides to create Ni-based ultralight micro-lattices [18], microstrereolithography that is capable of fabricating simultaneously strong and ultralight metal- and ceramic-based micro-lattices [19], Photonic Professional TPL-DLW System that can fabricate nanoscale polymer CLSs [20], and pyrolysis technique that enables the shrinkage of glassy carbon CLSs from microscale to nanoscale [21]. A summary of the recent AM methods that can fabricate nanoscale CLSs is given in [22]. The possibility of fabrication of the CLSs using a wide variety of AM techniques foster researchers to develop simulation-based design optimization processes for custom material and structure design as described in Section 1.2.

1.2. Design of CLSs via Topology Optimization

The design of CLSs has seen rapid development during the last decades, both in research and industrial applications due to their mechanical advantages and emerging availability of production

using AM techniques. CLS performance can be customized by simply altering the cross-sectional properties of the interconnected struts without changing the overall dimensions of the structure. Computational models are used with optimization algorithms to design the cross-sectional properties of the strut members. The extension of design optimization to the optimization of material layouts is known as topology optimization [23]. Topology optimization operates on a fixed FE mesh of either discrete or continuum elements to optimally distribute material in the material layout. Discrete topology optimization is also known as ground structure optimization [24], where the topology problem is solved by determining the optimum number, the position, and the mutual connectivity of structural member elements. In ground structure optimization, a ground structure, which is a grid of all elements connecting the nodes in the design space, is optimized selecting optimal cross-section parameters of the ground structure truss members [25]. Each member in the ground structure is modeled as truss or beam elements, and each element is associated with a design variable that defines the element size or its contribution to entire topology. The converged optimization result is supposed to drive the value of all the design variables either close to the lower and upper limits so that a certain topology is defined. The simplicity of truss or beam elements and their prediction capability for lattice structure performance allow the use of automated design processes to efficiently optimize the topology of the lattice structures using optimization algorithms.

Ground structure optimization of the lattice structures requires often hundreds or thousands of members, which hinders the optimization process due to the high computational cost. Hence, most optimization research has been done using two-dimensional (2D) example structures due to the limitations set by the available computational power [26], [27]. Moreover, the effectiveness of the optimization process is dependent on the optimization algorithm. Global optimization methods

such as simulated annealing (SA) and genetic algorithm (GA) are usually provide effective solutions for different problem formulations and constraints. However, these algorithms have the issue of high computational time especially when the number of variables becomes too large. Chu et al. [28] compare the performance of a global optimization algorithm, namely particle swarm optimization (PSO) and a gradient-based algorithm, namely Levenberg-Marquardt (LM) method, on the optimization of 2D lattice structures and show that the gradient-based optimization method can reach the optimal solution faster. It is also shown that the computational time of the optimization process increases with an increase of design variables, which are the cross-sectional properties of the beam elements in the structure.

In recent years, the 3D applications that can be fabricated by AM techniques have been the focus of researchers due to the increased computational power. Wieding et al [29] implemented the optimization process of the 3D bone scaffold design with lattice cells using the beam element FE model to match the bone elastic modulus. One notable method that deal with the large scale discrete optimization problems for AM-fabricated lattice structures was proposed by Stankovic et al [30]. This method is based on the application of the optimality criteria [31], which enables the use of minimum potential energy of the overall system obtained directly from the FE analysis of the structure for the sensitivity analysis in the optimization process. Thus, a reduction in the computational cost can be achieved in the discrete topology optimization process [30]. Nevertheless, when a very large number of members exist, the required memory for solving the FE model at each iteration increases the computational cost dramatically [32]. Hence, discrete topology optimization is still limited in finding high quality solutions for large-scale structures of 10,000 or more members due to the convergence to the local minima. To decrease the number of design variables, the structure can be designed with periodic lattice cells and/or surrogate modeling

methods are preferred since those strategies mitigate the computational cost [33], [34]. The computational advantage of periodic lattice structure optimization is also utilized by many researchers in a hierarchical multiscale design process that incorporates ground structure optimization at mesoscale or lattice cell level with macroscale (or product) level simulations to also design the overall product dimensions [35]. Although the periodic lattice structure approach can decrease computational cost, efficient optimized structures are obtained only when evenly distributed loads are applied to the structure; the structure is over designed when the applied load on the structure is not uniform.

To overcome the increased computational cost of the conventional ground structure optimization method for non-periodic lattice structures, a size matching and scaling (SMS) method has been developed [36], [37]. The SMS method matches the optimized lattice cell to the stress information obtained from the solid body FE analysis of the structure. Then, a two-variable optimization process is used to determine the structure's minimum and maximum cross-sectional properties so that the computational cost can be mitigated compared to the cost of the ground structure approach due to the dramatic decrease in the number of design variables. To overcome the problems of handling multiple loading conditions for lightweight discrete lattice structure designs, Al-Zahrani et al. [38] proposed the relative density mapping (RDM) method, which utilizes the relative density information obtained from continuous topology optimization process to identify the members in the optimal lattice topology and to compute the diameter of each individual member in the lattice structure. This method significantly reduces the computational cost of optimization process compared to grounds structure optimization and SMS methods since it only requires the continuous topology optimization results and completely eliminates the time consuming size optimization process of the lattice structure members. Even though the SMS and

RDM methods provide considerable computational cost reduction, the performance of the optimized structures is still limited compared to the performance of the structures obtained from the conventional ground structure optimization process [38].

As different from the optimization processes mentioned above for the problems with fixed topology, moving size or connections are also considered in the lattice structure optimization. Brackett et al. [39] proposed a design methodology to generate lattice structures with varying cell size rather than fixed, having the performance dependent on the orientation of the structural elements, which was stated to be challenging to determine. Ning and Pellegrino [40] introduced a size distribution field using multiple optimization steps was implemented to control the lattice microstructure of the lightweight sandwich beam designs. Delaunay triangulation was used to reduce the number of control variables to a manageable size. The sandwich structure is optimized for sizing with the best topology solution obtained. Shea and Smith [41] determines the optimal topology, shape, and member sizes using graph grammars and simulated annealing methods for transmission tower designs with lattice structures.

The truss or beam elements, used in modeling the strut members of the lattice topology in the above mentioned optimization processes, ignore the effect of joints of struts on the product response. Hence, the designed structure may result in inaccurate prediction compared to the fabricated design of the models. This issue can be eliminated when solid FE elements are used in the modeling of the lattice materials. However, using solid elements for modeling the entire structure hinders the optimization process because a large number of solid elements are required to model the structure. Homogenization-based topology optimization, proposed first by Bendsøe and Kikuchi [42], can alleviate this computational burden caused by the solid elements. This approach utilizes a multiscale modeling technique to simplify the simulations by discretizing the

global structure domain into hexahedral solid elements. Each solid element in the global structure model represents a composite material with a microstructure that has a rectangular void (i.e. a simple cubic lattice cell) with a size parameter (and a rotation parameter) of the void that produces a density value for the corresponding element. (i.e. a large void means a low material density and vice versa). A homogenization method is utilized for each global element to model the detailed microstructure with some homogenized properties. Then, these homogenized properties are used at the global structure model instead of modeling the detailed microstructure of each element in the optimization to find the corresponding densities of elements for the given objective functions and constraints [43]. The details of the homogenization-based topology optimization and a more detailed literature review are given in Chapter 2. Since the multiscale modeling and homogenization approaches are crucial for the design of CLSs using homogenization-based topology optimization process, a general introduction to these concepts is provided in Section 1.3.

1.3. Multiscale Modeling and Homogenization

1.3.1. Multiscale Modeling

Multiscale modeling is used to describe a material domain or a system by multiple models that focus on different scales of resolution. The current surge of interest for multiscale modeling is due to the growing need in various engineering fields to solutions to problems in different scales to obtain more reliable designs and to mitigate the computational complexity. Rapid advances in computational capabilities have made it possible to investigate the effects of details at finer scales on the overall performance so that multiscale modeling techniques can be used for the design of materials, structures, and systems. In particular, the information based on defects, microstructure, and their interaction from the atomic scale is passed to micro-scale and eventually to macro-scale

by bottom-up multi-scale modeling strategies [44]. Efficient multiscale modeling methods have been utilized in a wide range of engineering applications in the literature such as modeling the vapor deposition process in chemical engineering [45], modeling the tissue perfusion in biomedical engineering [46], flow analysis in the geotechnical engineering [47], etc. Multiscale modeling methods have also been used in the design processes of materials and mechanical components to develop more reliable structures and products by utilizing the detailed fine scale information [48]-[51]. Various deterministic multiscale modeling techniques in solid mechanics area, which attempt to develop linking mechanisms between the fine scale and coarse scale constitutive equations by using explicit definitions, have been developed including variational multiscale method [52], heterogeneous multiscale method [53],[54], multiscale finite element method [55], etc.

Existing multiscale techniques used in various disciplines can be classified into two different strategies as (1) concurrent multiscale modeling and (2) hierarchical multiscale modeling [56], [57]. In concurrent multiscale modeling techniques, the individual scale analyses are fully coupled and used concurrently. The information needed by the macroscale or coarser scale models are computed from the finer scale models during the computation of the coarser scale models. The concurrent nature of the computations provides more accurate predictions, but these techniques are often computationally more expensive than the hierarchical approaches since all computations are carried out concurrently [50].

In hierarchical multiscale modeling techniques, some properties or information required for the macroscale model are computed using separate fine scale models without coupling. More specifically, the physical system's deterministic effective parameters, i.e. properties, constants, or representative unit processes, are calculated at finer scales transferred up through scales to form effective or equivalent parameters by using scale-linking mechanisms which are called upscaling

or homogenization techniques [58]. The individual scale analysis that is performed separately from the other scales allows for a simpler technique than the concurrent technique for information exchange across scales. Moreover, when considered in design processes, distinct objectives might exist at each level of the hierarchy, which requires individual analysis of models at different scales [1]. Therefore, hierarchical multiscale modeling techniques have been widely used in literature for mechanical analysis [59] and design [49]. [50]. Homogenization-based topology optimization [42], introduced in Section 1.2, is an example of using multiscale modeling approach in the design of CLSs. It utilizes a simplified model with homogenized properties that represent a microscopic level material in the design optimization process.

1.3.2. Upscaling/Homogenization

Upscaling, or homogenization, is a way of substituting a heterogeneous material with microscopic details to model the material as a continuum with homogenized properties. In bottom-up hierarchical multiscale modeling techniques with multiple scale levels of interest, if the homogenized material properties can be determined at one level using a homogenization method, then a constitutive law that can explain how the material behaves with these homogenized properties can be used at the subsequent scale level. Thus, simplified models defined by some homogenized or effective material properties can be used in product design and analysis rather than modeling the entire domain with detailed fine scale information.

The earliest homogenization methods are called analytical or classical homogenization methods [60], which have been developed to predict homogenized material properties of matrix-inclusion problems using the theory of continuum micromechanics, such as Eshelby method [61] and its extensions like Mori-Tanaka method [62] and self-consistency methods [63]. Various

methods of volumetric averaging such as the Voigt [64] and Reuss [65] models have also been proposed. In the studies such as Gibson and Ashby [3], Wang and McDowell [66], [67], closed-form expressions for the effective material properties are provided for several 2D lattice cells and honeycombs. These analytical homogenization methods are developed based on many assumptions such as periodicity and the uniformity of the material, and there exist many restrictions on the geometry, on the type of the microstructure, etc. To eliminate these limitations, computational homogenization methods, which are based on the finite element (FE) method of the representative volume element (RVE) or the unit cell model of the microstructure, have been developed [68]. The homogenized tensors are determined from the fine scale FE analysis responses using some analytical upscaling formulations such as asymptotic homogenization method [69], discrete homogenization method [70], reduced order homogenization method [71], etc.

The application area of computational homogenization methods is not restricted to matrix-inclusion problems since detailed microstructure of the material can be modeled in the FE model of the RVE. Hence, the computational homogenization methods have also been used to characterize the material properties of the cellular structures. Of these studies related to the cellular structures, most of them focus on employing computational homogenization methods to determine the deterministic effective material properties of unit cells for multiscale analysis [72], [73]. Hutchinson and Fleck [74] and Elsayed and Pasini [75] introduced matrix-based techniques to characterize the material properties of 2D lattice cells. Vigliotti and Pasini [70] extended this approach to the analysis of three-dimensional 3D lattice cells. These studies generally assume the lattice elements behave like beam or truss elements, which cannot capture the deformation of the material at the cell joints and has inaccurate results for increasing values of relative density.

As stated in Section 1.2, shell elements to model 2D lattice structures and solid FE elements to model 3D lattice structures are utilized to address the issue of modeling with beam or truss elements. Bendsøe and Kikuchi [42] used shell elements for modeling the 2D square lattice cell and utilized asymptotic homogenization method in homogenization-based topology optimization method. On the other hand, the lattice structures with designed microstructural materials that has intermediate densities that cause problems when those are fabricated with the conventional manufacturing techniques because of the limitations of the fabrication techniques. With the current advancements in the AM area it is now possible to fabricate these intermediate densities which produce the optimized lattice cells. Hence, recently the homogenization-based topology optimization is utilized by many researchers in the design of medical implants. Arabnejad and Pasini [76] implemented the asymptotic homogenization method to derive the closed-form expressions of the effective material properties for various 2D lattice cell types for the whole range of relative density. In a following study, Khanoki and Pasini [77] integrated this homogenization approach with optimization process of lattice-based structures for the multiscale design of orthopedic hip implants. The optimization process is similar to the topology optimization with homogenization that is first introduced by Bendsøe and Kikuchi [42] in the sense that the relative densities are found for discretized regions in the structure during the optimization process. The homogenized properties are used at macroscopic level FE analysis of the hip implant geometry to generate a graded lattice material.

Although the homogenization-based topology optimization enables the design of CLSs in a computationally efficient manner, there exist increased variations and uncertainties at the strut level in the microstructure and geometry induced by the AM process parameters. These fine scale details and uncertainties are needed to be considered in multiscale modeling process of the CLSs

to have the desired performance from the AM-fabricated lattice structures. Existing studies on CLS area, on the other hand, have rarely utilized a multiscale modeling technique to account for the uncertainty effects at a small scale levels resulting from AM fabrication of lattice structures. The challenges of available engineering analysis and design processes when the fine scale uncertainties are considered is discussed in Section 1.4.

1.4. Uncertainties in Engineering Analysis and Design

A true representation of the uncertainties is crucial for the accurate characterization mechanical performance of the engineering structures with computational models because the different representation of the uncertainties may lead to different interpretations of the given system. Primarily the uncertainty in a system can be divided into two categories as "Aleatory uncertainty" and "Epistemic uncertainty." The former is also known as irreducible uncertainty or the inherent uncertainty of the system while the latter is the uncertainty due to the lack of knowledge and/or data. Epistemic uncertainty can be reduced when more information is gathered for the present state of the system. However, aleatory uncertainty inherently exists and therefore cannot be reduced. For example, when the diameter of each layer fabricated to build a strut member of a CLS is measured, there will be a certain statistical distribution of the data. Such statistical information, gathered from experiments for an uncertain variable, are in the definition of aleatory uncertainty.

In this dissertation, we limit our scope and research for the case where only aleatory uncertainty is considered. As it cannot be reduced, aleatory uncertainty should be quantified to be able to account for its effect on the predictions made by the computational models. If sufficient data is available, aleatory uncertainty can be quantified using a probability density function (PDF) that provides a parametric distribution model (Gaussian, Gamma, Extreme value, etc.) for the

statistical data of an uncertain variable. The parameters of a PDF are estimated by fitting the distribution to the underlying available statistical data. More details about uncertainty quantification methods are provided in Chapter 2 while this section is continued with the review of computational modeling of CLSs under uncertainties.

1.4.1. Uncertainties in Computational Modeling of CLSs

In the area of CLSs fabricated by AM technologies, the uncertainty effects of process parameters on the fabricated strut members result in a discernable mismatch between the mechanical performances of the simulated and fabricated structures. The reason is that the fabricated struts that comprise the CLSs have uncertainties and imperfections in material and geometry due to the limited resolution and inherent uncertainties in the process parameters of the AM techniques. Accordingly, additional efforts are required to estimate the performance of the additively manufactured structures accurately. Cansizoglu et al. [79] show the effect of build angle and orientation on overall material properties of lattice structures fabricated by the EBM process. Parthasarathy et al. [80] experimentally prove that the diameters of the struts in the lattice-based scaffolds fabricated by EBM process differ from the diameter values of their 3D CAD models. Harryson et al. [81] report that the members (i.e. struts) of lattice structures in AM-fabricated implants have a rough texture with varying cross-sections, which result in inaccurate FE model predictions if not considered. However, the computational models of the designed lattice structures will not account for the material imperfections such as microporosity and the variations on the strut geometry such as the surface roughness by their nature. Additional efforts are needed to account for these details in the computational models. Cahill et al. [82] show that the FE models of lattice-based scaffolds that consider the rough surface caused by the SLS process on the strut

members resulted in better predictions than the models with smooth strut surfaces when compared to experimental results (Figure 1.3(a)). Similarly, Campoli et al. [83] and Ravari et al. [84] consider the geometric variations in the strut's diameter along their length in FE models of the lattice structure specimens and show that the incorporation of variations improves model predictions.

Although the computational models of the lattice structures that considers the geometric variations produce improved predictions compared to the reality, tremendous amounts of computational effort are needed to solve these detailed lattice structure models as the complexity of the model increases dramatically. To overcome this computational issue, several researchers attempt to investigate the mechanical behavior of the lattice structures at two sequential levels: (1) individual strut level (2) lattice level. Tsopanos et al. [85] and Gumruk et al. [86] show experimentally that the material properties obtained from tensile tests of individual struts differ from the material properties obtained from the tensile tests of the regular dog-bone shape specimens for the same material fabricated by SLM process. Hence, they utilized the material properties, obtained from strut level experiments with individual strut specimens, in the lattice structure FE model by assuming constant strut cross-sections (Figure 1.3(b)). Thus, the computational complexity that increases by considering the detailed variations in FE model of the lattice structure is mitigated while having improved accuracy. Doyle et al. [87] generate high-resolution FE models of individual struts based on the micro-CT scan images obtained from the fabricated strut specimens by SLS process to capture the heterogeneity in mechanical properties and variations on the strut geometry. Suard et al. [88] implement the same FE model generation approach at strut level to investigate the surface roughness and the porosity in the struts fabricated by EBM process and to predict the effective strut diameter and elastic properties. Then, these strut

level effective properties are used in modeling the lattice cell model to simplify the characterization process of the overall material properties of the lattice structures (Figure 1.3(c)).

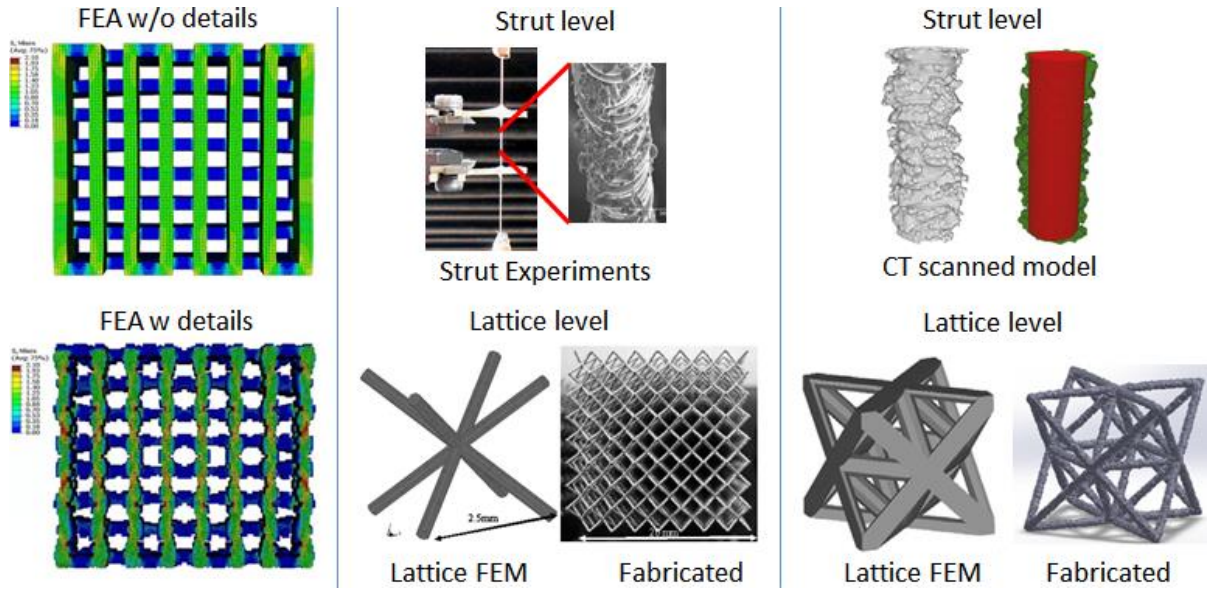

(a) FEA of CLS without details (top) and FEA with details (bottom) [82]. (b) Two level modeling of CLSs fabricated by SLM [85], [86]. (c) Two level modeling of CLSs fabricated by EBM [88].

Figure 1.3. Computational modeling of CLSs

Although the characterization of the equivalent or homogenized properties at strut level had produced improved predictions at lattice structure level compared to the predictions made without the strut level experiments, existing studies usually deal with the variations at strut level in a deterministic way and ignore the effect of uncertainties. Moreover, fabricating single struts each time for experiments can be time-consuming and expensive. The designer should be able to expect to predict the mechanical properties of the lattice structures with minimal experimental cost and design time. Park et al. [89] develop a voxel-based FE model generation process of individual struts with the geometric variations on the strut surfaces o mimic the FDM process. The uncertainties of the fabricated layer diameters are considered in predicting the equivalent strut

diameters based on the simulation results of the voxel-based strut models. Similar to the work of Suard et al. [88], the equivalent strut diameter is used at the lattice level to estimate the effective elastic properties of the lattice structures with reduced complexity using a deterministic homogenization method. Although uncertainties are considered at strut level to find the equivalent strut diameters, the effective properties of the lattice structures are predicted again in a deterministic setting.

Uncertainty, however, gains importance in lattice structure performance because there is a higher probability of introducing manufacturing error when lattice structures are fabricated by the AM processes. Since the length scale of the fabricated strut members of a lattice structure is usually very small, the mechanical responses of the fabricated structures will be much more sensitive to the unavoidable uncertainties. For this reason, unlike the aforementioned multi-level modeling approaches which use only the deterministic equivalent values for characterizing the effective properties of the lattice structures, the uncertainties are needed to be quantified at finer scale levels and propagated to the lattice structure level for more reliable predictions. In Section 1.4.2, the computational challenges of multiscale modeling techniques when fine scale uncertainties are considered are discussed.

1.4.2. Multiscale Modeling under Uncertainty

The multiscale modeling and homogenization methods described in Section 1.3 have found wide applications in the simulation and design of materials, (whether they are lattice structures or other materials such as composites) in a deterministic setting. On the other hand, uncertainties induced by the manufacturing processes on the material and geometry of the fabricated parts prevent to have a safe design that can perform according to the design specifications. Deterministic

approaches cause severe limitations when the randomness at fine scale should be taken into account for reliable designs since a fully resolved stochastic treatment of the problem would be computationally prohibitive. Consequently, stochastic analysis methods are integrated with the deterministic techniques to propagate the uncertainty information across scales [78]. Multiscale stochastic finite element method [90] and stochastic variational multiscale methods [91] are some examples that have been developed for stochastic multiscale modeling. A stochastic RVE (SRVE) can be used to characterize the homogenized material properties using an upscaling sampling scheme to determine the probability model of fine scale information [92], [93].

These methods, on the other hand, have two main issues that increase the computational cost when uncertainties are considered. The first problem is that the upscaling processes used for multiscale modeling lack efficient computational techniques and usually require complex linking mechanisms; that penetrates the explicit governing equations at continuum level for the calculation of homogenized macroscopic parameters that can account for microscopic uncertainties [94], [95]. The lack of efficient computational techniques is compounded when these multiscale modeling techniques are used in the design optimization processes. The 'curse of dimensionality' in obtaining statistical moments for multiple random variables and the intense programming effort are the drawbacks for constructing such models. To address this computational issue, upscaling methods that will not require penetration of complex equations is needed.

The upscaling process can also be achieved through optimization where the homogenized properties are found for a coarser FE model that can represent the fine scale model with uncertainties. The dimensionality in the optimization, on the other hand, should be reduced in these methods since a large number of sample values must be predicted to represent the uncertainties of the homogenized properties accurately. In that regard, Koutsourelakis [97] introduce a stochastic

upscaling method through optimization that utilizes the rate distortion theory, which enables the representation of the distribution of the homogenized input variable with a relatively small number of sampling points. Even though this approach provides a dimension reduction in the optimization process, the accuracy of the results is questionable as it attempts to represent the distribution of a small number of samples. Arnst and Ghanem [98] utilize Polynomial chaos expansion (PCE) [99] to reduce dimensionality for predicting the homogenized data in the upscaling process through optimization. Since these methods for upscaling through optimization eliminate the use of complex explicit equations to find homogenized properties, they are promising to be used at multiple levels to characterize the properties of lattice structures with fine scale uncertainties.

The second issue is that the multiscale modeling techniques usually deal with the homogenization at the microstructure level of the material. Uncertainties that exist at the scale levels finer than the microscale levels are typically ignored in the homogenization process since including all of the fine scale details and uncertainties into the microstructure model involve enormous computational complexity. The solution to this problem is to decompose the microstructure into different levels and propagate the uncertainties between scales by utilizing homogenization methods at multiple levels. For instance, Shokrieh and Rafiee [100] investigate the material properties of a composite material, i.e. a carbon nanotube reinforced polymers, in four different levels to propagate the uncertainties at the nanoscale level to the final macroscale level. Different upscaling approaches are utilized for homogenization at each scale level since different laws exist for various scales, which increase the computational complexity of the multiscale modeling techniques. Hence, the lack of efficient computational techniques and homogenization methods still offers research opportunities which needed to be explored.

Overall, the uncertainties induced by the AM process parameters have a considerable effect on the overall product performance, but the current simulation and experimental efforts are not effective for the certification of CLSs fabricated by AM under uncertainties. Therefore, it is essential to deliver an improved upscaling framework that accurately quantifies the effects of input uncertainties at multiple scale levels. The framework should also be able to propagate the uncertainties from one scale level to another without requiring an excessive computational cost. Moreover, efficient validation techniques will be needed to assess the accuracy of predictions made by the multiscale modeling techniques used for uncertainty propagation across multiple levels. Thus, these multiscale modeling techniques can be integrated into the design process of the structures to account for the finer scale uncertainties. The verification and validation approaches used in prediction assessment of computational models are introduced in Section 1.5.

1.5. Verification and Validation (V&V) in Computational Modeling

Over the last two decades, validation and verification (V&V) of computational models has been the focus of a significant number of study and a relatively large literature exists and expanding [101], [103]. The consistency and the distinction in the definitions of verification and validation terms is well established today as provided by science and engineering communities such as the American Institute of Aeronautics and Astronautics (AIAA) guide for fluid mechanics [102], the American Society of Mechanical Engineers (ASME) guide for Computational Solid Mechanics [103], etc. Although the V&V application areas show variety, the definitions are general: Simply stated, verification is the accuracy assessment of a simulation model by known exact mathematical models, while validation is the evaluation of the model predictions by the real world [101].

More importance is given to the validation processes in the literature for assessing the reliability of computer predictions since verification is often an achievable possibility due to the today's powerful computers while the validation is the major challenge for the computational models [104]. The fundamental validation strategy involves identification and quantification of the error and uncertainty in the computational models, estimation of experimental uncertainty, comparing the computational results with the experimental data by a validation metric, and finally measuring the difference by a rejection criterion (i.e. a threshold value of the validation metric) to assess the validity of the model [101]. For the complex systems under consideration, on the other hand, the true validation experiments are difficult, expensive or impractical to conduct at the system level. Therefore, the validation process can be divided into several phases of increasing complexity, beginning with low-level unit problems, then benchmark cases, then subsystem cases, and finally the complete system [103]. When the validation of models is very difficult or impractical because of the limited knowledge of physical characteristics or material properties, calibration or parameter estimation with statistical methods gains importance in the validation assessment. This procedure is represented by a validation pyramid [105] starting with calibration model at the bottom, and the prediction model at the top of complex systems. The complexity and the cost of experiments increases as we move up (i.e. approaching the prediction) and the pyramid gets narrower, showing that the number of experiments decreases from bottom to top with increased complexity.

One key fundamental step in V&V efforts is to quantitatively assess the comparison of the model predictions with corresponding experimental observations using a validation metric. Various types of quantitative metrics have been proposed over the years for the validation of computational models. Oberkampf [101], Liu et al. [106], and Ling and Mahadevan [107] have

attempted to collect and discuss various validation metrics. Depending on the nature or form of the model output and experimental data, the validation metric may involve comparison of means or variances or even two probability distributions. Hypothesis testing methods have been explored to make a decision (model is accepted or rejected) based on a test statistic method according to the differences between the moments or distributions of the model and experiment results for model validation assessment in recent literature [108], [109], etc. Among these metrics, the area validation metric [101], which measures the area between two CDFs, is shown to be superior to the existing validation metrics in many papers [106] - [109]. Ferson et al. [110] extended the use of area validation metric for the cases of multiple validation sites and proposed the u-pooling method to assess the global predictive capability of a model. Li et al. [111] introduced new validation metrics that allows the use of the u-pooling method for the cases when there are more than one responses and when the responses are correlated.

Validation of multiscale models proceeds in a similar model to the validation process of the complex systems; ideally, experimental validation would occur at each scale level simulated (e.g. macroscale and microscale). Because of the important role that validation plays in interpreting the results of computational studies, it is desirable to develop multiscale modeling strategies and the validation methods concurrently. Accordingly, some studies are found in the literature that implement validation processes for multiscale modeling. Farrell and Oden [112] utilizes the above-mentioned validation pyramid method at atomic scale level for the validation of a coarse-grained model that represent the atomistic scale at a coarser scale. Oden et al. [113] present a multiscale system validation approach for polymeric materials, but this approach only replaces the physical calibration experiments with the micro scale model outputs (called “virtual experiments”) and replace the validation experiments with outputs of a hybrid model that includes both molecular

model and finite element model. Oskay and Fish [114] presented a calibration and validation framework wherein the input parameters used in the microscopic level homogenization method are calibrated using the macroscopic level experiments. These multiscale model validation approaches indicate that validation of the fine scale models can currently be done using either detailed fine scale simulations or macroscopic level experiments since the finer scale level (e.g. microscopic level) experiments are not usually available. Hence, when the validation of models or simulations of multiple levels of scales is of interest, development of effective validation approaches for fine scale models is still a largely open problem.

1.6. Research Questions and Hypothesis

The goal of this dissertation is to develop an efficient multi-level upscaling and validation framework for quantification of uncertainties at small scale levels of complex structures/materials, and for the propagation of these uncertainties to the macroscopic level computational models that will be used in mechanical analysis and design of complex engineering structures for accurate prediction of reality. For this study, we constrain our analysis of complex structures to cellular lattice structures (CLSs) fabricated by AM techniques, which are being used in recent engineering applications due to their light weight and high strength characteristics. However, the framework is generalized to apply to any complex engineering structure that incorporates computationally intensive simulations and/or expensive experiments under uncertainties.

As stated in Section 1.4.1, since a large variety of uncertainties exist at the strut level of the CLSs due to the layer-by-layer manufacturing process, evaluating the structure performance using direct simulations of the final structure with fine scale details is computationally infeasible. Moreover, the current simulation and experimental efforts in this area are not effective for the

certification of CLSs fabricated by AM under uncertainties. To be able overcome this computational issue, we need to concentrate on the trade-off between two goals that determine the efficiency of the developed computational models: "minimizing the complexity" and "maximizing the accuracy." Instead of simulating all of the details at once, multiscale modeling processes with upscaling/homogenization methods are utilized in the literature to address this trade-off. However, as stated in Section 1.4.2, there are two main computational issues with the upscaling methods: (1) The homogenized properties are often determined by complex linking mechanisms that link the fine scale domain with a coarser scale domain defined by explicit governing equations. (2) The available multiscale modeling techniques usually deal with the homogenization at one scale level of the material. Hence, when the increased uncertainties at fine scales (e.g. on the strut members induced by AM at the microscopic level) are considered in multiscale modeling, these multiscale modeling techniques still possess increased computational complexity. This computational burden becomes much greater when the multiscale modeling techniques are used in the design optimization due to the repetitive (or iterative) nature of these processes. To address these issues, the following research question is formed as the ***Research Question 1***:

> ***Research Question 1*:** How can we efficiently quantify and propagate the fine scale uncertainties to predict the performance of human scale structures?

An answer to this question will provide us a multi-level upscaling framework that will enable the quantification of uncertainties at small scale levels and propagation of them to the macroscopic or human scale level with minimal computational effort. We hypothesize that an improved homogenization method that is based on the upscaling through optimization approach described

in Section 1.4.2 can eliminate the use of complex linking mechanisms to provide the homogenization of the fine scale domain with propagated uncertainties in a computationally efficient manner. In upscaling through optimization, the homogenized properties of the coarse scale model are found with an optimization algorithm that matches the fine scale model responses with the coarse scale model responses. Hence, a simulation-based coarse scale domain FE model, which can represent the fine scale domain FE model with some homogenized properties, can be constructed without penetrating the explicit governing equations of the coarse scale domain. PCE is used to handle the dimensional complexity while quantifying the uncertainties of the homogenized properties in the upscaling method. An effective objective function to match the fine and coarse scale model responses is also integrated into the upscaling method, along with a hybrid optimization algorithm to reach the optimum solution quickly.

Moreover, for accurate quantification of the uncertainties on the final structure performance, the small scale level uncertainties in the material properties (e.g. porosity) and in the geometric properties (e.g. surface roughness, diameter, etc.) must be quantified based on the statistical data of the fine scale input variables. For this purpose, it is hypothesized that in the improved upscaling method, the fine scale input uncertainties can be quantified using parametric distribution models. Then, these quantified uncertainties can be utilized in the generation of fine scale FE models and propagated to the lattice structure level FE models through the upscaling method, which can be used at each level of interest sequentially. More details about these improvements in the proposed upscaling method are explained in Chapter 3. Thus, the uncertainties of the homogenized properties can be quantified efficiently at each level of interest and propagated across multiple levels sequentially from bottom up with the proposed upscaling method. Then, ***Hypothesis 1*** to address Research Question 1 is:

Hypothesis 1: A multi-level simulation-based upscaling method based on PCE can enable the efficient quantification and propagation of uncertainties at each scale level sequentially.

Our general goal is not only to establish principles for constructing a meaningful multi-level upscaling framework that preserves the key properties of the fine scale models on which they are based but also to develop a meaningful validation approach for the prediction accuracy assessment. In a hierarchical multi-level modeling framework, the validation should be conducted at each level of interest to evaluate the accuracy of the predictions made when the homogenized properties are used in the simulation. However, the scale of the lower levels is too small, and experiments are usually very expensive or impossible. Furthermore, the level of the available experiments may be different from the level of the homogenization in such a hierarchical modeling approach. Alternatively, a limited number of experiments may exist at the same level, which may not be sufficient to evaluate the predictions under uncertainty. Hence, we need to formulate a validation approach that can leverage from the available experimental data in the most efficient way to minimize the experimental cost in evaluating the prediction accuracy of computational models used in the multi-level upscaling method. This leads to the following question formed as ***Research Question 2***:

Research Question 2: How can we improve the prediction accuracy of computational models used at multiple levels while minimizing the experimental cost?

For a hierarchical multi-level modeling framework, a top-down decomposition of the system or product at macroscale level into multiple sub-levels (e.g. mesoscale, microscale, etc.) requires a hierarchical validation approach similar to the validation pyramid approach [105] used for complex engineering systems. However, at finer scale levels, it is difficult or impractical to implement physical experiments since the scale is too small to physically model. Therefore, in the multi-level modeling, the validation with experimental results is performed at the levels where the validation experiments could be achieved. At a level of scale where the experiments are not available, we hypothesize that we can use a "pre-validation" step, in which a different fine scale model than the one used in the upscaling process (e.g. a larger size of the model at the same level) will be employed for the validation of the homogenized properties. This step can increase the confidence in the predictions made at the level where the experiments are not available. For example, micro-CT scan images of the experimental specimens can be used to reconstruct the computational models at the levels where the experiments are not possible and to quantify the uncertainties of input parameters used in the modeling process. This approach will enable the validation of the predictions of the generated models with those of the reconstructed models at small scales where the individual physical experiments are not available so that a generalized validation step that can be used at each level can be developed.

Another way of using the available experimental data in the most efficient way is to utilize a validation metric that can make a decision about the validity of the predictions by accounting for the number of experiments. For this purpose, we hypothesize that the u-pooling method, which is based on the area validation metric [110], can be integrated with a hypothesis testing method that considers the number of experiments for making a decision. Thus, the number of experiments can be increased by considering multiple validation sites in the evaluation of the accuracy, and a

decision criterion can be set correctly regardless of the available number of experimental data, which is the issue of the existing validation metrics. This metric can be used at any level as the validation metric that will allow for the user to quantify the validity of the model without requiring time-consuming approaches and different validation metrics. The details of the validation approach will be given in Chapter 4. ***Hypothesis 2*** to address Research Question 2 is:

> ***Hypothesis 2:*** The experimental cost can be reduced by using a hierarchical validation approach integrated with an efficient validation metric.

Once the multi-level upscaling and validation of a lattice structure is achieved, the model predictions can be used in designing lattice structures to eliminate the expensive simulations in the design process. For this purpose, we need to integrate the multi-level upscaling method into a design framework which will enable accurate prediction of reality while designing the cellular lattice structures. Hence, to accurately and efficiently design a lattice structure by accounting for the small scale details and uncertainties, the last research question of this dissertation is presented as ***Research Question 3***:

> ***Research Question 3*:** How can the proposed multi-level upscaling framework be used for the realistic design of complex engineering structures?

To answer the ***Research Question 3***, we hypothesize that a stochastic meta-modeling technique can be developed based on the upscaling method predictions on the homogenized properties of given lattice cell types. More specifically, the uncertain homogenized properties of the lattice cells

are determined in terms of PCEs using the proposed multi-level stochastic upscaling method for various density values of the corresponding lattice cell. Then, a meta-model can be developed for each PCE coefficient using the pre-calculated PCE coefficient values at some densities as the training data. This developed meta-model can be used to design lightweight CLSs to match the target properties so that the use of expensive simulations in design can be eliminated while achieving a realistic prediction of the effective properties of the CLS designs. Thus, the use of the proposed multi-level upscaling and validation approach for the design of the CLS will prove the efficacy of the proposed approach in engineering design problems. The details of this procedure as well as an application example that is designed to match the target elastic modulus are given in Section 5. Hence ***Hypothesis 3*** is:

> ***Hypothesis 3*****:** The proposed framework can be used for developing a stochastic meta-model to predict the homogenized properties of CLSs with the propagated uncertainties that will be employed in the design of engineering structures.

1.7. Current Research

The goal of the current research is to efficiently quantify the fine scale uncertainties induced by the manufacturing process at small scale levels and propagate them to the final structure level for realistic prediction of the designed structure performance. To achieve this goal, a multi-level upscaling and validation framework is proposed in this dissertation. The proposed framework utilizes an efficient uncertainty quantification approach with an improved stochastic upscaling method. The upscaling method finds the homogenized properties using the simulation-based fine scale and coarse scale models and the PCE to efficiently propagate the quantified fine scale

uncertainties across multiple levels and finally to the end structure model. The improved upscaling method is integrated with the validation pyramid approach for the assessment of the prediction accuracy at each scale level. A validation metric is also proposed to achieve the comparison of model predictions with experimental data for minimal experimental cost while evaluating the predictions made at each level of scale in terms of accuracy. Thus, the current research establishes a multi-level upscaling and validation framework for efficient uncertainty quantification and propagation in the modeling process of lattice structures. The proposed framework is generalized to apply to any complex engineering structure that incorporates computationally intensive simulations and/or expensive experiments associated with fine scale uncertainties.

This proposed framework is also used for design by developing meta-models of homogenized properties of CLSs fabricated by AM with propagated uncertainties from the fine scale levels. In existing design approaches, the homogenized properties of a CLS are estimated in a deterministic setting by applying a homogenization method to the model of a lattice structure with continuum level elements. However, since a discernable mismatch is seen between the performance of the designed lattice structure and that of fabricated one using AM, the increased uncertainty effects of process parameters on the strut members must be considered in an efficient way. Thus, a multilevel uncertainty quantification and validation approach are developed and integrated into the design of lattice structures to accurately predict the reality and to eliminate the use of expensive simulations in design. The following chapters describe important aspects of the proposed framework for uncertainty quantification and validation of the cellular lattice structures, which will result in the accurate design of lattice structures with efficient PCE-based meta-models. In Section 1.8 the organization of the dissertation is described.

1.8. Thesis Organization

The organization of chapters of the dissertation is given in Table 1.1. In Chapter 1, an introduction along with literature review is provided about CLSs, the design of these structures using topology optimization methods, and the concept of multiscale modeling, homogenization, and verification and validation. Uncertainty in of complex structures, specifically in cellular structures fabricated by AM processes, are also introduced. The challenges of the modeling approaches, which are to be addressed when uncertainties are considered, are discussed. The chapter is ended by presenting the research questions and the corresponding hypotheses.

Table 1.1. Organization of the Dissertation

Chapter 1	Introduction
Chapter 2	State of the Art
Chapter 3	Improved Stochastic Upscaling Method
Chapter 4	Multi-level Validation Approach
Chapter 5	Application of Upscaling Method to Design CLSs
Chapter 6	Conclusion and Future Work

In Chapter 2, the state of the current research in the fields of uncertainty quantification and propagation is described, and the theoretical foundations are introduced. The technical description of the homogenization methods used in the multiscale modeling processes of materials and the basics of the ones that are the most prevalent are also provided. Moreover, boundary conditions

used in the homogenization processes are discussed. Verification and validation of computational models are introduced, and the current state of the validation metrics utilized in the assessment of prediction accuracy are also discussed. The literature and the theory of the optimization approaches to design the cellular lattice structures are provided. In the light of the presented state of the art, the reasons are discussed in details to justify why the suggested methods are utilized in the proposed upscaling and validation framework.

In Chapter 3, the detailed explanation of the theoretical framework for the stochastic upscaling method through optimization is provided. The improvements proposed to provide a computationally efficient upscaling approach for uncertainty quantification and propagation is explained in detail. In particular, the formulation of the optimization process in the stochastic upscaling method and the proposed exponential loss function for effective matching of responses are described. The justifications of using PCE as the dimension reduction method in the upscaling approach are discussed. The general framework of the improved upscaling method and the multi-level upscaling approach are presented. The applicability and efficacy of the proposed upscaling method are demonstrated by utilizing it for three engineering examples including the evaluation of the accuracy of various objective functions in a simple bar example, reliability assessment of a lattice-based storage tank design, and uncertainty quantification and propagation at multiple levels for lattice structure specimens fabricated by a material extrusion process. These examples are used to validate the *Hypothesis 1* for the *Research Question 1*.

In Chapter 4, the multi-level validation framework that utilizes the idea of validation pyramid is introduced in detail. The formulation of the proposed validation metric that integrates the u-pooling method and the Kolmogorov-Smirnov test in quantitative prediction assessment is also discussed and the proposed validation framework integrated with the upscaling method used

at each level sequentially is introduced. The general multi-level upscaling and validation framework is used for accurate uncertainty quantification and propagation of two lattice structure examples fabricated by material extrusion and selective laser melting processes. The efficacy of the proposed framework is demonstrated for predicting the lattice structure performance under uncertainty in these examples. These examples are used to validate the H*ypothesis 2* proposed to address *Research Question 2.*

In Chapter 5, the applicability of the proposed upscaling and validation framework in designing CLSs is demonstrated. A PCE-based metamodeling approach is developed to eliminate the use of expensive simulations in the design of cellular lattice structures. This approach is utilized to generate the meta-model for the elastic modulus of a lattice cell fabricated by SLM process based on the quantified uncertainties by the proposed upscaling method. An illustrative example of micro-aerial vehicle fuselage design, which validates the efficacy of the proposed framework, is shown to match the target elastic modulus based on the developed PCE-based meta-models. This example was used to validate the *Hypothesis 2* for the *Research Question 3.*

In Chapter 6, the main points outlined in the dissertation along with the contributions of the proposed framework are summarized. The limitations of the current research are discussed, and some indications for possible future work are provided.

CHAPTER 2. STATE OF THE ART

In this chapter, state of the art in research related to the uncertainty quantification, validation, multiscale modeling and design of CLSs are presented along with the theoretical foundations. The methods used in the literature are reviewed to address the main issues in computational analysis and design of cellular lattice structures, identified in Chapter 1, as decreasing the computational complexity and experimental cost for (1) uncertainty quantification at fine scales (2) upscaling/homogenization for material characterization with propagated uncertainties (3) systematic validation at multiple scale levels (4) realistic design of CLSs by accounting for uncertainties. This review is presented in six sections. In Section 2.1 and Section 2.2, the most widely used methods are introduced for the uncertainty quantification and propagation in computational models, respectively. In Section 2.3, upscaling/homogenization concept is introduced, the available approaches are described in three categories, the boundary conditions used in modeling the fine scale details are reviewed, and their advantages and disadvantages are discussed to address the identified challenges. In Section 2.4, verification and validation approaches are described in general, and the state of the art review of the validation metrics used for the prediction assessment is provided, and the challenges are revised. In Section 2.5, the theoretical foundations of the deterministic and stochastic topology optimization processes employed in the design of lattice structures are described along with the issues existing regarding the computational efficiency when the uncertainties induced by AM processes are considered in the design. The summary of this chapter is given in Section 2.6.

2.1. Uncertainty Quantification

Uncertainty Quantification (UQ) term could encompass the whole field of statistics since the term defines the process of identifications, quantitative characterization, and reduction of uncertainties in computational and real world applications [101]. The UQ can be viewed as two different types of coupled components. The first one is the inverse assessment of the input uncertainty where the parametric uncertainties are estimated based on available statistical data. The second one is the forward propagation of the input uncertainty, defined by statistical parameters and distribution models using inverse assessment of the input uncertainty, to quantify the model output uncertainties using computational models [115]. Both cases should be considered in modeling the uncertainties in the analysis and design of materials and/or structures. The focus of this research is to develop a framework for both the uncertainty quantification of input parameters and uncertainty propagation to model outputs as well as across multiple scale levels in a bottom-up fashion. To differentiate between these two components (i.e. uncertainty quantification and propagation), in this study, "Uncertainty Quantification" term is used only for the first case, i.e. the inverse uncertainty assessment of random input variables. "Uncertainty Propagation" term is used for the second case, i.e. the forward propagation of the uncertainty to model outputs. Hence, these two are reviewed in two separate sections, i.e. uncertainty quantification is discussed in this section while the uncertainty propagation is reviewed in Section 2.2.

The quantification of uncertainties for the random input variables is considered in two different categories depending on the direct availability of the statistical data. In cases where the experimental measurements or the statistical data are available for a random input variable of the model, the uncertainty is expressed as a probability distribution with some statistical parameters or as interval boundaries of uncertain data. This uncertainty quantification process is called

"statistical modeling" of the random input variables. In cases where the experimental measurements or the statistical data are not directly available for the input variable but available for the output variable of the model, uncertainty quantification for the random input variable is accomplished by so-called "parameter calibration." In parameter calibration, an optimization process is used to find the statistical parameters of the random input variable of the model that minimize the discrepancy between the available statistical data of the output and the output data calculated by the model with predicted input parameters. In the analysis and design under uncertainty, uncertainty quantification of input parameters is necessary since the uncertainty propagation can be achieved using the quantified statistics of the input variables. Hence, if the input variable distribution and parameters are not known, either statistical modeling or parameter calibration methods are used to quantify the uncertainties of the input variables depending on the given data.

2.1.1. Statistical Modeling of the Input Uncertainties

Statistical modeling is the process of finding the statistical parameters and distribution model for the available uncertain data. The simplest modeling procedure is to calculate the arithmetic mean and the standard deviation of the data. For a random variable X with the probability density function (PDF), denoted by $p(x)$, the r-th statistical moment is calculated by

$$M_r(X) = E_r[(X - \mu_Y)] = \int_{-\infty}^{\infty} (x - \mu_X)^r \; p_X(x)\, dx \tag{2.1}$$

The mean of X is calculated for $r = 1$

$$\mu_X = E(X) = \int_{-\infty}^{\infty} x\, p_X(x) dx \tag{2.2}$$

which is also known as the average or the expected value $E(.)$ for a continuous variable. In the case where the random variable X takes discrete random values from a finite data set, i.e. $X = \{x_1, x_2, \ldots, x_n\}$, having the corresponding probabilities $p(x) = \{p_1, p_2, \ldots, p_n\}$, the expected value of the random input variable can be defined as

$$\mu_X = E[x] = p_1 x_1 + \ldots + p_n x_n = \sum_{i=1}^{n} x_i\ p_i(x) \tag{2.3}$$

by averaging the expected values, Eq. (2.3) can be written as

$$\mu_X = \frac{1}{n} \sum_{i=1}^{n} x_i \tag{2.4}$$

Thus, the mean or average is the sum of the numerical values for each particular value of the random variable in the statistical data divided by the total number of data. The mean is also used to describe the central tendency of a random variable. That means the mean is the distance from the origin to the centroid of the PDF.

Standard deviation is calculated as a measure that is used to quantify the amount of variation or dispersion of a set of statistical data values. For a continuous random variable, the root square of the statistical moment equation (Eq. (2.1)) when $m = 2$, gives the standard deviation of the random variable X. In the discrete random variable case, the standard deviation is given by

$$\sigma_X = \sqrt{\frac{1}{n}\sum_{i=1}^{n}\left(x_i - \mu_X\right)} \tag{2.5}$$

where the square of σ is the variance of the data. Once the mean and standard deviation are calculated the distribution model can be assumed as a normal distribution in the simple case. This assumption is true based on the Central Limit Theorem (CLT) if the sufficiently large number of data is available [2]. CLT states that regardless of the underlying distribution, the arithmetic mean of a sufficiently large number of iterates of independent random variables will be approximately normally distributed.

Although this assumption gives some information about the uncertainty, the underlying distribution may differ from the normal distribution in many cases. Hence, considering other distribution models or types is necessary for a more accurate uncertainty quantification process. Various distribution models are available to fit on a given statistical data (e.g. Gaussian or Normal, Lognormal, Gamma, etc.). For the fitting distribution models to the uncertain data and selecting the best-fitted distribution model, two statistical modeling methods exist; by goodness-of-fit (GOF) tests or by model selection methods.

2.1.1.1. Goodness-of-fit (GOF) Tests

The GOF tests are based on a hypothesis testing method such as Cramer-von Mises [116], Anderson-Darling (A-D) test [117], and Kolmogorov-Smirnov (K-S) test [118]. In these hypothesis testing methods, a hypothesis is established by stating that a given data set with a specific cumulative distribution function (CDF) accurately represents a true population. This hypothesis is then evaluated by comparing the predicted CDF and the empirical CDF (ECDF) of

the statistical data. ECDF of a random variable X with independent and identically distributed (iid) observations $X = \{x_1, \ldots, x_n\}$ is calculated by

$$F_E(x) = \frac{1}{n}\sum_{i=1}^{n} I(x_i, x) \text{ where } I(x_i, x) = \begin{cases} 1, & x_i \le x \\ 0, & x_i > x \end{cases} \tag{2.6}$$

where $I(.)$ is the indicator function that is equivalent to 1 if $x_i \le x$ or 0 in other cases. Once the ECDF is calculated for the given data, a difference between this ECDF and a theoretical CDF is measured in terms of a statistic. The hypothesis is accepted only if the statistic calculated from the data is less than a threshold value that is determined as a function of the significance level and sample size; otherwise, it is rejected.

The Cramer-von Mises test [116] is based on the integrated difference between an empirical CDF and a predicted CDF, weighted by the predicted PDF. It is known a very powerful method, but its application is limited to the symmetric and right-skewed CDFs [119]. The A-D test is another hypothesis testing method used widely to quantify uncertainties of input variables. The A-D test is found to be a powerful test since it can consider the tails of the distribution in the statistic calculation [120]. The issue with the A-D test is that it requires different critical values dependent on the type of the distribution being tested. On the other hand, K-S test critical values are independent of the type of the distribution being tested, which makes the K-S test more suitable for testing an unknown distribution. Hence, although A-D hypothesis test is known to be more accurate from K-S test, the applicability of K-S test for any distribution model makes it a better choice [121] than the other test methods.

Kolmogorov-Smirnov (K-S) Test

The K-S test is used to check whether an ECDF differs from a predicted theoretical CDF by evaluating the maximum vertical distance between the two CDFs. The maximum distance, denoted by d_{KS} is calculated by

$$d_{KS} = \max_x \left| F_E(x) - F_M(x) \right| \tag{2.7}$$

where $F_M(x)$ and $F_E(x)$ are the predicted CDF and the ECDF of the statistical data, respectively. Since d_{KS} is a random variable, the CDF of d_{KS} is related to a significance level α as

$$p\left(d_{KS} \le d_{KS}^{\alpha}\right) = 1 - \alpha \tag{2.8}$$

for the confidence level, $1 - \alpha$. Here, d_{KS}^{α} is a critical value obtained from a standard mathematical table presented by Haldar and Mahadevan [122]. The maximum difference between $F_M(x)$ and $F_E(x)$ of the i^{th} sample x_i, for $i = 1, 2, \ldots, n$ is calculated as

$$d_{KS} = \max_{1 \le i \le n} \left| F_E(x_i) - F_M(x_i) \right| \tag{2.9}$$

If the maximum difference d_{KS} calculated from samples is smaller than d_{KS}^{α} based on the significance level α, the null hypothesis that the given samples come from the hypothesized CDF is accepted; otherwise, it is rejected. Similarly, the *p*-value also can be used to test the null hypothesis. The *p*-value is a measure of how much evidence we have against the null hypothesis and calculated as the CDF value of d_{KS}. If the *p*-value is larger than α then the null hypothesis is accepted; otherwise, it is rejected. The test accepts the null hypothesis more strongly when the *p*-value is greater. In the K-S test, since d_{KS} is known to follow the Kolmogorov distribution, the *p*-value is calculated from the Kolmogorov CDF at d_{KS} [118]. Accordingly, using the calculated *p*-

values for various distribution models, a hypothesized CDF with the highest *p*-value is selected as the best fitted marginal CDF in the K-S test.

Although the K-S test can make a decision regardless of the underlying distribution type, since GOF tests are based on an acceptance/rejection criterion, they are more suitable to decide whether a distribution type fits or not rather than evaluating the fitting performance of different distribution types. Hence, GOF tests are preferred more on comparing whether two CDFs come from the same distribution or not while the model selection methods are preferred to select the best candidate distribution model for a given statistical data.

2.1.1.2. Model Selection Methods

Model selection methods select the appropriate distribution model that gives the minimum information loss value among different candidate models. An information loss value is calculated for various distribution models, and the one that has the minimum information loss is selected as the distribution type. A candidate distribution model is fitted to the available data based on Maximum Likelihood Estimation (MLE) [123] using the likelihood functions of the distribution models to find the corresponding optimal statistical parameter values. The goal in MLE is to identify the statistical parameter values that describe the data for a selected distribution type. Given a set of parameter values θ of an unknown PDF, a joint density function of an iid sample is

$$p(x_1,...,x_n \mid \theta) = p(x_1 \mid \theta) \cdot ... \cdot p(x_n \mid \theta) \tag{2.10}$$

If we assume $\{x_1, \ldots, x_n\}$ are fixed parameters of the function and θ are the unknown variables, this function is called the likelihood:

$$\mathcal{L}(\theta; x_1,...,x_n) = p(x_1,...,x_n \mid \theta) = \prod_{i=1}^{n} p(x_i \mid \theta) \tag{2.11}$$

It is usually more convenient to work with the logarithm of the likelihood function, called the log-likelihood:

$$\ln \mathcal{L}(\theta \mid X) = \sum_{i=1}^{n} \ln p(x_i \mid \theta) \tag{2.12}$$

The estimated parameters $\hat{\theta}$ of the distribution model are found by maximizing $\ln \mathcal{L}(\theta \mid X)$. The hat over θ indicates that it is an estimation. This estimation method is defined MLE of $\hat{\theta}$:

$$\hat{\theta} = \left\{ \arg\max_{\theta} \ln \mathcal{L}(\theta \mid X) \right\} \tag{2.13}$$

For many models, MLE can be found as an explicit function of the observed data. However, for other models, no closed-form solution to the maximization problem is known or available. In those cases, MLE is found using optimization methods [123].

To select the most plausible distribution model representing the data out of N_D given types of distribution models, $\mathcal{D}_j$, where j = 1, 2, …, N_D, the maximum ln $\mathcal{L}$ value for each model is compared to each other as the information loss (*IL*) value. According to the Bayes' theorem, the likelihood is denoted by $\mathcal{L}_j = p(X \mid \theta_j, \mathcal{D}_j)$ for each model. Then, for the distribution types $\mathcal{D}_j$, that give a better fit to the data, the likelihood factor $p(X \mid \theta_j, \mathcal{D}_j)$ will be higher. Hence, the best model is chosen maximizing an objective function $IL_{MLE}(\mathcal{D}_j \mid X)$ over j that is defined by

$$IL_{MLE}(\mathcal{D}_j \mid X) = \ln \mathcal{L} = \ln\ p\left(X \mid \hat{\theta}_j, \mathcal{D}_j\right) \tag{2.14}$$

The use of MLE in model selection by Eq. (2.14) favors the distribution models with more statistical parameters, which makes it inefficient for selecting the best-fitted distribution [125]. To overcome this issue, various information loss evaluation methods such as Akaike information criterion (AIC) [126], Akaike information criterion correction (AICc) [127] and Bayesian information criterion (BIC) [124] are developed based on the MLE method. They show the difference in the calculation of the information loss value. AIC and AICc consider the number of statistical parameters k_p in the computation while the BIC method also considers the number of samples, n, in the calculation of information loss.

AIC is proposed to determine the distribution type based on MLE as

$$IL_{AIC}(\mathcal{D}_j \mid X) = -2\ln\ p\left(X \mid \hat{\theta}_j, \mathcal{D}_j\right) + 2k_{p,j} \tag{2.15}$$

where k_p is the number of estimated parameters of the j-th candidate distribution function. Based on the minimum AIC value among various distribution fits on the data, the optimal distribution is selected. **AICc** method has a modified term in the evaluation of AIC value thus improves the accuracy of the AIC when the number of samples is small [127].

$$IL_{AICc}(\mathcal{D}_j \mid X) = -2\ln\ p\left(X \mid \hat{\theta}_j, \mathcal{D}_j\right) + 2k_{p,j} + \frac{2k_{p,j}(k_{p,j}+1)}{n - k_{p,j} - 1} \tag{2.16}$$

Bayesian Information Criterion (BIC) is similar to AIC that use MLE function. BIC also considers the number of samples, n in the calculation of the information loss

$$IL_{BIC}(\mathcal{D}_j \mid X) = -2\ln p(X \mid \hat{\theta}_j, \mathcal{D}_j) + k_{p,j} \ln n \tag{2.17}$$

Bayesian update method is another method that shows the difference from these methods in the sense that the weight of each candidate distribution function is calculated by integrating the likelihood function over a distribution parameter. Bayesian formulation is given by

$$p(\mathcal{D}_j \mid X, I) = \frac{p(X \mid \mathcal{D}_j, I)\, p(\mathcal{D}_j \mid I)}{p(X \mid I)} \tag{2.18}$$

where *I* refer to prior information. $p(X \mid \mathcal{D}_j, I)$ is the likelihood function, $p(\mathcal{D}_j \mid I)$ is the probability of observing the prior information on the *j*-th candidate distribution, and $p(X \mid I)$ is the normalization constant based on any relevant additional knowledge *I*. $p(X \mid I)$ is considered as a constant it can be ignored, and a weight for each candidate distribution can be calculated as based on the Bayesian formulation as

$$W_j = \frac{1}{\lambda(\Lambda^{\mu})} \int \prod f_j(x_i \mid a(\mu,\sigma), b(\mu,\sigma)) d\mu \tag{2.19}$$

where f_j indicates the value of the PDF of the j-th candidate distribution in given data x_i; *a* and *b* are the values of parameters of the j-th candidate distribution calculated from the mean μ and standard deviation σ of the data. $1/\lambda(\Lambda^{\mu})$ represents the prior information on the mean of the candidate distribution, and λ is the Lebesgue measure, representing the interval length of Λ^{μ}. After calculating the weights of each candidate model, they can be converted to a normalized weight by

$$w_j = \frac{W_j}{\sum_i^q W_i} \tag{2.20}$$

Through a relative comparison of the weight of each candidate distribution, w_j, the distribution with the highest weight is selected as the most appropriate model for the given data [128]. Although the Bayesian method is very effective on the selection of the distribution, its increased computational complexity compared to the other MLE based methods hinders its application [129]. MLE-based methods are preferred due to their simplicity. **Among these model selection methods, BIC is known as having a higher convergence to the true model since it also considers the number of samples in the calculation of the information loss [127], [130]. Hence, in this study BIC is utilized for the uncertainty quantification of the input variables from the available uncertain data.** Once various distribution types of distributions are fitted to the data and the corresponding information loss values are calculated using BIC, the distribution type with the smallest information loss value is chosen as the best fit for the data of the homogenized variable.

The candidate parametric distributions, which are considered in model selection for uncertainty quantification, are Uniform, Normal, Lognormal, Gamma, Exponential, Weibull, Gumbel, and Extreme Type II distributions. These are the distribution types most frequently used in engineering [2]. The PDF, mean and variance formulations of these distributions are given in Table 2.1.

Table 2.1. Marginal PDFs, Mean, and Variance of various distributions.

Distribution	PDF	Mean (μ)	Variance (σ^2)
Uniform	$\frac{1}{x_{\max} - x_{\min}}$	$\frac{x_{\max} - x_{\min}}{2}$	$\frac{(x_{\max} - x_{\min})^2}{12}$
Normal	$\frac{1}{\sigma\sqrt{2\pi}} \exp\left(-\frac{(x-\mu)^2}{2\sigma^2} \right)$	μ	σ^2
Lognormal	$\frac{1}{xb\sqrt{2\pi}} \exp\left(-\frac{(\ln x - a)^2}{2b^2} \right)$	$e^{a+b^2/2}$	$\left(e^{b^2} - 1\right)e^{2a+b^2}$
Gamma	$x^{a-1} \frac{1}{\Gamma(a) b^a} \exp\left(-\frac{a}{b} \right)$	ab	ab^2
Exponential	$a \exp(-ax)$	a^{-1}	a^{-2}
Gumbell	$\frac{1}{b} \exp\left(\frac{a-x}{b} - \exp\left(\frac{a-x}{b} \right) \right)$	$a + 0.5772b$	$\frac{\pi^2}{6} b^2$
Weibull	$\frac{b}{a} \left(\frac{x}{a} \right)^{b-1} \exp\left(-\left(\frac{x}{a} \right)^b \right)$	$a\Gamma\left(1 + \frac{1}{b} \right)$	$a^2\Gamma\left(1 + \frac{2}{b} \right) - \mu^2$
Extreme Type-II	$\frac{a}{b} \left(\frac{b}{x} \right)^{a+1} \exp\left(-\left(\frac{b}{x} \right)^a \right)$	$b\Gamma\left(1 - \frac{1}{a} \right)$	$b^2\left[\Gamma\left(1 - \frac{2}{b} \right) - \Gamma^2\left(1 - \frac{1}{b} \right) \right]$

2.1.2. Parameter Calibration

Calibration is known as the inverse characterization of the unknown statistical parameters of random input variable based on the available statistical data of the output or response. Usually, the statistical parameters of a random input variable (e.g. material properties) of a computational model are predicted by an optimization process to match the computed responses with the available experimental measurements. In that regard, calibration is required to find the input variables when the experimental observations or statistical data is available for the output data. A calibration process as an inverse characterization process using optimization methods is necessary for estimating the input parameters of the computational models since there is no closed form equation of the input variable exists in terms of the known response. The model updating formulation for calibration is given by

$$Y_E(X) = Y_M(X, \hat{\theta}) + e \tag{2.21}$$

where $Y_M(X, \hat{\theta})$ denotes the computational model response that depends on the input variable(s) denoted by X with parameters θ, and $Y_E(X)$ is the known output data or experimental observations. The calibration process eliminates the possible errors between the available data and computational model predictions, denoted by e since a match between the experimental and model outputs is desired in the calibration to find the unknown parameters of the input variables of the model. Hence, it is also known as an inverse problem.

Calibration process falls into two broad categories as Bayesian and frequentist, and both methods have their advantages and disadvantages [131]. The Bayesian method is built upon the Bayesian parameter estimation process that updates the parameters based on a prior. However, the

prior can be difficult to determine and therefore absolute conclusions cannot be made. In frequentist processes, the statistical tests or model selection methods such as MLE and BIC can be utilized to quantify the input variable uncertainties in terms of a parametric distribution model. The frequentist approach may produce errors which may not be controlled, but it avoids the Bayesian prior and therefore provide a less subjective conclusion. Moreover, the frequentist approaches are easier to implement and therefore preferred over the Bayesian approach [132].

The statistical modeling processes explained in Section 2.1.1 can also be considered as the calibration processes since in the model selection processes, the input parameter values of a distribution model are determined from the known statistical data in an optimization process using MLE. The calibration process that is defined in this section, on the other hand, focuses on the cases when the statistical data is available for the output or response variable of a physical system rather than the input variables. Unlike the direct distribution fit to data by MLE, first, the computational model is used to compute the responses with the prediction of the input variable parameters. Then a comparison between the experimental measurements and the model outputs is performed at each iteration in the optimization process for calibration. This calculation of the model outputs using the computational model increases the computational cost of the MLE process. Because MLE has to be utilized for fitting various types of distribution models to determine the best fit using the model selection methods such as BIC method, the computational demand of the calibration process increases dramatically.

As the calibration process enables the prediction of the unknown input uncertainties based on the available output uncertainties using a computational model, it can be considered as a backward propagation of the uncertainties (i.e. from outputs to inputs). Therefore, uncertainty propagation methods such as Polynomial Chaos Expansion (PCE) [99] can be used alternatively

for calibration to represent the distribution of the unknown input data instead of a parametric distribution model in the calibration process. PCE can approximate a distribution with deterministic constants that are independent of the distribution type. Thus, only one calibration process will be sufficient to find the deterministic constants that quantify the input variable uncertainties. PCE was originally proposed by Ghanem and Spanos [133] to represent the propagated uncertainties on the model response, but it was suggested to use in the stochastic calibration processes of input variables as well [134], [135]. The details of the PCE is given in Section 2.2.3 as it is considered as an uncertainty propagation method.

2.2. Uncertainty Propagation

Once the uncertainties of the input variables are quantified using model selection or parameter calibration processes, uncertainty propagation is achieved for the probabilistic analysis of a problem using the computational model to predict the uncertain response or output variable. The uncertainty propagation methods can be categorized as the non-intrusive sampling methods (e.g. as Monte Carlo sampling (MCS) [136], Latin Hypercube sampling (LHS) [137], Stochastic Expansions such as PCE [133], etc.) and intrusive methods (e.g. first- and second-order reliability methods, stochastic finite element method, etc.). The non-intrusive methods have the advantage of generating sampling points directly without considering the system equations explicitly. In other words, sampling methods can be used with black-box models to propagate the input uncertainties. This section presents the main sampling-based uncertainty propagation methods and discusses their strengths and weaknesses. More information about the intrusive methods can be found in [2].

2.2.1. Monte Carlo Sampling (MCS)

Monte Carlo method takes its name from the famous casino in Monaco. It is developed for the randomness and iterative procedure in gambling in casinos. Nowadays, it is used in a broad area to handle the randomness in any problem. Inverse transform method is used to generate random variables from the specified PDF in MCS. When the CDF, $F_X(x)$, of a random variable, X, is known, the numerical value of $F_X(x)$, denoted by u is in the interval of [0,1]. Then, according to the inverse transform method, the inverse cumulative function is used to find the value of the random variable:

$$x = F_X^{-1}(u) \tag{2.22}$$

where u is the uniformly distributed random variable generated between 0 and 1. The corresponding target distribution CDF is used in Eq. (2.22) to obtain the random number for the random variable [2]. This process of sampling value generation of the random input variable is depicted in Figure 2.1. Once the sample for the random input variable is generated by Eq. (2.22), the random value of the response of the computational model can be calculated as the final step of the MCS process.

The computation procedure of MCS is as follows

1) Generate a uniformly distributed random variable sample u between 0 and 1.
2) Calculate the CDF of the sample from standard uniform distribution CDF.
3) Calculate the random variable sampling value from the inverse CDF of the target distribution of the random variable.
4) Conduct simulations using the generated sampling set.

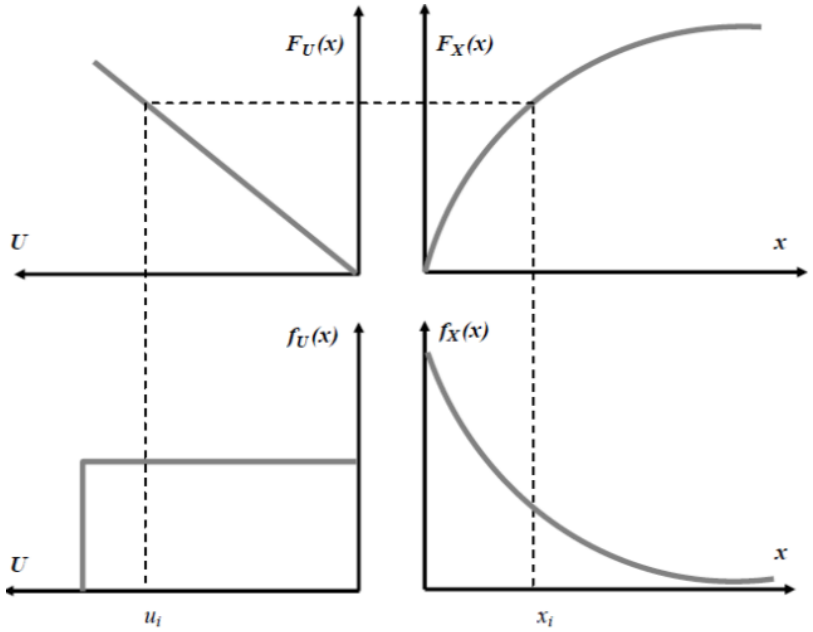

Figure 2.1. Monte Carlo sampling method using inverse probability theory [2]

The computational cost of MCS can be expensive if high accuracy is desired since a large number of sampling set is required. Therefore, variance reduction techniques such as LHS are integrated to reduce the computational cost while increasing the accuracy.

2.2.2. Latin Hypercube Sampling (LHS)

LHS is a special form of MCS, in which the distribution of a random variable is subdivided into *n* equal probability intervals including one analysis point each so that there are randomly mixed *n* analysis points. After this process is done for each random variable, the randomly selected *n* values are associated with others at random. Figure 2.2 represents the steps of LHS method.

The regularity of probability intervals on the probability distribution function ensures that each of the input variables has all portions of its range represented, resulting in relatively small variance in the estimates as well as less computational cost for the analysis.

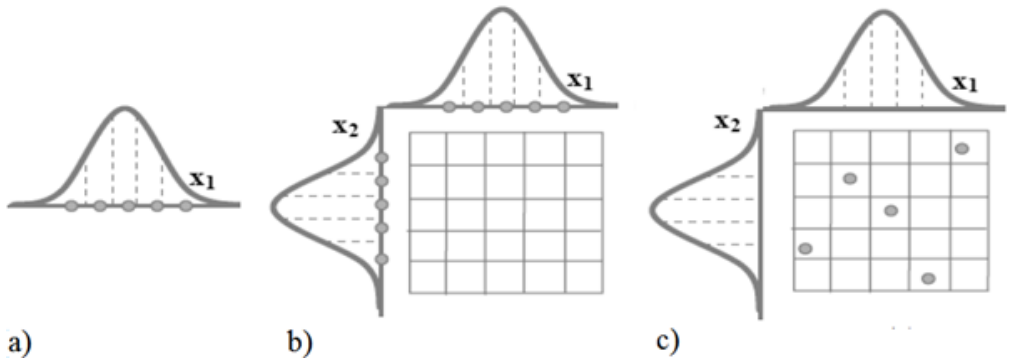

a) Step 1: Divide the distribution into n non-overlapping intervals and select one value at random for each interval. b) Step 2: Repeat the first step for all random variables. c) Step 3: Associate *n* values for each random variable with the ones for other variables at random [2].

Figure 2.2. Latin hypercube sampling basic steps.

2.2.3. Polynomial Chaos Expansion (PCE)

Polynomial Chaos Expansion (PCE) is considered as a stochastic expansion method, which is a very efficient tool for uncertainty propagation. It was first introduced as the homogeneous chaos by Wiener [99]. The purpose is to project a random variable onto a stochastic space with deterministic constants by introducing a series of orthogonal polynomials. When a random variable is denoted by $X(\eta)$, where η represents the randomness, PCE for a general random process can be written in the form

$$\begin{aligned} X(\eta) = b_0\Phi_0 &+ \sum_{i=1}^{\infty} b_{i_1}\Phi_1(\xi_{i_1}(\eta)) \\ &+ \sum_{i_1=1}^{\infty}\sum_{i_2=1}^{i_1} b_{i_1 i_2}\Phi_2(\xi_{i_1}(\eta),\xi_{i_2}(\eta)) \\ &+ \sum_{i_1=1}^{\infty}\sum_{i_2=1}^{i_1}\sum_{i_3=1}^{i_2} b_{i_1 i_2 i_3}\Phi_3(\xi_{i_1}(\eta),\xi_{i_2}(\eta),\xi_{i_3}(\eta)) \\ &+ \ldots \end{aligned} \tag{2.23}$$

where $\Phi_n(\xi_{i_1},...\xi_{i_n})$ denote the Askey-chaos orthogonal polynomials of order *n* in terms of the random variables $\xi_i = (\xi_{i_1},...\xi_{i_n})$. For notational simplicity, the expansion can be truncated to a finite number of terms and written as

$$X(\eta) = \sum_{i=0}^{P} b_i \Phi_i(\xi(\eta)) \tag{2.24}$$

where b_i and $\Phi_i(\xi(\eta))$ are one-to-one correspondences between the coefficients $b_i = (b_{i_1},...b_{i_n})$ and the functions $\Phi_n(\xi_{i_1},...\xi_{i_n})$, respectively. The orthogonal polynomials, Φ_n and the type of random variables, ξ_n, is chosen depending on the type of distribution of the random process. The Askey-scheme expansion is introduced as a generalized PCE, which enables the use of appropriate orthogonal polynomials and random variables depending on the type of the stochastic process. The orthogonal polynomials are listed in Table 2.2 for various distribution types.

Table 2.2. Representation of different distributions by PCE and underlying random variables [2]

Distribution type	Askey chaos (Φ_n)	Range
Gaussian	Hermite-chaos	(-∞, ∞)
Gamma	Laguerre-chaos	[0, ∞)
Beta	Jacobi-chaos	[-1,1]
Poisson	Charlier-chaos	-
Uniform	Legendre-chaos	[-1,1]

When the random process is Gaussian (i.e. normal) as in most cases, the polynomials Φ_n are Hermite polynomials and random variables ξ_n are a set of Gaussian random variables. Hermite polynomials can also be used in PCE for non-Gaussian random processes. Although a greater order of PCE is required to present the non-Gaussian random process using Hermite polynomials accurately, it eliminates the dependency of the PCE on the distribution type. When normal distribution is used, the random variable ξ has a standard normal distribution, N~[0,1]. When we consider a one-dimensional PCE, the random variable is written by using the Hermite polynomials:

$$X = b_0 + b_1\xi + b_2(\xi^2 - 1) + b_3(\xi^3 - 3\xi) + b_4(\xi^3 - 6\xi^2 + 3) + \ldots = \sum_{i=0}^{P} b_i \Phi_i(\xi) \tag{2.25}$$

where b_i, i = 0,1,2,..,P, are unknown coefficients and the set$\{\Phi_i\}$ contains the Hermite polynomials in the random variable ξ. The one-dimensional Hermite polynomials are defined by

$$\Phi_i(\xi) = (-1)^i [\Phi^{(i)}(\xi) / \Phi(\xi)] \tag{2.26}$$

where $\Phi^{(m)}(\xi)$ is the i^{th} derivative of the normal density $\Phi(\xi) = \frac{1}{\sqrt{2\pi}} \exp\left(-\frac{\xi^2}{2}\right)$. From Eq. (2.26), one can readily find

$$\begin{aligned} \{\Phi_i\} = \{&1, \xi, \xi^2 - 1, \xi^3 - 3\xi, \xi^4 - 6\xi^2 + 3, \xi^5 - 10\xi^3 + 15\xi, \\ &\xi^6 - 15\xi^4 + 45\xi^2 - 15 + \xi^7 - 21\xi^5 - 105\xi^3 + 105\xi, \ldots\} \end{aligned} \tag{2.27}$$

The advantage of the PCE is that the mean and standard deviation of the random variable can also be computed. Once the deterministic coefficients are determined, the mean of the random variable can be calculated by substituting the PCE in Eq. (2.25) into Eq. (2.1) when m = 1

$$\mu_X = \int x\ p(\xi)d\xi = \int\left(\sum_{i=0}^{P} b_i\Phi_i(\xi)\right)p(\xi)d\xi = \sum_{i=0}^{P} b_i \int \Phi_i(\xi)\, p(\xi)d\xi \tag{2.28}$$

Since $b_0 = 1$ and $\int \Phi_i(\xi)\, p(\xi)d\xi \cong 0$ for every $i > 0$

$$\mu_X = b_0 \tag{2.29}$$

Similarly, the variation of the random variable is calculated using the second statistical moment from Eq. (2.1)

$$\begin{aligned}\sigma_X^2 = \int \left(x - \mu_X\right)^2\ p(\xi)d\xi &= \int\left(\sum_{i=0}^{P} b_i\Phi_i(\xi) - b_0\right)^2 p(\xi)d\xi = \\ &= \left(\sum_{i=0}^{P} b_i^2 \int \Phi_i(\xi)^2 - 2b_0\sum_{i=0}^{P} b_i \int \Phi_i(\xi) + b_0^2\right)p(\xi)d\xi\end{aligned} \tag{2.30}$$

Considering the orthogonality property of Hermite polynomials, i.e. $\left\|\Phi_i(\xi)\right\|^2 = 1$, and substituting Eq, (2.29) into Eq. (2.30) with gives

$$\sigma_X^2 = \sum_{i=0}^{P} b_i^2 \left\|\Phi_i(\xi)\right\|^2 - 2b_0 b_0 + b_0^2 = \sum_{i=0}^{P} b_i^2 - b_0^2 \tag{2.31}$$

Finally, the standard deviation of the random variable X is found as the root square of the summation of the PCE coefficients except the first one [138]:

$$\sigma_X = \sqrt{\sum_{i=1}^{P} b_i^2} \tag{2.32}$$

In PCE given by Eq. (2.25) the unknown coefficients, b_i, must be determined to represent the stochastic process. These coefficients can be determined using intrusive or non-intrusive

methods. It has been utilized in Spectral Stochastic Finite Element Method (SSFEM) as uncertainty characterization method by Ghanem and Spanos [133] in an intrusive manner, i.e. the uncertainties are introduced explicitly into the FE equations. The intrusive application of PCE can provide an accurate representation of uncertainty, but the underlying governing equations or partial differential equations must be explicitly expressed. That means intrusive methods require access to modification of the analysis codes. However, the explicit expression of the equations might not always be possible. For example, the system at fine scale can be so complex that it cannot be explained with equations or accurate response can only be found by experimentation.

For these situations, non-intrusive methods, which treat the analysis code as a "black-box," are convenient to represent the uncertainty. Hence, the non-intrusive methods are preferred to implement so that the governing equations of the system can be treated implicitly. In that regard, probabilistic collocation method has been introduced by Tatang [139] to project the stochastic system responses onto the PCE. In this method, the deterministic coefficients of the PCE are determined using the model outputs at selected collocation points or sampling points of input variables. A stochastic response surface method has been proposed by Isukapalli [140]. The partial derivatives of the model outputs with respect to the model inputs are considered in this method to overcome the limitation of the probabilistic collocation method for large-scale models. Zein et al. [138] introduce an optimization-based algorithm that can generate a small size of sample points that can represent the uncertainty in estimating the PCE coefficients. Choi et al. [2] utilized a regression-based PCE method in Reliability-based Design Optimization process along with LHS to determine the collocation points such that the entire distribution can be represented efficiently with fewer sampling points. In this method, once the values of the output variable, $Y^M = \{y_1^M, \dots, y_n^M\}$, are calculated from the computational model simulation for the generated samples of the

input variables in the RBDO process, the coefficients of PCE of the output variable are computed by solving the following linear least squares problem:

$$\min_{b} \quad \sum_{j=1}^{n}\left(y_j^M - \sum_{i=0}^{P} b_i \, \Phi_i\left(\xi_j\right)\right)^2 \tag{2.33}$$

Thus, the uncertainties in the input variables of the computational model are propagated to the output variable with the use of PCE. Then, in estimating reliability, the samples of the output variable are generated through the PCE rather than using expensive simulations of the computational model. Nevertheless, a new PCE for the response is required to be estimated at each iteration as the response alters. This process still involves using the expensive simulations repeatedly at each iteration, which makes the optimization process inefficient. Coelho et al. [142] proposed a PCE-based meta-modeling approach to reducing the number of expensive simulations. PCE coefficients of the response are estimated over a range of interest of the deterministic design variables. Then, a meta-model of the PCE coefficients with respect to the design variables is generated using kriging interpolation. In the further studies, moving least squares interpolation [143], and spline functions [144] are utilized to achieve the mapping between the design variables and the PCE coefficients b_K. Then, these meta-models can substitute the actual expensive model in the reliability computation phase, and thus help in reducing the total cost of reliability calculation. **This approach of PCE-based meta-modeling is adopted in this research to develop the meta-models that can predict the stochastic homogenized coarse scale input variables that will be used in the design of CLSs.**

The efficient use of nonintrusive methods for PCE projection has also enabled researchers to implement the PCE in inverse parameter calibration processes described in Section 2.1.2. When

PCE is used in calibration, the uncertainties in the physical system outputs from experiments propagate through the inverse model. In the PCE-based calibration process, the deterministic coefficients of the PCE have to be calculated for the input variable(s) instead of estimating the statistical parameters and the distribution model. Assume that the relation of the input variable(s) and the response of a physical process is represented as

$$Y = f(X) \tag{2.34}$$

where Y is the known system responses (observed data) and $f(.)$ is the system governing equations or the computational model (e.g. FE model). To identify the input variables, the inverse solution of the direct problem given in Eq. (2.34) needs to be solved, i.e.

$$X = f^{-1}(Y) \tag{2.35}$$

In the case of availability of the linear explicit models $f^{-1}(.)$ that links the input variables with the output variable, the input variable values can be explicitly calculated for uncertainty quantification. However, an explicit formulation of $f^{-1}(.)$ is not possible when nonlinear and/or black-box computational models are used, which is the case when FE modeling technique is used. In this case, the problem is treated as an inverse problem, and the calibration process is used to find the optimal statistics of the input variables that minimizes the error between the known responses and predicted responses from Eq. (2.34). To reduce the dimensionality of the calibration, process the unknown input variable can be projected onto a PCE. Thus, the PCE representation of the unknown input variables transforms the optimization problem into a problem of determining a set of unknown deterministic PCE coefficients.

This process has been used by researchers in uncertain material property characterization problems using the experimental data [134], [135], [141]. Knowing that the application of the PCE can be generalized with Hermite polynomials and Gaussian process for any distribution model, it is possible to approximate the uncertainties in input variable using PCE with deterministic coefficients. Thus, the problem of uncertain input variable identification in the calibration process is shifted to the determination of the PCE coefficients for the input variables. The idea of inverse problem with PCE projection of the unknown input variable has also been used for upscaling to find the effective properties of a coarse scale model in a multiscale analysis problem [98]. **The use of PCE is very promising in multiscale modeling to reduce the computational complexity while propagating the uncertainty to the unknown input variables. Hence, in our work, the computational efficiency of this PCE-based upscaling process is improved to make it applicable for uncertainty quantification and stochastic homogenization at multiple scale levels of additively manufactured CLSs.**

2.3. Upscaling/Homogenization for Multiscale Modeling

Multiscale modeling is the process to investigate the material/structure domain at multiple scale levels to increase the speed of calculations in characterizing properties of materials and/or predicting overall structure performance instead of modeling all the details at once. Upscaling, or homogenization, or finding the effective medium, is used in multiscale modeling to substitute a heterogeneous property region with fine scale details with an equivalent homogeneous region at a coarser scale with an effective or homogenized property value. In the geophysical community, substituting a fine scale medium with a coarse scale one is referred to as “finding the effective medium.” In the seismic community, it is called “upscaling” and in solid mechanics, the general

term used is “homogenization” [145]. Hence, these terms can be used interchangeably as they refer to the same concept.

The objective of homogenization in solid mechanics is to develop equivalent continuum that has the same average mechanical response as the actual material for upscaling the information to find the effective properties of the material [146]. Homogenization is a very widely used strategy in multiscale modeling for material characterization of the heterogeneous materials at micro and/or macro scale especially for the composite materials. The small scale material behavior is often more complicated than that of a coarser scale model. This complexity and the limited computational resources make it impractical to perform all-in-one modeling and analysis that include all details of the smaller scales. It becomes necessary to build models which will result in valuable computational savings that greatly simplifies the pre-processing stage of the analysis to find effective material properties. Instead of performing a full-scale analysis of the entire domain, effective properties of the materials are determined by averaging the local behavior of the small scale structure of the material using upscaling/homogenization methods. Then, the structure is modeled as a homogeneous material at macroscale considering only the effective properties.

Homogenization methods utilized in the multiscale modeling of materials/structures can be classified into three areas: (1) Analytical homogenization methods, (2) Computational homogenization methods (3) Upscaling through optimization.

2.3.1. Analytical Homogenization Methods

Among numerous methods to predict the effective properties of materials a variety of analytical methods have been developed for homogenization. The simple bounds on the effective elastic moduli can be determined by the averaging approaches of Voigt [64] and Reus [65]. The Voigt

upper bound on the effective/homogenized elastic modulus, E_V, of a mixture of N_m material phases is predicted by

$$E_V = \sum_{i=1}^{N} f_i E_i \tag{2.36}$$

where f_i and E_i denote the volume fraction and the elastic modulus of the i^{th} constituent, respectively.

The Reuss bound of the effective elastic modulus, E_R is given by

$$\frac{1}{E_R} = \sum_{i=1}^{N} \frac{f_i}{E_i} \tag{2.37}$$

Eq. (2.36) is considered as the upper bound of the elastic moduli since there is no way of having a stiffer mixture of constituents than this simple arithmetic average of the individual constituent moduli given by the Voigt bound. Eq. (2.37) is considered as the lower bound of the elastic moduli since again there is no way of having a softer mixture of constituents than this harmonic average of the individual constituent moduli given by the Reuss bound [146].

Eshelby's method [61], which considers a homogeneous equivalent inclusion to the original inclusion, is considered the start of homogenization approaches. The homogeneous equivalent inclusion is assumed to have an appropriate strain, called the equivalent transformation strain, such that the stress field is the same with the actual inclusion. Assuming the strain is uniform within the inclusion, the stress in the inclusion σ^I can be calculated by

$$\sigma^I = C^M \left(\varepsilon^C - \varepsilon^T \right) \tag{2.38}$$

where C^M are the components of the elasticity tensor of the matrix material, ε^C is the constraining strain relative to the initial shape, ε^T is the transformation strain. Eshelby has shown that the constraining strain ε^C can be described in terms of the transformation strain ε^T using the equations

$$\varepsilon^C = S\varepsilon^T \tag{2.39}$$

The Eshelby tensor, *S*, is a fourth rank tensor determined using Poisson's ratio of the inclusion material and the inclusion's aspect ratio. Finally, the stress in the inclusion is determined by substituting Eq. (2.39) into Eq. (2.38) and simplifying

$$\sigma^I = C^M\left(S - I\right)\varepsilon^T \tag{2.40}$$

where *I* is the components of the fourth-rank identity tensor. The Eshelby's solution is based on the assumption that the inclusion is in the unbounded space (i.e. infinite space). This assumption also means that the constituents are not influenced by each other. Hence, this method is only applicable to the very low volume fraction of heterogeneous materials [147]. Mori-Tanaka method [62] and Self-consistent method [63] are improved versions of the Eshelby's method that can be applied to the higher volume fraction of materials with inclusions. Analytical homogenization methods have been used for homogenized property characterization in multiscale modeling of engineering applications modeled with composite materials [148].

Analytical formulations to find the effective properties of CLSs have also been developed in the literature. In these formulations, truss or beam deflection theory is used to model the mechanical behavior of the strut members in the CLSs, and the elastic constants of the lattice cells are determined by solving the deformation and equilibrium problems. Gibson and Ashby [3] show that the cellular structures have the following relationship in general:

$$\frac{E_h}{E_0} = C\left(\frac{\rho}{\rho_0}\right)^2 \tag{2.41}$$

where E_h and E_0 are the homogenized elastic modulus and the bulk material elastic modulus, respectively. C is a constant dependent on the cell geometry, ρ is the density of the lattice cell, and ρ_0 is the density of the bulk material of which the lattice structure is made. Deshpande et al. [6] use the linear elastic stress versus strain relationship to formulate the analytical expression of the elastic modulus of the octet-truss lattice structure. The maximum value of the elastic modulus E_h is formulated as

$$E_h = \frac{3\sqrt{2}\pi(D/l)}{10}E_0 \tag{2.42}$$

where E_0 denotes the elastic modulus of the bulk material, and D and l denote the strut diameter and strut length, respectively. Gumruk et al. [86] present the analytical formulation of the initial compression modulus (E_h) of a body-centered cubic (BCC) lattice cell as follows:

$$E_h = \frac{\sqrt{3}\pi(D/L)^2 E_0}{1+2(D/L)^2} \tag{2.43}$$

where L denotes the lattice cell size.

These kinds of analytical methods are very convenient to calculate the homogenized properties of materials; however, these are established based on many simplifications and assumptions. For example, analytical homogenization approaches such as Eshelby method ignore the consideration of the size and position of the inclusions, which leads to inaccurate results. The analytical formulations of CLSs utilize beam deflection theory, which cannot capture the

deformation of the solid material at the cell joints. Hence computational homogenization methods are developed as explained in Section 2.3.2.

2.3.2. Computational Homogenization Methods

Computational homogenization approaches are proposed to use an FE model of the material microstructure with details of the heterogeneity [149]. Since it is based on the FE modeling, any size or orientation of the inclusions can be considered in the analysis. Hence, it is applied to characterizing the heterogeneous materials with macroscopically and statistically homogeneous structure [150].

2.3.2.1. Representative Volume Element (RVE)

Computational homogenization methods are based on the concept of a representative volume element (RVE). An RVE can be defined as the smallest fundamental building blocks, also called repeating unit cell for a material with a periodic microstructure with the assumption of a volume containing a very large (mathematically infinite) set of microscale elements [152], [153]. When RVEs are assembled side by side into an infinite array, it forms the heterogeneous material with periodic microstructure. The assumption of the homogenization for an RVE is that since each RVE is indifferent from the next, the response of the entire array under macroscopically uniform loading is identical to the response of an arbitrary RVE under the same loading. For the selection of the optimal size of the RVE, the following two criteria have to be satisfied[151]. First, the RVE must be sufficiently small with respect to the dimensions of the macroscale structure so that it can be considered as a material point in the equivalent homogeneous continuum. Second, it must be large enough with respect to the scale of the inclusion phase to have elastic properties independent of the loading condition [152].

This concept of homogenization through an RVE is shown in Figure 2.3 for a heterogeneous medium in the domain Ω_x with a porous microstructure subjected to the traction t at the traction boundary Γ_t. As can be seen on the left side in Figure 2.3, a lattice structure can be considered as the fine scale heterogeneous medium in the computational homogenization methods because any geometry and inclusions (i.e. voids in the case of lattice cell) can be modeled using FE modeling techniques as the fine scale RVE. The unit cell is assumed to be periodically repeated inside the medium of each point $\mathbf{x} \in \Omega_x$. This heterogeneous material can be replaced by a homogeneous medium Ω with some predicted effective properties by any upscaling or homogenization method [154].

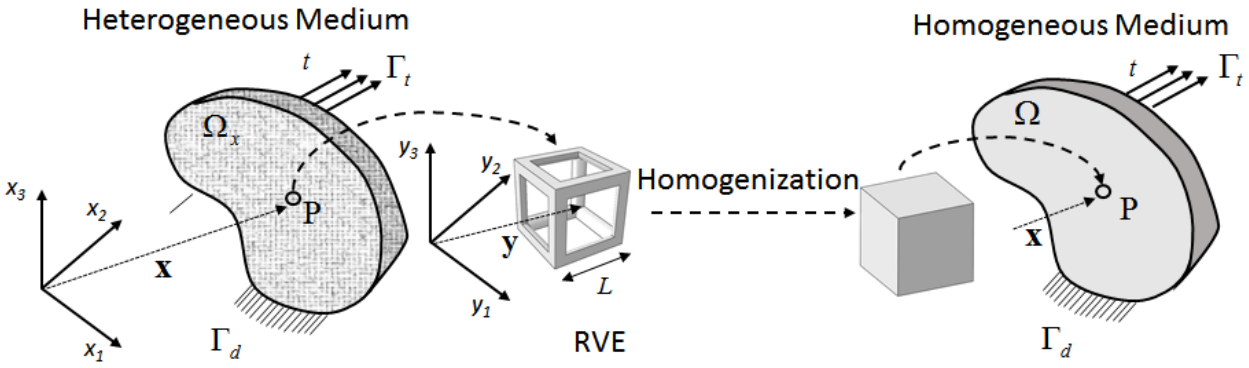

A fine scale computational model of the RVE of the heterogeneous medium can be generated with a complex structure (left). A homogenization approach is used to find the corresponding homogenized properties at a coarser scale that can represent the fine scale heterogeneous medium (right)

Figure 2.3. Illustration of the computational homogenization process.

In computational homogenization approaches, a linking mechanism between the fine scale RVE and the homogenized coarse scale domain is required for upscaling. Usually, the continuum level constitutive laws are used to estimate the homogenized properties at a coarse scale. For elastic

materials, Hill [152] shows that this upscaling process can be achieved by assuming that the average of the product of the stress and strain tensors at fine scale equals to the product of their averages at a coarse scale. This condition is called Hill-condition and given by

$$\overline{\boldsymbol{\sigma} : \boldsymbol{\varepsilon}} = \overline{\boldsymbol{\sigma}} : \overline{\boldsymbol{\varepsilon}} \tag{2.44}$$

where the bar above the symbols stands for the averaging operator. The Hill condition can be generalized to heterogeneous materials [150]

$$\overline{\boldsymbol{\sigma} : \boldsymbol{\varepsilon}} - \overline{\boldsymbol{\sigma}} : \overline{\boldsymbol{\varepsilon}} = 0 \Leftrightarrow \int_{\Gamma} \left(\mathbf{t}(\mathbf{x}) - \overline{\boldsymbol{\sigma}} \cdot \mathbf{n}\right) \cdot \left(\mathbf{u}(\mathbf{x}) - \overline{\boldsymbol{\varepsilon}} \cdot \mathbf{x}\right) d\Gamma = 0 \tag{2.45}$$

where Γ is the boundary of an RVE and **t**, **u**, **n**, **x** are the traction, displacement, normal and position vector, respectively. This condition is satisfied for an infinite homogeneous body, but for a finite heterogeneous body, the applied boundary conditions have an influence on the predicted effective properties. Therefore, the periodicity of the RVE necessitates the use of appropriate boundary conditions which will represent the entire structure. Since these boundary conditions are applied on the RVE, and subsequently, the averaged response of the RVE is used in the homogenization process to determine the effective properties, the choice of the boundary conditions requires a thorough motivation.

2.3.2.2. Boundary conditions on RVE

The commonly used boundary conditions in micromechanics to satisfy this condition are three types of uniform boundary conditions [150], [153], [154]. The first one is called kinematic uniform boundary condition (KUBC), also called Dirichlet or essential boundary condition. In KUBC, uniform displacements are applied to the boundary of an RVE:

$$\mathbf{u}(\mathbf{x}) = {}^{0}\boldsymbol{\varepsilon} \cdot \mathbf{x}, \qquad \mathbf{x} \in \Omega_x \tag{2.46}$$

where ${}^{0}\boldsymbol{\varepsilon}$ is the applied constant strain tensor prescribed on the RVE. Then, based on the Hooke's law the homogenized stiffness tensor is given by

$$\bar{\boldsymbol{\sigma}} = {}^{KUBC}\mathbf{C} \cdot {}^{0}\boldsymbol{\varepsilon} \tag{2.47}$$

The second one is called static uniform boundary condition (SUBC), which is also called Neumann boundary condition, where uniform tractions are prescribed on the edges

$$\mathbf{t}(\mathbf{x}) = {}^{0}\boldsymbol{\sigma} \cdot \mathbf{n}, \qquad \mathbf{x} \in \Omega_x \tag{2.48}$$

where ${}^{0}\boldsymbol{\sigma}$ is the given constant stress tensor prescribed on the RVE. For KUBC the homogenized compliance tensor is introduced by

$$\bar{\boldsymbol{\varepsilon}} = {}^{SUBC}\mathbf{S} \cdot {}^{0}\boldsymbol{\sigma} \tag{2.49}$$

where the compliance tensor is the inverse of the stiffness tensor.

An RVE is called to be well-defined when the responses under KUBC and SUBC boundary conditions coincide [146]. In addition to these two uniform boundary conditions, mixed uniform boundary condition (MUBC) is introduced as the combinations of the KUBC and SUBC, inspired by the fact that in experimental set-ups, it is very difficult to realize the uniform boundary conditions [150], [155].

$$\left(\mathbf{t}(\mathbf{x}) - {}^{0}\boldsymbol{\sigma} \cdot \mathbf{n}\right) \cdot \left(\mathbf{u}(\mathbf{x}) - {}^{0}\boldsymbol{\varepsilon} \cdot \mathbf{x}\right) = 0 \qquad \mathbf{x} \in \Omega_x \tag{2.50}$$

In fact, the case of uniaxial tensile conditions, where in one part of the specimen, displacements are prescribed whereas on the remaining part of the sample, forces are prescribed, belongs to the family of mixed boundary conditions [156]. Hazanov and Huet [150] show that KUBCs and SUBCs provide the bounds for the stiffness tensor for MUBC and effective elasticity tensor

$$ {}^{SUBC}\mathbf{S}^{-1} \leq {}^{eff}\mathbf{C} \leq {}^{KUBC}\mathbf{C} \tag{2.51} $$

Hence, it is seen that the KUBC overestimate the effective moduli whereas the SUBC underestimate the effective moduli. The reason is explained as follows: When a displacement is applied to the one face, it constrains the boundary on the other face to keep the relative displacement constant according to the strain on that boundary. Hence, a displacement boundary condition applied to the RUC will not be appropriate since it will result in the flat surface remain flat after deformation. However, the deformation of the surface of an RVE in a periodic structure cannot remain flat after deformation. If boundary surfaces are forced to be flat while it has to deform to have a wavy surface due to the periodicity, it will be over constrained, and the result will be different.

2.3.3.3. Periodic boundary conditions (PBCs)

Periodic boundary conditions (PBCs) are established for this purpose by considering the deformation of an RVE relative to a fixed global coordinate system when the material exhibits a periodic microstructure [157], [158]. In PBC, the displacement $u(x_0)$ of a particular point x_0 is considered within an arbitrary reference RVE relative to the global coordinate system with the coordinates **x**. Since all RVEs are identical, this point has its mirror images in every RVE from

which it is separated by a multiple of some characteristic distance L that does not depend on the particular location x_0. The characteristic distance L that separate image points between adjacent RVEs defines, in fact, the microstructural scale length of the RVE (see Figure 2.3). We now consider the mirror image of the point in an RVE adjacent to the reference RVE and write displacement components of that point to first order in L as follows: For a square-shaped RVE with a length scale L (Figure 2.3) the PBCs are specified by

$$\mathbf{u}(\mathbf{x}+\mathbf{L}) = \mathbf{u}(\mathbf{x}) + {}^{0}\boldsymbol{\varepsilon}\cdot\mathbf{L} \tag{2.52}$$

where $\mathbf{L} = L\mathbf{n}$. For an RVE with random microstructure, PBCs given in above equations with the appropriate constraints must be applied directly to the RVE. Proceeding to the RVE boundary, the displacement difference between any two equivalent points (x, $x+L$) ϵ S separated by the characteristic microstructural length L can be related to the average strain components ${}^{0}\boldsymbol{\varepsilon}$. The vector $\mathbf{L}$ that defines the characteristic microstructural scale of the investigated RVEs is associated with the three pairs of unit cell faces in 3D case. In addition, tractions, $\mathbf{t}$, must be continuous across the adjacent RVEs at the characteristic or equivalent points so that

$$\mathbf{t}(\mathbf{x}+\mathbf{L}) = -\mathbf{t}(\mathbf{x}) \tag{2.53}$$

Eqs. (2.52) and (2.53) define the PBCs that hold for and RVE with an arbitrary microstructure, which need to be applied in the micromechanical analysis of an RVE. Xia et al. [159] prove that the traction equation is automatically satisfied by only using the displacement equation in a displacement-based FE method. Hence, only Eq. (2.52) is necessary to apply PBC on RVE.

PBCs can provide reasonable estimates of the effective properties even if the microstructure does not have the actual periodicity [160]. It was also shown that PBCs provide better approximations of the effective properties for the small size of RVEs because PBC estimates are always bounded by the estimates of PUBC and KUBC [160]. PBC was also found to be providing better solution compared to the MUBC in both elastic and plastic behavior of the material [7].

Once the fine scale RVE is modeled with the appropriate boundary conditions, the homogenized model at coarse scale should be defined. For elastic materials, the generalized Hooke's law for the homogeneous material is written as

$$\bar{\boldsymbol{\sigma}} = {}^{eff}\mathbf{C} \cdot \bar{\boldsymbol{\varepsilon}} \tag{2.54}$$

alternatively, in matrix form

$$\bar{\sigma}_{ij} = {}^{eff}C_{ijkl} \cdot \bar{\varepsilon}_{kl} \tag{2.55}$$

where the stress and strain tensors are found by the volume averages over the RVE, given by

$$\bar{\sigma}_{ij}(\mathbf{x}) = \frac{1}{V}\int_V \sigma_{ij}(\mathbf{x})dV \tag{2.56}$$

$$\bar{\varepsilon}_{ij}(\mathbf{x}) = \frac{1}{V}\int_V \varepsilon_{ij}(\mathbf{x})dV \tag{2.57}$$

To find these volume averages, a displacement-based FEM can be used. When displacement-based FEM is used to model the RVE with PBC, the global stiffness equation is given by

$$[K]\{U\} = \{F\} \tag{2.58}$$

where [*K*] is the system global stiffness matrix, {*U*} and {*F*} are the global displacement and global nodal force vectors, respectively. When the displacements are defined as the boundary conditions on RVE, above equation produces the corresponding forces based on the global stiffness matrix constructed based on the element type and material used in FEA. When we assume a uniform strain field as boundary conditions, the displacement field on the boundary of an RVE is given in the matrix form:

$$^{0}u_i = \bar{\varepsilon}_{ij} L_j \tag{2.59}$$

for i^{th} direction. When $^{0}\varepsilon_{ij}$ is applied as a constant strain, the average of effective macroscopic strain $\bar{\varepsilon}_{ij}$ is the same as the applied constant strain, i.e. $^{0}\varepsilon_{ij} = \bar{\varepsilon}_{ij}$ in volume average strain equation Eq. (2.57). Then the PBC equation in Eq. (2.53) can be written as

$$u_i(\mathbf{x} + L) - u_i(\mathbf{x}) = {}^{0}u_i \tag{2.60}$$

Since *L* is constant for each pair of the parallel boundary surfaces, with specified $^{0}\boldsymbol{\varepsilon}$, the right side of Eq. (2.60) becomes constants and such equations can be applied in the FEA as nodal displacement constraint equations. Then the global stresses can be obtained from the stress distribution on the RVE calculated by FEA through Eq. (2.56).

By using Gauss's theorem this volume integration can be transformed to surface integration over the entire boundary surfaces [159]. Thus, instead of the volume average of stresses, the resultant reaction forces on the boundary surfaces in an FEA can be used to calculate the average stress on j^{th} boundary surface as follows:

$$\bar{\sigma}_{ij} = \frac{(P_i)_j}{A_j} \tag{2.61}$$

where A_j is the area of the j^{th} boundary surface and $(P_i)_j$ is the i^{th} resultant traction forces in each direction on the j^{th} boundary surface. Then, to find the effective constants in the macroscopic stiffness matrix, the global stress-global strain relation of the periodic structure can be written as

$$[\bar{\sigma}] = [k]\{\bar{\varepsilon}\} \tag{2.62}$$

where k is the effective macroscopic stiffness matrix.

In the above formulation of homogenization process, the homogenized constitutive model constants are found by inverting the Eq. (2.62), which imposes computational complexity. For instance, assume that a 2D RVE will be modeled as an isotropic elastic material, which is the simplest case of Hooke's law. Then, it would be sufficient to apply the PBCs under tensile conditions by prescribing displacement on surfaces in one direction (e.g. surfaces in y_2 direction for the RVE in Figure 2.3). Since the boundary conditions represent a tensile or compressive configuration, the following holds: $\sigma_{22} = 0$, $\sigma_{12} = 0$, $\varepsilon_{12} = 0$. Then, the stiffness tensor is a fourth order tensor in 2D and gives the material constants by the constitutive equation of Hooke's law:

$$\sigma = {}^4D^e : \varepsilon^e \tag{2.63}$$

from Eq. (2.63), the effective Young's modulus and Poisson's ratio of the isotropic material is simply obtained by

$${}^4D^e = \frac{\nu E}{(1+\nu)(1-2\nu)}\left(II + \frac{1-2\nu}{\nu} {}^4I \right) \tag{2.64}$$

where E is the effective Young's Modulus, v is Poisson's Ratio, I is the second order unit tensor, and ${}^{4}I$ is the fourth order unit tensor. Then, the following expressions for effective Poisson's ratio and elastic modulus are readily obtained:

$$\overline{\upsilon} = -\frac{\varepsilon_{22}^{e}}{\varepsilon_{11}^{e}} \text{ and } \overline{E} = \frac{\sigma_{11}}{\varepsilon_{11}^{e}} \tag{2.65}$$

As seen, even for this simplest case, the complex tensors are needed to be solved. For more complicated constitutive models (e.g. viscoelastic or plastic material models) the computational cost working with such tensor is a burden. The complexity also increases when homogenization methods with more advanced linking formulations are utilized such as asymptotic homogenization method [42], [76], discrete homogenization method [70], etc. Furthermore, a thoroughly motivated selection of a constitutive model at the macroscopic level remains difficult.

2.3.3. Upscaling through Optimization

As stated in Section 2.3.2, the computational demand of the homogenization methods is high because of the inherent complex linkage formulations that are based on the continuum theory. In a deterministic sense, a simple alternative to these homogenization methods is to use the calibration process described in Section 2.2 (or the inverse material characterization process) for upscaling a fine scale model to a coarser scale model with homogenized properties. This method can also be called parameter retrieval through optimization, where the homogenized material at coarse scale is treated as a black-box function rather than directly solving the explicit constitutive model equations. When black-box functions are used such as FEM, direct solution for the homogenized

properties is not available since the black-box functions are not invertible. Hence, an optimization process is utilized to find the optimal homogenized properties that enable the matching of the homogenized model responses with the fine scale model responses.

This process is similar to the calibration process described in Section 2.2 since the computational model input parameters (i.e. coarse scale model) is predicted based on existing observations or measurements (i.e. fine scale model responses). The application of the homogenization through optimization is seen when fine scale uncertainties are considered in homogenization [97] and [98]. The inverse material property characterization method is also called the stochastic upscaling method [97] as the uncertain homogenized properties at an upper (or coarser) scale is determined based on the lower scale (or finer scale) uncertainties of the material. In Figure 2.4, the flowchart of this upscaling method through optimization is depicted for a deterministic case for a complex plate example introduced in [98].

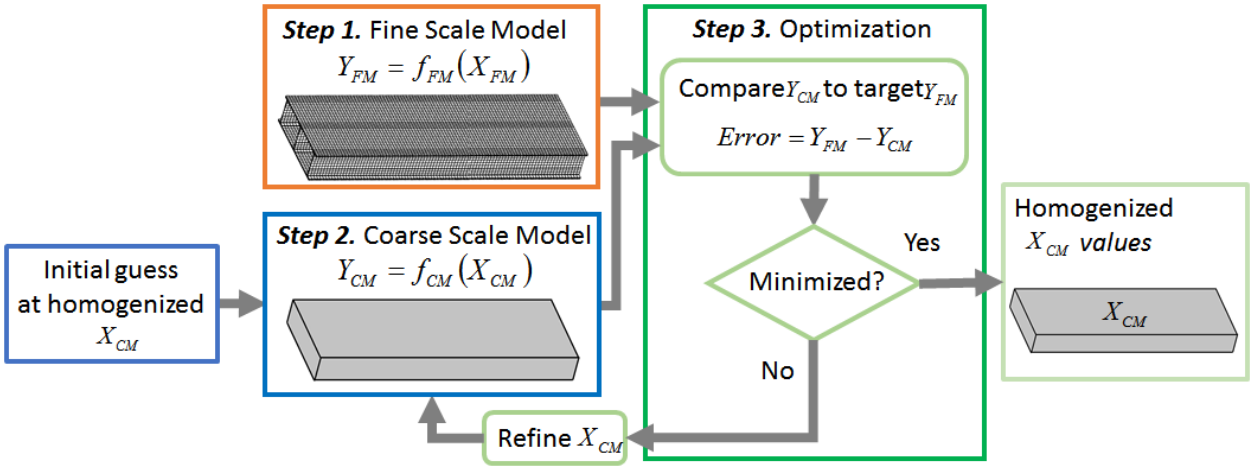

Figure 2.4. Flowchart of the upscaling method through optimization with the complex plate example in [98].

In this upscaling method, there exist three main steps. In the first step, the fine scale model of the structure is constructed with detailed information of the material as $Y_{FM} = f_{FM}(X_{FM})$ where the

responses Y_{FM} are calculated with the functional relationship $f_{FM}(.)$ using the input variables X_{FM}. In the complex plate example shown in Figure 2.4, the fine scale model is an FE model of 2 skin plates, three longitudinal ribs and twelve elongated L-shaped members that are connected with the adhesive material [98]. In the second step, a corresponding coarse scale model $Y_{CM} = f_{CM}(X_{CM})$ is developed, which is a simple FE model homogenized properties X_{CM}. In Figure 2.4, a Bernoulli beam is used as the coarse scale model which represents the fine scale model. The third step is the optimization. As stated in Section 2.2, because the coarse scale model cannot be reversed explicitly, it is treated as an inverse problem where a parameter retrieval process through optimization is applied. Specifically, an initial guess is made for $\mathbf{X}_{CM}$ and the corresponding coarse scale model responses Y_{CM} are calculated. Then, error or difference between the fine and coarse scale responses is calculated. If the error is minimized using an optimization algorithm, the homogenized values of $\mathbf{X}_{CM}$ are obtained. Otherwise, $\mathbf{X}_{CM}$ values are refined. The coarse scale model responses are calculated again, and the error is minimized by repeating this process.

As stated earlier, this upscaling process through optimization is very promising to mitigate the computational cost of the homogenization methods that has complex linking formulations with explicit governing equations at the coarse scale. Stochastic upscaling methods introduced in existing references such as [97], [98] to consider the effects of uncertainties at the fine scale levels on the homogenized properties also imply that this approach has a potential to use in material characterization in a multiscale modeling framework. Another advantage of the stochastic upscaling process is that it enables the calibration of the coarse scale FE model input variables based on the fine scale details. Thus, when these homogenized input variables are used at a subsequent level, for which the fine scale model is generated using the coarse scale FE model of the lower level, any numerical

errors can be eliminated that may occur when the other homogenization processes are used. The stochastic upscaling method through optimization is improved in this research to be able to use it as a multi-level uncertainty quantification approach for the efficient design of cellular lattice structures.

2.4. Verification & Validation (V&V)

Verification and Validation (V&V) process of computational models have seen a large interest for the last two decades because V&V procedures are the primary means of assessing accuracy in computational models. As can be viewed in the following figure verification is defined as the accuracy assessment of a computational model by known exact mathematical models while the validation is defined as the evaluation of a computational model by the real world experiments.

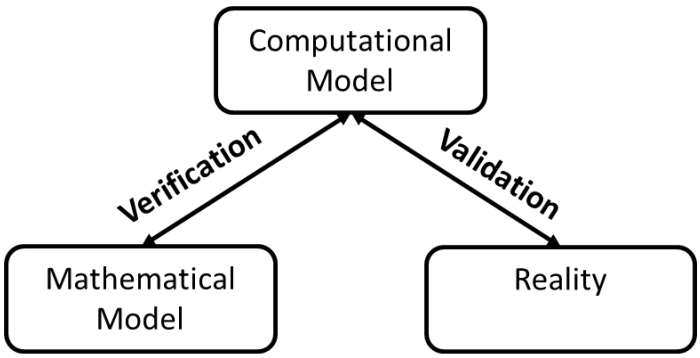

Figure 2.5. Relation of the verification and validation with the computational model

2.4.1. Verification in Computational Modeling

Computational models are developed to predict the outcome of the problem for which the mathematical models are not explicitly available or too complicated. A mathematical model of a physical problem usually comprises a set of partial differential or integral equations with

associated boundary conditions and constitutive equations. The mathematical model for a physical process, on the other hand, can model relatively simple cases since the complexity of the model dramatically increases for complicated cases. Therefore, computational models, which are the numerical implementation of the mathematical model, are developed to be able to solve the problems. For example, we can have the explicit mathematical expression for a one-dimensional beam bending problem, while for a three-dimensional crossbar under bending these mathematical expressions are too simple to have accurate results. Hence, a finite element model of the cross-bar is developed as a computational model to predict the behavior of the bar. This computational model has the fundamentals of the mathematical expression for the simple beam bending case, and it enables the application of the expression for the complicated situations. Hence, it is expected that the computational model should give very accurate results for the simple case when the results are compared with the mathematical expression. A verification process is implemented to check the accuracy of the computational model against the mathematical model. In a more general definition, verification is the characterization of the numerical approximation errors associated with a computational model to evaluate its predictive capability [103].

The verification process can be divided into two categories. The first one is the ***code verification*** that determines whether the computer program or the code can correctly implement the intended algorithms. For code verification, the correct solution of the intended algorithm must be known. Since it is very challenging to have this exact or correct solution, usually simplified model problems are chosen. Code verification addresses both the correctness of the chosen numerical algorithm and the correctness of the written source code to ensure there are no coding mistakes. Since coding mistakes can be eliminated when they are identified, their effects on the numerical solution are tough to estimate. To minimize the errors due to the coding errors or

mistakes, good software engineering practices and specific techniques for scientific computing software should be employed. Various code verification techniques have been proposed and can be checked for further understanding [101]-[103],[162],[163].

The second category is the ***solution verification*** **(or calculation verification)** which ensures a given computational model simulation of a mathematical model is sufficiently accurate for the intended use. In other words, solution verification is implemented for the computational model(s) that will be used to make the prediction for a particular problem. It depends on the code verification because code verification ensures that the numerical algorithm is consistent and convergent and mistake-free. Once the code verification is done, the solution verification can ensure that the simulations will converge to the exact solution of the mathematical model for the intended application or problem. In solution verification, the main focus is to estimate the numerical errors that occur when a mathematical model is discretized and solved using the computational model. Hence, the solution verification is carried out in terms of the responses or outputs to find the numerical error. Solution verification can be performed by using the computational model itself to produce high-resolution reference solutions. For instance, the computational model can be investigated with various size of meshes or different arrangement of the mesh elements. Such studies enable to assess the rate at which self-convergence is achieved in the responses thus the error is estimated and controlled for the chosen resolution or discretization.

Numerical errors can arise due to the *round-off, statistical sampling, iteration, and discretization*. *Round-off errors* occur because of the use of finite digits. It can be reduced by using more significant digits in the computation. Due to the advancements in the computational power, the round-off errors can be avoided since it has a very small effect compared to the other error types. A very practical approach to assessing the effects of the round-off error on a simulation

prediction is to run the simulation with the desired precision, then re-run the simulation with larger precision and compare the solutions. The precision level is chosen when the residuals can no longer be reduced due to round-off error [101].

Statistical sampling error is another error to be estimated in verification. For stochastic analysis, some realizations are needed to determine the mean quantity of the response. The statistical sampling error can be estimated by assessing the convergence of the desired system response quantities with the increased number of realizations, iterations or time steps. If the number of realizations is the case, for example, the simple approach is to estimate the mean value of the different number of realizations and compare the running average with a true average which is estimated for a very large number of realizations. Then, the smallest number of realization which produces a sufficiently small error compared to the actual average is determined as the number of realizations. A better approach would be to determine a stopping criterion for the realizations based on the convergence of the standard deviation of the response. A desired 0.02% error can be considered for this purpose [164].

Discretization error arises because the spatial domain is decomposed into a finite number of nodes/elements. For complex scientific computing problems that involve nonlinearities, geometric complexity, multi-physics and multiple scales, generating an appropriate mesh to solve the problem is often inadequate. Therefore, it is often the largest numerical error and is difficult to estimate for practical problems. *Iteration errors* occur when an iterative method is used to solve the system of algebraic equations resulting from the discretization of the mathematical model. Iterative methods are often required for the cases where nonlinear discretization employing implicit algorithms are used. Even for the linear discretization direct solution methods can be used, but if there exist a large number of unknowns, iterative methods are more efficient than the direct

methods. When iterative methods are utilized, an iterative convergence approach is necessary to find the difference between the current numerical solution at iteration *k* and the exact solution of the discrete equations. In most cases, the exact solution is not available, and therefore, a convergence criterion in terms of the difference, ε_h^{k+1}, (either absolute difference in Eq. (2.66) or relative difference in (2.67)) between successive iterates is calculated:

$$\varepsilon_h^{k+1} = \left| f_h^{k+1} - f_h^{k} \right| \tag{2.66}$$

$$\varepsilon_h^{k+1} = \left| \frac{f_h^{k+1} - f_h^{k}}{f_h^{k}} \right| \tag{2.67}$$

where f_h^{k+1} and f_h^{k} are the responses at iteration *k*+1 and *k*, respectively. This iteration convergence checking approach can also be used to check the mesh convergence to evaluate the *discretization error* as well. In that regard, denser meshes are generated for the same model and the difference from the previous coarser mesh result is computed using Eq. (2.66) alternatively, (2.67). If sufficient convergence is achieved, at iteration *k*, the corresponding mesh size is used in the simulations. Numerical errors can be neglected if they are sufficiently small. In the cases when the numerical errors are relatively high and certain, then these errors can be removed from the numerical simulations by considering a bias error. If the numerical errors are not known as certain those can be treated as epistemic uncertainties, which are the uncertainties due to a lack of knowledge of the actual value of the error. Moreover, depending on the contribution of the quantitative assessment of the errors, the code is revised by focusing on the reason to decrease that error type.

2.4.2. Validation in Computational Modeling

Validation is a way of assessing whether or not the model prediction is within some tolerance determined by the user based on the application when compared to the quantitative observations or measurements for a physical system or experiment. Hence, the available physical observations are crucial to any validation assessment. However, experimental data are often expensive especially for complex systems. The validation experiments, therefore, should be chosen to provide optimal information for the validation of the computational models. In the case of complex systems hierarchical validation processes are preferred [102], [103]. The hierarchical validation process can be considered as a validation pyramid depicting the increasing complexity of the physical scenarios [105]. In Figure 2.6, the validation pyramid approach is shown for an aircraft structural design.

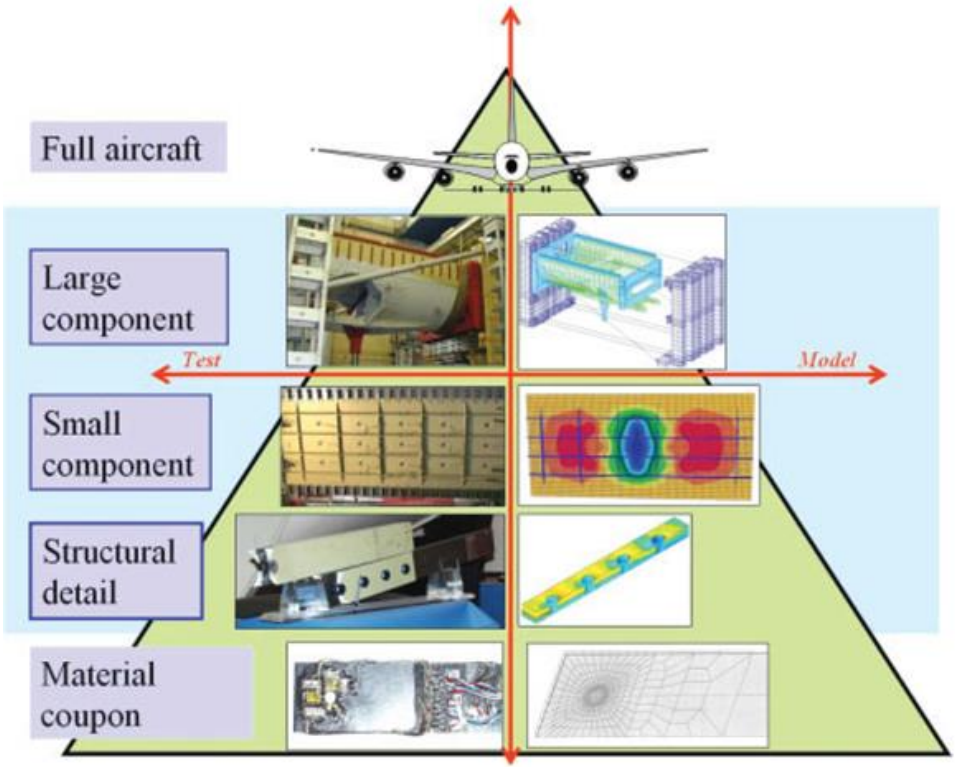

Figure 2.6. Validation pyramid approach for an aircraft structural design [105]

The left side of the pyramid has the experiments with increasing complexity while the right side has the corresponding computational models. At the lowest level of the pyramid, a calibration process described in Section 2.2 is achieved for subcomponents of the system based on simple experiments. Combinations of subcomponents are then tested against more complicated models which have less number of experimental repetitions. At the highest level of the pyramid, if there exist some experimental observations for the complete system, the validation test is achieved for the full model.

In Figure 2.7, the flowchart of the V&V process at each level of interest taken from the ASME V&V guide [103] is demonstrated. The left side of the flowchart depicts the computational model, while the right side is the experiments. Once the code verification and solution verification are completed for the computational mode, the uncertain simulation responses or outputs are obtained by utilizing uncertainty quantification methods described in Section 2.1 and Section 2.2. Then, a comparison with the validation experiments should be made. One key fundamental challenge in V&V efforts is to compare the model predictions with corresponding experimental observations given uncertainties in both. This step is critical because it defines how the model will be challenged against the physical data depending on the intended use of the model.

The comparison can be conducted qualitatively or quantitatively. Qualitative methods often involve the comparison of the computational model against experiment results graphically with histogram, box plots, and scatter plots to make a subjective judgment on whether the computational model has sufficient accuracy for its intended applications. However, those do not quantify the degree of agreement and therefore are insufficient for validation. A validation assessment method should be able to answer the question whether the computational model accurately represents the reality as well as it should support whether the degree of confidence with

which we accept or reject a model is adequate for the intended model use. Statistics-based quantitative methods are needed for this purpose.

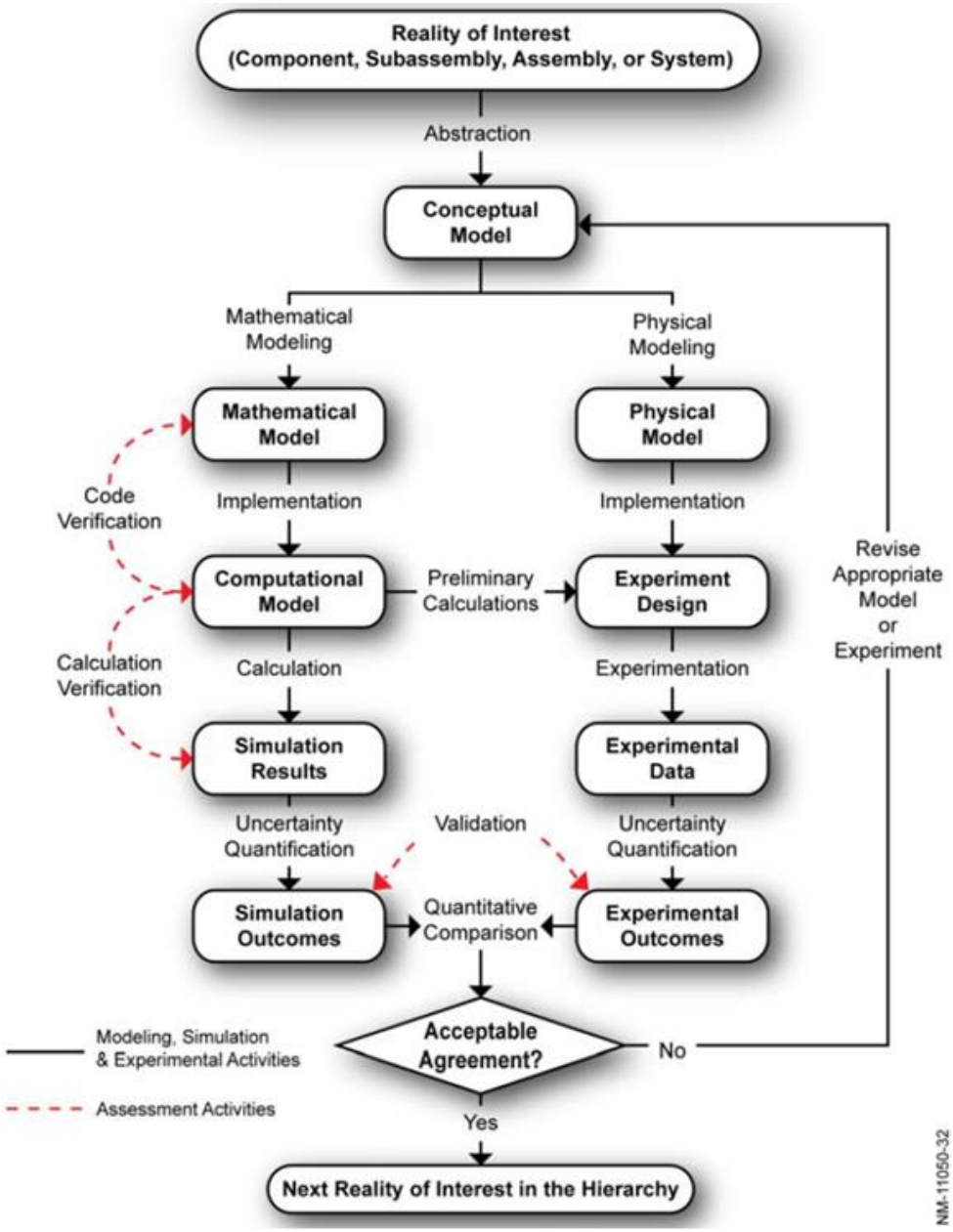

Figure 2.7. Verification and Validation flowchart at each level of complex systems

A *validation metric* or a measurement system can provide a quantitative assessment of the comparison. By definition, a *validation metric* provides a quantitative measure of agreement

between the predictions of a computational model and physical experiment outputs. The output of a validation metric is compared to the validation requirement to assess whether or not the agreement is sufficient. If the metric value is larger than the given threshold, then the model predictions are accepted, and the next level of interest can be performed. If the metric value is smaller than the given threshold, then the model predictions are rejected. Then the model has to be revised, and validation has to be done again until sufficient agreement is obtained based on the validation metric. Because uncertain quantities are involved, care must be taken to choose the response quantities and validation metric so that the model is correctly and sufficiently challenged. Since the validation metric is the key element of the validation, it is explained in a separate section in Section 2.4.3.

2.4.3. Validation Metric

This review investigates several validation metrics proposed in the literature to address both accuracy and adequacy requirements for model V&V. There is no correct way to define a validation metric, but for selecting a validation metric, there exist some key considerations or features. First of all, it should be determined what the model is being asked to predict (depending on the intended use of the top-level model) as well as what types of experimental data are available or needed. Second, the metric should be a quantitative measure of the agreement between predictions and experiments. It should also provide the same assessment for any user or decision maker independent from their individual preferences, meaning it should be objective. Another desirable feature of a validation metric is the ability to account for the uncertainties in the predictions and physical observations. A validation metric is desired to consider a statistical

confidence level associated with the amount of available experimental data. The validation metric should measure the agreement when there are multivariate responses and multiple validation sites.

2.4.3.1. Classical Validation Metrics

Various types of quantitative metrics have been proposed over the years for the validation of computational models. Oberkampf and Barone [165], Liu et al. [106] and Ling and Mahadevan [107] have attempted to collect and discuss various validation metrics. Depending on the nature or form of the model output and experimental data, the validation metric may involve comparison of means or variances or even two probability distributions. When mean and standard deviations are compared, simply the estimated error is given by the difference between the predicted mean and the mean of test results. For instance, we can measure the mismatch between model responses (Y_M) and experimental observations (Y_E) by defining a metric, d_E, as

$$d_E(Y_M, Y_E) = E\left(\left|Y_M - Y_E\right|\right) \neq \left|E(Y_M) - E(Y_E)\right| \tag{2.68}$$

where E denotes the expectation (or the mean) of the corresponding random response, which can be calculated using Eq. (2.4). This idea can be generalized for a higher order of moments and the equality in a higher order moment implies equality in the lower order moments. Another metric is an average relative error which is defined as the ratio of the absolute value of the difference between two mean values and the mean of the test results.

These metrics assume that the mean and standard deviation of both model and experiment results can be obtained accurately. In real, on the other hand, the number of experiments is not sufficient to accurately determine the statistic parameters of the outputs (e.g. when epistemic and aleatory uncertainties exist). Hence, these methods do not work well when a few experiments

and/or simulations are conducted for validation. In addition, the use of moment matching is simple, but a subjective decision criterion is required to evaluate the metric result. Hypothesis testing methods or Goodness of fit tests explained in Section 2.1 have been explored for model validation assessment in recent literature to address these issues [108], [166]. In this method, a Boolean decision is given (model is accepted or rejected) based on a test statistic method according to the differences between the moments or distributions of model and experiment outputs. The decision is made between the plausibility of two hypotheses: First, the null hypothesis, denoted by H_0, represents something (usually null hypothesis is formulated as the model prediction being equal to an observation) that is believed to be accurate. Second, the alternative hypothesis, denoted by H_1, represents the opposite hypothesis to null hypothesis H_0 (usually the alternative hypothesis is formulated as model prediction being not equal to the observation). In classical hypothesis testing, a test statistic T is defined as a function of the difference between some estimators of observation and prediction, and then the actual value of statistic t is estimated based on the validation data. The test statistic follows a certain distribution such as t distribution, F distribution, etc. Thus, a corresponding probability (p-value) that the test statistic falls outside a range defined by the computed value of the test statistic under the null hypothesis is calculated. The p-value is an indicator of how good the null hypothesis is because a better H_o corresponds to a higher probability of the test statistic falling outside the range. The null hypothesis is rejected if the computed p-value is less than a significance level (α) and thus the model is rejected.

There are various test statistics used in hypothesis testing methods. When normally distributed outputs are assumed, the mean and variances are compared and tested using t-test statistic and F-test statistic, respectively [106]. The problem of these classical hypothesis testing methods is that for validation of entire distribution, it is not adequate to compare only the first two

moments. Moreover, when only one physical experiment data point is available at each validation site, the hypothesis testing is not applicable because the mean and variance of the physical observations cannot be calculated with only one sample [106]. Hence, the hypothesis testing is used to compare the differences between the two CDFs using other test methods such as Anderson-Darling (A-D) test [117], Kolmogorov-Smirnov (K-S) test [118] and Cramer-von Mises test [116], which were described in Section 2.1. Even though these methods are simple to estimate, the problem of hypothesis testing is that it only allows a Boolean decision (accept or reject) and does not quantitatively measure the discrepancy between predictions and observations [107].

Zhang and Mahadevan [167] applied Bayesian hypothesis testing and the Bayes factor metric for validation of limit state-based reliability prediction models. In Bayes approach, the statistical parameters such as mean are treated as random variables and updated by the experiment data. If we observe *k* failures out of *n* tests in our model to predict the failure probability *p* for a physical system, then the Bayes factor metric is derived as

$$B = (n+1)(n!/(n-k)!k!)\,p^k(1-p)^{n-k} \tag{2.69}$$

When $B > 1.0$, it is concluded that the model predicts well the experiments. The Bayes factor metric has been extended to the validation of more generalized outputs [168]. When the null hypothesis H_0 defines that the model is true and alternative hypothesis H_1 is defined as the opposite of H_0, the Bayes factor metric is the ratio of posterior distributions of two hypotheses of the model prediction [168]. Rebba and Mahadevan [169] introduced the equality-based formulation $\left(H_0 : y_m = y_D, H_1 : y_m \neq y_D\right)$ and the interval-based formulation $\left(H_0 : |y_m - y_D| < \varepsilon, H_1 : |y_m - y_D| > \varepsilon\right)$ for Bayesian hypothesis testing, where y_m is the model

prediction for a particular input x and y_D is the test value. Bayes factor metric can identify the acceptance of a model even when only one observation is available [106]. However, the Bayesian metrics are affected by the subjective choice of the prior. It would be more useful for a decision maker to have a direct, objective and quantitative measure of the "reliability" or probability of success of the model. Also, using simple probabilities to express the validation results would be easier to interpret than the aforementioned complicated probability metrics or Bayes factors. Simple metrics are preferred for this reason. Another motivation for the use of simple metrics for comparison is that one can avoid the debate over major philosophical differences between frequentist and Bayesian hypothesis testing while performing model validation. Moreover, similar to the classical hypothesis test, Bayesian hypothesis methods are also only suitable for reaching a yes or no conclusion for model selection. They cannot quantitatively assess the accuracy of a model by measuring the discrepancy between model predictions and experiments while distance based methods can be used for model selection as well as for quantifying the model error to update the model prediction in practical validation activities.

A frequentist's metric [106] can be used to overcome the drawbacks of the classical and Bayesian hypothesis metric methods. The distance between the mean of predictions and experiment results is measured, and a confidence interval of test data can be constructed based on the standard deviation of the test data (s) and compared with the metric result (i.e. the estimated error in the model, $\hat{e}$.

$$\left(\hat{e} - t_{\alpha/2}(N-1) \cdot \frac{s}{\sqrt{N}}, \hat{e} + t_{\alpha/2}(N-1) \cdot \frac{s}{\sqrt{N}} \right) \tag{2.70}$$

In this confidence interval, $t_{\alpha/2}(N-1)$ is the $1-\alpha/2$ quantile of the *t* distribution for *v* = *N-1* degrees of freedom. The metric can be the average absolute error metric mentioned before. If the error is smaller than the confidence interval then the model is accepted as adequate [101], [170]. In this metric, the decision criterion of accepting or rejecting a model is separate from the metric itself since no null hypothesis is used. Thus, it allows for the one to objectively quantify the variation of the error while making a decision separate from the metric itself. Nevertheless, the confidence interval requires at least two experiments. That means it is not usable if there is only one experiment (because *N*-1 becomes zero if there is one experiment). Also, if only mean values are used, the metric cannot account for the variation of the model and experiment results. This issue might lead a wrong decision about the model if the means are the same, but the variations are different.

A simple validation metric, called the *z*-metric, which quantifies the difference between uncertain model and test results in the form of a simple measure of error, is proposed by Ref. [171]. Since the model and experimental results are both random variables, the *z* value of the metric will be a random variable. The CDF of the *z*-metric is used to calculate the probability that the computed error is acceptable (not greater than a specified amount) since the error and probability are related in the CDF. A smaller error corresponds to a smaller probability that the error will be met. Rebba and Mahadevan [169] proposes a model reliability metric in which a simple validation metric is defined as $r = P(-\varepsilon < d < \varepsilon)$, which can also estimate the model reliability. This metric indicates that the probability that the difference *d* between experiment result and model prediction is within a small interval. A confidence requirement *c* is determined to accept the model prediction only when $P(-\varepsilon < d < \varepsilon) \geq c$. Even though the variability is accounted for the validation of these methods, the details of the distributions (i.e. higher order moments) can be ignored.

For a distribution model, it is not always easy to know what statistics are relevant for a particular application and therefore, the entire distribution must be considered in a validation metric. One of the very popular approaches is the maximal probability, i.e., vertical difference between the two CDFs given by Eq. (2.7) that defines the K-S statistical test for comparing distributions. Another widely used measure of discrepancy is the Kullback-Leibler divergence (i.e. relative entropy) [172]:

$$d_{KL} = \int_{-\infty}^{\infty} p(x) \log \frac{p(x)}{q(x)} dx \tag{2.71}$$

where x is the random variable (i.e. the response), the probability function p represents the observations from experiments, and the probability function q denotes the observations from model predictions. Relative entropy is commonly used in information theory and also in physics to measure the entropy of the distribution p with respect to the distribution q. L_1 norm and L_2 norms are also utilized to consider the entire CDF. L_1 norm is known as the sum of the absolute differences between the model predictions and experimental observations:

$$d_{L1} = \sum_{i=1}^{n} \left| y_{M,i} - y_{E,i} \right| \tag{2.72}$$

The average of the L_1 norm can also be used, which is called "mean absolute error" (MAE):

$$d_{L1} = \frac{1}{n} \sum_{i=1}^{n} \left| y_{M,i} - y_{E,i} \right| \tag{2.73}$$

L_2 norm, which is the square root of the sum of the square of the differences, is given by:

$$d_{L2} = \left(\sum_{i=1}^{n} \left(y_{M,i} - y_{E,i} \right)^2 \right)^{1/2} \tag{2.74}$$

In the least squares minimization given by (2.33), the L_2 norm formulation without the square root is utilized. The average of it is also a widely used error checking method and called "mean squared error" (MSE) or "squared distortion":

$$d_{L1} = \frac{1}{n} \sum_{i=1}^{n} \left(y_{M,i} - y_{E,i} \right)^2 \tag{2.75}$$

These metrics, given in Eqs. (2.72)-(2.75), are also used in statistical modeling and calibration processes outlined in Section 2.1 and 2.2, and in the stochastic upscaling methods through optimization described in Section 2.3.3 to evaluate the result in the optimization processes for predicting the input properties by minimizing the differences between the target or experimental responses and model responses.

2.4.3.2. Area validation metric

Despite the extensive use of the metrics above in the validation processes, these metrics cannot be applicable when the number of experiments and simulations differ from each other. One validation metric that can be used to overcome these drawbacks is using the "area validation metric" [110]. The area between the CDF of the model output denoted by F and the CDF of the experiment output denoted by S_n is calculated as the measure of mismatch between them. Mathematically, the area between the curves is the integral of the absolute value of the difference between the functions

$$d_A(F, S_n) = \int_{-\infty}^{\infty} \left| F(x) - S_n(x) \right| dx \tag{2.76}$$

The stochastic prediction from the model can be characterized as a CDF, $F(x)$ where x denotes the predicted variable. For discrete case, the CDF is referred to as an empirical CDF, and it is built by the data set including the discrete values of the variable x, i.e. observations. ECDF is a non-decreasing step function with a constant vertical step size of $1/n$ where n is the sample size of the data set. The locations of the steps correspond to the values of the data points. The distribution for the data x_i, $i=1,2,\ldots,n$, is given by Eq. (2.6). An ECDF is an exact representation of the distribution of the data when it is discrete, regardless of the amount of data hence a better modeling of distribution of discrete data opposed to a continuous CDF. It does not require any assumptions to represent the data, for instance, as is needed to construct a histogram of a data set. Moreover, it preserves all the statistical features of the distribution such as its scatter, dispersion, central tendency, location, etc. [101].

Unlike the validation metrics in hypothesis testing methods and the reliability-based methods, the area metric has no probability interpretation. It is merely the difference between the entire distributions (i.e. CDFs) of predictions and experiment results; its physical unit is the same as the quantity of interest. Therefore, the area validation metric can be viewed as a direct measure of prediction error. [110]. A large area difference indicates that the disagreement between the model predictions and the experimental measurements is high. Since the area metric has the physical unit of the quantity of interest and represents the prediction error of a model, the threshold of model rejection/acceptance can be set up based on the error tolerance limit in the prediction domain. Moreover, the area metric can be used even when only a few data points from

computational models or experiments are available. The lack of experimental data can also cause a larger area metric value. It is also applicable when the simulation and experimental measurements are given by a p-box [101].

2.4.3.2. *u*-pooling method

When the data is sparse at multiple validation sites, the agreement between two distributions can be measured by using the *u-pooling* method introduced by Ferson et al. [110] as an extension of the area metric to multiple validation sites. It allows o assess the global predictive capability of a model by pooling all the physical experiments at multiple validation sites into a single aggregated metric using the probability integral transformation (PIT) theory [173]. In PIT, if Y is a random variable or response of a model with its CDF, $F_Y(y)$, then the CDF values of Y denoted by $U = F_Y(y)$ follows a standard uniform distribution (i.e. $U \sim$ Uniform(0,1)).

The illustration of the u-pooling method for two validation sites ($n_{VS} = 2$) corresponding to two prediction CDFs $F_M^{(k)}(.)$ where $k = 1,...,n_{VS}$ is given in 0. Let the experimental observations for each validation site are denoted by $Y_E^{(k)} = \{y_E^{(k)}(j)\}$ where $j = 1,...,n_E^{(k)}$ and $n_E^{(k)}$ is the number of experimental observations at k^{th} validation site. In 0, the first validation site has two experimental observations $n_E^{(1)} = 2$, i.e. $Y_E^{(1)} = \{y_E^{(1)}(1), y_E^{(1)}(2)\}$, while the second validation site has one experimental observation $n_E^{(1)} = 1$, i.e. $Y_E^{(2)} = \{y_E^{(2)}(1)\}$. For each experimental observation $y_E^{(k)}(j)$, a corresponding u-value is calculated using the corresponding prediction CDF model:

$$u_t = F_M^{(k)}(y_E^{(k)}(j)),\ t = 1,...,n_T \tag{2.77}$$

where n_T denotes the total number of experimental observations at all validation sites calculated by $n_T = \sum_{k=1}^{n_{VS}} n_E^{(k)}$. As seen in Figure 2.8(a), there exist three experimental observations $n_T = 3$ in total. Then, the ECDF of the *u*-values is calculated using Eq. (2.6). According to the probability integral transformation, if the model CDFs accurately predicts the experimental observations, then the ECDF of the *u*-values must follow a standard uniform distribution (SUD). Thus, the ECDF of the pooled u-values is compared with the CDF of the SUD to make a decision for validation of the predictions as shown in Figure 2.8(b). This comparison can be made by the area validation metric given by Eq. (2.76).

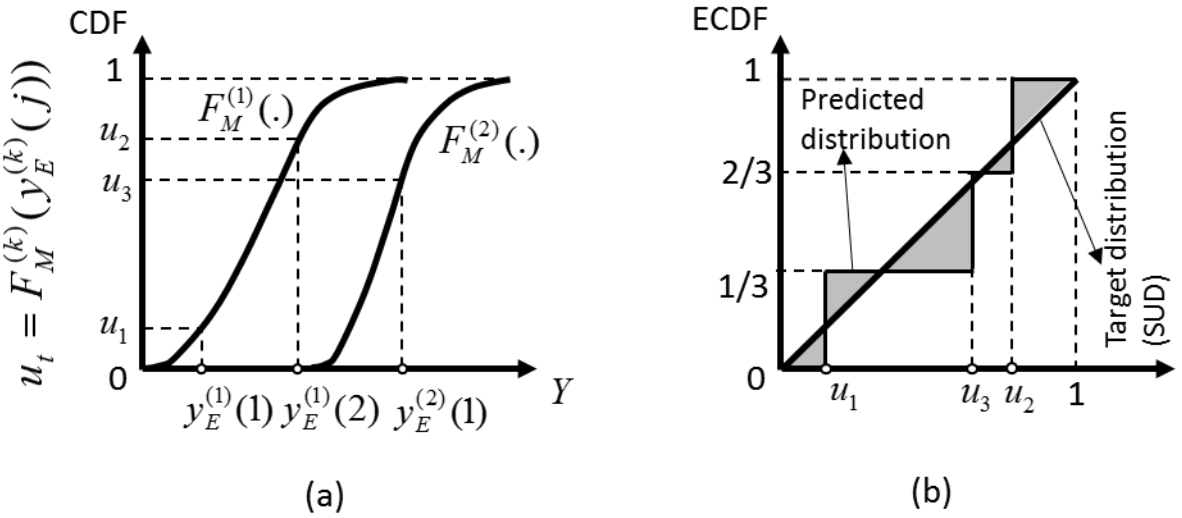

(a) Calculate the CDF values (*u* values) of each experiment response from the prediction CDF of corresponding validation site. (b) Comparison of the ECDF of all *u* values with the CDF of SUD.

Figure 2.8. Illustration of the u-pooling metric

Area metric and the u-pooling method can be used for validating a single response model as well as a model with multiple uncorrelated responses. However, they are not appropriate for validating multiple correlated responses [106]. Li et al. [111] introduces two new metrics, namely PIT metric

and t-pooling metric. In PIT metric, the joint CDF of model responses and multivariate experimental observations are transformed into a univariate CDF and a random data sequence following the multivariate PIT theorem to make a comparison between the empirical CDF of the data sequence and the PIT distribution of the joint CDF of model responses. The other method, t-pooling metric, allows for pooling observations of multiple responses observed at different validation sites similar to the u-pooling method. It compares the empirical CDF of the twice transformed observations with the standard uniform distribution.

The distinctive disadvantage of area validation metric is that it is challenging and/or subjective to determine a model acceptance threshold. Because the metric value has the same unit as the responses, for different applications, the analyst must decide the threshold to accept the model based on his/her beliefs. The u-pooling metric overcomes this drawback since the area metric value in u-pooling is always between 0 and 0.5, where 0 indicates a perfect match and 0.5 indicates the worst match. Thus, it allows quantifying the discrepancy between experiments and computational model, and the model acceptance is determined with respect to the accuracy requirement of the problem. **Nevertheless, the accuracy requirement is determined by the allowable error based on practical needs and the application, and the area metric threshold does not account for the number of available experiments while making a decision of accepting or rejecting the model predictions.**

2.5. Topology Optimization

Cellular lattice structures (CLSs) find a wide application area from aerospace parts to medical implant scaffolds where light weight and high stiffness is required. The current computational approaches to design CLSs are based on the topology optimization process. Hence, in the

following subsections, the theory discrete and continuous topology optimization, and Reliability-based topology optimization are described.

2.5.1. Deterministic Design Optimization

Advances in the computational abilities allow for designers to use optimization methods in the design process of the complex engineering systems. With the rapid development of technology, these methods are integrated with the computational tools so that they can be usable in the early design stage. Thus, more efficient, economical and creative products can be produced. Optimization is used in every aspect of human life from daily activities to industrial applications. As a simple daily example, people optimize their way to go to work; students optimize their weekly schedule by choosing the courses that benefit the most. As an industrial application, companies design automobiles having high efficiency as well as having better performance. Without an optimization, it is not possible to find an optimum solution.

Optimization finds broad applications in automotive, aerospace, construction and manufacturing industries. In engineering problems, in particular, mathematical programming techniques are used as optimization methods. The problem must be formulated as a system whose performance is controlled by some input variables and specified by a well-defined objective function. The goal of optimization is to search for the minimum (or maximum) of the objective function $f(X)$ of a problem to find the best value for each design variable X_i, $i \in 1,...,n$, that it depends on. A vector of the design variables, $X = (X_1, X_2,..., X_n) \in R^n$ in the n-dimensional design space R, represents a single design for a set of values where n denotes the number of design variables in the optimization problem. The problem is bounded by some constraints regarding

geometry, performance, safety, cost, and manufacturability. These constraints can have inequality and/or inequality form. Engineering optimization processes provide the best design that satisfies all the constraints and bounds while minimizing the objective function. A generalized mathematical formulation of the optimization problems can be presented as follows:

$$
\begin{aligned}
&\textit{Given} && X && : \text{vector of design variables} \\
& && f_j(X) && : j^{\text{th}} \text{ objective function} \\
& && g_k(X) && : k^{\text{th}} \text{ inequality constraint} \\
& && h_l(X) && : l^{\text{th}} \text{ equality constraint} \\
&\textit{Find} && X = \{X_1, X_2, ..., X_n\} && \text{to} \\
&\textit{Minimize} (\text{or Maximize}) && f_j(X), && j = 1,2,...,n_f \\
&\textit{S}\text{atisfy} && g_k(X) \le 0, && j = 1,2,...,n_g \\
& && h_l(X) = 0, && l = 1,2,...,n_h \\
& && X_i^l \le X_i \le X_i^u, && i = 1,2,...,n
\end{aligned}
\qquad (2.78)
$$

where n_f, n_g, n_h, n, are the number of objective functions, equality constraints, inequality constraints, and design variables, respectively. X_i^l and X_i^u are the lower and upper bounds on the design variable X_i.

This formulation is not unique and may show differences depending on the application area and the problem. The optimization is not only used for the design of engineering applications. Statistical modeling techniques (section 2.1), calibration processes (section 2.2) and stochastic upscaling methods (Section 2.3.3) also utilize optimization processes for modeling purposes. Therefore, there is not a unique optimization formulation to be able to solve all optimization

problems. For example, if there is a single objective function with a few design variables, traditional methods can be used such as graphical solution method. However, real world engineering problems are too complex to be able to design with a few design variables. In topology optimization process there is a high number of design variables that are needed to be considered in the design. Hence iterative optimization algorithms are utilized to find the optimal design where the design variables are updated automatically based on the solution of the model [174].

2.5.2. Stochastic Design Optimization

It is important to consider the uncertainties in material properties, external loading, and boundary conditions, etc. in the computer-aided design stage. The traditionally used safety factors do not usually lead to an optimal design for a given level of safety because different safety factor values are required for various structural members or different failure modes. Recently, probabilistic approaches are coupled with design optimization methods to design structures that achieve desired objectives even when uncertainties are present. The design optimization processes that account for uncertainties can be grouped into two main classes: *Robust design optimization* (RDO) and *reliability-based design optimization* (RBDO).

2.5.4.1. Robust design optimization (RDO):

RDO is one of the widely used approaches, which aims at reducing the variability of the structural performance caused by regular fluctuations in the design parameters. The practical concept of robust design was first proposed by Taguchi, and a review of Taguchi methodology is given by Tsui [185]. Simply, the robust optimization consists of considering the objective function means

(μ) and standard deviations (σ) as objectives to be minimized. Then, in robust optimization formulation, the minimization part of Eq. (2.78) is written as:

$$Minimize \qquad \mu_{f_j}, \sigma_{f_j} \qquad j = 1,2,...,n_f \tag{2.79}$$

Thus, the structural robustness is assessed by a measure of the performance variability around the mean.

2.5.4.2. Reliability-based design optimization (RBDO):

When the uncertainties are often described by probability distributions, a reliability-based approach can be a more convenient option to evaluate the worst case scenario and the probability of failure. Hence, RBDO [2] is utilized that minimizes the objective function of the optimization problem while considering probabilistic constraints instead of the conventional deterministic constraints in contrast to robust design optimization methods. The formulation of a general RBDO process can be written as

$$\begin{aligned} &Find && X = \{x_1, x_2, ..., x\} \quad \text{to} \\ &Minimize \text{(or Maximize)} && f_j(X), \qquad j = 1,2,...,n_f \\ &Satisfy && P_k\left|G_k(X,\xi) < 0\right| \le P_{R,k}, \qquad k = 1,2,...,n_g \end{aligned} \tag{2.80}$$

where $G_k(.)$ represents the limit state function, ξ denotes the uncertain variables, $P_{R,k}$ denotes the specified probability of failure level. The limit state function can be formulated as

$$G_k(X,\xi) = R(X,\xi) - S(X,\xi) \tag{2.81}$$

where R is the resistance and S is the response of the system that is investigated. The structure is known as safe when $G_k \geq 0$ while it fails when $G_k < 0$. When sampling methods are used, the result of limit state function for each sampling set is evaluated based on this criterion. The number of samples that falls into the failure regions are divided by the total number of samples to calculate the failure probability. Then, the probability constraints are evaluated in RBDO. Hence, the probability of failure of a structure is an indication of times the structure violates its permissible safety limits. Deterministic equality and inequality constraints, given in Eq. (2.78), can also exist in the RBDO formulation in Eq. (2.81).

2.5.3. Topology Optimization

The extension of design optimization to the optimization of material layouts is known as topology optimization. Topology optimization operates on a fixed FE mesh of either continuum or discrete elements to optimally distribute material in the material layout. In the continuum element-based topology optimization, the shape of the external and internal boundaries and the density of each continuum element in the structure are optimized using a homogenization method. In the discrete element-based topology optimization, the problem is solved by determining the optimum number, position, and mutual connectivity of structural member elements [23]. Additive manufacturing techniques allow for the manufacturing of complex structure designs, obtained by the continuum or discrete element-based topology optimization processes [175].

Uncertainties can also be considered in the topology optimization processes described in Section 2.5.3. Robust topology optimization (RTO) has been studied to minimize the expected value and variance or standard deviation of the compliance or total strain energy of the structure that satisfies the volume constraint [186]. Reliability-based topology optimization (RBTO) has also been

studied where the deterministic compliance value of the structure is minimized under a reliability constraint [187]. The flowchart of both deterministic and reliability-based optimization approaches are given in Figure 2.9.

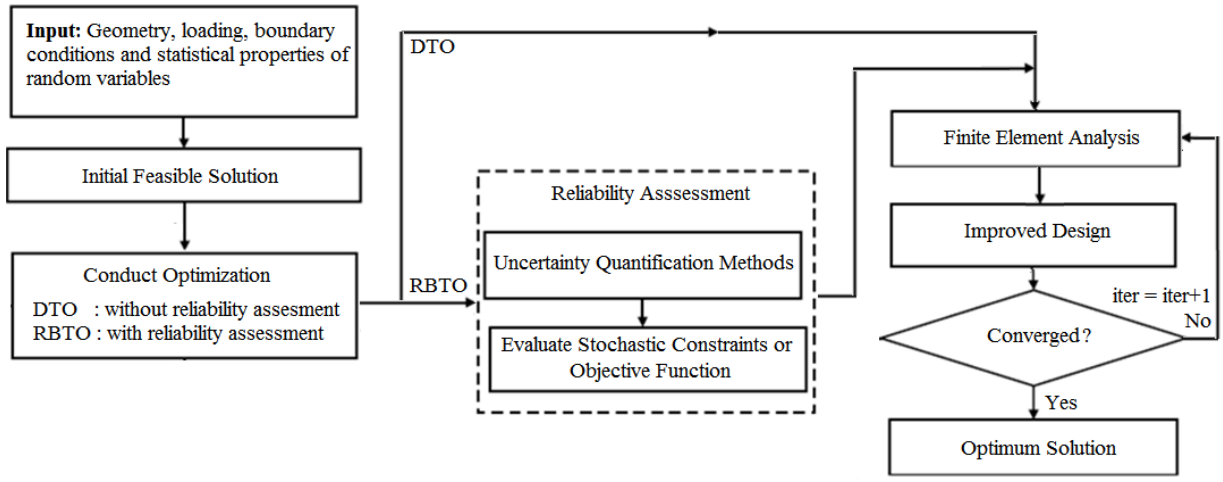

Figure 2.9. Flowchart of deterministic and Reliability-based topology optimization

2.5.4. Discrete Topology Optimization

In the discrete topology optimization approach, a ground structure, which is a grid of all elements connecting the nodes in the design space, is optimized by selecting the optimal cross-section parameters of the ground truss members. Hence, this method is also called ground structure method [176]. Each truss member in the structure is associated with a design variable that defines the element size or its contribution to the entire topology. Hence, the design variables are usually the thickness, diameter, or the area of the cross-section of each truss member.

In the optimization process, FEA is invoked, and the information required by the objective function is evaluated at each iteration. Truss or beam elements are used in the FE modeling of the

lattice structure for the ground structure optimization. The FEA formulation for beam elements is given by

$$\{F\} = [\mathbf{K}]\{\mathbf{U}\} \tag{2.82}$$

$$\{\mathbf{U}\} = [\mathbf{K_{red}}]\{F\} \tag{2.83}$$

where F denotes the force vector, **K** the global stiffness matrix, **U** the displacement vector, and $\mathbf{K_{red}}$ the reduced global stiffness matrix after applying the boundary conditions. The global stiffness matrix **K** is formed by the element stiffness matrices after applying global coordinate transformations. A simple formulation for ground structure optimization is to find the stiffest structure by minimizing the compliance (C) of the structure as the objective. The compliance to minimize is calculated from the FEA formulation by

$$C = F^T\mathbf{U} = \mathbf{U}^T\mathbf{K}\mathbf{U} \tag{2.84}$$

One constraint that is considered in the ground structure optimization process is that the volume of the lattice structure is to be less than or equal to a maximum allowable volume, denoted by V_{allow} and given by

$$\sum_{i=1}^{n} A_i L_i - V_{allow} \leq 0 \tag{2.85}$$

where A_i denotes the cross-sectional area of each element i and L_i is the length of that particular element. When circular cross-sections are used in the modeling of truss members in the ground structure, for example, the diameter of each element (D_i) can be considered as the design variables. Then, the cross-sectional area for the circular cross-sections is calculated by $\pi \cdot D_i^2/4$ for each

element *i* to find the volume of the lattice structure. This constraint can also be written in terms of weights by simply multiplying the volume by the density of the material.

Also, in the optimization formulation, to satisfy an allowable stress limit (S_{allow}) for the truss members in the lattice structure, a stress constraint can be defined by

$$S_{\max} - S_{allow} \leq 0 \tag{2.86}$$

where S_{max} denotes the maximum von Mises stress calculated in the lattice structure. Thus, the ground structure optimization can be formulated from Eq (2.78) as

$$\begin{aligned} &\text{Find} && D \\ &\text{Minimize} && C \\ &\text{subject to} && \sum_{i=1}^{N} \frac{\pi \cdot D_i^2}{4} L_i - V_{allow} \leq 0 \\ & && S_{\max} - S_{allow} \leq 0 \\ & && D_l \leq D \leq D_u \end{aligned} \tag{2.87}$$

where D_l and D_u denote the lower and upper bounds for the design variables respectively. The converged optimization result is supposed to drive the value of all design variables close to the lower and upper limits so that a definite topology is defined.

Ultimately, the ground structure approach is considered as a size optimization problem, where the cross-sectional parameters of lattice members are continuous design variables. The cross-sections of the members are sized to support the applied loads on the structure. At the end of the optimization process, each of the truss members can either exist or vanish depending on the problem boundary conditions. This decision is achieved by setting the lower bound of the cross-

sectional parameters is near zero (e.g. $D_l = 0.001$) and the members with cross-sections near zero are removed after the optimization to obtain the optimal material layout.

2.5.5. Continuum (Homogenization-based) Topology Optimization

Bendsøe and Kikuchi [42] introduced the topology optimization process based on the Cheng and Olhoff's approach [177] that finds the optimal thickness distribution of elastic plates, as an alternative to the shape optimization process [178]. Topology optimization was defined in [42] as "the shape optimization problems are transformed to material distribution problems using composite materials." In that regard, topology optimization process is a shape optimization process that finds the optimal material distribution based on the use of an artificial composite material with microscopic voids under given macroscopic boundary conditions. The microscopic optimal void distribution is considered using the asymptotic homogenization method [161] to determine the macroscopic constitutive equations of the material with microscopic material constituents instead of the shape optimization by the boundary variations of a structure. In the topology optimization approach, a 2D composite material in microscopic scale, which is a solid material including square voids in its center [42], or a layered material (i.e. mixture of two materials) [179] can be described by a density function that can take values in the range of [0,1] depending on the size of the void. This density function can be generalized for any material including voids by calculating the volumetric density by the ratio of the void volume to the entire element volume. The use of square voids is the simplest choice of composites, and more complicated microstructures show similar performance resulting no apparent benefit [179]. Thus, the optimal topology is determined by filling the design space with this microstructure material with a void or removing the material from the design space in the optimization process depending on the macroscopic boundary conditions.

In other words, if the initial design is considered as a block of space, this space is filled with material in the topology optimization, or if the initial design is considered as a block of material, the material is removed from the block in the topology optimization [179]. In fact, both are considered simultaneously at each iteration based on the density function to find the optimal layout of the structure.

Consider that a mechanical body structure occupies a reference domain Ω in R^3 with a boundary Γ as shown in Figure 2.3. Let the body is subjected to body forces $\boldsymbol{f}$ and boundary tractions $\boldsymbol{t}$ on boundary Γ_T and displacements on boundary Γ_D. For optimal design for minimum compliance, the continuum topology optimization formulation is given by

$$\begin{aligned} \underset{\mathbf{x}}{\text{Minimize}} \ &: \ C(X) = \mathbf{U}^T\mathbf{K}\mathbf{U} = \sum_{e=1}^{N} (x_e)^p \mathbf{u}_e^T \mathbf{k}_0 \mathbf{u}_e \\ \text{subject to} : \ &V(X) \le V_0 \\ &: \ \mathbf{K}\mathbf{U} = \mathbf{F} \\ &: \ \mathbf{0} < X_{\min} \le X \le \mathbf{1} \end{aligned} \tag{2.88}$$

where **U** and **F** are the global displacement and force vectors, respectively. **K** is the global stiffness matrix, $\mathbf{u_e}$ and $\mathbf{k_e}$ are the element displacement vector and stiffness matrix, respectively. X is the vector of design variables (i.e. densities), $X_{\min}$ is a vector of minimum relative densities to avoid the singularity. n is the number of elements used to discretize the design domain; p is the penalization power, $V(x)$ and V_0 are the material volume in the optimization and the allowable design domain volume [180].

The FE model in Eq. (2.88) comprises continuum level elements, which require the material properties as the inputs in the FEA. The continuum topology optimization process is depicted in Figure 2.10 with the example taken from [42]. For a periodic medium with known

microstructure, the material properties of the periodic microstructure must be obtained at the continuum level using a homogenization process during the optimization. Homogenization processes are, on the other hand, computationally expensive to use at each iteration for each element in the finite element analysis of the macroscopic structure. Hence, before the optimization, the homogenization process is applied to find a continuous relation between the density and the effective material properties. To achieve this relation in a computationally efficient manner, the homogenized material properties are determined for certain density values (Figure 2.10(a)) and a curve is fitted to have a continuous variation of the material density and material properties (Figure 2.10(b)). The relationship between the homogenized elasticity tensor and the density is given by

$$E_{ijkl} = E_{ijkl}(\rho) \tag{2.89}$$

where ρ is the density of the cell, which is a function of the cross-sectional parameters (e.g. diameter or thickness) of the struts. In the optimization process, each element in the finite element model of the domain will have a design variable (i.e. a density value). Then, the material properties corresponding to this density value for each element is calculated using the curve fit in the analysis at each iteration during the optimization process (Figure 2.10(c)). The topology optimization, which is conducted based on the homogenization process, provides an optimal design that includes microstructures that have varying densities (Figure 2.10(d)).

The intermediate densities are, on the other hand, difficult or impossible to produce using the traditional manufacturing techniques. Hence, strategies to eliminate the intermediate densities are introduced. Bendsøe and Kikuchi [42] introduced a lumping process to determine if the element should be fully solid or void instead of having intermediate densities. In the lumping process, a cut-off value is defined for the material density to enable the design with only fully solid and void

elements (Figure 2.10(e)). Bendsøe [179] utilized an artificial density function between [0,1] with a power-law equation. Then Eq. (2.89) is written as

$$E_{ijkl}(\rho) = \rho^{p} E^{0}{}_{ijkl} \tag{2.90}$$

where $E^{0}{}_{ijkl}$ denotes the elasticity tensor of the main material used to manufacture the microstructure and p is a penalization power value introduced to have a design with only fully solid and void elements. The density of the material is defined as a continuous variable, i.e. $0 \leq \rho \leq 1$. This approach is known as direct approach [179] or more commonly as Solid Isotropic Material with Penalization (SIMP) approach [181], [182]. The reason for the latter description is that an isotropic material is considered to simplify the optimization process [182]. In this case, the elasticity matrix-density relation can be written in terms of the elastic modulus E^{0} of the material with a constant Poisson's ratio, independent of density. Then Eq. (2.90) is written as

$$E_{e} = \rho_{e}^{p} E^{0} \tag{2.91}$$

where e represents the element number. Thus, the homogenized elasticity modulus of each element e is calculated by this simple artificial equation in the optimization process. This design is also called black and white design where void elements are represented by white and the solid elements are represented by black color (Figure 2.10(e)). The penalization value, p, in Eq. (2.91) must be sufficiently high to obtain a black and white design. For large values of p, the intermediate densities give a small stiffness which can then be considered as void elements. It is usually chosen as $p \geq 3$ to penalize the intermediate densities [183].

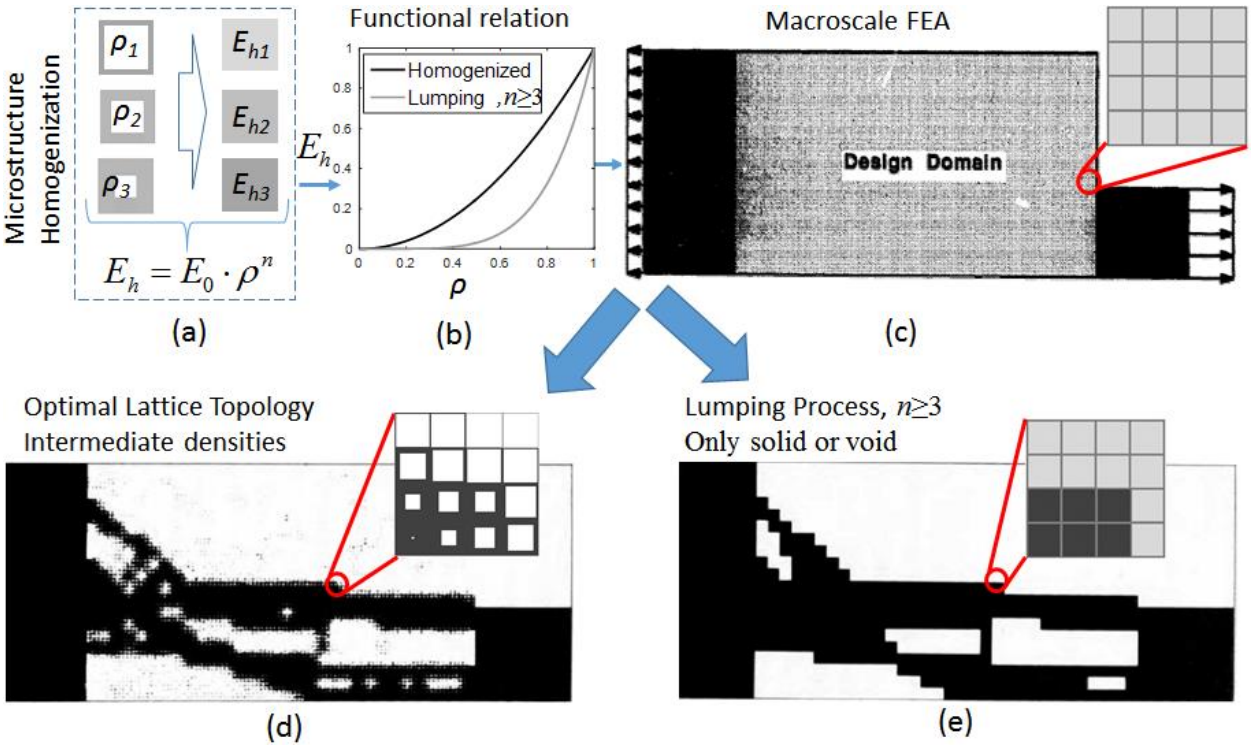

(a) Homogenization is performed for a set of density values at microscopic level and (b) a functional relation is established, (c) Topology optimization is conducted on macroscale FEA to find the optimal densities of each continuum level element under boundary conditions, (d) Optimal lattice topology is obtained at the end of optimization (e) Optimal material topology when a lumping process is used.

Figure 2.10. Continuum topology optimization with homogenization [42].

The topology optimization also involves working with anisotropic materials. However, considering anisotropy increases the design variables required to describe the structure as well as increases the requirements of the finite element code [183]. For example, the rotation of the square void is considered in 2D optimization process in [42] and both the rotation and two edge length of the rectangular voids are considered in [184], in which the edge values and the rotation angle of the voids are the design variables instead of the density alone for each element.

2.5.6. Reliability-based Topology Optimization (RBTO)

As seen in Figure 2.9, in RBTO, the stochastic constraints or stochastic objective functions are evaluated in addition to the deterministic topology optimization. Hence, the RBTO problem involves minimizing the compliance subject to a given allowable volume constraint of the material and the reliability constraints. The design variable is considered as the deterministic density values for each continuum level element. Then, the formulation of the RBTO problem is given by

$$\begin{aligned} &\text{Find} && : X \\ &\underset{\mathbf{x}}{\text{Minimize}} && : \; C(X) = \mathbf{U}^T\mathbf{K}\mathbf{U} = \sum_{e=1}^{N} (x_e)^p \mathbf{u}_e^T \mathbf{k}_0 \mathbf{u}_e \\ &\text{subject to} && : \; P_k\left|G_k(X,\xi) < 0\right| \le P_{R,k} \\ & && : \; V(X) \le V_0 \\ & && : \; \mathbf{K}\mathbf{U} = \mathbf{F} \\ & && : \; \mathbf{0} < X_{\min} \le X \le \mathbf{1} \end{aligned} \tag{2.92}$$

The random variables denoted by ξ are considered as the external loads of the structure and the geometric dimensions, while the design variables X (i.e. the densities of material in each of the finite elements) are considered as deterministic [187]. The compliance C was calculated deterministically in the topology optimization process. As different from the above formulation Kim et al. [188] minimized the volume of the structure under the reliability constraint of maximum displacement in the structure while Luo et al. [189] used a reliability constraint of maximum stress in the structure. On the other hand, the compliance of the structure calculated also have uncertainties, which are needed to be considered as in the robust optimization process. For this purpose, several alternatives of the topology optimization formulation were implemented. For example, Tootkabani et al. [190] set the weighted sum of the expected value and standard deviation of the compliance as a constraint while minimizing the weight of the structure under the

uncertainties exist in material properties. Torii et al. [191] utilized the robust topology optimization where the weighted sum of the mean and standard deviation of the compliance was minimized with a reliability constraint. It is seen that various alternative formulations are available for the topology optimization when considering the uncertainties.

2.5.7. Multi-level Homogenization-based Topology Optimization

Traditionally, topology optimization has been applied to design macroscopic structures where a black-and-white material distribution is determined [180] as mentioned in the previous section. In recent years, an ever-increasing research interest is seen in multi-level material design and optimization. Specifically, the original homogenization-based topology optimization proposed by Bendsoe and Kikuchi [42] was expanded by assuming that a cellular material can be designed with a second-level or microscale level design problem at each continuum level element of the macroscopic level structure. Theocaris and Stavroulakis [192] utilized a certain set of cellular structures at microscale level, for which the homogenized elastic moduli were computed by analytic or numerical homogenization techniques, to seek the optimal microscale material arrangements in the topology optimization process at the macroscale level. Rodrigues et al. [193] introduced a hierarchical scheme of topology optimization where a second level topology optimization problem is carried out at the microscale level to optimize the material microstructure. Two coupled topology optimization problems are solved: The outer problem deals with the spatial distribution of material at the macroscopic scale while the inner problem finds the microstructure topology. Thus, a different microstructure for each element at the macroscale can be achieved in this approach. Coelho et al. [194] extended this approach for the application of 3D structures, and Xia et al. [195] extended its use for nonlinear cases. Liu et al. [196] proposed a similar two-level

topology optimization process where a uniform material microstructure is determined at microscale that periodically repeats for every macroscale element unlike the approach in [193]-[195] where the microstructure of the material shows the difference for each macroscale element. Andreasen and Sigmund [197] utilized a similar multi-level topology optimization to design poroelastic actuators. A state-of-the-art review and some recent developments in this field can be found in the review article [198] and the references therein.

2.5.8. Uncertainties in CLS Design

Although the existing studies provide successful applications of the topology optimization process for multi-level material and structure design, deterministic multi-level optimization processes are carried out in the literature. Uncertainties, on the other hand, is required to be considered if reliable or robust designs are needed. In that regard, Guo et al. [199] introduced a multiscale robust optimization model considering applied load as a bounded uncertain variable with unknown probability information. A uniform microstructure that repeats periodically for each macroscale element is considered as similar to the approach introduced in [193]. The goal is to minimize the worst case structural compliance under available material volume constraint to find the optimal material distribution in the micro and macro scale levels concurrently.

Uncertainties also exist in fine scale material and geometry properties, which are should be taken into account during the multi-level design process. The downside of the above mentioned multi-level design approaches using hierarchical or multi-level topology optimization is the high computational burden because the homogenization method is required for each element to find the homogenized properties of the microstructure during optimization [198]. When the uncertainties are considered the computational demand increases dramatically as the repetitive analysis of the

model is required to model the uncertainty. An analytical representation or surrogate modeling of homogenized properties of the microstructure will not be possible since the underlying microstructure topology is not known at the beginning of the design process. Moreover, the continuity of the material in the optimized microstructure and for different continuum level elements may not be achieved when the topology optimization is used to determine the microstructures for each macroscale element [200].

To overcome the computational issues of these hierarchical topology optimization approaches, a database that gives the relation of the effective material properties of pre-defined cellular lattice cells with the element densities can be utilized instead of optimizing the microstructure with topology optimization. The database can be used to generate a continuous function of the homogenized properties based on various microstructure types as implemented in deterministically implemented in [192]. Or analytical formulations can be created for a certain number of pre-determined lattice cell type as a database, then the best lattice cell type can be chosen in the optimization process for each element based on this database by means of interpolation schemes. In fact, the original topology optimization proposed by Bendsoe and Kikuchi [42] and later used by Khanoki and Pasini [77] utilizes an analytical model of only one predetermined lattice cell type that produces the homogenized material properties such as the one given by Eq. (2.90). Thus, the macroscale model in the optimization uses directly the approximated effective material properties of the lattice cell without solving the computationally expensive microscale level lattice cell model. This functional relationship can be found for various lattice types and used in the optimization process to identify the optimal material layout.

Although the use of pre-determined lattice types for designing the material layout is a very efficient procedure, these existing studies are carried out in a deterministic setting. The

approximated models will not provide good predictions when uncertainties of material and geometric properties are taken into consideration. More specifically, when AM techniques are used for fabrication of these designs with optimized lattice cells, although the lattice cell strut cross-sectional parameters such as diameter values are set deterministically in the CAD model, the material and geometry of the AM-fabricated struts will have uncertainty due to the layer by layer manufacturing process. **That means the same CAD model with the same deterministic strut diameter value(s), will have different material properties and strut diameters when repeatedly fabricated by the same AM technique with the same AM process parameters.** Therefore, even if the design variables are deterministic, there will be uncertainty in the density values of each continuum level element of the macroscale level structure as well as in the homogenized material properties of the lattice cells. Eventually, the uncertainty in the geometry and material properties will influence the overall response of the structure, and the corresponding model will produce uncertain results. Therefore, the uncertainties at the strut level need to be propagated to the lattice level and should be utilized in the topology optimization. **However, the functional relationships between the density and homogenized material properties, given by Eq. (2.90), would not produce accurate results when these uncertainties are considered.**

In those cases, stochastic meta-models can be developed to predict homogenized properties with the propagated the uncertainties across multiple levels. Thus the computational demand can be reduced significantly especially when the uncertainties are involved. To the best knowledge, this is a relatively new field that there has been very limited research. Many potential developments can be achieved for either optimization, multiscale modeling or model reduction. **In this research, the applicability of the proposed upscaling method, which can accurately propagate the uncertainties while estimating the homogenized material properties, in developing such a**

stochastic meta-model approach is demonstrated. Specifically, a PCE-based metamodeling approach is developed using the upscaling method predictions for the uncertainty of homogenized material properties of lattice cells. Then, this metamodeling approach can be used in matching the target properties of the engineering applications to eliminate the expensive simulations and tedious optimization processes. The details of the application of the proposed upscaling method to the design of lattice structures are given in Chapter 5.

2.6. Summary

In this chapter, state of the art in uncertainty quantification and propagation approaches, multiscale modeling and homogenization approaches, verification and validation techniques, and design optimization approaches are examined. The stochastic upscaling method through optimization is identified as the upscaling or homogenization procedure of choice for propagating uncertainties across multiple levels. Based on the benefits and limitations of the existing research, the BIC method is shown to be appropriate for uncertainty quantification of input variables with parametric distribution models. The main issues in the current validation metrics are also discussed, and the potential of the u-pooling method is reviewed. The lattice structure design approaches using topology optimization are described in detail, and the issues regarding the computational complexity when uncertainties are involved are discussed. The necessity of the simulation free design approaches is also explained, and the applicability of the PCE-based upscaling method for this purpose is discussed.

The organization of the remaining of this dissertation is as follows: The details of the proposed stochastic upscaling method with the improvements made for better computational efficiency are provided in Chapter 3 along with the application examples that shows its

applicability at one scale level as well as multiple scale levels. In Chapter 4, the proposed multi-level validation approach for prediction accuracy assessment is introduced. Two lattice structure applications fabricated by two different AM process are provided in detail to demonstrate the efficacy of the proposed approach. The application of the proposed multi-level upscaling method in the design of CLSs is demonstrated in Chapter 5.

CHAPTER 3. IMPROVED STOCHASTIC UPSCALING METHOD

The objective of this chapter is to develop methodologies to address the *Research Question 1* in Chapter 1. A computationally efficient upscaling technique is formulated that enables the uncertainty quantification and propagation at multiple levels of scales as stated in *Hypothesis 1*. Then, its efficacy is evaluated by implementing the method for engineering examples. In Section 3.1, the theoretical framework of the stochastic upscaling method through optimization inspired by the work of Arnst and Ghanem [98] is established and the proposed improvements to increase its computational efficiency to be able to implement it as a general uncertainty quantification and homogenization method are introduced in Section 3.2. The flowchart of the improved upscaling method is developed and described in Section 3.3. In Section 3.4, the proposed multi-level upscaling framework is explained in general terms so that it can be used for not only lattice structures but also any other related engineering problem. Some application examples of the improved upscaling method are demonstrated for one level and two level upscaling processes in Section 3.5. Specifically, the efficiency of the proposed objective function, the applicability of the PCE for distribution types other than Gaussian distribution, and the effectiveness of the improved upscaling process when used for reliability estimation of the lattice-based structures are demonstrated with detailed examples. The proposed multi-level upscaling framework is implemented for the characterization of the overall elastic material properties of lattice structure specimens fabricated by a material extrusion process with the propagated uncertainties to evaluate its efficacy.

3.1. Stochastic Upscaling Method

There exist a wide variety of stochastic homogenization methods that considers the analytical integration of the stochasticity into micro-continuum theory. A straightforward and robust way is to utilize sampling methods for the deterministic homogenization methods to obtain the distribution of the effective properties. As stated in Section 2.3.3, stochastic upscaling methods, which utilize optimization to find the homogenized input variables of a coarse scale model, are introduced in existing references such as [97], [98] to consider the effects of uncertainties at the fine scale levels on the homogenized properties. The advantage of upscaling methods through optimization is that they can apply to any application and scale level of interest because the black-box computational models at fine and coarse scales can be utilized. Thus, the homogenized properties can be estimated without penetrating the underlying governing equations. Moreover, the upscaling process eliminates the need for complex linking formulations between fine and coarse scale models because it is treated as an optimization problem.

In the stochastic upscaling method, the statistical data of the homogenized property that represents its statistical distribution is to be found unlike the deterministic upscaling approach explained in Section 2.3.3 that finds only one value of the homogenized property by matching the coarse scale and fine scale model outputs through an optimization process (Figure 2.4). Hence, in the optimization process, the probabilistic performance of the coarse scale model response is matched with that of the fine scale model response instead of matching only one response value at each scale in the optimization process. The general steps of the stochastic upscaling method are depicted in Figure 3.1 for a lattice structure model at fine scale, which will be defined by continuum level elements at a coarser scale.

Similar to the deterministic upscaling process in Figure 2.4, the stochastic upscaling processes introduced in [97] and [98] consists of three main steps, as shown in Figure 3.1. The first step is constructing the fine-scale model of the given system or structure and computing the quantities of interest or responses. The second step is to build a coarse-scale model that can accurately represent the fine-scale model in a reduced dimension. The final step is the homogenization procedure via an optimization process to match the probabilistic performance of the fine and coarse scale responses. Consequently, the optimum homogenized input variable samples of the coarse-scale model that will enable the homogenization of the fine-scale heterogeneity are determined. The details of these three steps are given in the following sub-sections.

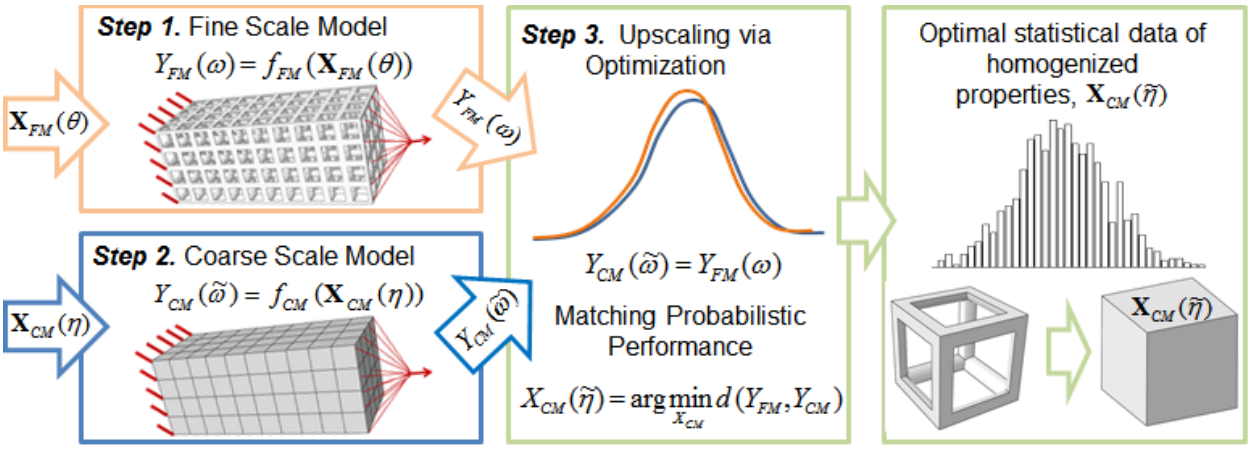

Figure 3.1. Stochastic upscaling through optimization

3.1.1. Constructing the Fine Scale Model

The stochastic fine-scale model is constructed in the first step to obtaining the fine-scale responses based on fine scale input variables with uncertainties. Let the fine-scale input variable vector is denoted by $\mathbf{X}_{FM}$ and its uncertainty is expressed by θ. Let the response of the fine-scale model is denoted by Y_{FM} , and its uncertainty due to input uncertainties is represented by ω. The response data can be obtained using the input variable by either experimentation or a computational model

of the actual physical system such as a black-box FEM solver. In either case, the uncertain response of the fine scale model can be written as a function of the random input variable(s) of the form

$$Y_{FM}(\omega) = f_{FM}(\mathbf{X}_{FM}(\theta)) \tag{3.1}$$

where $f_{FM}(.)$ denotes the computational model function or the experimentation. For the stochastic process, the MCS method can be used for generating the sampling set of the input variables and computation of the response values for each sampling point. Then, the fine scale response samples are denoted by $Y_{FM}(\omega) = \{y_{FM}(\omega_j)\}$ where $j = 1,...,n_{FM}$ and n_{FM} denotes the number of samples. Each evaluation of Eq. (3.1) implies a call to the black-box FEM solver for each sampling point and provides the corresponding response sample $y_{FM}(\omega_j)$ at fine scale. Then, this data is used to infer a lower-dimensional description of the fine scale model that captures the evolution of the system at a coarser scale.

3.1.2. Constructing Coarse Scale Model

A coarse scale model is identified as the second step to determine the homogenized input parameters that will correspond to the heterogeneous fine scale variables to represent the high dimensional fine scale model with a lower-dimensional (coarse scale) model that retains the responses. There is no restriction for identifying the coarse scale model since different models can represent the same fine scale model appropriately. The important point is that a simpler model results in a lower computational cost, which is desired. Depending on the complexity of the fine scale model, either the same geometry or a simpler geometry can be selected to represent the fine scale model with homogenized parameters. A black-box FEM solver or a simple analytical model can be used to obtain the coarse scale model response.

Let the homogenized input variable vector for the coarse scale model be denoted by $\mathbf{X}_{CM,}$ and its uncertainty is expressed by η. Similarly, let the response of the coarse-scale model is denoted by Y_{CM}, and its uncertainty due to input uncertainties is represented by $\tilde{\omega}$. This stochastic response at coarse scale can be computed as a function of the input variable vector

$$Y_{CM}(\tilde{\omega}) = f_{CM}(\mathbf{X}_{CM}(\eta)) \tag{3.2}$$

where $f_{CM}(.)$ denotes the black-box computational model at coarse scale. For the stochastic process, the MCS method can be used for generating the sampling set of the input variables and computation of the response values for each sampling point. Then, the coarse scale response samples are denoted by $Y_{CM}(\tilde{\omega}) = \{y_{CM}(\tilde{\omega}_j)\}$ where $j = 1,...,n_{CM}$ and n_{CM} denotes the number of samples at the coarse scale. Each evaluation of Eq. (3.2) implies a call to the black-box FEM solver for each sampling point and provides the corresponding response sample $y_{CM}(\omega_j)$ at coarse scale. The unknown input variable samples are needed to be determined to have the equality of the coarse scale responses with the fine scale responses.

3.1.3. Optimization Formulation based on Probability Theory

The third step of the stochastic upscaling process is to identify the unknown homogenized variables ($\mathbf{X}_C(\eta)$) of the coarse scale model. To predict the homogenized input variables that can compute the responses at the coarse scale, the upscaling methods attempts to find the equality between the fine scale and the coarse scale models responses. In other words, homogenized coarse scale random input variables $\mathbf{X}_C(\eta)$ are predicted such that

$$Y_{FM}(\mathbf{X}_{FM}(\theta)) = Y_{CM}(\mathbf{X}_{CM}(\eta)) \tag{3.3}$$

This equality given by Eq. (3.3) can be achieved by evaluating the expected value of the information loss between the fine scale (target) model and the coarse scale model outcomes. In this work, a probability-based formulation is described to solve the equality in Eq. (3.3). Let the random response *Y* takes on various values *y* within the range $-\infty < y < \infty$. A random response or variable is represented by an uppercase letter, and its particular value is represented by a lower case letter. The bold uppercase letter represents a vector of the random variables or responses. Let the information loss between the fine and coarse scale responses is denoted by $U(Y_{FM}, Y_{CM})$ for a given $\mathbf{X}_{CM}$. Since the responses are random variables, the information loss is also a random variable. There can be different outcomes, i.e. $u \in U$ corresponding to different probabilities defined by a probability density *p(u)*. According to the probability theory, an expected value of the information loss for a given $\mathbf{X}_{CM}$ can be determined by the integration of the information loss and its pdf for the continuous case as

$$U(\mathbf{X}_{CM}) = E(U(Y_{FM}, Y_{CM})) = \int u(y_F, y_C)\, p(u) du \tag{3.4}$$

Analytical evaluation of this equation is difficult when the function integral is not available in closed form. However, the expected value can easily be estimated by generating Monte Carlo or Latin Hypercube samples for a random input variable $X_{CM} = \{x_{CM}(1),...,x_{CM}(n_{CM})\}$ where n_{CM} is the number of samples, which is equivalent to the number of fine scale model samples, i.e. $n_{CM} = n_{FM} = n$. Once the coarse scale model responses are obtained as $Y_{CM} = \{y_{CM}(1),...,y_{CM}(n_{CM})\}$, the information loss is calculated for each sampling point in the response vector as $U(Y_{FM}, Y_{CM}) = \{u(y_{FM}(1), y_{CM}(1)),..,u(y_{FM}(n),.y_{CM}(n))\} = \{u(1),...,u(n)\}$ having the corresponding

probabilities p_1, …, p_n. Then, the expected value of the information loss for a certain number of simulations can be defined as

$$U(\mathbf{X}_{CM}) = E[U(Y_{FM}, Y_{CM})] = p_1 u(1) + ... + p_n u(n) \tag{3.5}$$

In short, Eq. (3.5) can be written as

$$U(\mathbf{X}_{CM}) = \sum_{j=1}^{n} u(j)\ p_j \tag{3.6}$$

by averaging the expected values, Eq. (3.6) becomes

$$U(\mathbf{X}_{CM}) = \frac{1}{n} \sum_{j=1}^{n} u(j) \tag{3.7}$$

If there are several possible preferences for the input variables, decision makers prefer a smaller expected value of the information loss to a greater expected value. In this case, if $U(\mathbf{X}_{CM}(i))$ are the expected values of the different preferences $\mathbf{X}_{CM}(i) = \mathbf{X}_{CM}(1), \mathbf{X}_{CM}(2), ...$ then the expected values are assessed by

$$\mathbf{X}_{CM}(1) > \mathbf{X}_{CM}(2) \Leftrightarrow U(\mathbf{X}_{CM}(1)) < U(\mathbf{X}_{CM}(2)) \tag{3.8}$$

In other words, Eq. (3.8) indicates that a possible choice of $\mathbf{X}_{CM}$ is preferred to another possible choice of $\tilde{\mathbf{X}}_{CM}$ if and only if $U(\mathbf{X}_{CM}) < U(\tilde{\mathbf{X}}_{CM})$. Generalizing this approach, a decision maker chooses the optimal design to

$$\min_{\mathbf{x}_{CM}} U(\mathbf{X}_{CM}) \tag{3.9}$$

This selection can be achieved by using an optimization procedure to find the optimal homogenized $\mathbf{X}_{CM}$ that minimizes the objective depending on the difference between the fine scale quantity of interest, Y_{FM}, and the corresponding coarse scale quantity of interest, Y_{CM}. Then, the statement of the optimization procedure can be represented by

$$\mathbf{X}_{CM}(\tilde{\eta}) = \arg\min_{\mathbf{X}_{CM}} U(Y_{FM}, Y_{CM}) = \arg\min_{\mathbf{X}_{CM}} \frac{1}{n}\sum_{j=1}^{n} u(j) \tag{3.10}$$

Here, $\tilde{\eta}$ denotes the estimated random quantities of the unknown homogenized input variables. This optimization process is also known as a stochastic inverse problem since the goal of this procedure is to find the unknown input values and distributions using the known response values and distributions [201]. In inverse engineering problems, the optimal input variables are determined by finding the expected output, (i.e. displacement, stress, temperature, etc.) as close to the target or desired output. This procedure can be utilized in multiscale modeling for upscaling the heterogeneity at fine scale to a coarse scale model in a nonintrusive manner [98].

3.2. Improvements on Stochastic Upscaling Method

3.2.1. Quantification of Fine Scale Input Uncertainties

In the stochastic upscaling method, it is crucial to accurately represent uncertainties of the fine scale input variables, denoted by $\mathbf{X}_{FM}$. to be able to have accurate predictions of the fine scale responses, Y_{FM} in Eq. (3.1). When the statistical data of the input variables are available (through experimental measurements or existing references), the uncertainty quantification methods described in Section 2.1 can be utilized. Uncertainty quantification using parametric distribution models with defined statistical parameters of a random variable enables the generation of the

statistical samples from its distribution model using sampling methods easily for the simulations of the fine scale model. Zhang et al. [203] shows that fitting different distributions to the data can change the result; especially, the probability of failure of a structure is the concern of the structural analysis or design. Hence, it is important to determine the optimal stochastic parameters and distribution type to represent the distribution of the variable with high accuracy. As stated in Section 2.1, BIC method given by Eq. (2.17) is a straightforward and efficient method for uncertainty quantification of available statistical data. The number of samples, *n*, and the number of stochastic parameters, *k*, are taken into account for the evaluation of goodness of fit via BIC, thus, providing a better judgment for determining the optimal distribution [129]. In BIC method, the MLE approach in Eq. (2.13) is used to identify the statistical parameters of the candidate the distribution models, and the best-fitted distribution model for the data of a fine scale input variable is determined by comparing the information loss calculated by Eq. (2.17).

3.2.2. Proposed Objective Function – Exponential Loss Function

For different situations, different objective functions that can describe the predicted information loss on the outcome of the corresponding preference can be used. The objective function to match the fine and coarse scale model outputs in the upscaling process is crucial since the convergence of the optimization algorithm is dependent on how well the objective function is defined. A continuous objective function is desired in the optimization process to find the optimal point. If the objective function is discrete, the optimization algorithms may not work well. On the other hand, many different distance metrics can be used as an objective function. It is common to utilize the MAE or MSE distance metrics given in Eqs. (2.73) and (2.75), respectively to calculate the information loss in the optimization process. For *n* number of samples, those can be written with

the notations of the fine and coarse scale responses and the expected value of information loss in Eq. (3.7) is given by

$$U_{L1} = \frac{1}{n}\sum_{j=1}^{n}\left|y_{CM}(j) - y_{FM}(j)\right| \tag{3.11}$$

$$U_{L2} = \frac{1}{n}\sum_{j=1}^{n}\left(y_{CM}(j) - y_{FM}(j)\right)^2 \tag{3.12}$$

MSE is also known as the squared distortion and used in the stochastic upscaling process for homogenization in [97] and as a least square minimization in inverse problems in [201]. Another option for the information loss calculation is to use relative entropy (Eq. (2.70)) as suggested in [98]. Shell [202] also utilizes the relative entropy for finding effective properties of fluid flow in the multiscale analysis. If the PDFs of fine and coarse scale responses are denoted by $p(Y_{FM})$ and $p(Y_{CM})$, the relative entropy is given by [98]

$$U_{RE} = \frac{1}{n}\sum_{j=1}^{n}\log\left(\frac{p(y_{FM}(j))}{p(y_{CM}(j))}\right) \tag{3.13}$$

Moreover, Arnst and Ghanem [98] suggested using the moment matching method given by

$$U_{MM} = \sum_{r=1}^{m}\left|M_r(Y_{CM}) - M_r(Y_{FM})\right| \tag{3.14}$$

where $r = \{1,\ldots,m\}$ are the degree of the moments, and M denotes the moment of the response at the coarse and fine scales.

The objective function must penalize the non-optimal points greatly so that the minimum or maximum point can be reached quickly. In this research, to increase the computational

efficiency by enabling the fast convergence of the optimization process to an optimal point, a more efficient objective function called “exponential loss function” is employed. The exponential loss function is the exponential of the negative squared difference between the fine and coarse scale outputs of interest and is given by

$$U(Y_{CM}, Y_{FM}) = e^{-(Y_{CM} - Y_{FM})^2} \tag{3.15}$$

When the exponential loss function in Eq. (3.15) is substituted into (3.7) the expected value of the exponential loss is written as

$$\hat{U}(X_{CM}) = \frac{1}{n}\sum_{j=1}^{n} \exp\left\{-\left(y_{CM}(j) - y_{FM}(j)\right)\right\}^2 \tag{3.16}$$

where $\hat{U}()$ defines the expected value of the exponential loss, y_{FM} and y_{CM} are evaluated by using the fine and coarse scale models given by Eq. (3.1) and Eq. (3.2), respectively. The fine scale model given by Eq. (3.1) can also be based on physical experiments instead of FEM simulations. In this case, the target fine scale responses are obtained using the experimental observations, which corresponds to the calibration process described in Section 2.2. The benefit of the exponential loss function given by Eq. (3.16) is demonstrated by comparing results obtained by using the other objective functions described above in the examples provided in Section 3.5.1 and Section 3.5.2.

3.2.3. Dimension Reduction using PCE

As stated earlier, in the deterministic upscaling through optimization, only one value for each homogenized variable is determined in this optimization process in Eq. (3.10). In the stochastic upscaling method, when sampling methods are utilized for the uncertainty representation, on the

other hand, the number of responses at the fine scale is dependent on the number of sampling points, *n*, as seen in Eq. (3.16). Since there must be a coarse scale response corresponding to each fine scale response to evaluate the objective function, the number of samples at the coarse scale must be equivalent to the number of samples at the fine scale. Hence, the number of design variables is equal to the number of samples, *n*. In other words, the values for the sampling data are to be found in the optimization process rather than one single value of the homogenized input variable(s). For an accurate representation of the probability densities, the number of samples is required to be high (e.g. 1000 samples are used in [98]). However, the computational cost of the optimization process increases dramatically with a large number of sampling data since *n* number of design variables has to be updated at every iteration during the optimization process. Hence, a dimension reduction approach is required to reduce the computational complexity during the optimization process of the stochastic upscaling method.

The easy solution to this computational issue is that the first two moments (i.e. mean and variance) of the unknown homogenized input variable can be considered as the unknown parameters to simplify the problem rather than considering all of the unknown sampling data in the optimization process. In that regard, in the optimization process, those unknown moments are initiated and used to generate the sampling data based on an estimated distribution model. Then, for each sampling set, the simulation of the coarse scale model is performed to calculate the corresponding response value. Once the responses are obtained for each sampling point, those are compared with the fine scale responses. If they match sufficiently, then the moments are saved. Otherwise, new values of the moments are determined based on the optimization algorithm and these steps are repeated.

The issue with the use of moments to reduce dimensionality is that those may not be sufficient to accurately model the homogenized variable distribution if only the first two moments are utilized. More than two moments of the homogenized variable (e.g. third and fourth moments that defines the skewness and kurtosis of distribution, respectively) can be considered to represent the input distribution accurately. For either case, on the other hand, knowledge about the type of the distribution of the homogenized input variable is required to generate the input sampling points based on the parametric distribution model and to calculate the coarse scale model response. In inverse problems, the distribution type of the homogenized variable is unknown since the only known information in the upscaling process is the fine scale response data. To address this issue, various distribution models could be fitted, and the upscaling process could be achieved for each distribution model to find the one that gives the most accurate coarse scale model responses when compared to the fine scale responses. However, this process would require multiple upscaling processes to be carried out, which increases the computational burden. Hence, it is often difficult to predict the distribution model of the unknown homogenized input variable, and thus the accuracy of the resulting coarse scale model might be worsened [98].

Koutsourelakis [97] introduced an upscaling method that utilizes the rate distortion theory, which enables the representation of the distribution of the homogenized input variable with a relatively small number of sampling points at a coarser scale. Even though this approach provides a dimension reduction in the optimization process, the accuracy of the results is questionable as it attempts to represent the distribution of the homogenized variable with a small number of samples. Another approach is to project the homogenized input variable onto a PCE after constructing the coarse scale model as suggested by Arnst and Ghanem [98]. In this case, the PCE representation of a coarse scale input variable is given by

$$X_{CM}(\hat{\eta}) = \sum_{k=0}^{P} b_k \Phi_k(\xi(\hat{\eta})) \tag{3.17}$$

where b_k are the undetermined coefficients of the P^{th} order PCE (k = 0,1,…,P), and Φ_k denotes orthogonal polynomials. Here, $\tilde{\eta}$ denotes the estimated random quantities of the unknown homogenized input variable. Depending upon the type of random variables, ξ, the orthogonal polynomials can be selected from Table 2.2. As stated in Section 2.2.3, Hermite polynomials with standard normal samples $\xi \sim N(0,1)$ can be used as a generalized PCE to represent any distribution model. Then, the only unknown parameters in the optimization process become the deterministic coefficients, b_k. Thus, in the optimization process, only a few PCE coefficients b_k are determined instead of the sampling points. The homogenized coarse scale input variable data, X_C, are found by using the optimal PCE coefficients in Eq. (3.17). By substituting Eq. (3.17) into Eq. (3.2), the coarse scale model can be described by

$$Y_{CM}(\tilde{\omega} \mid b) = f_{CM}\left(\sum_{k=0}^{P} b_k \Phi_k(\xi(\hat{\eta})) \right) \tag{3.18}$$

where ξ are generated by MCS from $N(0,1)$ [98]. By substituting Eq, (3.18) into Eq. (3.15), the corresponding exponential loss function becomes

$$U(Y_C, Y_F) = \exp\left\{ -\left(f_{CM}\left(\sum_{k=0}^{P} b_k \Phi_k(\xi(\hat{\eta})) \right) - Y_{FM} \right)^2 \right\} \tag{3.19}$$

where $k = 0,\ldots,P$ are the number of coefficients. Eq. (3.19) is integrated into Eq. (3.16) so that the expected value of the exponential loss to be maximized as the objective function in the optimization process is given by

$$\hat{U}(b) = \frac{1}{n}\sum_{j=1}^{n} \exp\left\{ -\left(f_{CM}\left(\sum_{k=0}^{P} b_k \Phi_k(\xi(j)) \right) - y_{FM}(j) \right)^2 \right\} \tag{3.20}$$

Then, the optimization formulation given in (3.10) is reformulated as

$$b = \arg\max_{b} U\left(Y_{FM}(\omega), Y_{CM}(\tilde{\omega} \mid b)\right) = \arg\max_{b} \frac{1}{n}\sum_{j=1}^{n} u(j) \tag{3.21}$$

This optimization procedure implies that the expected value of the exponential loss in Eq. (3.20) is at its maximum when all the coarse scale response values are equivalent to the corresponding fine scale response values. To achieve this maximization, the design variables, *b*, (i.e. the PCE coefficients) are changed during the optimization in a way that the coarse scale response values calculated by Eq. (3.18) are as close as possible to the fine scale response values during the optimization. Consequently, the coarse scale model can accurately approximate the fine scale responses using the estimated homogenized input variable to maximize the expected value of the information loss in Eq. (3.20).

The optimization using Eq. (3.21) can be performed without any constraints; however, we hypothesize that additional moment-based constraints can be introduced to increase the convergence speed and accuracy for the stochastic parameters at the coarse scale (e.g., mean, standard deviation, etc.). If the distance between the moments of the computed fine and coarse scale responses is less than a pre-defined value, ε, the corresponding constraint can be written as

$$\left| M_r(Y_{CM}) - M_r(Y_{FM}) \right| \le \varepsilon \tag{3.22}$$

where r is the degree of the moment, and M denotes the moments of the responses at the coarse and fine scales. The pre-defined value ε should be chosen appropriately to obtain a satisfactory convergence. In Eq. (3.22), the i^{th} order moments of a random variable Y with a PDF of $p_Y(y)$ can be derived by Eq. (2.1) where the mean μ_Y is given by Eq. (2.2). Thus, the final optimization statement proposed in this research can be defined as finding the optimal PCE coefficient values, b, by maximizing the expected value of the exponential loss function in Eq. (3.20) such that it satisfies the moment constraints:

$$\begin{array}{ll} \textit{Find} & b \\ \textit{Maximize} & \widehat{U}(b) \\ \textit{subject to} & \left| M_r(Y_{CM}) - M_r(Y_{FM}) \right| \le \varepsilon \end{array} \tag{3.23}$$

3.3. Flowchart of the Improved Stochastic Upscaling Method

In this section, the flowchart comprising the basic steps of the proposed upscaling method is presented. The improved upscaling method has four main steps as different from the original upscaling method shown previously in Figure 3.1. One additional step is included to quantify the input uncertainties of the fine scale model. The proposed upscaling method flowchart for the i^{th} level of interest among N number of levels is depicted in Figure 3.2, and the four steps are explained in the following subsections.

3.3.1. Step 1) Fine Scale Model Inputs

The first step of the upscaling flowchart involves the uncertainty quantification of the fine scale model inputs. This step is necessary to have an accurate fine scale model that will be used in the upscaling process if the uncertainties of the input variables at fine scale are not known.

Experimental measurements or existing references can be used to collect the statistical data for the input variables of the fine scale model. Once the statistical data of the input variables are collected from experimental measurements or existing references, BIC method is utilized to identify the statistical parameters and the distribution model that provides the best fit for the data of each fine scale input variable in $\mathbf{X}_{FM,i}$.

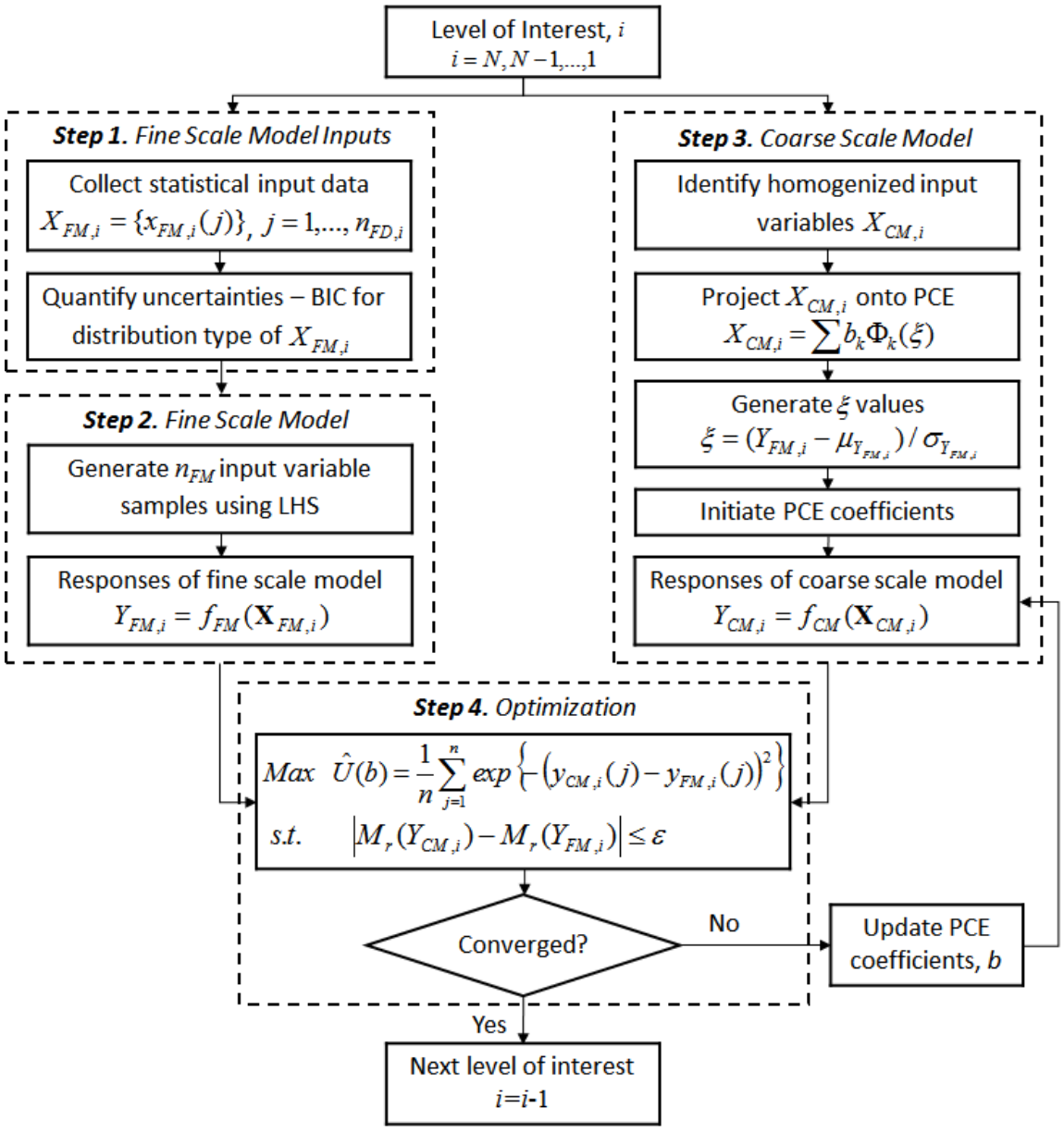

Figure 3.2. Improved stochastic upscaling flowchart

3.3.2. Step 2) Fine Scale Model

The fine scale model given by Eq. (3.1) can be constructed using either experimentation or FEM or analytical equations. Experiments are very difficult or impossible to conduct if the level of scale is small (e.g. microscale level). Similarly, modeling the fine scale details with analytical equations is usually not possible. Hence, numerical modeling techniques such as FEM is preferred to construct the fine scale model. Once the fine scale input uncertainties are quantified using BIC method in step 1, the samples of the fine scale input variables are generated from the corresponding distribution models (Figure 3.2). These generated samples of the input variables are used in the fine scale model to propagate input uncertainties to the fine scale responses.

In the improved stochastic upscaling method LHS is used to generate the samples instead of MCS, which was used in the existing upscaling methods (i.e. [98]). LHS will enable the accurate propagation of the input uncertainties to the fine scale responses with a fewer number of samples as explained in Section 2.2. The appropriate number of samples, n, which will accurately represent the distribution of the fine scale response is determined by checking the convergence of the mean and standard deviation of the calculated response for the various number of samples as described in Section 2.4.1. Once the optimal number of samples are determined, the fine scale responses are obtained from the fine scale model simulations for input samples generated by LHS.

3.3.3. Step 3) Coarse Scale Model

At the coarse scale, the input variables, X_{CM}, which will represent the homogenized values for fine scale inputs, are determined as shown on the right side of Figure 3.2. The coarse scale model is constructed to introduce the functional relation between the homogenized variables and the responses. To reduce the dimensionality, PCE is utilized for the homogenized input variables as

given in Eq. (3.17). As stated earlier, Hermite polynomials with uncertain values from standard normal distribution ξ are used in PCE since it can represent any distribution with deterministic PCE coefficients so that the necessity of determining the underlying distribution becomes trivial. If there exist more than one homogenized variables to be found, a separate PCE is constructed for each homogenized variable and corresponding PCE coefficients become the variables to be determined in the optimization process.

The accuracy of the PCE representation dependent on how well ξ samples are generated. In the existing upscaling method [98], samples are generated for random variable ξ in PCE using MCS (or LHS in the proposed method) before the optimization loop. Then these generated ξ samples are utilized in the upscaling process to find the homogenized property values. However, when the upscaling is run again for the same fine scale data, a new sample set of ξ is generated, which will be different from the previous one. A different order of PCE may be necessary for each generation of ξ sample set to accurately represent the fine scale model due to the randomness of the generation of the ξ samples. This randomness increases the computational complexity as the upscaling process must be repeated to find the optimal PCE order and coefficient values.

A better option proposed in this study is to extract ξ information from the known fine scale responses as

$$\xi = \left(Y_{FM} - \mu_{Y_{FM}}\right) / \sigma_{Y_{FM}} \tag{3.24}$$

This approach was initially introduced for the accurate propagation of the known input uncertainties to the unknown system response when the system response is projected onto a PCE with Hermite polynomials [2]. Since the unknown system response is known as a function of the

known input variables, the input uncertainties can be propagated to the response using this method. A similar functional relationship exists in upscaling approach between the unknown homogenized input variables and the known fine scale model responses. That is, the unknown homogenized coarse scale input variables can be calculated as a function of the known model responses, which is an inverse functional relationship. Hence, this approach can be used in the upscaling process to propagate the response uncertainties to the unknown homogenized variables. When used in PCE, the uncertain values ξ calculated by Eq. (3.24) provides the propagation of the uncertainty of fine scale responses to the coarse scale homogenized properties, thus enabling the accurate representation of the fine scale data with the constructed coarse scale model.

Another important issue in PCE projection is that the optimal number of coefficients in PCE must be determined for accurate estimation of the homogenized variables at the coarse scale. For the evaluation of the optimal truncation order, a convergence criterion must be used. The weak-Cauchy convergence criterion [92] is employed in the developed framework. The truncation order is equivalent to the number of coefficients. According to this criterion, first, an optimal truncation order q is guessed, and an order m is constructed, where $m = q+1, q+2$. Then, the PCE is written with the order of q approximation and the corresponding order of m approximation as follows:

$$X^{(q)}(\nu) = \sum_{k=0}^{q} b_k \Phi_k(\xi(\nu)), \; X^{(m)}(\nu) = \sum_{k=0}^{m} b_k \Phi_k(\xi(\nu)) \tag{3.25}$$

The L_2 norm or squared difference between the two approximations gives a measure of error to determine the optimal order of gPCE by

$$e = \left(X^{(q)} - X^{(m)}\right)^2 \tag{3.26}$$

where *e* denotes the measure of error. If *e* is sufficiently small, that means the result does not change when the order of PCE increases. Thus, the optimal truncated order of gPCE is determined.

3.3.4. Step 4) Optimization

As shown on the right side of Figure 3.2, the PCE coefficients, *b*, are initiated to start the optimization. In the optimization step, the coarse scale inputs are computed with PCE, using the estimated coefficients, *b*, as design variables, and the coarse scale responses are calculated by the coarse scale model. Then, the objective function, which is the expected value of the exponential loss between coarse and fine scale responses, is computed using Eq. (3.20). If there are moment constraints in the optimization statement, those are calculated as discussed in the previous section. When the convergence is achieved for both the objective function and the constraints, the optimum design variables (i.e. PCE coefficients, *b*) are obtained for the homogenized coarse scale input so that the coarse scale model that represents the fine scale properties is attained. Otherwise, the design variables, *b*, are updated, and the optimization step is repeated as presented on the bottom side of Figure 3.2.

The optimization algorithm used for the optimization process is crucial to find the optimal point efficiently. The existing methods utilize global optimization methods such as simulated annealing in [97] and genetic algorithm (GA) in [98]. However, as stated in [98], these global optimization algorithms are very slow to converge to the optimal point although they do not have the issue of being trapped in local optima. To overcome the computational issue, gradient-based methods can be used, but those are more likely to get trapped in local optima. In this framework, a hybrid procedure of a gradient-based method, namely SQP, and a global optimization algorithm, namely GA, is utilized for the optimization procedure to improve the computational efficiency. In

general, the SQP method is sensitive to the choice of the initial guess. It may often lead to a convergence failure and can get trapped in local optima since it is a gradient-based optimization algorithm. To overcome these disadvantages, first, GA is used to perform a preliminary search in the solution space for determining the initial point. The computational cost of GA is reduced by using a high tolerance value for objective function evaluation since the proposed process only needs to locate the neighborhood of the global optimal solution. Then, SQP is applied to refine the GA solution so that the objective function quickly converges towards the potential global optimum. The efficiency of the hybrid procedure is evaluated in the application examples in Section 3.4.

3.4. Multi-level Stochastic Upscaling Framework

As mentioned in the introduction, when there exist large geometric uncertainties in the finer scales of a structure, modeling by using detailed geometries is neither feasible nor efficient with the existing modeling and analysis techniques. The solution is to describe the structure by multiple models that focus on different levels of scales and to enable linking with the subsequent level from bottom up. In the proposed multi-level framework, the improved upscaling process explained in the previous section and shown in the flowchart in Figure 3.2, is repeatedly utilized at multiple scale levels of interest ($i=1,2\ldots,N$), where N is the smallest scale level as depicted in Figure 3.3, to identify the overall homogenized properties ($X_{CM,1}$) at the largest scale level with efficient uncertainty propagation.

In Figure 3.3, i denotes the level of scale that the upscaling process is implemented. The outputs at fine and coarse scale are denoted by $Y_{FM,i}$ and $Y_{CM,i}$ for each level. It should be noted that for the sake of simplicity, the uncertainty parameters of the input and output random variables

such as θ, ω, η and $\tilde{\omega}$ are omitted from the notations of the variables in the sequel. This framework shown in Figure 3.3 starts with the smallest scale level of interest defined by $i=N$ and the upscaling flowchart in is repeated at each scale level. The homogenized coarse scale input variables ($X_{CM,i}$), which are determined at one level by the upscaling process given in Figure 3.2, are used at the subsequent larger scale level as the input variables of the fine scale model, (i.e. $X_{CM,i} = X_{FM,i\text{-}1}$ as seen in Figure 3.3). This process is repeated at each level until eventually the overall homogenized properties $X_{CM,1}$ are identified at the final level, i=1. This multi-level upscaling procedure is implemented in the Section 3.5.4 to the example of the characterization of homogenized structural properties of the AM-fabricated lattice-based cellular structure.

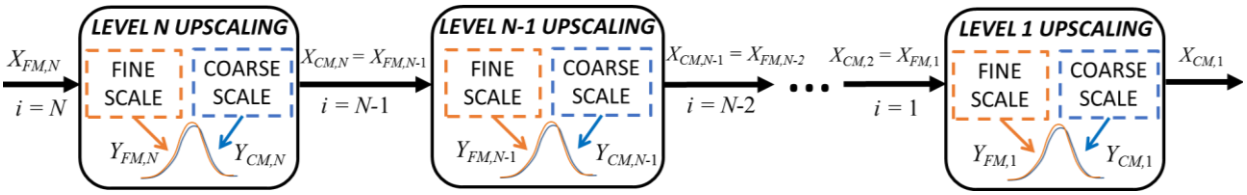

Figure 3.3. Multi-level stochastic upscaling framework

3.5. Validation Examples of Improved Upscaling Method

The improved upscaling method is used for three application problems at one scale level and one lattice structure example at two scale level to demonstrate its efficiency and accuracy. In the first problem, the efficacy of the proposed objective function (i.e. the exponential loss function) over the objective functions used in literature is demonstrated for a random variable with known PCE coefficients. In the second example, the efficacy of the improved upscaling method is compared with the existing upscaling methods used in the literature, i.e., the upscaling method with rate distortion theory [97], generalized methods of moments [98], and relative entropy [98], [202] for

an elastic bar example with heterogeneous material at fine scale. This example also exhibits the efficient homogenization of the heterogeneous stochastic fine-scale material at the coarse scale, while the geometry remains the same. It is also shown in this example that the Hermite polynomials can be used for distributions different from Gaussian. In the third example, the presented method is utilized for the reliability estimation in the multiscale design of a hydrogen storage tank. This example demonstrates how the proposed method can be applied to a practical engineering problem with a high number of random variables. The computational burden due to the repetitive simulations of the complex lattice structure model of the storage tank at a fine scale is decreased significantly by the homogenization of the material and geometry with a simpler and accurate representative coarse-scale model. In the last example, the multi-level upscaling framework is utilized for material characterization of CLSs fabricated by material extrusion to show its efficacy in prediction capability compared to the experimental results.

3.5.1. An Example to Analyze the Proposed Objective Function

The first example investigates the effectiveness of the proposed exponential loss function by comparing the plot of the function for the parameter space of PCE coefficients with the plot of the existing objective functions. It is assumed for this example that the coarse scale homogenized property is known and represented by the following first order PCE

$$X_{CM} = 10 + 2\xi \tag{3.27}$$

where ξ are generated from the standard normal distribution. That is the two coefficients of the PCE are known to be $b_0 = 10$, $b_1 = 2$. Moreover, it is known that 25 samples are available as follows and represented by this PCE projection of the homogenized property:

E_C = [5.874647 7.062636 7.342557 7.668426 8.25839
8.433907 8.728871 8.949994 9.167294 9.392595
9.602803 9.829377 10.05609 10.18138 10.34734
10.52961 10.84077 11.12732 11.21508 11.50672
11.95405 12.20175 12.36421 13.22063 14.19648]

Now we assume that the PCE projection of this data is not known. We want to find the optimal PCE coefficients using an optimization procedure. Then, it is expected that the value of the objective function must be at its minimum when $b_0 = 10$, $b_1 = 2$ since the data was drawn from Eq. (3.27). We can plot a mesh grid of all possible solutions to the PCE coefficients based on the objective function value instead of an optimization process. For this purpose, first, a design space of 100 samples was uniformly generated using LHS from the range of [0,20] for b_0 and the range of [0,4] for b_2. Then, for each b_0, b_1 coefficient values, the values of the random variable X_{CM} were calculated using the 1st order PCE given by $X_{CM} = b_0 + b_1 \cdot \xi$. The number of generated random variables ξ using LHS was 25 from $N(0,1)$.

Three different objective functions are utilized for this example, namely mean absolute error (MAE), squared distortion or MSE, and the proposed exponential loss function. The objective function values were calculated for each sampling data and plotted to see how the objective function behaves for various values of the coefficients. The MAE was calculated using Eq. (3.11) and the plots of results are given in Figure 3.4. Similarly, the squared distortion was calculated using Eq. (3.12) and the plots of results are given in Figure 3.5. Finally, the expected value of the proposed exponential loss was calculated using Eq. (3.16) and the plots of results are given in Figure 3.6.

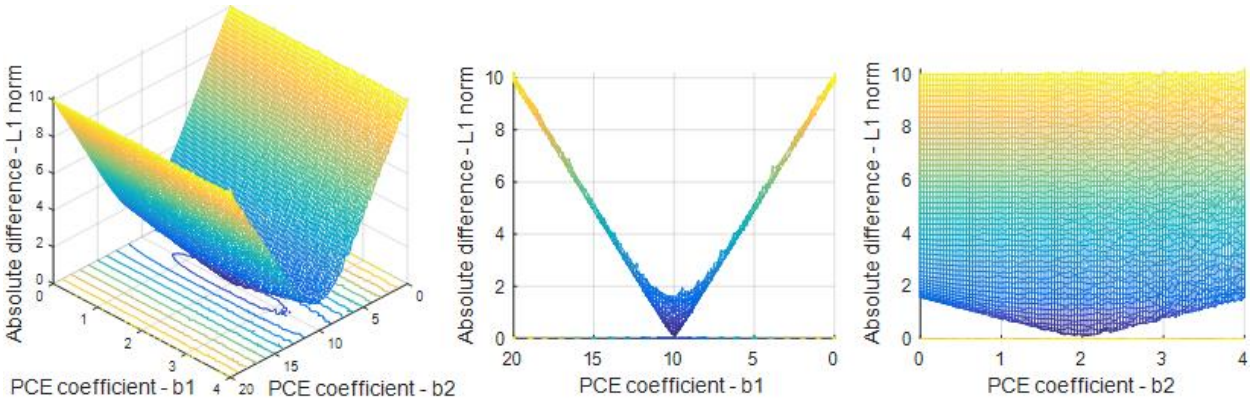

(a) (b) (c)

Figure 3.4. (a) Plot of PCE Coefficients vs absolute difference (b) PCE coefficient b_0 (c) PCE coefficient b_1

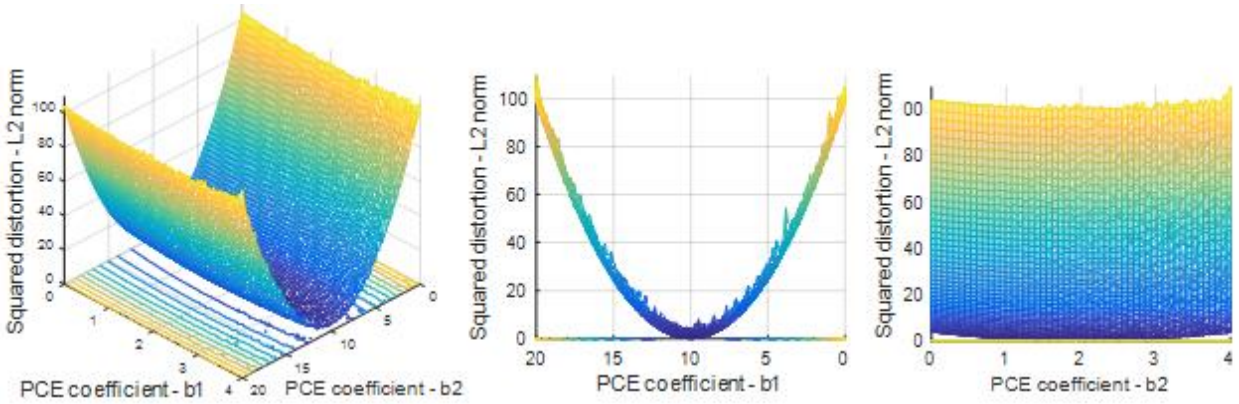

(a) (b) (c)

Figure 3.5. (a) Plot of PCE Coefficients vs squared distortion (b) PCE coefficient b_0 (c) PCE coefficient b_1

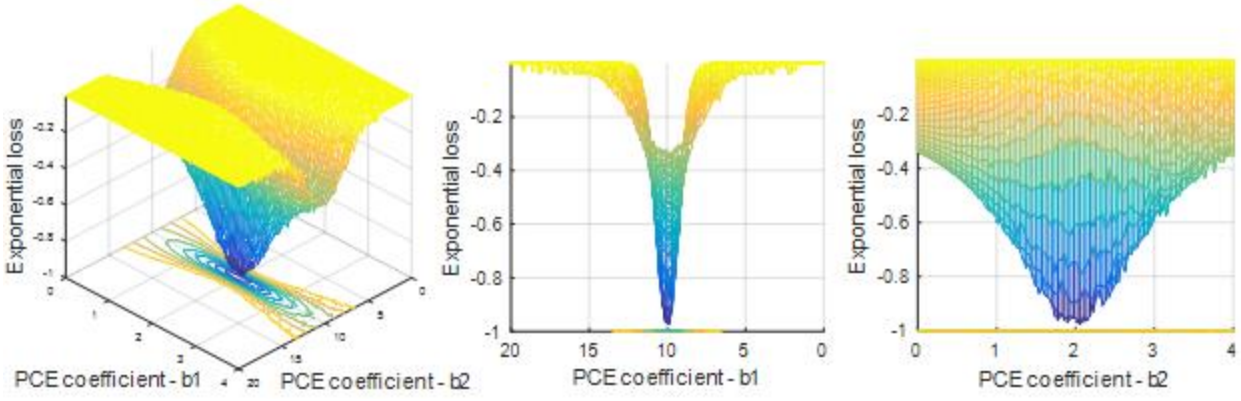

(a) (b) (c)

Figure 3.6. (a) Plot of PCE Coefficients vs exponential loss (b) PCE coefficient b_0 (c) PCE coefficient b_1

The results in these figures indicate that the objective function becomes minimum when $b_1 = 10$ and $b_2 = 2$ as expected. On the other hand, it is seen that the optimal points can more clearly be found when the exponential loss is used because the plots in Figure 3.6 has steeper surfaces than the ones in Figure 3.4 and Figure 3.5 towards the optimal point. This can be attributed to the fact that the exponential loss function penalizes the non-optimal points more severely than the other objective functions. For this reason, it is expected that the exponential loss function will enable finding the optimal point much more quickly than the other functions in the optimization process. Also, it will not have a convergence issue to a non-optimal point since the change of the function is much steeper as seen in Figure 3.6. Thus, this example proves that the use of exponential loss function is a better choice to use in the optimization step of the upscaling method.

3.5.2. One-Dimensional Elastic Bar

The proposed upscaling procedure is applied to a one-dimensional linear elastic bar which was originally presented by Koutsourelakis [97]. The bar, shown in Figure 3.7 has a unit length ($L = 1$) with the unit cross-sectional area ($A = 1$). The left end of the bar is fixed so that it cannot move in any direction. A horizontal unit force ($F = 1$) is applied to the end cross-section on the right.

Step 1. Fine scale input uncertainties

In step 1 of the proposed upscaling method, the input variable uncertainties are to be quantified for the fine scale model. The governing equation, for which the fine scale and coarse scale models are generated to model the elastic bar for the displacement $y(x)$ is given by

$$\frac{d}{dx}\left(E(x)\frac{dy(x)}{dx}\right)=0 \tag{3.28}$$

where E denotes the Young's Modulus of the material and x is the length of the bar from the fixed end in [0,1]. At fine scale, it is assumed that the Young's Modulus of the bar is the heterogeneous input variable with uncertainty. The random variability of $E(x)$ is formulated as

$$E(x)=1+0.5\cos\left(2\pi\frac{x}{x_0}+\phi\right) \tag{3.29}$$

where ϕ is the phase angle and the constant x_0 is used to control the length scale of heterogeneity. The uncertainty of the Young's Modulus is due to the phase angle, ϕ, which is assumed to be quantified by a parametric distribution model, i.e. uniform distribution in [0, 2π].

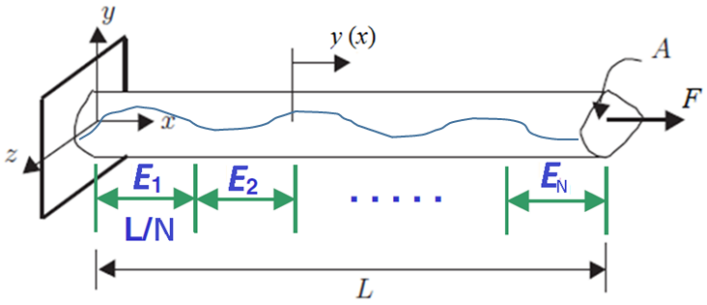

Figure 3.7. One-dimensional bar subjected to axial force *F*

Step 2. Fine scale model

In step 2, the fine scale model of the elastic bar is constructed. The bar was discretized to N = 1,000 beam elements with equal length, and each element was assumed to have a different Young's Modulus, $E(x)$, for which the sample values were generated by Eq. (3.29) with the quantified uncertainties of the phase angle, ϕ. The distance, x, is the length of the part of the bar between the

center point of the element and the fixed end. The constant, x_0, was assumed to be equivalent to 10. For each element, n = 1,000 samples of ϕ were generated to account for the uncertainty of the Young's Modulus. Then, the tip displacement at x = 1, was computed from the fine scale model simulation for each sample set.

Step 3. Coarse scale model

In step 3, the coarse scale model is constructed as a homogenous linear elastic bar, consisting of only one beam element with a homogenized Young's Modulus value. A simpler analytical formulation can be derived to calculate the tip displacement at the coarse scale (Y_{CM}) by deriving Eq. (3.28) with the boundary conditions of $y(0) = 0$ and $E(1)\frac{dy}{dx}\Big|_{x=1} = F = 1$:

$$Y_{CM} = 1/E_C \tag{3.30}$$

where E_C denotes the homogenized Young's Modulus for the elastic bar at the coarse scale. During the upscaling procedure, E_C was written as a PCE so that only the coefficients, b, of the polynomials become the design variables in the optimization process. Legendre polynomials are selected as the basis of the PCE since the PDF of the input variable (i.e. phase angle ϕ) is the uniform distribution. The first few terms in the Legendre Polynomials set $\{\Phi\}$ are given by

$$\begin{aligned}\{\Phi\} = \{1, \xi, \frac{1}{2}(3\xi^2 - 1), \frac{1}{2}(5\xi^3 - 3\xi), \frac{1}{8}(35\xi\zeta^4 - 30\xi^2 + 3),\\ \frac{1}{8}(63\xi^5 - 70\xi^3 + 15\xi), \ldots\}\end{aligned} \tag{3.31}$$

Thus, the random variability of E_C at the coarse scale can be written in terms of PCE,

$$E_C(\xi) = \sum_{k=0}^{P} b_k \Phi_k(\xi) \tag{3.32}$$

Step 4. Optimization for upscaling

The random ξ values are generated by using a uniform distribution between [-1, 1] to use in Legendre polynomials (Table 2.2). In step 4 of the upscaling process, the coarse scale displacement values were computed by using Eq. (3.30), and the expected value of the exponential loss function given by Eq. (3.16) was maximized with no constraints.

The upscaling procedure was conducted for the different orders of the Legendre polynomials to find the optimum number of coefficients to represent E_C accurately with the PCE. Figure 3.8(a) and Figure 3.8(b) depict the optimal values of the objective function corresponding to the different order of P for the PCE and the number of total iterations (GA+SQP) in the optimization, respectively.

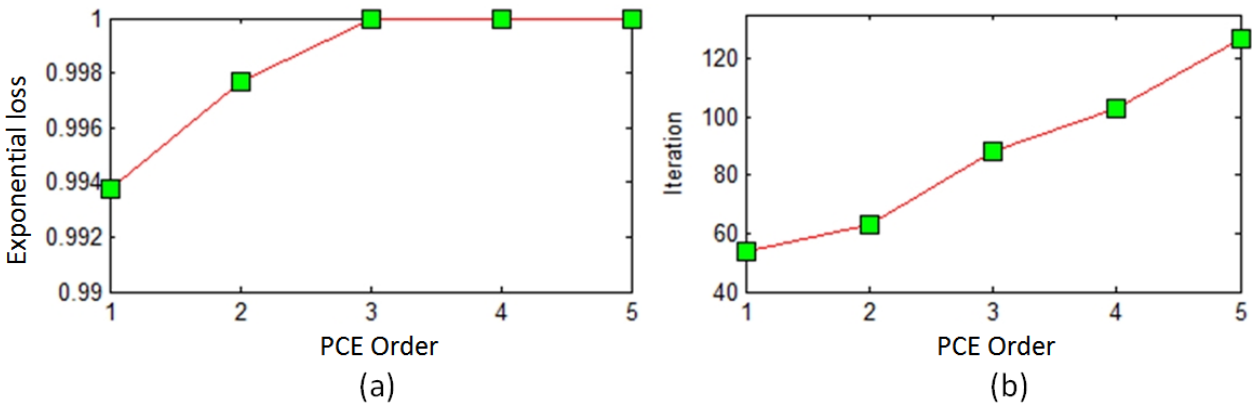

(a) convergence of the objective function (b) number of iterations

Figure 3.8. Results for the different order of PCE

It can be seen from Figure 3.8(a) that the exponential loss value converges when P=3. Hence, P=*3* is used as the guessed truncation order in Eq. (3.32). The error values were also computed using

the weak-Cauchy convergence criterion given by Eq. (3.25). The obtained error values were 4E-12 for fourth and fifth order expansions. It is seen that there is no significant change in the exponential loss function value after the third order. Moreover, the computational cost increases with the increase of the order of the polynomial, as can be seen from Figure 3.8(b), since more coefficients are required to be optimized. Based on these observations, the PCE can be truncated at the order of 3 for minimal computational effort.

Once the optimum order of the PCE was determined, the homogenized Young's Modulus value was estimated by the upscaling procedure. It is known that the exact or target homogenized Young's Modulus is given by the following equation [97]

$$E_T(x) = 1 + 0.5\cos(\phi) \tag{3.33}$$

The statistical data obtained for the homogenized Young's Modulus with the proposed upscaling method are compared with the target distribution calculated by Eq. (3.33) as shown in Figure 3.9. The continuous line in the figure represents the exact values for the Young's Modulus while the histogram represents the homogenized data with the upscaling method. It is seen that the optimal distribution of the homogenized Young's Modulus matches well with the exact values.

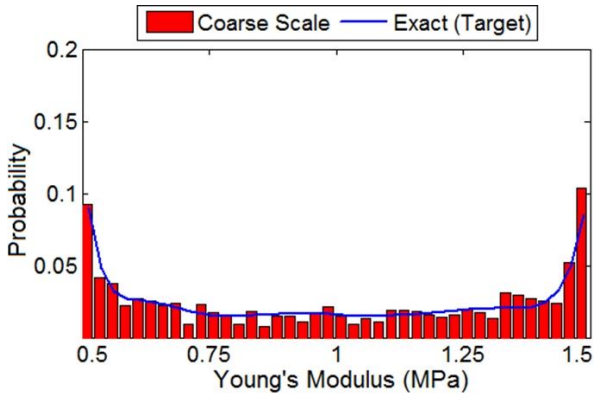

Figure 3.9. Accuracy comparison of Young's Modulus distribution

3.5.2.1. Comparison of displacement results with existing methods

To evaluate its performance, the averaged squared distances (i.e. the error) between the exact values, E_T, and estimated values, E_C, are computed by

$$d = \sum_{j=1}^{n} (E_C(j) - E_T(j))^2 \tag{3.34}$$

The obtained value of the averaged distance is 1.5E-5, which is small enough to conclude that the coarse scale homogenized approximation determined by the upscaling procedure for Young's Modulus is accurate. Thus, the homogenized values can be used to compute the displacements with the coarse scale model. The cumulative distribution functions (CDFs) of the displacement values at the coarse scale calculated in the upscaling process are compared with the fine scale results as shown in Figure 3.10(a). These results are compared with the results given in [97] and shown in Figure 3.10(b).

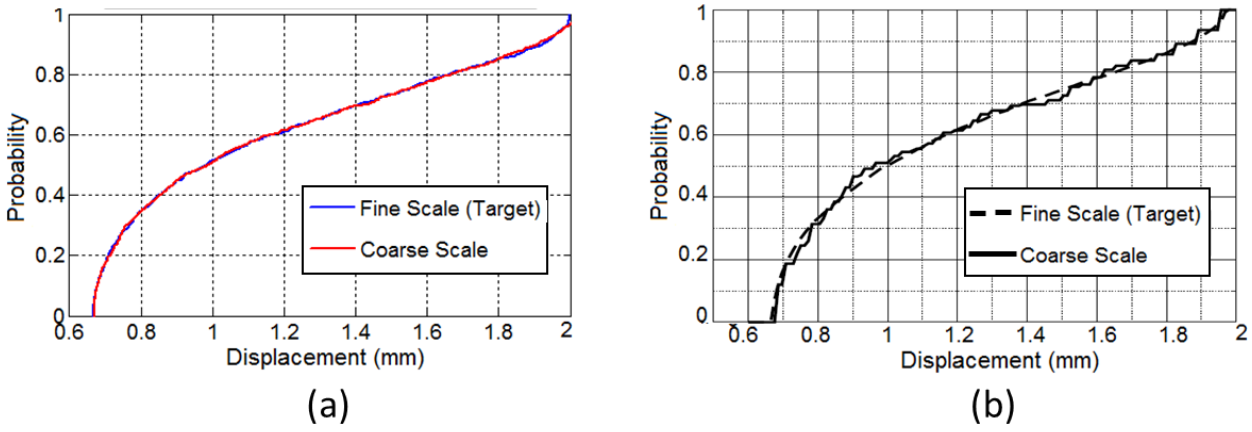

(a) Improved upscaling method (b) Upscaling with distortion theory [97]

Figure 3.10. Comparison of fine and coarse scale displacement CDFs

As seen in Figure 3.10(a) the CDF of the coarse scale displacement, computed by the homogenized Young's Modulus value, is almost identical to the CDF of the fine scale results. Figure 3.10 (b) shows, on the other hand, the coarse scale results obtained from the existing upscaling method with distortion theory [97] have slight deviations from the fine scale results. Hence, it is seen that the improved upscaling method gives better approximation compared to the existing method. The averaged squared distance value for the displacements was obtained as 5.6E-6 from Eq. (3.34). Although very high accuracy was achieved, the moments calculated for the displacement results were not accurate enough in comparison with the fine scale moment results as seen in Table 3.1. Hence, the first three moments were used as the additional constraints and the optimization was performed again. The relative error values, given in Table 3.1, are very small when constraints are used, while they rise when constraints are not used. Also, adding moment constraints decreased the number of iterations from 37 to 30 in the optimization while the averaged distance value remained the same. Hence, it is seen that the constraints facilitate finding the optimal solution more quickly with better accuracy.

Table 3.1. Comparison of the (%) relative errors for the first three moment results

	1st moment	*2nd moment*	*3rd moment*
w/o constraints (%)	1.1E-3	1.3E-2	1.7E-1
with constraints (%)	1.5E-9	1.25E-8	6.4E-10

To validate the accuracy of the proposed method, existing multiscale modeling schemes in the literature were implemented for the same structure. The same pre-determined initial point with GA was used for all different objective functions for better evaluation in this comparison. The average

squared distances (*d*) were computed by using Eq. (3.34) for displacement results. The obtained results are summarized in Table 3.2.

Table 3.2. Comparison of the results for different upscaling methods

		Iter(SQP)	*Time (sec)*	*d (Eq.* **(3.34)***)*
Proposed Method		30	0.75	5.6E-5
Distortion Theory		20	0.65	1.29E-4
Relative Entropy		15	0.53	1.1E-2
Generalized Method of Moments	2 Moments	9	0.46	2.6E-3
	3 Moments	31	0.72	2E-4
	4 Moments	33	0.75	3.1E-3

As shown in Table 3.2, the average squared distance value is at its lowest value when the proposed method is used. For the generalized methods of moments [98], the computational time and the iteration numbers are comparable with the proposed method's results, but error (*d*) values are greater than the proposed method. The errors calculated for the distortion theory [97] and relative entropy [98] give closer values to the proposed method but still the proposed method has the highest accuracy with comparable computation time. The optimization time for the existing objective functions was shorter than the proposed method since the objective function converges earlier than the optimal point as seen in Table 3.2. The proposed exponential loss function, on the other hand, has a much smaller *d* value, which means that it can eliminate early convergence in the optimization and finds a better optimal point since exponential loss penalizes the non-optimal points more severely than the existing methods as shown in the first example. At this point, it is also reminded to the reader that the same hybrid optimization technique (i.e. GA and SQP) is used

for these different methods in this comparison. If the optimization techniques, which were proposed for these methods in the literature (i.e. only GA in [98] and Simulated Annealing in [97]), were used, the convergence time for the existing methods would be much higher than the proposed method.

It should be noted here that the large portion of the iterations in the optimization was performed by GA due to its inherent randomness and slow convergence rate. Although the tolerance value was high (1E-2) for GA, the number of iterations for GA was 51 while the SQP iterations were only 30 for a third-order PCE. The exponential loss value was computed as 0.9981 with GA, and it was maximized to 0.9999 by SQP. To achieve a similar level of accuracy by using only GA, the tolerance value had to be decreased to 1E-12, and even after 2,111 iterations the exponential loss value was 0.9998. It is evident that the iteration number using the hybrid algorithm of GA and SQP is much lower than that of GA, which proves the statement in the previous paragraph.

Consequently, these results validate that the proposed upscaling procedure does not only accurately estimate coarse scale parameters, but also provides computational efficiency due to the low computation cost of proposed optimization technique.

3.5.2.2. Effectiveness of Hermite polynomials for PCE projection

The final study of this problem involves the applicability of the Hermite polynomials for any distribution type. As stated in PCE explanation, Hermite polynomials can be used for any type of distribution, but the relatively greater order of PCE is required if the distribution is not normal. The same procedure explained above was utilized to determine the optimal order of PCE based on the exponential loss function result using the Hermite Polynomials given in Eq. (2.27). The random

ξ values were generated from $N(0,1)$ with LHS since Hermite polynomials were used. The average value of the exponential loss and the number iterations for the different order of PCEs are depicted in Figure 3.11.

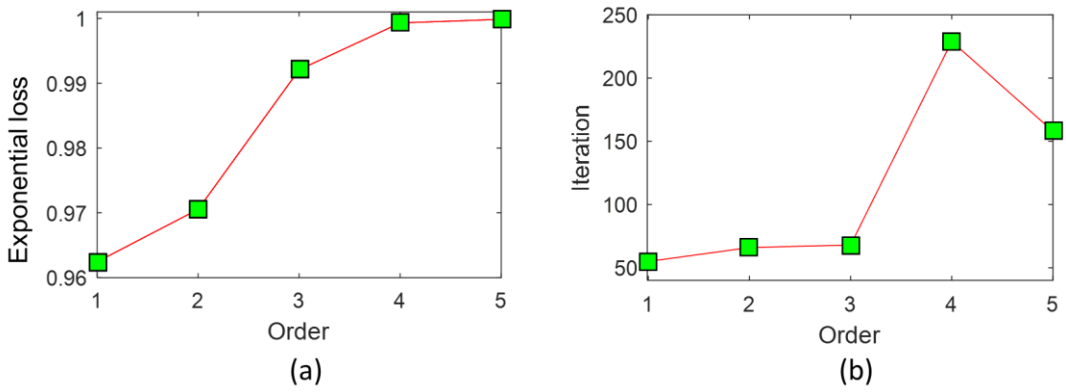

(a) convergence of the objective function (b) number of iterations

Figure 3.11. Results for the different order of PCE with Hermite Polynomials

As seen in Figure 3.11(a), the convergence in the objective function value is obtained after the 4th order PCE. It is seen that the convergence occurs for a greater order of PCE when compared to the results given in Figure 3.8(a) for Legendre Polynomials. The number of iterations to find the optimal PCE coefficient is also increased compared to Figure 3.8(a). The objective value was 0.9999 for a 3rd order PCE with Legendre polynomials while the same value was obtained for a 5th order PCE when Hermite Polynomials are used. Although a higher order PCE was required for accurate prediction with Hermite polynomials, these results show that the applicability of the Hermite Polynomials is not restricted only to the normal distribution since it can accurately make a prediction for this case where the parameter is not normally distributed as in this example. This result verifies the statement that Hermite polynomials can be used for any distribution type although a larger of PCE is required. Thus, it is concluded that Hermite polynomials can be used in PCE without concerning about the distribution type of the parameter that is projected on PCE.

3.5.2.3. The effectiveness of generating ξ values with Eq. (3.24)

When Hermite polynomials are used in PCE, instead of randomly generating the ξ values from the standard normal distribution using MCS or LHS, the known responses of the fine scale model can be used to obtain those values. That is, ξ values can be obtained using the formulation in Eq. (3.24) when Hermite polynomials are used as proposed in the improved upscaling method. The same example was solved by this approach, and the objective function values for the different order of PCEs are depicted in Figure 3.12.

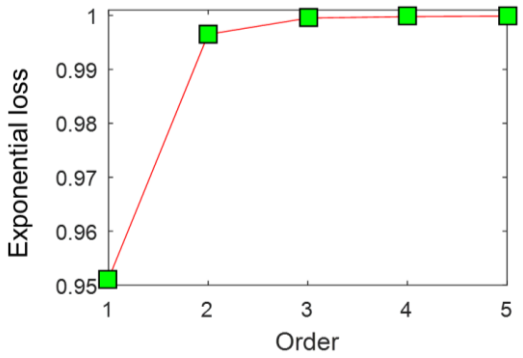

Figure 3.12. Objective function values when ξ values were obtained using Eq. (3.24)

As seen in Figure 3.12, a 3rd order PCE with Hermite polynomials was sufficient to have a high accuracy in the upscaling process as the objective function value is converging after this point. It is seen that this approach provides good accuracy with a smaller order of PCE compared to the results in Figure 3.11 where random sampling was used. Hence, Eq. (3.24) is recommended to use in the improved upscaling process.

3.5.3. Multiscale Reliability Analysis of a Hydrogen Storage Tank

The coarse scale model with homogenized properties can be used for reliability assessment of the application so that the fine scale heterogeneity and randomness are taken into account with low

computational effort. To estimate the probability of failure for accurate reliability assessment, first, samples are generated using the stochastic parameters of homogenized input variables by MCS, and the coarse scale model is repeatedly called to compute the response for each sample. Second, the limit state function, which defines the failure and safe regions for a design domain, is evaluated for each response. Then, the probability of failure is calculated by the ratio of the number of samples that are in the failure region and the total number of samples. Since a coarse scale model is used for reliability estimation, the computational effort of MCS can be reduced dramatically. The presented upscaling method is utilized for the reliability estimation a hydrogen storage tank that is designed using lattice cells as the inner lining in [34] as shown in Figure 3.13.

Hydrogen is a promising energy source that has about three times greater energy content by weight than gasoline. However, it is challenging to store enough hydrogen since a significant amount of space is required. The available compressed hydrogen tanks for the light-duty vehicular applications are larger and heavier than the design requirements. A possible solution is to utilize cellular lattice structures as the inner lining of a rigid hydrogen storage tank as shown in Figure 3.13. The weight of the tank can be significantly decreased while a reliable design of the storage tank is obtained to store sufficient amount of hydrogen at high pressure [34], [35]. However, the high number of random variables at fine scale due to the complexity of the geometry and the heterogeneity of the material increases the computational effort dramatically for the reliability estimation. Therefore, the proposed multiscale framework is applied for the probabilistic failure analysis of the storage tank design at coarse scale using homogenized geometry and material properties to reduce the computational cost.

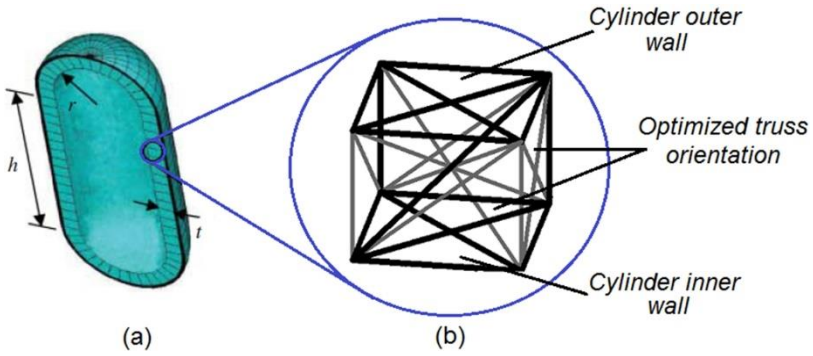

Figure 3.13. Hydrogen storage tank: (a) cross-section of the tank; (b) optimized unit cell [34].

Step 1) Fine Scale Input Variable uncertainties

The length (h) of the given storage tank in Figure 3.13(a) is 1.35 m, its inner radius (r) for the cylindrical portion of the tank is 0.3 m, and the wall thickness (t_w) is 8.29 mm. In the optimal unit cell, shown in Figure 3.13(b), the black colored truss members have a 10 mm^2 area of the cross-section (A_1) while the cross-sectional area of gray colored ones (A_2) is 7 mm^2. It is assumed in this study that the quantified uncertainties of random variables at fine scale are as given in Table 3.3.

Step 2) Fine scale Model

The fine scale FE model of the lattice structure for the cylindrical portion of the tank is illustrated in Figure 3.14. The trusses in the lattice structure are made of carbon composite (HM graphite fiber). The inner and outer walls are made of carbon epoxy material, which have the properties listed in Table 3.3. For each stochastic parameter, 1,000 MCS samples were generated, and the fine scale FE model was simulated for each parameter set. The maximum displacement of the tank wall caused by the pressure of the hydrogen was used as the quantity of interest of the fine scale model in the upscaling procedure. When the detailed FE model is considered as the fine scale model, it can be upscaled to a simpler solid coarse scale model so that the reliability estimation can be achieved with trivial computational cost.

Table 3.3. Statistical parameters and distribution types of random input variables at fine scale for the hydrogen storage tank

Parameter		***Distribution***	***Mean***	***Std Dev***
Pressure, P_{in} (MPa)		Lognormal	25.4	2.54
Graphite fiber	*E* (GPa)	Normal	379	37.9
	v	Normal	0.2	0.01
Carbon epoxy	v_{12}	Normal	0.27	0.0162
	v_{23}	Normal	0.54	0.0324
	v_{13}	Normal	0.27	0.0162
	E_1 (GPa)	Weibull	(147, 13.23)	
	E_2 (GPa)	Weibull	(10.3, 0.927)	
	E_3 (GPa)	Weibull	(10.3, 0.927)	
	G_{12} (GPa)	Weibull	(7, 0.56)	
	G_{23} (GPa)	Weibull	(3.7, 0.296)	
	G_{13} (GPa)	Weibull	(7, 0.56)	
Area 1, A_1, (mm^2)		Uniform	[9.8, 10.2]	
Area 2, A_2, (mm^2)		Uniform	[6.8, 7.2]	
Wall thicknesses, t, (mm)		Extreme Value	(1.5, 0.45)	

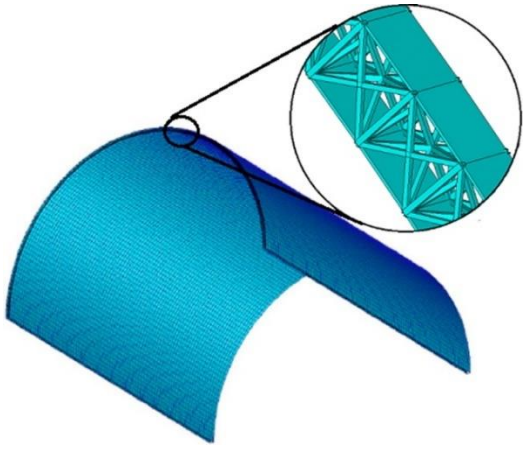

Figure 3.14. Fine-scale FE model of the mesostructured hydrogen tank

Step 3) Coarse Scale Model

At the coarse scale, a homogenous wall geometry and material were predicted using the upscaling method. The maximum displacement values at coarse scale can be computed using a simple analytical model of the tank pressure

$$Y_{CM} = f_{CM}(P_{in}, r, t_w, v_{CM}, E_{CM}) = \frac{P_{in}\, r^2 (2 - v_{CM})}{2 E_{CM} t_w} \tag{3.35}$$

where P_{in} denotes the internal pressure on the wall, r is the radius of the tank and t_w is the thickness of the wall. For the upscaling process, either the Young's Modulus, E_{CM}, and the Poisson's Ratio, v_{CM}, can be treated as two different design variables, or $K_{CM}=(2-v_{CM})/E_{CM}$ can be considered as one homogeneous input variable. Both cases were studied in the upscaling process to compare the efficacy of the method.

First, one homogeneous input variable, K_{CM}, was determined by utilizing the proposed upscaling procedure. To reduce the number of design variables, the random variability of homogenous K_{CM} is represented by the gPCE as

$$K_{CM} = \sum_{k=0}^{P} b_k \Phi_k(\xi) \tag{3.36}$$

Thus, the coefficients, *b*, of the gPCE become the design variables and the first three moments are used as constraints in the optimization process. To determine the optimum number of coefficients that represent K_{CM} accurately, the upscaling procedure is conducted for different orders, *P*, of the Hermite polynomials. The weak-Cauchy convergence criterion given by (3.25) was used to calculate the error values between the results of the different order of PCEs. *P=4* is used as the guessed truncation order in Eq. (3.26). The obtained error value was 9.4E-6 for the first order expansion while it was 2.1E-9 for both second and third order expansions. As seen, there is no significant change after second order. Moreover, the number of iterations was 53 for the first order PCE while it was 54 for the second order and increases to 83 when a third and fourth order PCE was used. Based on these observations, the PCE can be truncated at the order of 2 for minimum computational effort and maximum accuracy.

For the case of two variables, the random variability of homogenous E_{CM} and ν_{CM} is represented by the gPCE as

$$E_{CM} = \sum_{k=0}^{P1} b_k \Phi_k(\xi) \tag{3.37}$$

$$\nu_{CM} = \sum_{k=0}^{P2} c_k \Phi_k(\xi) \tag{3.38}$$

Thus, the coefficients denoted by vectors *b* and *c* become the design variables in the optimization process and E_{CM} and ν_{CM} are homogenized separately. Since it was found that

accurate estimations could be made by a 2nd order gPCE in the previous case, the same order was also used for both E_{CM} and ν_{CM}, as well.

Step 4) Optimization for upscaling

The PDFs of the displacements obtained by the upscaling procedures with one homogenized variable and two homogenized variables are compared with the PDF of the fine scale quantities of interest as shown in Figure 3.15.

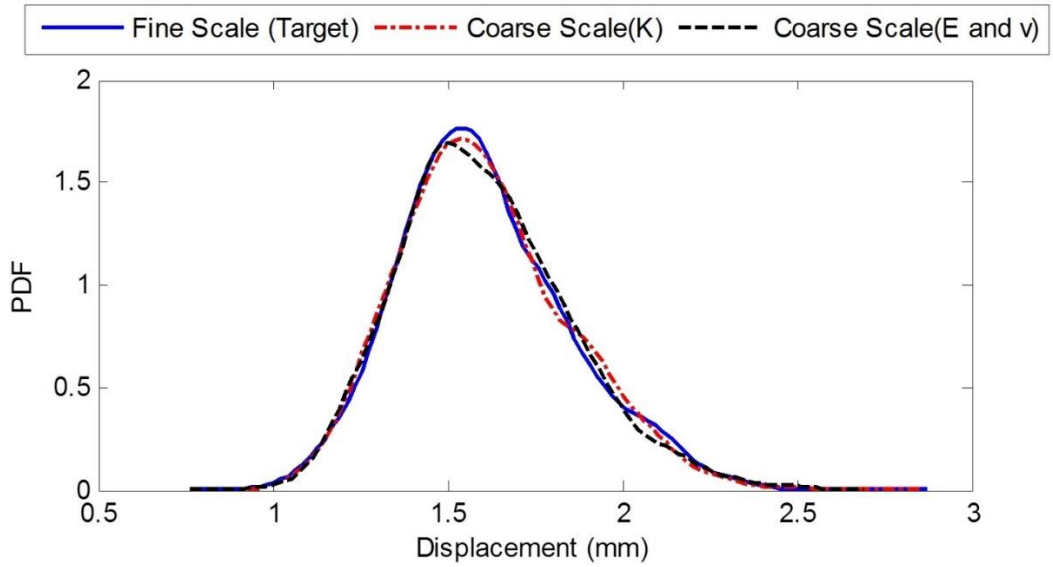

Figure 3.15. PDF results of the quantities of interest at both scale levels

It is observed that the results are very close to the fine scale results for both cases. The averaged distance value, calculated by Eq. (3.34) with the output values (i.e. displacements), was 1.15E-4 when K_{CM} was used as one homogenized variable; while it was 1.75E-4 for the case of two homogenized variables. Both models provide high accuracy for the quantities of interest. The computation time of the responses at the coarse scale was 3.36 and 4.33 seconds for the cases of

one variable and two variables, respectively, while the calculation of the responses at fine scale was about an hour. It is seen that depending on the requirements of the problem, the geometry and the material can be homogenized either separately or as one variable and a very efficient coarse scale model, which takes into account the fine scale heterogeneity, can be created using the proposed upscaling procedure. Also, the number of iterations for one variable was 54 while it was 98 for the case of two variables. The reason for the increase in iterations is due to the doubled number of design variables which is related to the procedure of determining PCE coefficients for two homogenized variables. This result shows that the computational cost increases when the number of homogenized variables is increased for the coarse scale.

Since the case of one homogenized variable gave better accuracy, it was used at coarse scale for the reliability estimation of the storage tank. For reliability assessment, a limit state function, G, is defined based on the requirement. G was defined as the difference between the coarse scale model response, which is the maximum displacement of the storage tank wall, y_{max}, and the maximum allowable displacement, y_{allow} for the tank.

$$G = y_{allow} - y_{\max} \tag{3.39}$$

For reliability estimation, 100,000 samples were generated using MCS for the homogenized input variable (K_{CM}), and the maximum displacement results for each sample were calculated using the coarse scale model. After evaluating the limit state function for each response, the probability of failure (P_f) of the structure was predicted for different maximum allowable displacement values (y_{allow}) as listed in Table 3.4. For the validation, true P_f values were computed at fine scale by generating 100,000 samples for each fine scale random input variable with the stochastic parameters in Table 3.3. The results of the presented method are compared with the

different methods in literature (i.e. rate distortion theory [97], generalized methods of moments [98], and relative entropy [98]) and with fine scale model results in Table 3.4. The mean squared error (MSE) values are calculated using Eq. (3.34) and compared in Figure 3.16.

Table 3.4. Probability of Failure values for maximum displacement

Displacement Limit (mm)		*1.75*	*2*	*2.25*	*2.5*	*2.75*
Fine Scale (Target)		0.23614	0.05642	0.00971	0.0015	0.00015
Proposed Method		0.23748	0.05921	0.01055	0.00155	0.00014
Distortion Theory		0.25306	0.06633	0.0118	0.00125	0.00011
Relative Entropy		0.26382	0.06302	0.00905	0.00075	0.00006
Generalized Method of Moments	**2 Moments**	0.20507	0.06409	0.02164	0.00703	0.00212
	3 Moments	0.23967	0.06006	0.01117	0.00161	0.00017
	4 Moments	0.23165	0.05349	0.00863	0.0011	0.00013

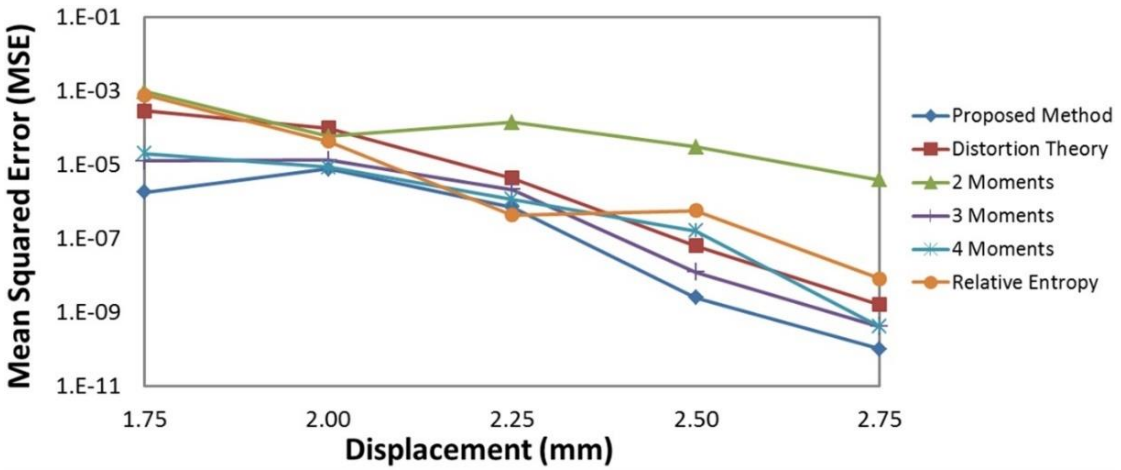

Figure 3.16. Comparison of mean squared error values for different methods

The results in Table 3.4 show that the proposed upscaling method gives the most accurate P_f values to the target values for various displacement limits and corresponding probability levels, thus providing the lowest MSE values as presented in Figure 3.16. Generalized method of moments with 3 and 4 moments provide the closer results than the other methods when the displacement limit is 2 mm and 2.75 mm. However, when the displacement limit is 1.75 mm, 2.5 mm and 2.75 mm, the P_f results of proposed method is clearly more accurate than the existing methods. In addition to lower error values, the computational cost of the proposed upscaling method was found to be less than the other existing methods, as it had been proven in the first example. The computational time to estimate the reliability at the coarse scale was about 10 seconds at the coarse scale, while it was about 65 hours at the fine scale. Comparing the values show that the coarse scale model gives conformal and accurate results while reducing the computational requirement drastically. Thus, it can be concluded that the proposed upscaling method is a viable tool for reliability estimations.

3.5.4. Multi-level Upscaling of CLSs Fabricated by Material Extrusion

The multi-level upscaling framework explained in Section 3.4 is applied for the characterization of homogenized structural properties of the AM-fabricated CSLs, shown in Figure 3.17. To conduct the material characterization of AM-fabricated cellular structures using the proposed method, tensile test specimens were fabricated in a Stratasys® Fortus 400mc using the ABS-M30 material presented by Park et al. [89]. The center of the specimens was modeled as lattice structures by periodic simple cubic (SC) unit cells with 5x5x5mm dimensions having 1.5 mm strut diameters in each unit cell as illustrated in Figure 3.17(a). The cubic unit cell was rotated counterclockwise about the Y axis by 15°, 30°, and 45° to fabricate four different lattice structures

as shown in Figure 3.17(b). In-house tensile tests were conducted for these AM-fabricated structures. These actual experimental data were utilized to demonstrate the effectiveness of the proposed multi-level upscaling procedure.

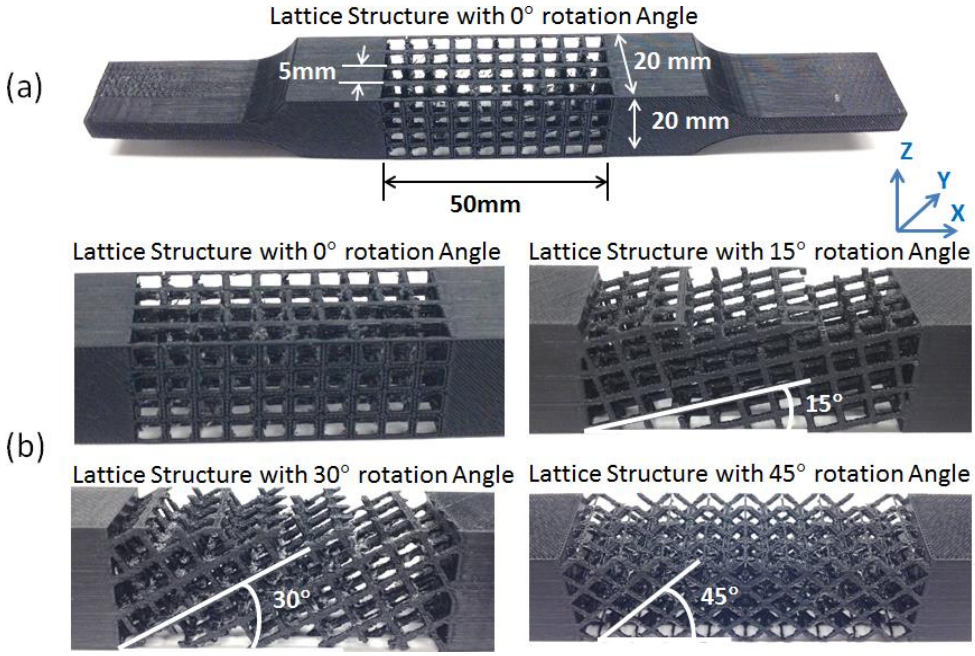

(a) Dimensions of the lattice structure. (b) Four lattice structure type with different rotation angles

Figure 3.17. Fabricated lattice structures for the tensile test.

The lattice structures fabricated by material extrusion comprise struts that have variations at each layer (Figure 1.3). The proposed multi-level modeling framework is used to relieve the difficulty of modeling of these variations with details of geometric uncertainties while preserving the accuracy of the results by utilizing proposed multi-level upscaling process with two levels of scales (N=2); i=1 refers to the macroscale level (i.e. lattice level), and i=2 refers to the mesoscale level (i.e. strut level), as seen in Figure 3.18. At mesoscale level, the purpose is to determine the homogenized structural element variables, denoted by $X_{CM,2}$ such as the homogenized diameters of each strut in the structure, by utilizing the upscaling process. Then, at the macroscale level,

instead of modeling every strut in the structure with details of variations, the struts are modeled by the homogenized diameters identified at the mesoscale level so that the overall homogenized structural properties denoted by $X_{CM,1}$ can be determined at this level by utilizing a second upscaling process. The details of the proposed framework will be provided in the subsequent sections. All of the input and output variables that were used in the proposed multi-level upscaling framework of lattice-based cellular structure in Figure 3.18 are listed in Table 3.5 to clarify the following descriptions.

3.4.5.1. Mesoscale (Strut) Level Upscaling

The scope of the mesoscale level is to identify the homogenized structural element variables, such as the homogenized diameters of each strut in the cellular structure, denoted by $X_{CM,2}$. The strut level upscaling is demonstrated in Figure 3.18 with $i = 2$.

Step 1) Fine scale input uncertainties

For upscaling at the mesoscale level in the multi-level modeling of lattice structures, first, the uncertainties of fine scale input variables, which corresponds to the uncertainties with the structural elements (i.e. struts in the lattice structures), are identified. These input variables are denoted by $X_{F,1}$ in Figure 3.18 and include the structural properties that comprise the struts such as the layer thickness, the layer diameter, the angle of the strut, etc.

The fabricated cellular structures have struts with different rotation angles (Figure 3.17(b)). These struts have deviations in geometry due to the uncertainties in the FDM manufacturing process. For the mesoscale level upscaling process, the uncertainties in the geometric variables of the struts are predicted and quantified based on the fabricated structure experiments. Stochastic input variables, used to describe the fine scale strut geometry of an angled strut with a circular

cross section, are illustrated in Figure 3.19. These variables will have uncertainties due to the process parameters.

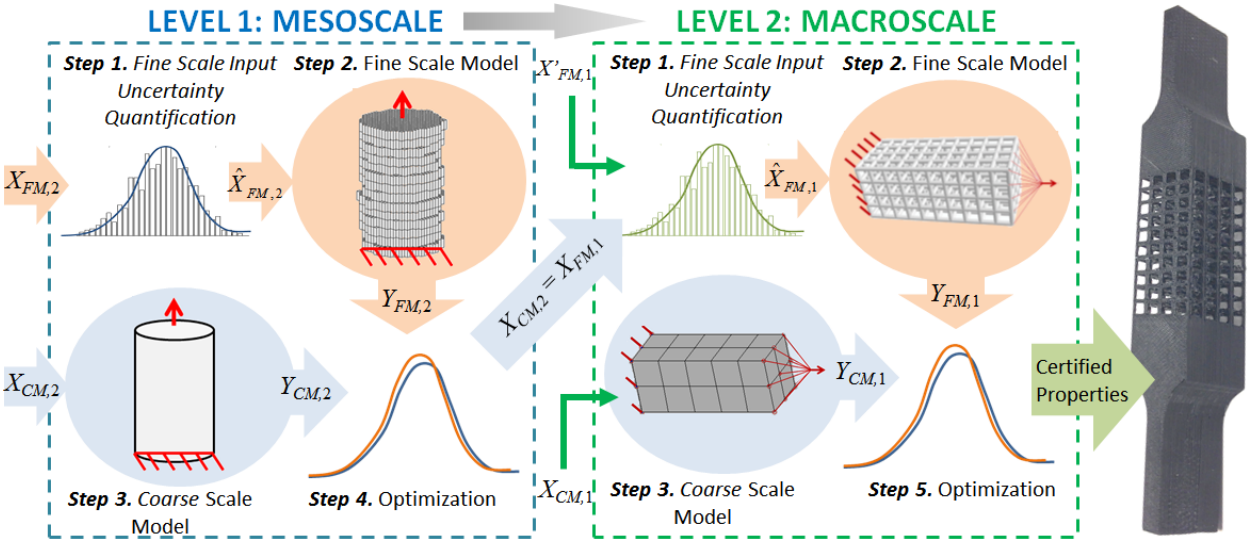

Figure 3.18. Proposed multi-level stochastic upscaling framework for cellular structures

Table 3.5. Descriptions of input and output variables at each level for the multi-level upscaling of lattice-based cellular structures

		Input	*Description*	*Output*	*Description*
Mesoscale (Strut) Level	*Fine scale FEM*	$X_{FM,2}$	Strut material and geometry properties, (layer thickness, layer diameter, angle, etc.)	$Y_{FM,2}$	Total reaction force
	Coarse scale FEM	$X_{CM,2}$	Homogenized diameters	$Y_{CM,2}$	Total reaction force
Macroscale (Structure) Level	*Fine scale FEM*	$X_{FM,1}$ $X'_{FM,1}$	Homogenized diameters Material properties of struts	$Y_{FM,1}$	Total reaction force
	Coarse scale FEM	$X_{CM,1}$	Homogenized Young's modulus and Poisson ratio	$Y_{CM,1}$	Total reaction force

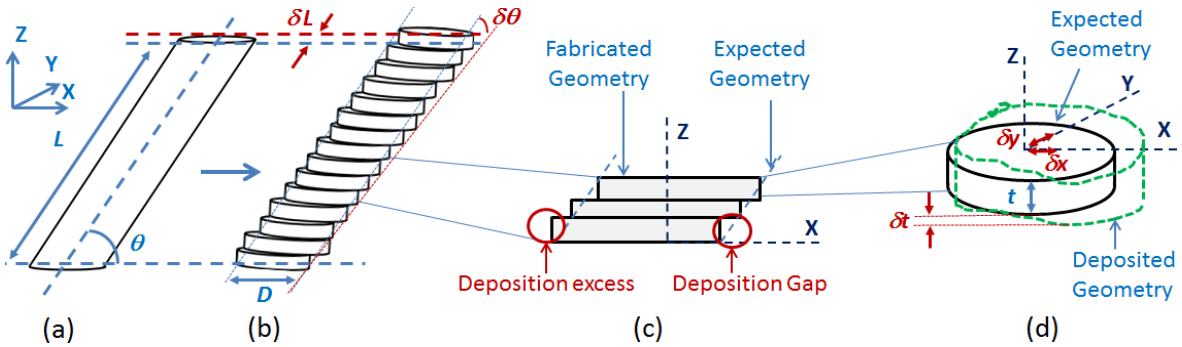

Figure 3.19. Geometric variables that possess uncertainty on struts due to the process parameters

The expected geometry of a strut with circular cross-section, which has a rotation angle, θ about Y axis is shown in Figure 3.19(a). Due to the uncertainties caused by process parameters, the strut fabricated by the FDM process is obtained as in Figure 3.19(b). When the deposited layers are closely observed as in Figure 3.19(c), it is seen that the fabricated geometry has excess portions and missing portions (gaps) after deposition of layers due to the resolution effect of layer thickness, *t*. Therefore, the overall diameter of a fabricated strut, *D*, is different than what is expected or designed. In Figure 3.19(d), a layer of a fabricated strut is depicted with exaggerated dashed lines. It should be noted that the deviations on the circular pattern shown are not as bad as it is seen in this figure for the fabricated structures but the drawing has been exaggerated to merely illustrate the deviations on the layers more clearly. Also, the details of the deposition path in the layer are not shown in this figure for simplicity. Additional details of the effect of the deposition parameters on the geometry of the layer can be found in Refs. [204], [205]. In the FDM process, the precision errors of process parameters such as road width, air gap, and raster orientation create uncertainties on the cross-sectional shape of each layer shown in Figure 3.19(d). Moreover, there are other precision issues such as the transition points where the start and end points of the deposition on each layer create a slight geometric discontinuity defect as shown darker in Figure 3.19(d) on the

dashed line. Consequently, the diameter of each deposited layer will be an uncertain input variable that affects the overall diameter of the strut.

Furthermore, inherent errors on the positioning of the nozzle head cause deviations for the position of the center of each layer. These deviations are taken into consideration as the deviation on the X axis, represented by δx, and deviation on the Y axis, represented by δy, in Figure 3.19 (d). The build angle, θ, is also an uncertain parameter since the nozzle head positioning errors create a cumulative change in the build angle, represented with $\delta\theta$ in Figure 3.19 (b). Air gap errors, shrinkage errors caused by the temperature and errors of deposited material thickness induce uncertainty on the thickness of each layer, t. The deviation on the thickness due to the uncertainties is shown with δt in Figure 3.19(d). The deposited strut length, L, also has uncertainties, causing deviations in length, represented by δL due to these process parameters errors. The uncertainties of these geometric input variables are quantified based on the fabricated specimens, and corresponding uncertainty parameters are summarized Table 3.6. COV denotes the coefficient of variation. The material properties of ABS-M30 material, given in Table 3.6, have been determined by actual experiments [89] and no porosity in the struts is considered for this example. All random variables at fine scale are assumed to be normally distributed.

Table 3.6. Statistical parameters of the input variables at fine scale

Uncertain Geometric Properties				
Variable	***Unit***	***Symbol***	***Mean***	***COV***
Diameter	mm	D	1.5	0.025
Angle about Y	degree	θ_Y	0,15,30,45,90	0.01
Angle about X	degree	θ_X	90	0.01
Thickness	mm	t	0.178	0.015
Deviation on X	mm	d_x	0.1	0.05
Deviation on Y	mm	d_y	0.1	0.05
Length of Strut	Mm	L	2.5	0.02
Thickness	mm	T	0.178	0.015
Uncertain Material Properties				
Variable	***Unit***	***Symbol***	***Mean***	***COV***
Young's Modulus	MPa	E	2039	0.04
Poisson's Ratio	-	v	0.3	0.04

Step 2) Fine Scale Model

All of the uncertainties mentioned above must be taken into account while modeling the struts in a cellular structure. Since it will be a tedious and infeasible procedure to include all of the details at the cellular structure level, first, the effect of these parameters are modeled at the mesoscale level for individual struts. To utilize the proposed upscaling process to determine the homogenized variables, a fine scale model of the struts and a corresponding coarse scale model that can represent it with homogenized variables are required. In this study, FEM is used as the modeling technique for both fine and coarse scale models to show that the proposed method can effectively identify

the homogenized input variables in a non-intrusive manner. The implicit formulation for the FEM is given by

$$f = [K] \cdot u \tag{3.40}$$

where K is the stiffness matrix of the element used in FEM. f and u denote the force vector and displacement vector, respectively. At the fine scale, a voxel-based FE modeling procedure that accounts for the uncertainties of geometrical input parameters of deposited struts is utilized for the struts. The generated model involves the FEM of 8-node brick elements. Each deposited layer of a fabricated strut is filled with these brick elements with a 0.075mm mesh size in X and Y directions based on the uncertainty information of the input variables. The mesh size in the Z direction is the same as the layer thickness, which is 0.178mm.

A sampling method is then utilized to generate the data of the random input variables at the fine scale ($X_{FM,2}$) using the stochastic parameters. Specifically, a stratified sampling scheme, LHS is used as proposed to generate $n_{FM,2}$ number of sampling points. Ultimately, the input uncertainties are propagated by a tensile test simulation of this fine scale FEM (the bottom part of the strut is fixed, and a displacement is applied on the top surface as shown in Figure 3.20), and the total reaction force is obtained as the fine scale output variable, $Y_{FM,2}$, for each sampling point.

The individual FE models of each strut with different angles, required for the four types of cellular structures, are created. For the structure with the unit cells of 0° rotation angle in Figure 3.17(b), horizontal struts along the X and Y axes (i.e. 0° angle struts), and vertical struts (i.e. 90° angle struts) on the Z axis are modeled. Similarly, for 15° rotated cellular structure, 0° struts on the Y axis, and 15° and 75° rotated struts on the XZ plane are modeled. For 30° rotated cellular

structure, 0° struts on the Y axis, and 30° and 60° rotated struts on the XZ plane are modeled. Moreover, for 45° rotated cellular structure, 0° struts on the Y axis, and 45° rotated struts on the XZ plane are modeled. Once the strut models are generated at different rotation angles, each model is rotated about the Y axis such that the struts will be vertical on the Z axis. The struts are rotated to facilitate the FEA since it enables conducting the tensile test simulation for each strut on the Z axis. An FEA for the tensile test for each sampling point for each strut is carried out by constraining the points at the bottom part of the model and applying a displacement of 1mm on the tip of the strut as shown in Figure 3.20. The total reaction force value at the fixed bottom part of the strut is obtained by FEA and corresponds to the fine scale output denoted by $Y_{FM,2}$ in Figure 3.18.

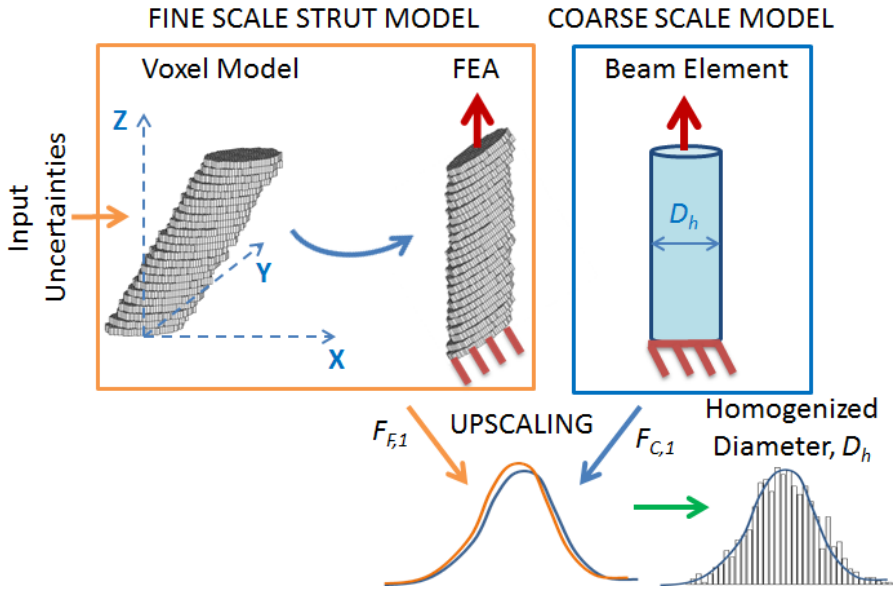

Figure 3.20. Mesoscale (i.e. strut) level upscaling for homogenized diameter

To determine the optimum number of sampling points, the accuracy of the mean and standard deviation of the reaction force for the strut at 90º are compared for various numbers of samples as illustrated in Figure 3.21. It is seen that the mean and standard deviation starts to converge after

200 simulations. Hence, the number of simulations can be taken as 200. On the other hand, the number of simulations was determined to be 500 at strut level to have a better approximation in the responses. Thus, for each strut at different angles, 500 samples of input variables are generated by LHS, and FEA is conducted to obtain the distribution of response at the fine scale.

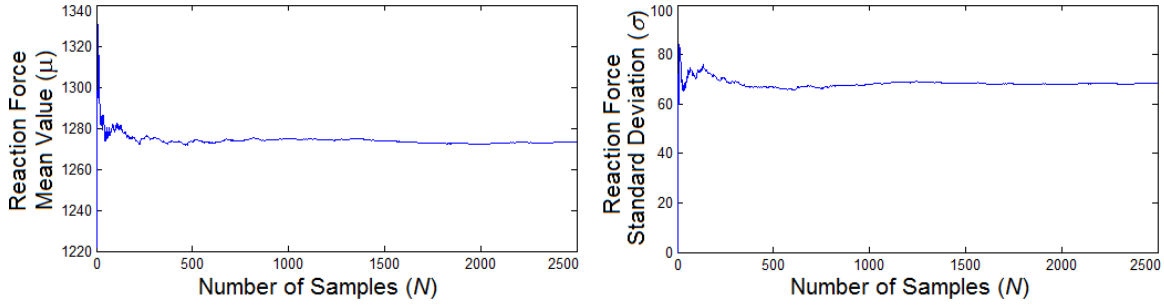

Figure 3.21. Mean value (left) and standard deviation (right) of the response for various number of samples

Step 3) Coarse scale model

In the third step of the upscaling process at the mesoscale level, a coarse scale FEM that can represent the fine scale FEM with homogenized parameters is constructed at the mesoscale level. It is preferred to use a relatively simple FEM technique that can accurately represent the detailed fine scale model to minimize the computational burden of repetitive simulations in the upscaling procedure. Hence, the struts are represented by a linear elastic beam element model at coarse scale, and the homogenized diameter of the strut at the coarse scale model is defined as the unknown homogenized input variable, denoted by D_h in Figure 3.20. The homogenized diameter corresponds to the homogenized input variable denoted by $X_{CM,2}$ in Figure 3.18. It was assumed that the material properties at the coarse scale (i.e. elastic modulus and Poisson's ratio) are the same as the fine scale properties. Similar to the fine scale model, the bottom part is fixed, and a displacement of 1mm is applied to the tip of the coarse scale model. Since the fine scale models

are rotated to an angle of 90º, the same coarse scale model can be used for each fine scale strut model. The coarse scale output is the total reaction force and is denoted by $Y_{CM,2}$ in Figure 3.18.

To reduce the dimensionality of the random quantities in the optimization process, the uncertainty of the homogenized diameter is projected onto a second order PCE

$$D_h = \sum_{k=0}^{2} b_k \Phi_k(\xi) \tag{3.41}$$

Thus, only the PCE coefficients, denoted by b are found in the optimization. Since the fine scale input parameters are assumed to be normally distributed, it is expected that the Hermite polynomials will provide sufficient accuracy for this problem. The uncertain values of ξ are obtained from the fine scale responses using Eq, (3.24). The PCE coefficients are initialized, and the total reaction force is calculated as the coarse scale output variable, $Y_{CM,2}$, by implementing a tensile test simulation of the coarse scale FEM.

Step 4) Optimization for upscaling

In the fourth step of the upscaling process given by Figure 3.18, the optimization of Eq. (3.20) (i.e. matching the probabilistic performance of $Y_{FM,2}$ and $Y_{CM,2}$) is conducted to determine the optimal PCE coefficients of the homogenized variables. The coarse scale PDF results of responses, obtained after optimization for each strut with 90º, 75º, 60º, 45º, 30º, and 15º rotation angles, were compared with the fine scale PDF results in Figure 3.22, and the error values were calculated by

$$error = \sum_{j=1}^{n} \left| \frac{y_{FM},i(j) - y_{CM,i}(j)}{_{FM,i}(j)} \right| \tag{3.42}$$

where $y_{FM,i}(j)$ and $y_{FM,i}(j)$ denote the fine and coarse scale responses at the j^{th} sampling point for n number of samples, respectively. As seen in Figure 3.22, the PDF of coarse scale responses is very close to the PDF of fine scale responses. The error values are on the level of 10^{-4}, which proves that the upscaling is achieved with a very high accuracy for all struts with different rotation angles.

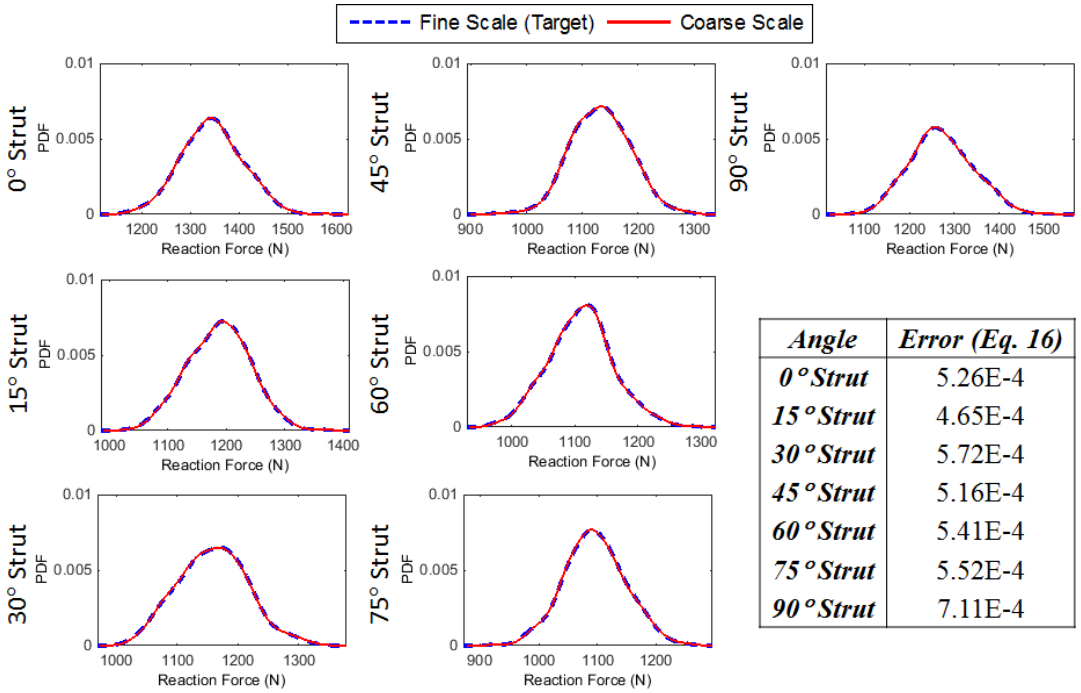

Angle	*Error (Eq. 16)*
0 ° Strut	5.26E-4
15 ° Strut	4.65E-4
30 ° Strut	5.72E-4
45 ° Strut	5.16E-4
60 ° Strut	5.41E-4
75 ° Strut	5.52E-4
90 ° Strut	7.11E-4

Figure 3.22. PDF plots of fine scale and coarse scale responses for struts with various angles and corresponding error values

3.4.5.2. Macroscale Level Upscaling

The upscaling process that is used at the macroscale level can be presented when $i = 1$ in Figure 3.3 and summarized on the right side of Figure 3.18. The uncertain homogenized diameters, which have been determined at the mesoscale level, are introduced at the macroscale level as the fine scale input variables, and the overall material properties of a coarse scale model are determined for the AM-fabricated parts using the stochastic upscaling technique, thus enabling an efficient multi-level structural property characterization procedure.

Step 1) Fine Scale Input Uncertainties

The statistical data of the homogenized variables, $X_{CM,2}$ (i.e. the strut diameters), which were obtained at the mesoscale level by the upscaling process, are introduced at the macroscale level as the fine scale input uncertainties of the fine scale model and are represented by $X_{FM,1}$. There are additional random input variables at the fine scale of the macroscale level, which is independent of the mesoscale level such as material properties of struts. Those are represented by $X'_{FM,1}$ in Figure 3.18. In the first step of macroscale level, the optimal distribution type and the statistical parameters of the homogenized variables that will be used at the macroscale level are determined by BIC for input uncertainty quantification at the fine scale. Different distribution types are fitted to the homogenized diameter data for this purpose. Six candidate distributions, i.e. Normal, Lognormal, Gamma, Gumbell, Frechet, and Weibull distributions, were chosen to fit the reaction force data using MLE by adjusting the stochastic parameters. Since Generalized extreme value (GEV) distribution can represent the last three distributions, it can be utilized for the estimation of Gumbell, Frechet, and Weibull distributions. Then, the goodness of fit of each distribution is calculated by BIC given in Eq. (2.68) to pick the best candidate of distribution that fits the data. The distribution type, which has the smallest BIC value, gives the best fit for the data of the homogenized diameter obtained by the upscaling procedure. The BIC values for strut diameters with different rotation angles are listed in Table 3.7 with bolded values for the best-fitted distributions. The optimal distribution types and the corresponding mean and standard deviation values for homogenized diameters are given in Table 3.8. The PDFs of the fitted distributions are illustrated in Figure 3.23 for 90^0 strut.

Table 3.7. BIC values for different type of distributions

Distribution	Normal	Lognormal	Gamma	GEV
0° Strut	-1.9609E+03	**-1.9612E+03**	-1.9612E+03	-1.9500E+03
15° Strut	**-2.0680E+03**	-2.0671E+03	-2.0675E+03	-2.0569E+03
30° Strut	-1.9825E+03	**-1.9832E+03**	-1.9831E+03	-1.9781E+03
45° Strut	**-2.0485E+03**	-2.0475E+03	-2.0479E+03	-2.0375E+03
60° Strut	-2.0665E+03	**-2.0669E+03**	-2.0669E+03	-2.0564E+03
75° Strut	-2.0455E+03	-2.0454E+03	**-2.0455E+03**	-2.0366E+03
90° Strut	-1.8359E+03	**-1.8378E+03**	-1.8373E+03	-1.8332E+03

Table 3.8. Distribution type and the stochastic parameters for homogenized strut diameters

Strut Angle	Distribution	Mean D_h (mm)	*Standard Deviation (mm)*
0° Strut	Lognormal	1.4483	0.0337
15° Strut	Normal	1.3610	0.0302
30° Strut	Lognormal	1.3446	0.0329
45° Strut	Normal	1.3294	0.0308
60° Strut	Lognormal	1.3161	0.0303
75° Strut	Gamma	1.3074	0.0309
90° Strut	Lognormal	1.4086	0.0381

As listed in Table 3.8, 15° and 45° struts have a normal distribution, the 75° strut has a gamma distribution, and the remaining struts have lognormal distributions based on the BIC results. Also,

the diameter values of struts in the fabricated lattice structures were measured using a digital caliper to compare the homogenized diameter values obtained by the upscaling method with the diameters of actually fabricated struts. An average diameter value for each strut was obtained by the measurements and compared with homogenized diameter values in Figure 3.24.

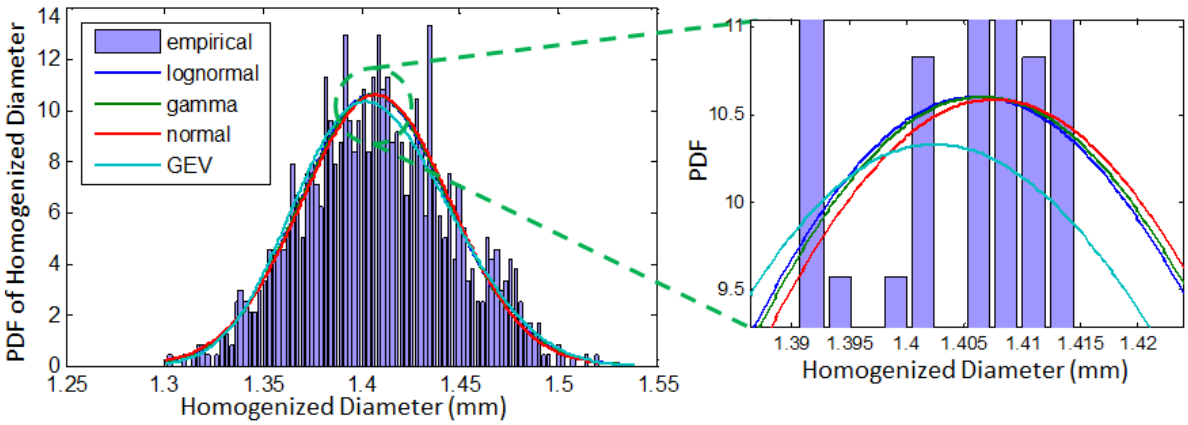

Figure 3.23. Histogram and fitted distributions for the homogenized diameter of the 90° strut

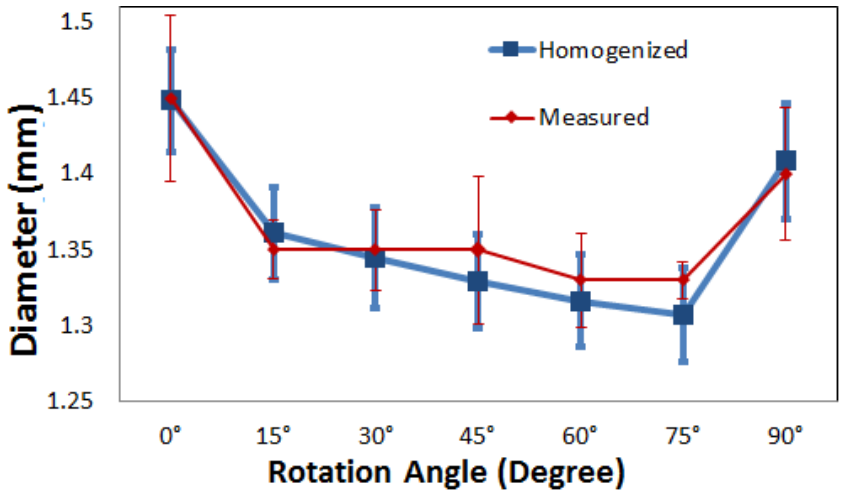

Figure 3.24. Comparison of homogenized diameter values with the measured diameter values

The largest measured diameter value was 1.45mm for 0° strut and the diameters of the other struts were less than or equal to 1.4mm. These measured results prove that the uncertainties caused by

manufacturing process parameters have a considerable effect on the geometry of fabricated struts and therefore must be taken into account for the modeling. The homogenized diameter values are predicted very closely to the measured diameter values as seen in Figure 3.24. The error values between the mean homogenized value, which were obtained by accounting for the uncertainties in the FEM of the mesoscale level, and the measured average value for each strut with different rotation angles, were calculated using Eq. (3.42). The largest error was calculated as 1.7% for the 75° strut when the errors were converted to percentage values. These results show that the mesoscale level upscaling procedure provides an accurate estimation of the diameter values of struts. Thus, the distribution of the results from tensile tests can be approximated by using only a single variable, i.e., strut diameter, with its own distribution at macroscale level for structural property characterization of lattice-based cellular structures.

Step 2) Fine Scale Model

In the macroscale level upscaling process, once the fine scale input uncertainties are quantified, the second step is to construct a fine scale FEM to model the details of the cellular structure. Since the coarse scale homogenized parameters obtained by the mesoscale level upscaling process are the shared variables between mesoscale and macroscale levels (i.e. $X_{CM,2} = X_{FM,1}$), a coarse scale model at the strut level that can correspond to the fine scale model of the macrostructure level is chosen to achieve accurate calibration of mesoscale level input parameters with the macroscale level model and homogenized parameters. Linear elastic beam elements were used at the fine scale for the FEM of the cellular structures built by 0°, 15°, 30°, and 45° degree rotated square unit cells, as shown in Figure 3.25.

Depending on the rotation angle of the struts in the lattice model, the corresponding homogenized strut diameter distribution and its parameters from Table 3.8 are used in the fine scale simulations. For instance, when the rotation angle of the unit cells in the lattice structure is 0°, there are only 0° and 90° struts in the lattice structure, as shown in Figure 3.25. Therefore, the homogenized diameter values obtained at the mesoscale level for 0° and 90° degree struts are used as the random input variables of the lattice structure with 0° rotation angle. A similar procedure is followed for the other lattice structures with different angles.

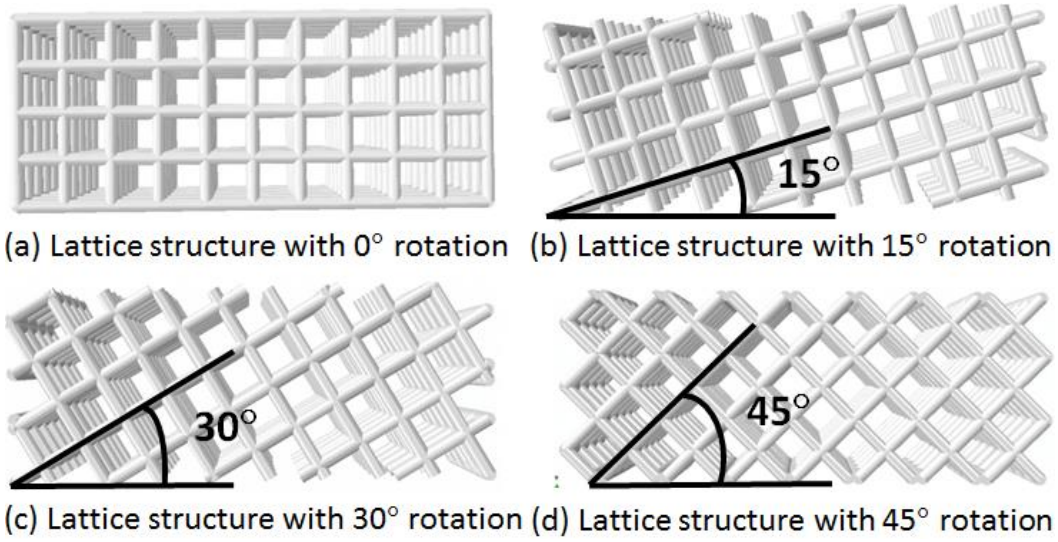

Figure 3.25. Fine scale model of lattice structures with various rotation angles

The samples for random input variables are generated by LHS using the statistical parameters for the homogenized input variables obtained quantified in step 1. The fine scale input variables with quantified uncertainties are denoted by a hat over the input variable symbol, i.e., $\hat{X}_{FM,1}$ in Figure 3.18. Tensile test simulations were performed by fixing one end and applying an axial displacement on the other end of the lattice structures, while randomly varying the input variables

to generate an expected distribution of the total reaction force at the fixed end of the structure as the fine scale output, $Y_{FM,1}$.

A convergence analysis for the mean and standard deviation of the fine scale response was again conducted to determine the optimal number of sampling points using the lattice structure FEM with 0° rotation angle. The convergence was obtained at about 200 samples. Hence, 200 sampling points were generated for input variables, and FEA was conducted for each lattice structure type at fine scale to obtain the responses that was used in the macroscale level upscaling.

Step 3) Coarse Scale Model

In the third step, the coarse scale model at the macroscale level is constructed. The main purpose of the upscaling is to determine the unknown homogenized elastic properties of the lattice structures (i.e. Young's Modulus and Poisson's Ratio). Based on the upscaling process, it is determined that the distribution of outputs (i.e. total reaction force, $Y_{CM,1}$) from tensile tests on the lattice structure can be approximated using a solid block of material using 3D isotropic solid mesh elements (i.e. 8-node brick element) as the coarse scale FEM. Since the solid elements have elastic material properties, i.e. Young's Modulus (E_h) and Poisson's Ratio (ν_h), as the input parameters, these can be considered as the homogenized unknown input variables, $\mathbf{X}_{CM,1}$ in Figure 3.18. It was shown with a bold character since there are two input variables which make it a vector. It should be noted that the FDM fabricated lattice structures can show anisotropy since the build direction used to fabricate the structure can affect the material properties. However, since the physical tensile test experiments were conducted only in the X direction of the fabricated structures in Figure 3.17, only the isotropic elastic material properties (i.e. properties only in X direction) were determined in this study.

Similar to the upscaling process at mesoscale level, the homogenized coarse scale input variables are projected onto the PCE using for dimension reduction in the optimization process. Since there are 200 sampling points, the optimization procedure will attempt to find 200 Young's Modulus and 200 Poisson's ratio values corresponding to each sample point. In order to reduce the number of design variables, the random variability of E_h and ν_h are projected onto the PCE as

$$E_h = \sum_{k=0}^{P_1} b_k \Phi_k(\xi) \tag{3.43}$$

$$\nu_h = \sum_{k=0}^{P_2} c_k \Phi_k(\xi) \tag{3.44}$$

Thus, only the coefficients, b and c of the PCEs are determined in the optimization. The number of coefficients, P_1, was taken as 3 and P_2 was taken as 2 in the optimization process, thus, reducing the number of design variables from 400 to 5. The uncertain values of ξ are obtained from the fine scale response data, $X_{FM,1}$, using Eq, (3.24). The PCE coefficients are initialized and the total reaction force is calculated as the coarse scale output variable, $Y_{CM,1}$, by implementing a tensile test simulation of the coarse scale FEM.

Step 4) Optimization

In the fourth step, the unknown PCE coefficients of the homogenized coarse scale input variables, $X_{C,2}$, are determined by matching the probabilistic performance of the coarse scale output, $Y_{C,2}$, and the fine scale output, $Y_{F,2}$, by utilizing the optimization process. Once the optimization process was implemented for each lattice structure with different angles, the PDFs of the responses at fine

and coarse scale were obtained. The corresponding errors between coarse scale and the fine scale results are also calculated by Eq. (3.42) and summarized in Table 3.9.

Table 3.9. The error values calculated for coarse scale model predictions

Structure	***0° Angle***	***15° Angle***	***30° Angle***	***45° Angle***
Error	4.60E-05	1.70E-05	3.91E-05	4.14E-05

As can be seen from the error results in Table 3.9. the homogenized input parameters of the coarse scale model that were obtained by the upscaling procedure can enable highly accurate computing of the PDF of the responses. As a result, the coarse scale model and the homogenized material properties can be used to represent the lattice structures.

5.4.5.3. Comparison of homogenized lattice material properties with experiments

Once the lattice level upscaling process is completed, the coarse scale model can be used to predict the lattice structure experiments. For this purpose, the distribution types and stochastic parameters of the predicted statistical data of the homogenized Young's Modulus and Poisson's ratio values are determined using the BIC method.

Different distribution types (i.e. Normal, Lognormal, Gamma, and GEV) are fitted to the homogenized Young's Modulus and Poisson's ratio data to evaluate the goodness of fit of these distributions using BIC. The BIC values for different distribution types are listed in 0 with bolded values that shows the optimal distribution types. The corresponding distribution types determined based on these BIC values, the mean and standard deviation values for homogenized material properties are listed in Table 3.11.

Table 3.10. BIC values for different type of distributions

Structure	Variable	Normal	Lognormal	Gamma	GEV
0° Structure	E_h	1.8251E+02	**1.8234E+02**	1.8240E+02	1.8259E+02
	v_h	-1.3418E+03	**-1.3434E+03**	-1.3429E+03	-1.3415E+03
15° Structure	E_h	-1.2148E+02	**-1.2168E+02**	-1.2162E+02	-1.1584E+02
	v_h	-1.6840E+03	**-1.6844E+03**	-1.6843E+03	-1.6783E+03
30° Structure	E_h	**-3.7692E+02**	-3.7686E+02	-3.7689E+02	-3.7054E+02
	v_h	**-1.3625E+03**	-1.3617E+03	-1.3621E+03	-1.3561E+03
45° Structure	E_h	**-5.8341E+02**	-5.8305E+02	-5.8317E+02	-5.8146E+02
	v_h	**-1.3407E+03**	-1.3387E+03	-1.3394E+03	-1.3387E+03

Table 3.11. Distribution type, mean and standard deviation estimated for homogenized variables for each lattice structure with different rotation angle

Structure	Variable	Distribution	Mean	Standard Deviation
0° Structure	E_h	Lognormal	131.6355	0.3727
	v_h	Lognormal	0.2735	0.0082
15° Structure	E_h	Lognormal	33.5542	0.1743
	v_h	Lognormal	0.3257	0.0035
30° Structure	E_h	Normal	14.4642	0.0921
	v_h	Normal	0.2116	0.0078
45° Structure	E_h	Normal	7.5350	0.0460
	v_h	Normal	0.2440	0.0083

As given in Table 3.11, the material properties of the lattice structures with 0° and 15° rotation angles have lognormal distributions and the others have normal distribution. The mean values of the homogenized Young's Moduli are compared to the experimental results that were obtained from actual tensile tests of the lattice structures fabricated by FDM in Figure 3.26.

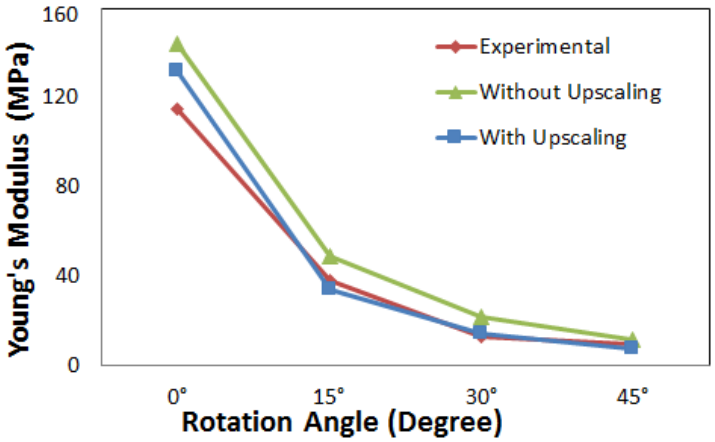

The standard deviations for experimental results are as follows: 0º Structure: 2.31 MPa, 15º Structure: 2.36 MPa, 30º Structure: 0.62 MPa, 45º Structure: 0.03 MPa.

Figure 3.26. Comparison of Young's Modulus results for each lattice structure.

Three lattice structure tensile test specimens were fabricated for each angle (i.e. 0º, 15º, 30º, 45º structures) and the average of Young's Modulus values were obtained from actual experiments. In addition, deterministic Young's Modulus results are compared with the results obtained without using the stochastic upscaling process in Figure 3.26. In this case, since our target while fabricating the structures is to have 1.5 mm diameters, the lattice structure FE models were generated with beam elements using 1.5mm diameters for the struts. Then, the deterministic effective Young Modulus values of the lattice structures were calculated by dividing the axial stress on the surface of the structure by the axial strain, without using the proposed upscaling procedure to see the effect of the upscaling procedure and uncertainty quantification on the prediction of material properties.

As can be seen in Figure 3.26, the Young's Modulus values decrease when the build angle of the unit cells is increased, and the simulation results agree well with the trend of the experimental results. It is observed that when there is no rotation (i.e. for the lattice structure with 0° rotation angle), the Young's Modulus of the structure is at least three times greater than the one obtained for the structures with rotation angles. This is the result of occurrence of more disconnected nodes on the lattice structure when the rotation angle increases. In addition, the results show that the homogenized values obtained by the upscaling procedure are closer to the experimental results than the values obtained without the upscaling procedure. For a better comparison of the results, the error between the experimental results and the FEA results were calculated for each structure using Eq. (3.42) with n=1 and listed in Table 3.12.

Table 3.12. Comparison of errors (Eq. (3.42)) for the overall Young's Modulus values

Structure	***0° Structure***	***15° Structure***	***30° Structure***	***45° Structure***
With Upscaling	0.14	0.11	0.13	0.18
Without Upscaling	0.25	0.28	0.69	0.28

Compared with the Young's Modulus values obtained without the proposed multi-level upscaling procedure, there is a significant reduction in the errors when the proposed method is utilized. The lowest difference in errors occurs for the structure with 45° rotation angle, and even for that case, the error reduction is about half of the error occurred when the proposed upscaling procedure is not used. The reduction in the diameter values caused by the uncertainties due to the manufacturing process parameters is not taken into account in the simulations without the upscaling method, thus resulting in greater errors in the estimation of overall material properties of fabricated structures.

Thus, the results prove that the proposed multi-level upscaling method provides an efficient estimation of material properties by accounting for the uncertainties at the mesoscale level.

3.6. Summary

In this chapter we introduced an improved stochastic upscaling method, which constructs an accurate and computationally efficient coarse scale model, to facilitate the engineering analysis at multiple scale levels by representing the heterogeneity and propagating uncertainty at fine scale to the end product performance with homogeneous input parameters. The BIC method for fine scale input uncertainty quantification, and the exponential loss function that can enable the match between the fine and coarse scale model responses in an efficient way were integrated into the stochastic upscaling method through optimization that utilizes the PCE method to represent the homogenized properties with reduced dimensionality under uncertainties. In addition, a hybrid procedure using both GA and SQP for solving the optimization for upscaling is integrated into the proposed method to improve the computational efficiency of the optimization step. In Section 3.5, the effectiveness of the proposed approach for uncertainty quantification and propagation has been validated thorough two elastic structural problems at one scale level and one lattice structure example at multiple scale levels, involving uncertainty and heterogeneity at finer scales due to the AM process. A significant reduction in computational cost is obtained since (a) the simulation-based optimization with exponential loss function is computationally less demanding and more accurate than the other existing objective functions (Section 3.3.1); (b) the introduced moment equality constraint provides a bounded design space so that better convergence speed is expected; (c) the PCE can reduce the number of variables to accurately model uncertainties; and (d) a hybrid GA and SQP algorithm can reach a global optimum with a quick convergence rate.

The comparison of the coarse-scale solution with the fine-scale full solution, which is used as a reference, provided efficient results when fine scale random input variables had either non-Gaussian distribution or Gaussian distribution for the examples with complex geometry and heterogeneous material properties at fine-scale levels. When the fine scale model is presented with more complicated coarse scale models, which may have more than one input variable, the application of the proposed method may be more challenging due to a higher number of design variables, as shown in the upscaling process of the hydrogen storage tank design. On the other hand, accurate solutions were obtained regardless of the complexity of the coarse-scale model. In conclusion, accurate reliability assessment is achieved since the fine scale complexity and heterogeneity can be represented by computationally efficient coarse scale models without losing accuracy by utilizing the proposed upscaling technique.

The efficacy of the presented multi-level upscaling framework has been shown on the material characterization of lattice structures that are fabricated with the FDM process in Section 3.5.4. PCE has been utilized to deal with the uncertainties in the diameter of the struts in the lattice-based cellular structures as well as the overall material properties of the structures. The developed multi-level technique has shown that the uncertainties that propagate from one level to another can be quantified efficiently. The actual test results of fabricated parts are integrated into the modeling procedure. The applied procedure has successfully identified the homogenized diameters and material properties while ensuring accurate matching of responses between fine and coarse scale models. It has been shown that the presented method is critical for the property characterization of additively manufactured cellular structures for which the analysis conducted without using the method would be computationally prohibitive due to the uncertainties at fine scales.

As mentioned earlier, although the example of this research is based on the cellular structures fabricated by the FDM process, the presented multi-level upscaling framework can be utilized as a general multiscale modeling procedure for any multiscale engineering application. The presented procedure has significant potential to effectively certify additively manufactured cellular structures, thus enabling the use of the AM-fabricated parts for critical applications such as parts in aircraft, vehicles, and medical products.

Further reduction of the errors can be achieved when the upscaling processes is implemented for homogenizing not only the strut diameters but also the strut material properties at strut level by considering the porosities in the fabricated struts. Moreover, a systematic validation approach is required to evaluate the predictive accuracy of the computational models used in the upscaling process. In Chapter 4, a validation approach is introduced for this purpose.

CHAPTER 4. MULTI-LEVEL VALIDATION APPROACH

This chapter deals with addressing the *Research Question 2* in Chapter 1 to be able to improve the prediction accuracy in upscaling approach with minimal experimental cost. As stated in *Hypothesis 2*, a hierarchical validation approach has been proposed to establish an accurate prediction of reality from the multi-level upscaling process. Specifically, the validation pyramid concept [105] is adapted to the multi-level upscaling process to introduce a hierarchical multi-level validation approach. In the proposed approach, first, the stochastic upscaling method is used for the homogenization of the geometry and material properties at each scale level of interest. The next step is the validation process, in which the experimental data is used to build confidence that the coarse scale model with homogenized properties can accurately predict the responses. The proposed framework of the hierarchical validation approach is described in Section 4.1.

In Section 4.2, an improved validation metric is proposed that integrates the so-called u-pooling method [110] with the Kolmogorov-Smirnov (K-S) test [118] for the quantitative assessment of the model predictions to use the available experiments in the most efficient way. The proposed metric both enables the assessment of the model performance for multiple validation sites and constructs an unbiased decision criterion while considering the number of available experiments based on the test statistic. The flowchart of the validation step used in the validation pyramid after upscaling step at each scale level is described in Section 4.3. Thus, the developed validation framework targets to minimize the required experimental cost while maximizing the model adequacy by applying the upscaling and validation steps at each scale level in bottom-up multiscale strategies. In Section 4.4, CLS specimens fabricated by AM techniques (i.e. by material extrusion and SLM processes) are used as the application examples to present the efficacy of the

presented approach. Ultimately, this research will enhance confidence in employing the developed multi-scale models to accurately predict the process path that will give the desired combination of properties in designs of engineering applications.

4.1. Multi-Level Validation and Upscaling Framework

The stochastic upscaling method introduced in Chapter 3 enables the use of black-box computational models at multiple scale levels to model the CLSs fabricated by AM. In that approach, a top-down decomposition of the system or product at a macroscale level into multiple sub-levels (e.g. mesoscale, microscale, etc.) also requires a hierarchical validation approach to be developed. Hence, it is hypothesized here that the validation pyramid approach introduced by Ref. [105] for complex engineering systems can be adapted to validate the computational models across multiple scale levels. The corresponding multi-level validation framework, which is based on the concept of the validation pyramid approach, is illustrated in Figure 4.1 for the application to the CLS example fabricated by FDM process that is discussed in Section 3.4.5.

In Figure 4.1, i represents the level of scale. The human scale level (e.g. an aircraft component) at the top of the pyramid is given by i=0 and defined to be the prediction level. This level involves the component or system that will be designed or analyzed with the computational models. The prediction level model is decomposed into multiple sub-levels to simplify the computational models. Then, the upscaling process is used to pass the information at the finer scales to the macroscale level from bottom to top. The first level is given by i=1 in Figure 4.1 and called the macroscale level. Simple coupon level experiments are utilized for validation at this level since those experiments are usually available. For the CLS example, this level corresponds to the validation of the lattice level computational model with the tensile test of the lattice structure

specimen. To account for finer scale details in the FE models, a mesoscale level, defined by i=2, is also utilized where the individual struts are modeled with detailed uncertainties of strut geometry and material. The mesoscale level can be broken down even further to microscale and/or atomistic scale levels ($i = 1,2,\ldots,N$) if necessary. Once the validation is achieved for the predictions at each level of interest from bottom to top, validated computational model at macroscale level, (i.e. i=1) is used for design or analysis of the engineering application at the prediction level.

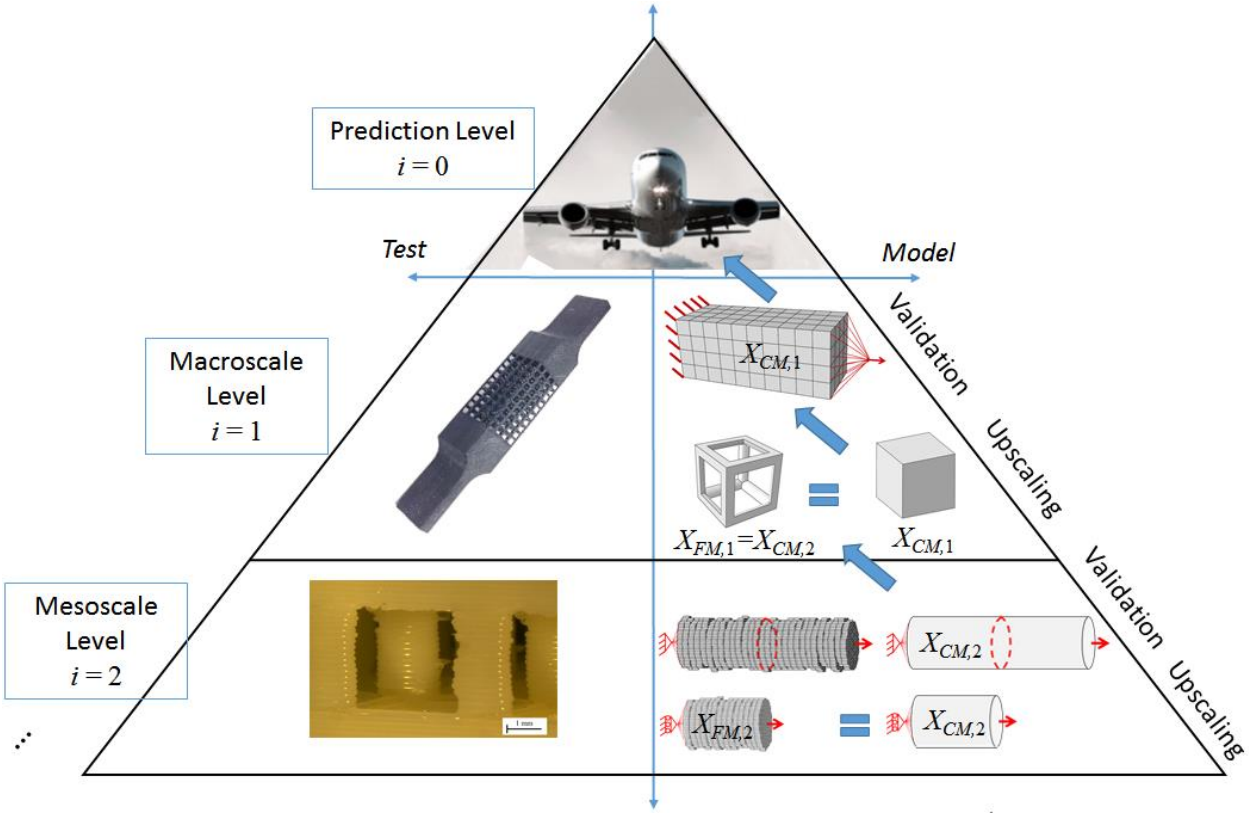

Figure 4.1. Multi-level validation approach with the application to the modeling of CLSs.

Differing from the existing validation pyramid approach, where only one calibration and multiple validation steps are used, in the proposed approach, the calibration and validation steps are used at each scale level of interest in an increasing hierarchy of models. The actual validation pyramid framework starts with a calibration process at the bottom of the pyramid to identify the

input parameter values of the model. In the proposed multi-level modeling approach, this corresponds to an upscaling (or homogenization) process in which the homogenized input parameters are determined for the model that will be used in the subsequent scale level. In the proposed approach, the stochastic upscaling method presented in Chapter 3 is used to determine the homogenized properties, as well as to quantify the uncertainties at each scale level.

This upscaling procedure is desired because homogenized parameters and the corresponding coarse scale model at one level (e.g. mesoscale level) are used at a higher scale level (e.g. macroscale level) to simplify simulations. In Figure 4.1, the input variables are denoted by X, where subscripts FM and CM represent the fine scale model and the coarse scale model at one level, respectively. The fine scale model, which is upscaled to a coarser scale, can either be a physical experiment or a detailed computational model. In the upscaling step of the validation approach, the fine scale models are considered as the ground truth and the homogenized properties of the coarse scale models are found by the upscaling method. The smallest representative model is chosen in the upscaling step of the corresponding level to minimize the computational effort.

Once the homogenized properties ($X_{CM,i}$) are predicted for the coarse scale model using the upscaling approach at one scale, validation experiments are needed to ensure that the coarse scale models corresponding to each level function properly. For this purpose, the experiments in the validation step are designed to challenge the computational model. Hence, a model that is different and/or more complex from the one used in the upscaling process is preferred to ensure the validity of the assumptions made for developing the prediction model. The homogenized inputs estimated by the upscaling process are used to model the experimental specimen with the coarse scale model. The coarse scale model outputs are compared with the experimental measurements for validation. However, one issue in the multiscale model validation process is that it is usually difficult or

impractical to implement physical experiments at scales finer than the macroscale level since the scale is too small to physically model. Then, the validation for the predictions of the coarse scale model with homogenized properties can be performed at the scale levels where the validation experiments can be achieved.

At scales where the experiments are not available or very expensive, a "pre-validation" step is introduced to increase the confidence of the computational models. In this step, the fine scale modeling approach is used instead of the validation experiments, which also allows for the decrease of the experimental cost. Similar to the validation step, a model that is different from the one used in the upscaling step and that can challenge the coarse scale model predictions at the same level is determined by the user. Thus, the validation methodology will have the generic steps for each scale level of interest and can be used in the validation of the computational models used in a bottom-up multiscale modeling process. It should be noted here that the pre-validation step does not guarantee that the predictions of the model are valid or accurate at the level where the experiments are not available since it is not a validation process with experiments; but, it gives some insight on the prediction level of the model. To use the pre-validation step at finer scale levels, one has to know that experiments are available at least at the macroscopic level (i=1). Otherwise, using the pre-validation step at each scale level without any experiments will not provide any validation for the models used in the multiscale modeling process. Hence, the highest level (i.e. level of macroscale) experiments are crucial for the proposed validation approach to evaluating whether the multi-level upscaling procedure adequately considered the interactions at all levels from bottom up. Then, at each level in the proposed validation pyramid, if the prediction outcomes agree with the experimental outcomes, the next level validation process will be processed. Otherwise, the computational model is modified until the desired values are attained.

Once the proposed validation framework is implemented successfully at each scale level, the validated computational models can be used at the prediction level shown in Figure 4.1 at the top of the pyramid (i=0) for analysis or design of the product of interest. Additional validation and accreditation steps can be introduced at this component or system level if the experiments are available, as discussed in [105].

4.2. Proposed Validation Metric

To quantitatively evaluate the validity of the computational models at each level of the validation pyramid and to use the available experimental data in the most efficient way, an appropriate validation metric is to be chosen. One important criterion that needs to be considered while choosing the validation metric is that more than one different validation sites can exist that output the same response parameter. The u-pooling method described in Section 2.4.3.2 is used in this research to assess the predictive capability of the models in the case of multiple validation sites.

The u-pooling method is advantageous over other validation metrics as it pools all of the observations at multiple validation sites into one distribution, which should follow SUD if an accurate prediction is made. Thus, the number of available experimental data can be increased in the validation process even if a small number of experiments are available. Ferson et al. [110] proposed to use the area metric described in Section 2.4.3.1 to evaluate the distribution of predictions obtained by the u-pooling method. However, in the area validation metric, a threshold value must be determined by the decision maker as a decision criterion to accept or reject the model predictions. This criterion will not give an unbiased decision based on the number of experiments. In other words, if the number of experiments is not sufficient, the area metric may result in making a wrong decision for the validation of the model [106]. Hypothesis testing

methods can be applied to the u-values to address this drawback of the area metric [110]. Among various hypothesis testing methods, the K-S test has the advantage of the applicability for any type of distribution as described in Section 2.1. Hence, we propose to use the K-S test to evaluate the predicted distribution by the u-pooling method instead of using the area metric. The K-S test can establish an acceptance/rejection criterion based on the number of available experimental observations or measurements. The K-S test uses the maximum distance between the target CDF and the predicted CDF to decide whether the predicted CDF is accepted or not as described in Section 2.1. When the u-pooling method is used, for i^{th} scale level, the maximum distance, denoted by d_{KS}, is calculated by

$$d_{KS,i} = \max_{u} \left| F_{SUD}(u) - F_{ECDF,i}(u) \right| \tag{4.1}$$

In the modified K-S test for the u-pooling method, if the u values are found to be drawn from the CDF of the SUD ($F_{SUD}(u)$), then the null hypothesis is $H_0 = 0$ (i.e. the model is not rejected); otherwise $H_0 = 1$ (i.e. the model is rejected) at a significance level of α according to Kolmogorov's distribution [118]. Since the K-S test statistic is calculated based on the number of experiments, it will provide an unbiased decision criterion in the validation process.

4.3. Flowchart of the Proposed Validation Step

The flowchart of the validation step in the validation pyramid at each level of interest with the proposed validation metric is shown in Figure 4.2.

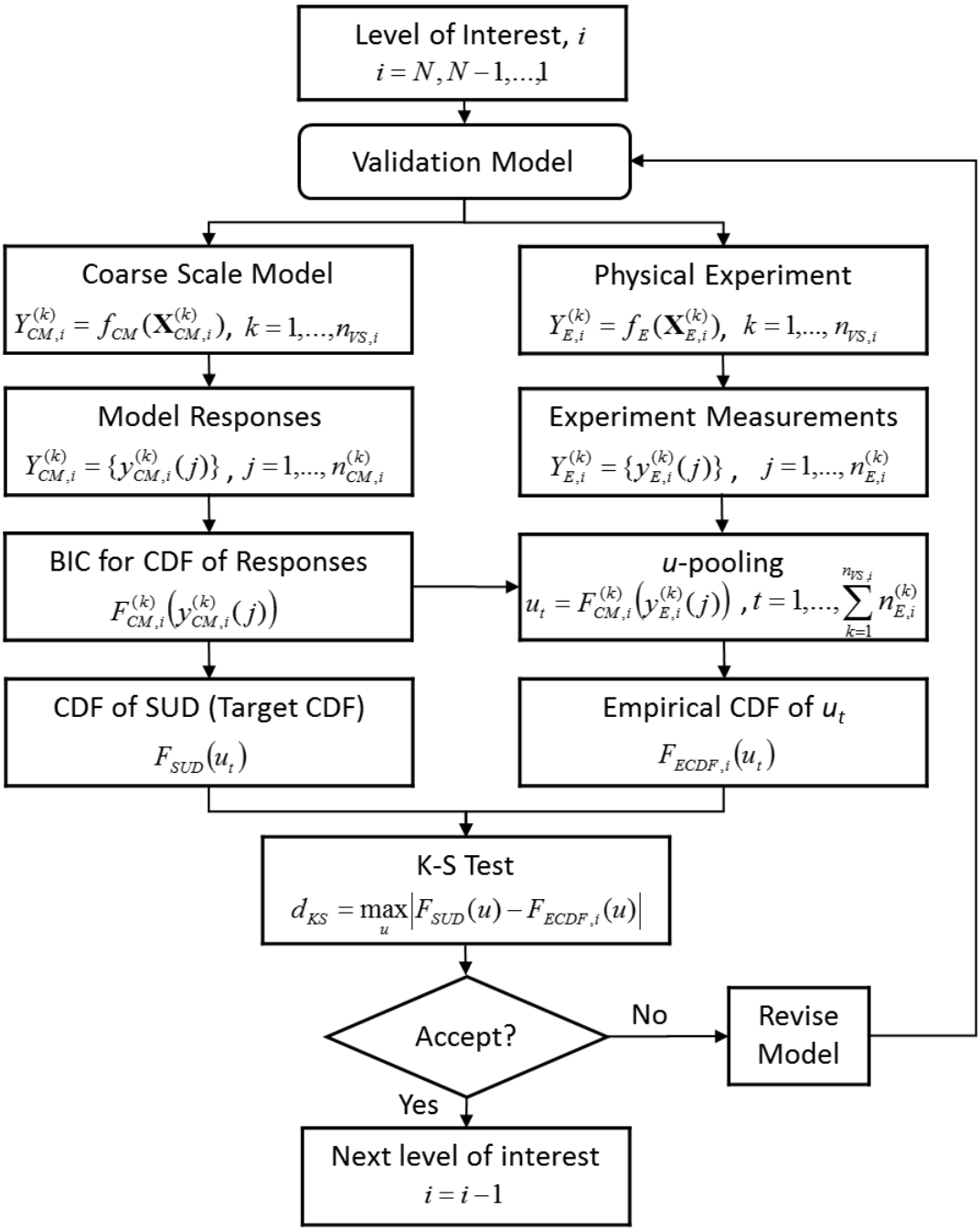

Figure 4.2. Flowchart of the proposed validation step

The proposed validation step has five steps as follows:

Step 1: Once the upscaling step is completed at the i^{th} scale level in the validation pyramid, the validation model is determined. The validation model is expected to be different from the model used in the upscaling step to challenge the prediction model.

Step 2: On the right side of the flowchart in Figure 4.2, the physical experiments are conducted for each validation site $k = 1,...,n_{VS,i}$. If the physical experiments are available, the observation data set $Y_{E,i}^{(k)} = \{y_{E,i}^{(k)}(j)\}$ are collected where $j = 1,...,n_{E,i}^{(k)}$ and $n_{E,i}^{(k)}$ denotes the number of experiments at the k^{th} validation site. If physical experiments are not available, a fine scale model of the validation model that is known as ground truth is generated as the pre-validation model. Then the fine scale model responses $Y_{FM,i}^{(k)} = \{y_{FM,i}^{(k)}(j)\}$ are collected as the experimental data of the pre-validation step where $j = 1,...,n_{FM,i}^{(k)}$ and $n_{FM,i}^{(k)}$ denotes the number of fine scale model simulations at the k^{th} validation site.

Step 3: On the left side of the flowchart in Figure 4.20, for each validation site, the computational model (i.e. the coarse scale model) is simulated for the validation model with homogenized properties obtained from the upscaling step. The coarse scale model responses $Y_{CM,i}^{(k)} = \{y_{CM,i}^{(k)}(j)\}$ are collected where $j = 1,...,n_{CM,i}^{(k)}$ and $n_{CM,i}^{(k)}$ denotes the number of coarse scale model simulations at k^{th} validation site. Then, the CDF models of the coarse scale responses at each validation site are constructed, i.e. $F_{CM,i}^{(k)}\left(y_{CM,i}^{(k)}(j)\right)$. The BIC method is proposed to use for estimating the best fitted distribution model to the coarse scale responses at each validation site.

Step 4: The u-pooling method is utilized to calculate the u-values of the experimental observations from the CDF models of the coarse scale responses predicted by BIC, i.e.

$u_t = F_{CM,i}^{(k)}\left(y_{E,i}^{(k)}(j)\right)$. Then, all of the u-values are transformed into one distribution using the ECDF formulation given in Eq. (2.6) and the ECDF of u-values is obtained as $F_{ECDF,i}(u_t)$.

Step 5: The ECDF of u-values $F_{ECDF,i}(u_t)$ is compared with the CDF of the SUD $F_{SUD}\left(Y_{CM,i}^{(k)}\right)$ based on the validation metric (i.e. the K-S test). The maximum vertical distance between these two distributions is calculated as the K-S test statistic. If the predicted CDF is accepted based on the K-S test, then the coarse scale model and its homogenized input parameters obtained in the upscaling step are passed onto the next level of interest in the multi-level validation approach. Otherwise, the assumptions of computational models at the current level are revised until accurate predictions are made.

4.3. Validation Example 1 - CLS fabricated by FDM

The proposed multi-level upscaling and validation framework is applied for the elastic material property characterization of an AM-fabricated CLS described in Section 3.4.5. For this example, only 0^0 lattice structure shown in Figure 3.17(a) fabricated in a material extrusion process (i.e. Stratasys® Fortus 400mc FDM machine) using ABS-M30 material is considered. The specimens are made of a space-filling polyhedral, the so-called simple cubic (SC) cell, which has vertical and horizontal struts in a cubic cell as shown in shown in Figure 3.17(a). Each cell has dimensions of 5×5×5 mm with 1.5 mm strut diameters and fills a space of 20×20×50 mm in the specimen.

In the example in Section 3.4.5, only the geometric uncertainties on the fabrication of layers were considered. Along with geometric uncertainties, the irregularities in the material properties at strut level are also needed to be taken into account for a better representation of the CLS with the FE modeling techniques. Hence, in this study, a modeling process is developed that considers

both the geometric and material irregularities at strut level. The proposed multi-level validation approach is used to quantitatively assess the predictions made by the models for predicting the effective elastic properties of the CLS. With accurate model predictions, it would be possible to reliably use the multiscale models in engineering design.

The ultimate goal of the multi-level upscaling and validation approach for this example is to be able to consider the mesoscale level (i.e. strut level) geometric and material imperfections and uncertainties when modeling the SC cellular lattice structure (SC-CLS). Eventually, each SC cell in the structure will be modeled as a solid continuum element with homogenized elastic properties so that the computational cost can be decreased when designing engineering parts using lattice materials while still considering the uncertainties at the finer scale levels. In the application of multi-level upscaling process for this CLS example, two different scale levels are considered. At the mesoscale level (i=2), the individual struts are modeled with detailed variations, while at macroscale level (i=1), the lattice cell is modeled using the homogenized strut properties with uncertainties propagated from the strut level. To show the applicability of the proposed validation approach, two computational model alternatives are considered at each scale level. The first models for both mesoscale and macroscale levels correspond to the models that were used in the multi-level upscaling of the CLSs presented in Section 3.4.5. That is, only the geometric irregularities at strut level are considered in the first models. The second model at strut level includes also the material imperfections. The details of the computational models used in the upscaling and validation process at each level are given in the following subsections.

4.3.1. Computational Models used in the Proposed Framework

4.3.1.1. Strut level (mesoscale level) models

The flowchart of developing the fine scale models of the struts is shown in Figure 4.3. There exist two strut models considered in this study. The first model is called *Strut Model 1*, which consists of only the geometric uncertainties (i.e. Steps (1)-(4) in Figure 4.3). As stated in Section 3.4.5, there exist uncertainties in the geometry of struts because the cross-sectional area of the struts that make the unit cells is not perfectly constant when fabricated by AM processes. They vary within a certain range depending on the parameters that are used during the AM process. Thus, the diameter of each cross-section for each layer deposited in the FDM process, the angle of the strut about the X and Y axis, and the deviation of the FDM printing tip in the X and Y axis are considered as the uncertain input geometry variables for the fine scale model of *Strut Model 1* with the quantified uncertainties listed in Table 3.6.

For *Strut Model 1*, deterministic elastic material properties of the ABS material are used at each simulation in the sampling procedure. That is, the mean values of the material properties given in Table 3.6 are used in the fine scale FEA, but the material uncertainties, such as the variation of material properties and porosity, are not included. Thus, only the effect of geometric uncertainties are considered to find the homogenized diameter of the struts in the upscaling process. A fine scale FE modeling technique that fills each deposited layer of the fabricated strut with voxel elements (i.e. 8-node brick elements) is used to accurately model the geometric uncertainties in the strut cross-sections as shown in Figure 4.3. Once the voxel model is generated with geometric uncertainties, FE simulation of the model is performed.

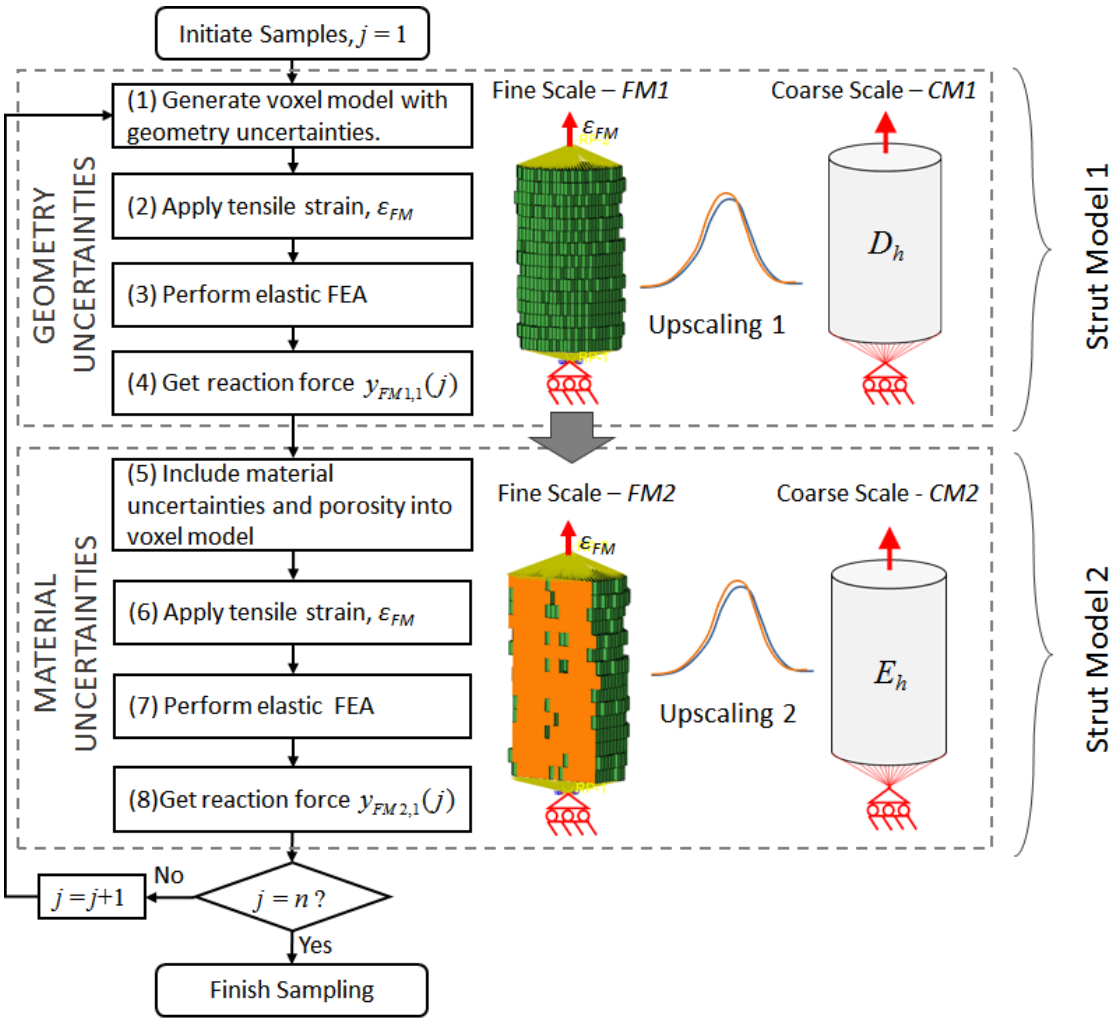

Figure 4.3. Flowchart of the strut level fine scale model generation process

Strut Model 2 includes also the second type of irregularities, i.e. the material imperfections such as porosity that occurs due to the path the material extrusion process follows. The material microstructure is simplified to contain voids in the strut that are considered to arise during the fabrication process using the material extrusion process. In addition, the porosity occurs inside the struts after the outer circumference of each layer is deposited. To mimic this behavior of material extrusion, the porosity is included as voids that are equivalent to the size of voxel elements, as illustrated in the second part of Figure 4.3. (i.e. in steps (5)-(8)). The coordinates for the center

point of each void are randomly generated such that the voids will be one thickness value inside the outer circumference at each deposited layer. Then, the corresponding voxel elements covered by these voids are automatically taken away in the finite element model. In this study, it was assumed that the struts fabricated by the FDM process have 15% porosity with a coefficient of variation (COV) value of 0.1. The porosity of the strut is simply calculated by the fraction of the total volume of the voids in the strut to the total volume of the strut model. The random void generation and element removal process are preformed until the target porosity value is reached for each sampling point. Although attributes such as orientation and circumference for irregular voids are ignored, the simplified model with voids still allows for accurate determination of the effective elastic material properties. In addition to the porosity, the material properties of the strut FE model (i.e. elastic modulus and Poisson's ratio) are assumed to have uncertainty with the statistical parameters given in Table 3.6.

For *Strut Model 2*, the modeling process starts with the generation of the strut by considering only the geometric uncertainties, i.e. steps (1)-(4) in Figure 4.3. The strut FE model generated in the first part with geometric uncertainties is retained and material properties of the voxel elements are changed based on the uncertainty of the material properties in steps (5)-(8) in Figure 4.3. A stratified sampling scheme, LHS, is used to generate *n* number of sampling data for the uncertain parameters. All uncertain input variables given in Table 3.6 are assumed to be following a normal distribution. Their standard deviations can be determined by multiplying their mean values by the corresponding COV values the variables.

For both *Strut Models 1 and 2*, one of the planes in the loading direction was displaced such that a homogenized strain of $\varepsilon_{FM} = 0.1\%$ is created in the strut FE model. The plane opposite to the displaced plane is fixed in the direction of the load to achieve tensile test simulation. A

relatively small length of strut, i.e. L_{strut} = 2.5 mm, is considered to reduce the computational complexity. The thickness and length of the strut was considered as deterministic variables as it was found that the change of these does not affect the response.

Ultimately, the total reaction force on the top face of the strut model is obtained from the FE simulation for each sampling point as the fine scale output denoted by $y_{FM\,1,1}(j)$ for *Strut Model 1* and $y_{FM\,2,1}(j)$ for *Strut Model 2*. Once the fine scale responses are obtained for each strut model, the stochastic upscaling method is used to determine the homogenized diameter and elasticity modulus of the struts. The struts are modeled by using beam elements for the homogenized coarse scale model in the upscaling process. Both the homogenized diameter and elasticity modulus are projected onto a 2nd order PCE in the upscaling process. *Strut Model 1* (i.e. the model with only the geometric uncertainties) is used first to determine the homogenized diameter for each strut model with different angles. Then, *Strut Model 2* (i.e. the model with both geometric and material uncertainties) is used to determine the homogenized elasticity modulus for each strut model.

4.3.1.2. Lattice level (Macroscale level) models

At the macroscale level, the homogenized properties from the strut level are passed onto two different fine scale models generated using the commercial FEM software. For *Lattice Model 1*, the fabricated CLS shown in Figure 4.4(a) is modeled using beam elements as the fine scale model as seen in Figure 4.4(b). It should be noted that the struts on the outer faces of the CLS are fabricated such that their cross-sections are semicircles as seen in Figure 4.4(a). It is usually difficult to model the strut with a semicircle cross-section using beam elements as the available cross-section models in Abaqus include the modeling option of entire circular cross-section. To simplify the modeling process of these struts on the outer faces of CLS for *Lattice Model 1*, the

cross-sections of these struts are modeled as full circles with the half of the corresponding strut diameter values. Moreover, the beam elements cannot account for the details of the connection points of the struts as seen in Figure 4.4(b). These drawbacks of the beam elements can be eliminated when solid continuum elements are used instead of the beam elements. Hence, for the *Lattice Model 2*, the CLS is modeled by 3D solid elements as seen in Figure 4.4(c). For both modeling techniques, one of the planes in the loading direction was displaced such that a strain of 0.1% is created in the CLS models. The plane opposite to the displaced plane is fixed in the direction of the strain to mimic the tensile test. Thus, only the mechanical properties associated with loading in the loading direction are presented.

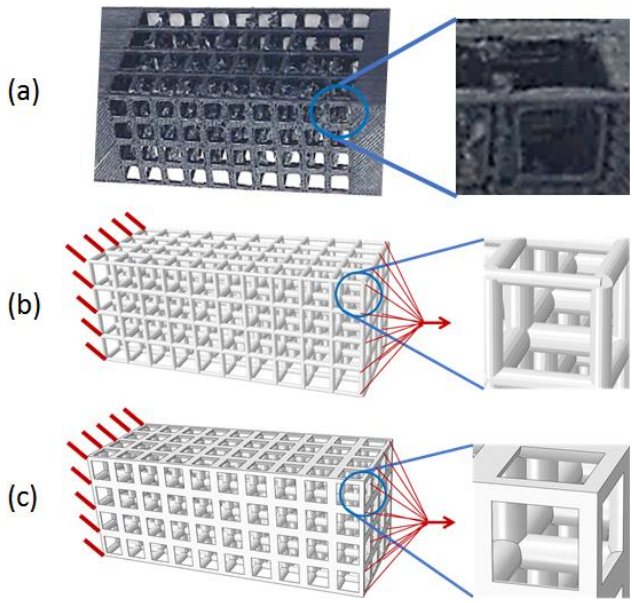

(a) Fabricated CLS (b) *Lattice Model 1* with beam elements (c) *Lattice Model 2* with solid geometry.

Figure 4.4. FE models of the CLS specimen

The FE model of the entire CLS with solid continuum elements is computationally very expensive. Hence, a lattice cell model that can represent the entire structure with a smaller number of unit cells is desired for *Lattice Model 2*. To determine the smallest fine scale *Lattice Model 2* size that

gives accurate results, a convergence study is performed with the different number of unit cells. The deterministic effective elastic modulus of the SC lattice material with 1.5 mm strut diameter is calculated for models having a different number of SC cells. Periodic boundary conditions (PBCs) are applied on the unit cell FE model. PBCs force the displacements of the nodes on each surface to be the same as those of the corresponding nodes on the opposing face; thus, representing the spatial periodicity of the deformation field of the entire structure for a unit cell model. A strain of 0.1% is applied in one direction to simulate the tensile test. Quadratic tetrahedral elements are used to mesh the structure. The effective elastic modulus is calculated for a corresponding coarse scale model with hexagonal solid elements that has the same size as the unit cells for each model and compared in Figure 4.5.

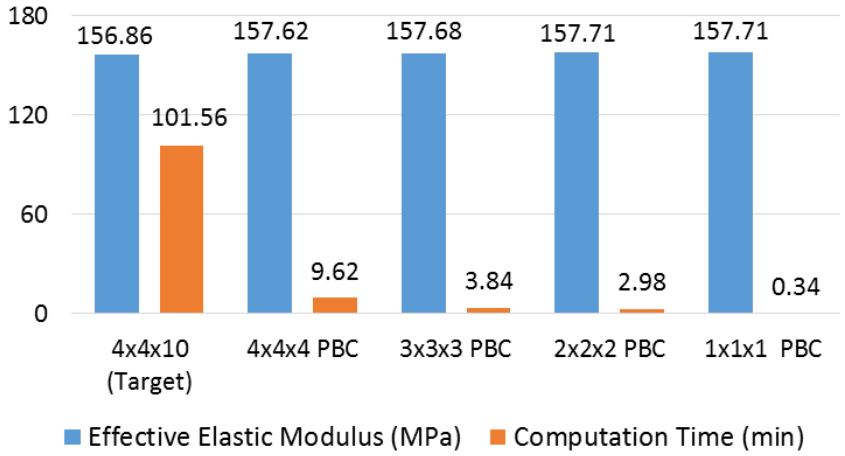

Figure 4.5. Results for solid element-based CLS models with different number of SC cells.

One can see that the simulation time of the entire model (i.e. 4×4×10) is significantly higher than that of the other models (~101 min). The computation time can be decreased by a smaller model with PBCs as seen in Figure 4.5. In addition, it is seen that all models provide similar results to the target model of the entire structure for the effective elastic modulus. Based on these results, since the model with one-unit cell has a very small computation time value, it is determined for *Lattice*

Model 2 that only one-unit cell model will provide sufficient accuracy when predicting the effective elastic modulus of the lattice structure under tensile test conditions.

A mesh convergence study is also conducted to determine the optimal size of the mesh elements. The computation time and effective elastic modulus values are given Figure 4.6 for various mesh sizes. It was found based on these results that a mesh size of 0.375 mm is appropriate, as the computation time increases dramatically for smaller mesh size values while the elastic modulus results converge. This mesh size corresponds to the quarter of the dimeter (i.e. 0.25×D). This mesh size is used when modeling the unit cell with solid elements.

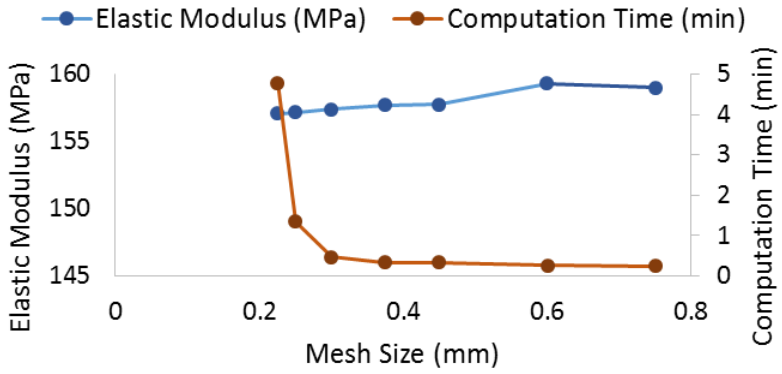

Figure 4.6. Mesh convergence of unit cell FE model with quadratic tetrahedral elements.

4.3.2. Results of Upscaling and Validation Steps

4.3.2.1. Results at strut level

For the predictions of *Strut Model 1*, (i.e. strut model with only geometric uncertainties), the homogenized diameters, that were previously found by using the upscaling method for seven different rotation angles (i.e. 0˚, 15˚, 30˚, 45˚, 60˚, 75˚, 90˚ strut angles) are compared with experimental measurements in Figure 3.24. These experiments at different validation sites (i.e. different rotation angles) can be pooled into one distribution the using u-pooling method. Thus,

this example shows how the number of experiments can be increased in validation process by using multiple validation sites. There are $n_E^{(k)}$ = 10 experimental measurements for each strut with different rotation angles (i.e. for each validation site) obtained using a digital caliper from the fabricated CLS in different angles. Thus, there are $n_{VS,1}$ = 7 validation sites and n_T = 70 measurements in total.

Once the distribution type and statistical parameters are determined using the BIC method after upscaling the homogenized diameters, the u-pooling method is utilized to pool all of these experimental measurements into one global metric. In the u-pooling process, the CDF values of the measured diameter values (i.e. *u* values) are calculated by using the corresponding model CDF determined by BIC in Table 3.8 at each validation site. As mentioned earlier, it is expected according to the u-pooling method that the ECDF of these *u* values of the experimental data should follow a uniform standard distribution CDF if the prediction models are accurate. ECDF of the experimental measurements is compared with the SUD in Figure 4.7.

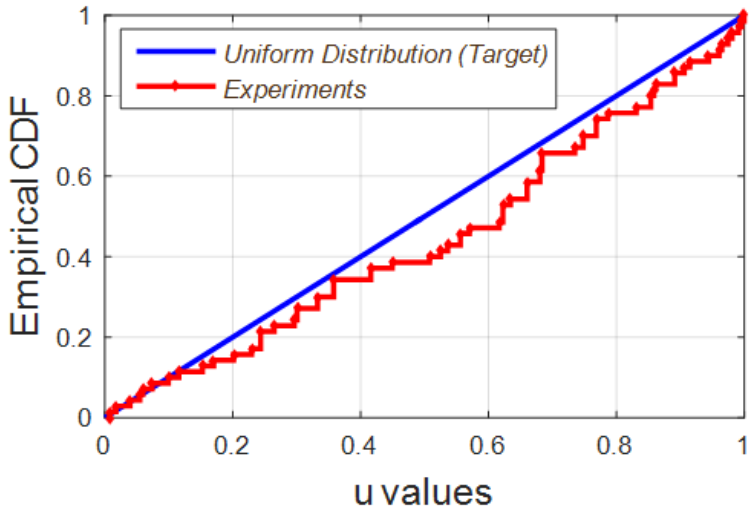

Figure 4.7. ECDF plot of u-pooling results for homogenized diameters for *Strut Model 1*.

Both the maximum distance and area metric between the target SUD and the ECDF of the *u* values were calculated in this study to compare the decision results made by the K-S test and the area metric. For the area metric, a threshold value of 0.1 is determined to make a decision about the model predictions. The maximum distance was calculated as 0.1454 for the K-S test while the area metric was calculated as 0.0561. Since the area metric value is less than the threshold value of 0.1, the predictions made by *Strut Model 1* is accepted. Similarly, the computational CDF models are not rejected by the K-S test based on the maximum distance with a significance level of 0.05. Hence, it is concluded that the predictions made by *Strut Model 1* and the upscaling step can be used at the lattice level.

For *Strut Model 2*, the uncertainty in the material properties and material porosity are also introduced to the fine scale models. Since the homogenized diameter values are determined for *Strut Model 1*, only the homogenized elastic modulus are determined for *Strut Model 2*. The upscaling is performed to find the homogenized elasticity modulus values for only 0˚ and 90˚ struts because the target CLS for this study only have struts with these rotation angles. Once the upscaling completed, the predictions made by coarse scale model with these homogenized diameter and elastic modulus is to be validated. However, there are no experiments at the strut level to validate the predictions made by the coarse scale model with material uncertainties. Hence, the proposed pre-validation step is used to increase the confidence in the predictions of the model. In that regard, the fine scale strut model with material and geometry uncertainties is considered as the ground truth model in the pre-validation step as illustrated in Figure 4.8. The pre-validation model is determined as a longer strut model with a strut length of L = 10 mm than the upscaling model. In the pre-validation model the bottom end of the strut was fixed in all directions to have a different scenario from the model used in the upscaling process. The tensile strain is applied on

the top end surface of the strut model and the lateral movements of the top surface are also fixed. If the homogenized properties are predicted with sufficient accuracy, the coarse scale model simulation should give close predictions to the predictions of the pre-validation fine scale model with the same boundary and loading conditions.

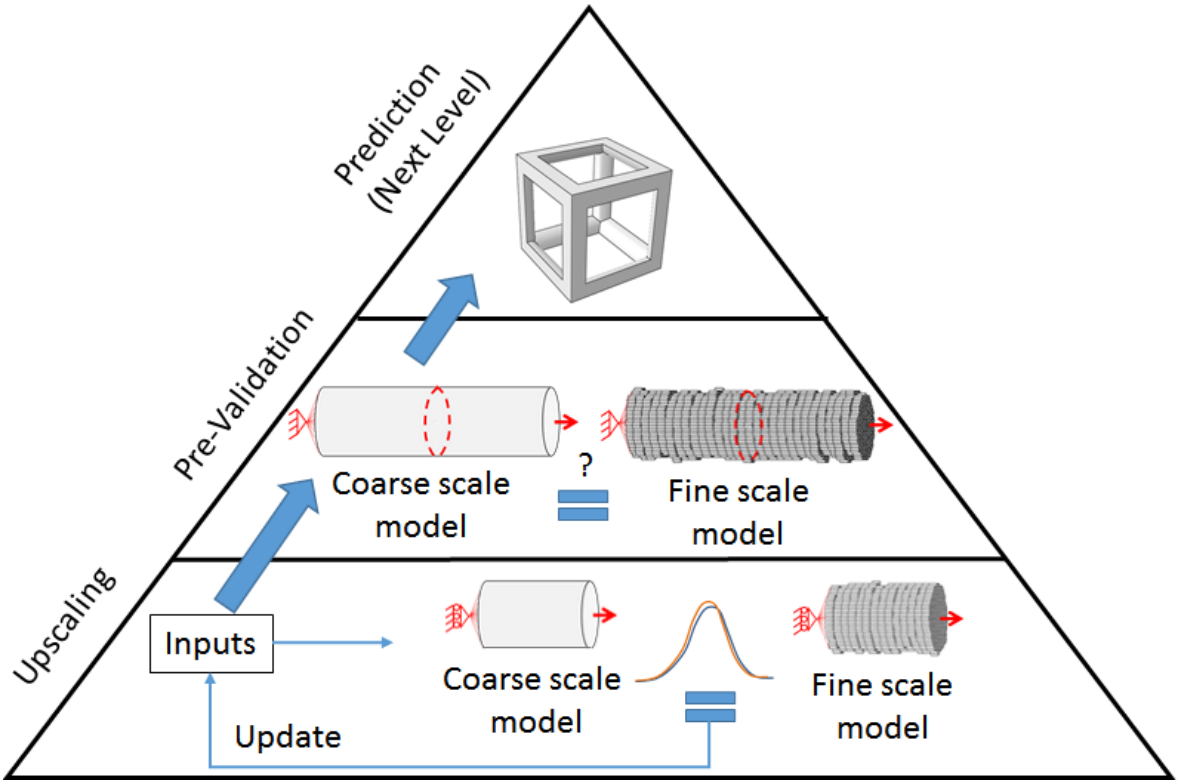

Figure 4.8. Validation pyramid for strut level with pre-validation step

The coarse scale model considered to represent this pre-validation fine scale model is generated with the same length using two different modeling techniques, i.e. beam elements and solid quadratic tetrahedral elements with constant diameter throughout the strut. Solid elements are used instead of a beam element, which is used in the coarse scale model of the upscaling process, because at the next level (i.e. at the lattice level), the same type of solid elements are considered to model the lattice cells. Since 0.25x*D* has been determined as the optimal mesh size for the lattice

structure, the same mesh size is used to model the strut at coarse scale. The optimal distribution types and statistical parameters for homogenized elasticity moduli are predicted as listed in Table 4.1 using BIC method to use in the pre-validation coarse scale models.

Table 4.1. Static parameters for homogenized elastic moduli at strut level.

Structure	***Mean (MPa)***	***Standard Deviation***	***Distribution***
0° Strut	1608.707	67.664	Lognormal
90° Strut	1698.362	71.489	Lognormal

The tensile test simulations were performed for both 0˚ and 90˚ struts and the reaction force values were obtained for each simulation. Only $n_{FM,1}^{(k)} = 50$ simulations were performed for the fine scale model of the pre-validation step due to the increased computational complexity when L=10 mm. Thus, $n_{VS,1}$ = 2 validation sites and n_T = 100 pre-validation measurements were found in total. To compare the effectiveness of the area metric and the K-S test depending on the number of experiments, the number of fine scale simulations for each pre-validation site was decreased to $n_{FM,1}^{(k)} = 10$ (i.e. n_T = 20) and $n_{FM,1}^{(k)} = 20$ (i.e. n_T = 40). At a coarse scale, $n_{CM,1}^{(k)} = 200$ simulations were performed and BIC was used to predict the distribution types and the statistical parameters of the reaction force values. The u-pooling method was used again to predict the CDF values (i.e. u values) of the fine scale responses. The ECDF of the u values are plotted in Figure 4.9 and the decision results are listed in Table 4.2 for three different n_T values. The area metric threshold is reduced to 0.05 for this pre-validation step since the fine scale model is used as the ground truth model.

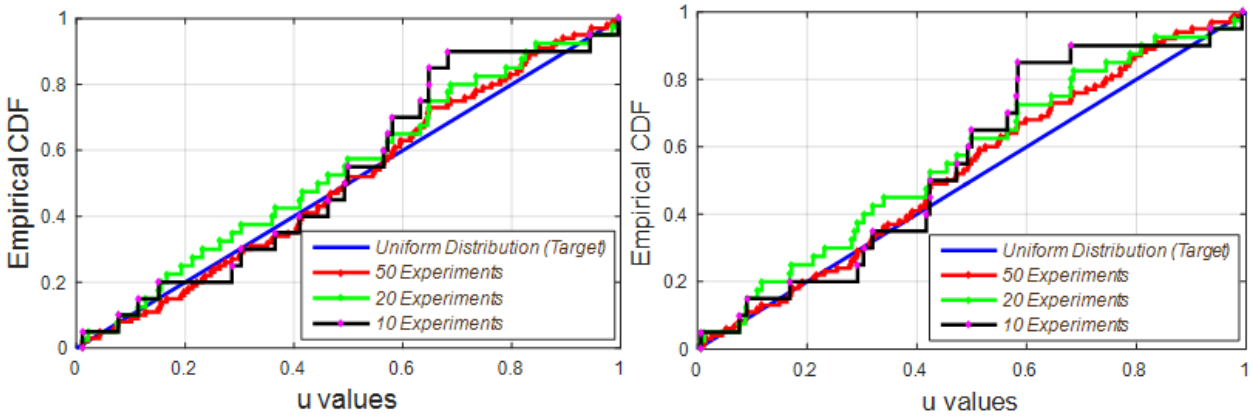

(a) (b)

(a) Results for *Strut Model 1* (i.e. beam element model at the coarse scale), (b) Results for *Strut Model 2* (i.e. solid quadratic tetrahedral element model at the coarse scale).

Figure 4.9. ECDF plots of u-pooling results for the pre-validation step

Table 4.2. Decision results for pre-validation step

	n_T	*Maximum Distance*	*p-value*	*Area Metric*	*K-S Test Decision*	*Area Metric Decision*
Beam Element Model	20	0.2171	0.2621	0.0553	Accept	Reject
	40	0.1117	0.6591	0.0420	Accept	Accept
	100	0.0821	0.4848	0.0256	Accept	Accept
Solid Element Model	20	0.2659	0.0974	0.0734	Accept	Reject
	40	0.1409	0.3701	0.0656	Accept	Reject
	100	0.0859	0.4275	0.0343	Accept	Accept

The CDF plots in Figure 4.9 and the maximum distance and area metric results in Table 4.2 for both coarse model techniques reveal that the prediction model is getting closer to the target distribution with an increasing number of experiments. This means that a favorable prediction was

made by the coarse scale models even if the number of experiments are 20; otherwise, the results would not approach to the target distribution. That also means that the metric distance should follow an increasing trend when the number of experiments are decreased if the predictions are correct. For the highest number of experiments (i.e. $n_T = 100$), the prediction model is accepted by both the area metric and the KS-test. If the predictions were accepted for the highest number of experiments, it is expected that the predictions made for a smaller number of experiments should also be accepted because the predictions are close the target distribution for a high number of experiments. However, when the number of experiments decreases, the area metric (the existing method) rejects the models because the resulting metric value becomes greater than the threshold value of 0.05 as seen in Table 4.2. In other words, these were rejected because the threshold value is the same for all three cases while the metric value increased with the decrease of number of experiments.

On the other hand, the K-S test in the proposed method accepts all three cases since the decision is made based on the number of experiments. That is, when a smaller number of experiments exists, the K-S test increases the threshold value as expected. In the area metric, on the other hand, the decision criterion value is 0.05 for all cases. Therefore, the models with a smaller number of experiments are rejected. The decision maker has to make a subjective change in the threshold value if the available number of experiments is a small number. However, since the K-S test considers the number of experiments in the decision criterion, it provides an unbiased decision without requiring further change of the criterion. These results show the effectiveness of the K-S test over the area metric in terms of the dependency on the number of experiments. Hence, according to these results, the coarse scale model predictions can be accepted using K-S test even if the number of experiments are very small as expected. Moreover, since both the beam element

model and the solid element model provide very close results to the fine scale model and accepted by both K-S test and area metric for n_T = 100, it is concluded that the predicted homogenized properties with upscaling process can be used for both coarse scale models at the next level (i.e. at the macroscale level) for lattice upscaling process.

The model selection capability of K-S test metric (i.e. maximum distance metric) and area metric is investigated next. At the pre-validation step, better predictions are expected to be made when beam elements are used as the coarse scale model compared to the solid element model simply because the same beam element model is used in the upscaling process to predict the homogenized properties. As seen in Table 4.2, for 100 experiments, both the maximum distance metric and the area metric values, calculated for the beam element model predictions, are lower than those calculated for the solid element model predictions. That means the beam element model makes better predictions than the solid model as expected. However, the maximum distance metric values calculated for beam element and solid element model predictions are so similar (i.e. 0.0821 and 00859, respectively). The reason of similar values when using the distance metric is that the maximum distance considers the point that has the maximum distance. Area metric, on the other hand, gives a distinctive difference when metric values are compared for both models (i.e. 0.0256 for beam element model and 0.0343 for solid element model) since the entire distribution is considered. Hence, based on area metric values, it is clear that the beam element model makes better predictions than the solid model.

Area metric provides a more reliable comparison among different model predictions since it considers the entire distribution in calculation of the metric. The advantage of area metric, which is shown in existing studies as its capability of choosing the best among multiple models [106], [107] is proven in this example as a discernible difference is obtained between both models.

Another advantage of the area metric in model selection is that the area metric can be back-propagated to the actual unit of the response to investigate the deviation of the model results from the experimental observations, as introduced by Ferson et al [110]. Thus, it is concluded based on these observations that K-S test should be used to accept or reject models due to its dependency to the number of experiments while area metric should be used if deciding among multiple models accepted by the K-S test. Finally, although the beam element model makes better predictions according to the area metric, rather than selecting one of those, both model predictions are passed onto the next level to compare prediction results with the real physical experiments at lattice level.

4.3.2.2. Results at lattice level

As mentioned previously, in *Lattice Model 1*, the entire CLS is modeled using beam elements, while a unit cell model is generated using solid continuum elements in *Lattice Model 2* at the fine scale. The number of samples is determined as $n_{FM,1}^{(k)} = 200$ for the fine scale simulations at lattice level for both *Lattice Model 1* and *Lattice Model 2*. In the multi-level upscaling process, three different modeling approaches were utilized: In the first modeling approach, the homogenized diameter values, obtained from *Strut Model 1* and given in Table 3.8, are used in *Lattice Model 1*. The material properties are assumed to be deterministic, which means no material property uncertainty effect occur at strut level. In the second and third modeling approaches, both the homogenized diameters and elastic moduli obtained from *Strut Model 2* are used in *Lattice Model 1 and Lattice Model 2*, respectively. The homogenized elastic moduli given in Table 4.1 are used in the fine scale model. Once the reaction force distribution is obtained from the fine scale simulations at the lattice level, the upscaling procedure is utilized to obtain the homogenized elastic modulus (E_h) of the SC lattice cell. For the coarse scale model used in the upscaling process, each

SC cell is represented by a solid hexahedral continuum element that accepts the homogenized elastic modulus as the material property. Once the upscaling process is completed, the distribution type and statistical parameters of the homogenized material properties are predicted using the BIC method and are listed in Table 4.3.

Table 4.3. Statistical parameters for homogenized material properties at lattice level.

Model	*Variable*	*Mean*	*Standard Deviation*	*Distribution*
Strut Model 1 - Lattice Model 1	E_h	131.6355	0.3727	Lognormal
Strut Model 2 - Lattice Model 1	E_h	110.5065	2.9409	Normal
Strut Model 2 - Lattice Model 2	E_h	115.4676	5.5123	Lognormal

Once the upscaling process is completed at lattice level, the next step is the validation of the coarse scale model results with the experiments for the tensile test specimen as shown in Figure 4.10. For the validation step at the macroscale level, there are $n_T = 3$ physical validation experiments for the SC-CLS specimens. The coarse scale validation model that corresponds to the experiment model, at the validation step, is generated with hexahedral solid elements using the homogenized elastic moduli in Table 4.3 estimated by the upscaling step at the lattice level.

Since the coarse scale model has solid hexahedral elements corresponding to each SC cell in the CLS, a large sampling size can be generated with trivial computational cost. Hence, the distributions of the reaction force of the coarse scale models are obtained from 200 simulations. BIC is used to predict the distribution of the reaction force for each coarse scale model. Then, the u-pooling results of the experimental measurements are determined using the distributions of each prediction model. The decision results are given in Table 4.4 for both the K-S test and area metric;

the distributions are shown in Figure 4.11. A threshold value of 0.1 is considered for area metric to make a decision.

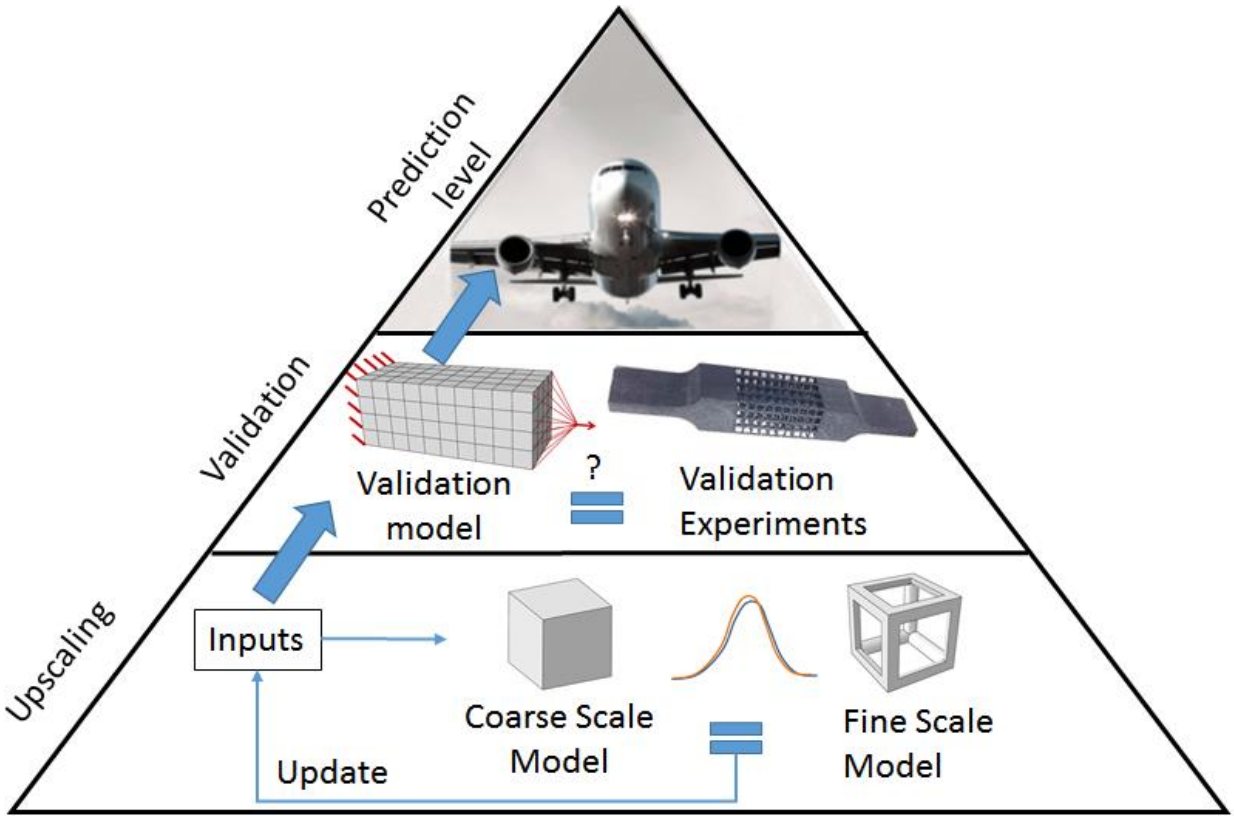

Figure 4.10. Validation pyramid at lattice level

Table 4.4. Decision results of macroscale level validation

Model	*Max. Distance*	*p-value*	*Area Metric*	*KS-Test Decision*	*Area Metric Decision*
Strut Model 1 – Lattice Model 1	1	1.1E-16	0.5	Reject	Reject
Strut Model 2 – Lattice Model 1	0.5940	0.1527	0.2877	Accept	Reject
Strut Model 2 – Lattice Model 2	0.5026	0.3274	0.1794	Accept	Reject

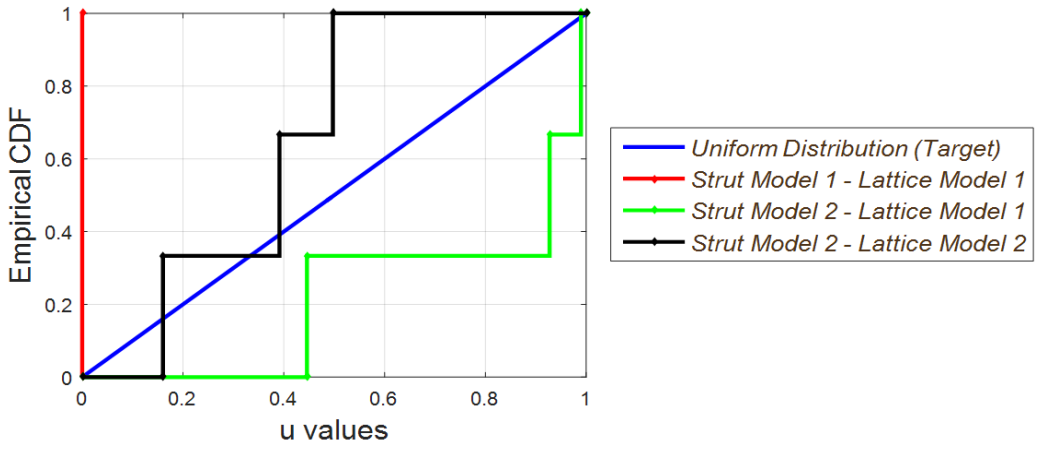

Figure 4.11. ECDF plots of u-pooling results used in validation.

As can be seen in Figure 4.11, the predictions made by both *Lattice Models 1* and *2* that use *Strut Model 2* follow the target distribution despite the small number of experiments. *Lattice Model 1* that uses *Strut Model 1*, however, fails to follow the target distribution. The results in Table 4.4 reveal that this model is rejected by both decision criteria. The reason that *Strut Model 1* is rejected is that no material imperfections and uncertainties at the strut level are considered in the modeling process. Therefore, the predicted mean value of the homogenized elasticity modulus (E_h = 131.64 MPa) is found to be far greater than the other model predictions as also seen in Table 4.4. These results also show that *Strut Model 2* gives more favorable predictions at the lattice level as the CDF's obtained by using the predictions made by *Strut Model 2* follow the target SUD as seen in Figure 4.11. These results also support the decision made at the pre-validation step of mesoscale level since at the pre-validation step the predictions of *Strut Model 2* have been accepted while *Strut Model 1* predictions were rejected. Hence, it can be concluded that even though the strut level experiments were not available for *Strut Model 2*, the pre-validation step at mesoscale gives an initial judgement about the model appropriateness. Then, the macroscale level validation step provides the final judgement for the validation of the models.

In addition, the results in Table 4.4 indicate that the area metric rejects all models if 0.1 is used as the threshold value. However, as stated earlier, the prediction CDF's shown in Figure 4.11 based on *Strut Model 2* follows the target distribution, as expected from a true prediction model. In fact, if a few number of samples were drawn from a distribution and their CDF was plotted, a very similar result to the CDF's of the lattice models based on *Strut Model 2* would be obtained. In that case, since the samples were drawn from the actual distribution, the CDF would follow the target distribution with a large stair shape, as the CDF of the lattice models based on *Strut Model 2* follows in Figure 4.11. Hence, it is expected that the predictions made by *Strut Model 2* are more likely to be accepted. The area metric threshold value of 0.1 must be increased by the user to take these observations into consideration for accepting these models. That is, a subjective evaluation of the results is required to change the threshold of area metric. The K-S test, on the other hand, accepted the predictions made by these models, as expected, since the decision criterion is adjusted in K-S test based on the number of experiments. Thus, these results reveal that the K-S test works well as an unbiased decision criterion in the proposed validation process due to its dependency on the number of experiments.

Finally, in this example, there are two accepted lattice models by K-S test that can be used for further predictions. A question that arises for this case is "which of these accepted models is more accurate?" To evaluate their accuracy, the area metric results can be compared as suggested in the strut level validation step where the predictions of the strut level models are evaluated. As seen in Table 4.4, the area metric value for *Lattice Model 1* is larger than that for *Lattice Model 2* (i.e. the fine scale lattice model with solid elements), indicating model 2 makes better predictions compared to the experimental results. The same result is obtained when the maximum distance metric values are compared; but, the difference is much larger for the area metric as in the case at

strut level, which proves again that area metric is more favorable to use for model selection. The reason of a greater metric value for *Lattice Model 1* could be that the beam elements cannot model the links of struts accurately. The structure stiffness is expected to be less than the actual since the links of the struts do not reflect the real part links when beam elements are used. Therefore, the homogenized elastic modulus of *Lattice Model 1* is lower than that of *Lattice Model 2* as given in Table 4.4. Thus, it is concluded that predictions made by *Strut Model 2* and *Lattice Model 2* (i.e. quadratic tetrahedral solid element-based modeling) should be chosen to model the lattice structure according to the proposed validation approach.

4.4. Validation Example 2 - CLS Fabricated by SLM

4.4.1. Materials and Methods

The recent advancements in metal-based AM technologies make it capable to fabricate strong, lightweight and complex lattice-based engineering structures. The SLM process gained interest for fabrication of metal CLSs since it enables the complete melting and fusing of the metal powder particles together to obtain almost fully dense parts. A laser source selectively scans a powder bed in the SLM process according to the CAD-data of the part to be produced. Different metal-based materials can be used in SLM such as titanium alloy (Ti6Al4V), stainless steel (SS316L), and aluminum alloy (AlSi10Mg), which will enable the design of customized CLSs.

The CLS specimens used in this example have body-centered cubic (BCC) lattice cells, which are comprised of diagonal struts that unite in the center of the cubic cell as shown in Figure 4.12(a). The strut diameter D and length L are modeled to be 0.5mm and 4mm, respectively for each BCC unit cell. The complete lattice structure has n=3 BCC cells in each direction, which

gives the overall dimensions of 12x12x12 mm^3. The corresponding lattice structure model, filled by 3x3x3 BCC unit cells, is modeled in the commercial FE modeling software Abaqus as shown in Figure 4.12(b). This BCC lattice structure is fabricated using SLM 280 HL machine with Al10SiMg material powder (also called CL31) and with 50 μm layer thickness as seen in Figure 4.12(c).

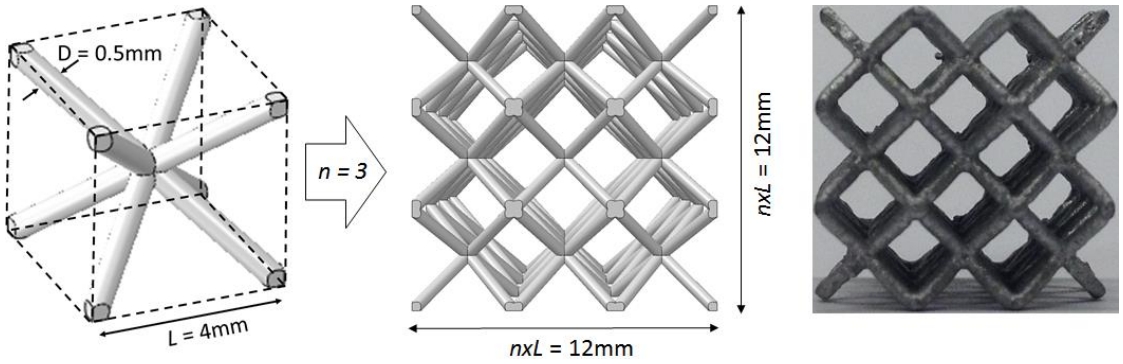

(a) BCC lattice cell, (b) CAD model of the test sample, (c) SLM-fabricated CLS with repeating BCC cells.

Figure 4.12. The CLS specimen designed with BCC lattice cells

In the previous example in Section 4.3, the uncertain input variables at the smallest scale level (i.e. at strut level) are assumed to have normal distributions, which may not be realistic. A through uncertainty quantification approach for the input variables is necessary before predicting the homogenized properties using the upscaling method. Hence, in this study, BIC method is utilized to quantify the strut level fine scale uncertainties induced by the AM process. Specifically, the 3D solid models of the fabricated struts are reconstructed using a computer tomography (CT) scanner (Zeiss metrotom 800, Georgia Institute of Technology, USA) to collect the statistical data for the uncertain input variables of the fine scale strut model. These strut level uncertainties are then used in combination with high resolution models that capture the real strut geometry and microstructure to predict the macroscale properties of the CLSs. Computer simulations and experimental

measurements, which are two interrelated approaches are used to gain knowledge of the strut level irregularities and porosity and their correlation to macroscopic strut properties. In that regard, a three-dimensional voxel–based model generation procedure was used to generate and simulate the strut fine scale models using the quantified uncertainties in a sampling method. The modeling process with quantified uncertainties enables the generation of the realistic strut models without using the fabricated strut specimens. Thus, the experimental cost at strut level can be minimized. The accurate knowledge and prediction of the overall mechanical properties, in particular the overall elastic modulus of the lattice material, is of considerable importance to the designer and is the primary focus of the present work.

4.4.2. Multi-Level Validation and Upscaling Framework

A strut model reconstruction process based on the CT-scan data is integrated into the multi-level upscaling and validation approach introduced in Section 4.1 to analyze the overall material properties of the lattice structures accurately accounting for the strut level uncertainties. The proposed multi-level validation framework, which is based on the concept of the validation pyramid approach, with the strut model reconstruction step is illustrated in Figure 4.13 for the application to the CLS described in the Section 4.4.1.

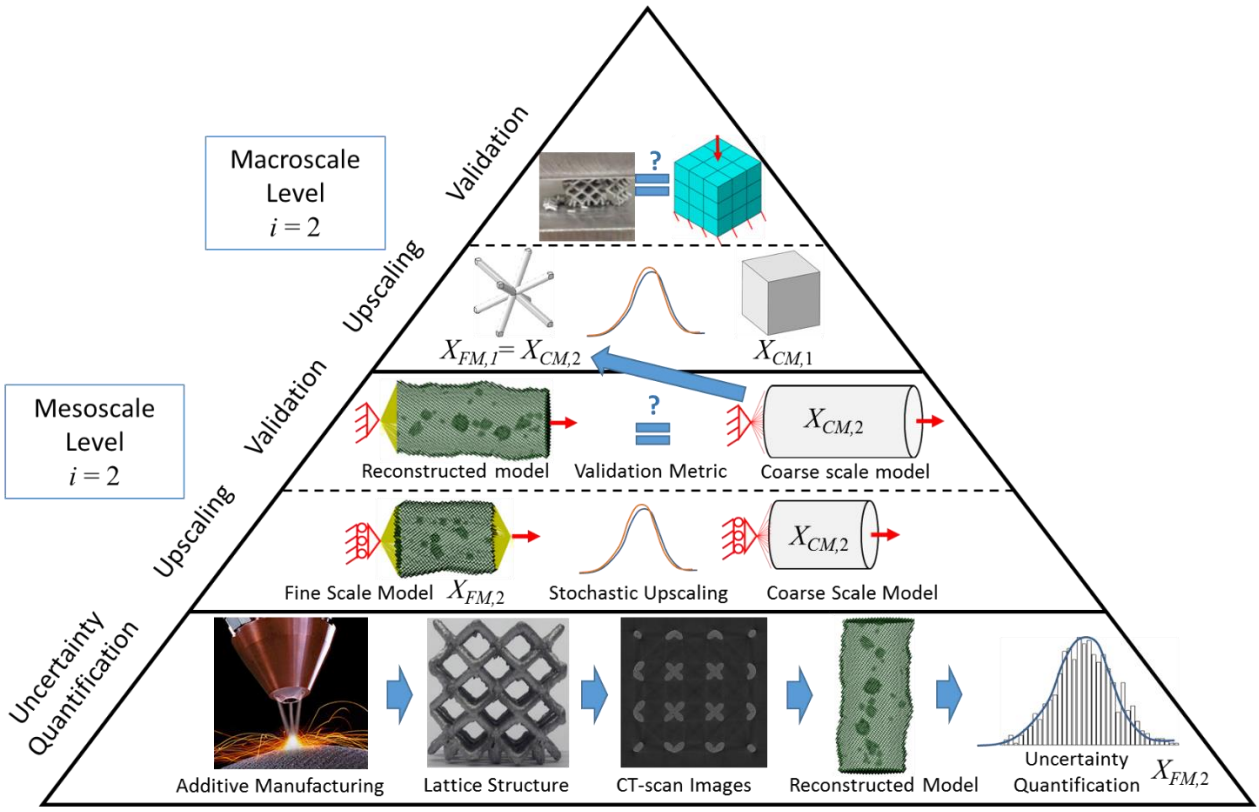

Figure 4.13. Validation pyramid for lattice structure with uncertainty quantification step at the bottom

In Figure 4.130, the lattice structure model is decomposed into multiple sub-levels as mesoscale level (i.e. strut level, $i = 2$) and macroscale level (lattice level, $i = 1$) to simplify the computational models. The multi-level upscaling process is used to pass the information at the finer scales to the macroscale level from bottom up. At the bottom of the pyramid the uncertainties of the material and geometric properties of the struts are quantified based on the strut models reconstructed from the fabricated parts using the CT-scan images. Once the statistical data are gathered for the strut properties from the measurements made on the reconstructed strut models, the BIC model selection method is utilized for uncertainty quantification of the gathered statistical data for the fine scale model input variables at the strut level. The strut fine scale model is generated using these quantified uncertainties and the FE simulations are conducted on this fine scale strut model. Then, the upscaling method is implemented at strut level to predict the homogenized coarse scale model

input variables denoted by $X_{CM,2}$. For the BCC lattice specimen, the homogenized diameter and the elastic modulus of struts are considered as the homogenized variables at strut level. For validation at strut level, the reconstructed models from the scanned images are simulated and the predictions are used as the pre-validation experimental data. The corresponding coarse scale models are generated with the predicted homogenized input variables and the validation process described Figure 4.2 is implemented to evaluate the validity of the coarse scale model predictions.

This process ensures that the generated strut model can mimic the reconstructed models, and thus the coarse scale model can be used at the lattice cell level with the homogenized strut level properties which become the fine scale model input variables, i.e. $X_{FM,1} = X_{CM,2}$. Once the upscaling method is utilized at lattice level to find the homogenized coarse scale model properties $X_{CM,1}$, the validation process described in Figure 4.2 is implemented at the top of the validation pyramid for the fabricated lattice specimens. The physical compression tests are conducted on the fabricated specimens and the experimental results are compared with the FEA results of the coarse scale model with predicted properties at the lattice level validation step. The details of these steps are given in the following sections.

4.4.3. CT Scanning and 3D model Reconstruction

The 3D model of the fabricated lattice structure is reconstructed through the scanned 2D slice images data using a reconstruction process depicted in Figure 4.14. The first step of this reconstruction process is to collect the 2D scanned images (Figure 4.14(a)). High resolution scans of the fabricated lattice structures were conducted using a computer tomography (CT) scanner (Zeiss metrotom 800, Georgia Institute of Technology, USA) at a resolution of approximately 13.53 μm. Prior to 3D model construction, it is necessary to perform image pre-processing for all

of these 2D slice images to ensure accurate quantification of the structure of the specimen. An appropriate segmentation algorithm is to be implemented to identify whether each pixel is occupied by solid or void in these 3D slice images. This segmentation process will allow to accurately model the porosity and the surface roughness of the struts in the structure. The solid and void phase can be distinguished by thresholding based on the gray level histograms of the images determined by the MATLAB Image Processing Toolbox since the difference between the densities of voids and solid part is large as shown in Figure 4.14(b). For each images the gray level histograms show two histograms based on the gray level of the pixels; darker gray areas show the voids (the histogram on the left) while the lighter gray areas show the solid pixels (the histogram on the right in Figure 4.14(b)).

A manual threshold can be set between these two histograms to separate the void and solid pixels for each image. However, setting a manual thresholding value may cause some inaccurate identification of voids since the pixels for voids may be considered as solid and vice versa. In addition, the threshold might be different for each slice image. To overcome these drawbacks of the manual thresholding process, a widely used automated process, namely Otsu method [206], is used in this study for segmentation. Once the gray level histogram for each 2D image data is evaluated in this segmentation process, the serial binary images are generated based on the calculated threshold values as seen in Figure 4.14(c). A comparison of the segmented binary image with the scanned image is given Figure 4.15.

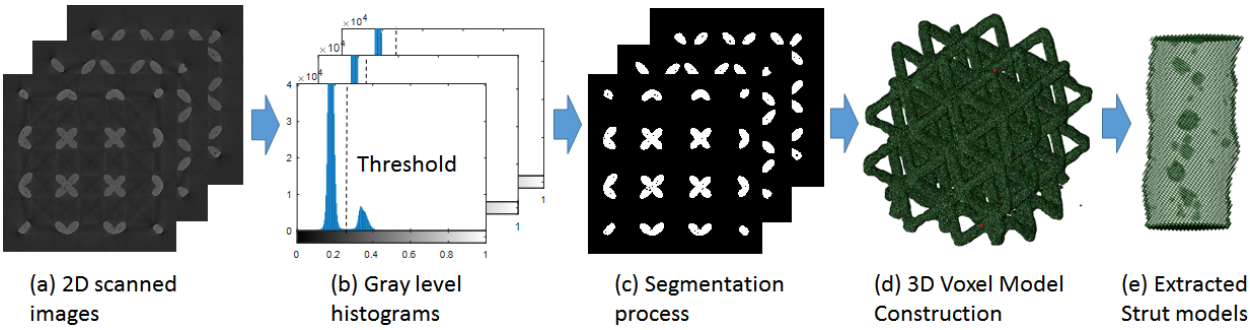

Figure 4.14. Schematic diagram of the 3D model reconstruction process using the 2D scanned image data

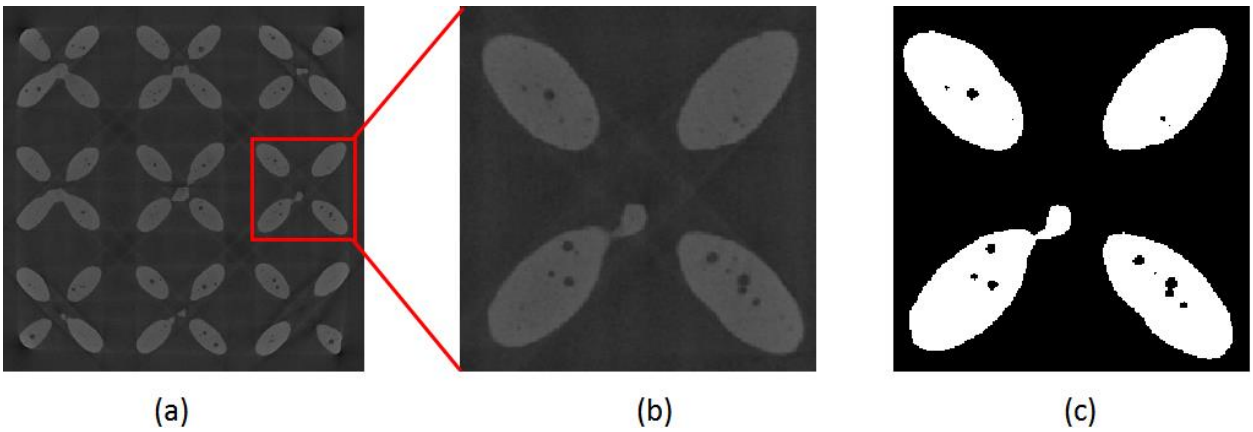

Figure 4.15. (a) CT-scan image for one layer, (b) Zoomed image of scanned data, (c) Zoomed segmented binary image

The 3D models generated from the CT-scan images can reveal plenty of information to quantify the uncertainties in the lattice microstructure and geometry. By analyzing the reconstructed 3D models, the features of the SLM-fabricated lattice structures such as internal defects and volume of solid struts can be determined. The presence of both porosities inside the material and the variations on the strut cross section geometry are visible in Figure 4.15. The uncertainties in material and geometry have to be quantified since those will influence the overall mechanical behavior of the material. For this purpose, the segmented binary images are combined to generate the 3D voxel model of the lattice structure specimen. The segmented binary images are converted

to a high resolution FE mesh with 8-noded hexahedral voxel elements as shown in Figure 4.14(d) using an in-house developed MATLAB algorithm that converts the binary image information to the voxel model. Then, the individual strut models, Figure 4.14(e), are extracted to quantify the uncertainties at strut level that will be used in the upscaling method.

4.4.4. Morphological Analysis of Fabricated Struts for UQ

In reconstruction of the 3D model of lattice structures, the CT-scan images were manipulated to have an element length of 27.06 μm to reduce the computational cost of the reconstruction process. It only takes 45 minutes to reconstruct the entire 3D model when 27.06 μm element size is used on an 8-core Intel i7 desktop computer. The reconstructed model with 27.06 μm consists of 10,580,902 elements, which is still very large for a simulation run due to large memory requirement of the entire lattice structure model. On the other hand, when individual struts are extracted from this model (Figure 4.14(e)), the model size is appropriate to make morphological analysis since the struts include about 35,000 elements with 27.06 μm.

Hence, individual strut models were extracted from the reconstructed lattice models. Analyses were performed on these struts to characterize the uncertainties of the surface irregularities (or roughness). As seen in Figure 4.14(e), there are irregularities along the outer surface of the struts and porosities in the fabricated struts shown as darker spots. These irregularities of strut surfaces and porosities will be the reason of the local heterogeneities leading to a lower stiffness and lower compressive strength of the material. Moreover, it will complicate the accurate prediction of mechanical properties by analytical models and FEA. The strut level uncertainties are investigated in terms of three main variables in this study: (1) the strut diameter uncertainty, (2) the strut angle uncertainty that gives the deviation from the center of each

fabricated layer, and (3) the porosity in the strut material. The combination of the uncertainties of the first two variables will result in the surface roughness in the voxel-based strut model. The uncertainty of the porosity in the fabricated struts is investigated in terms of the pore volume and pore size (i.e. the equivalent spherical diameter, defined as the diameter of a sphere of the same volume). Then, the BIC method is utilized for determining the distribution type and statistical parameters of these uncertain input variables that will be used to generate the voxel-based strut FE model for stochastic upscaling method.

4.4.4.1. Uncertainty quantification of strut diameter

Uncertainty quantification of the diameter of the strut layers is very important, since it has influence on both strut surface irregularities and strut material properties. Two methods are used in this study to have measurements; measurements from the reconstructed 3D models of the struts and measurements using a Vernier caliper. Measurements obtained from both methods are compared and justifications are given in uncertainty quantification of the strut diameter. For comparisons, uncertainties are considered as the standard deviation from the average measured diameters. For uncertainty quantification, BIC method is used to determine the optimal distribution type and statistical parameters of the strut diameter.

Fabricated Strut Diameter Measurements based on reconstructed 3D Model

Struts that form the BCC unit cells have an angle of 35.264^0 from the horizontal plane circular cross-sections. In order to generate a circular cross section perpendicular to the axis passing through the origin of an angled strut, the lateral layer cross sections that are fabricated in the layer by layer manufacturing process must be elliptical as seen in the CT-scan image in Figure 4.15. A stair shape occurs while building the circular struts in the SLM process because the layers

sliced in the CAD model of the part are built from bottom to top one by one and combined together to form the physical circular struts in the SLM process. The elliptic cross-section of each layer has two radius values, namely, the long radius (r_{long}) and the short radius (r_{short}) as shown in Figure 4.16(a). The stair-shape profile that exists to be able to achieve the continuity of the strut in the layer by layer AM process is depicted in Figure 4.16(b).

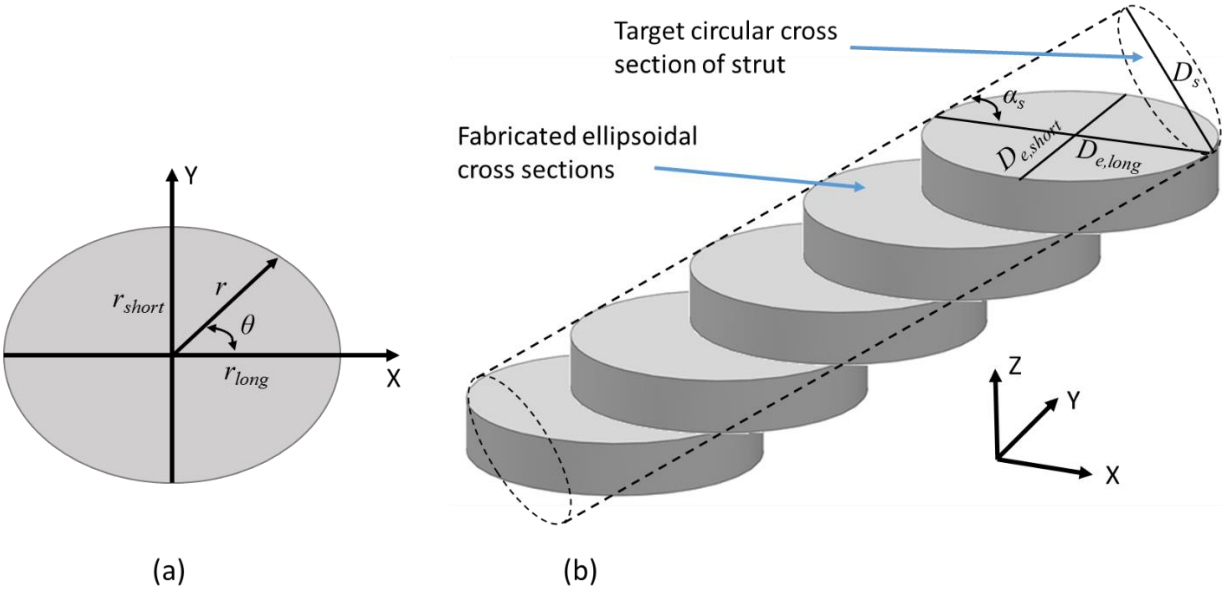

Figure 4.16. (a) Fabricated ellipsoidal cross-section (b) The stair shape during the fabrication of struts

The radius (r) at any point in a 2D ellipse cross-section geometry given by 0 (a) is calculated by the following equation:

$$r = \frac{r_{long} r_{short}}{\sqrt{r_{long}^{\ 2} \sin^2 \theta + r_{short}^{\ 2} \cos^2 \theta}} \tag{4.2}$$

where θ denotes the angle between the radius at the point of interest and the long radius. To achieve a circular cross-section for the strut, the short diameter, $D_{e,short}$, and long diameter, $D_{e,long}$, of the ellipsoid cross-sections in Figure 4.16(b) are calculated from the circular strut cross section diameter D_s based on the strut angle denoted by α_s as follows

$$D_{e,short} = D_s \tag{4.3}$$

$$D_{e,long} = \frac{D_s}{\sin \alpha_s} \tag{4.4}$$

where the subscript *e* represents the elliptic cross-section. In the generated the BCC cells, the struts have α_s = 35.264^0 angle with the lateral plane in the 3D printing process and the target model diameter of each strut is $D_{s,t}$ = 0.5mm. Then, the short target strut diameter of the elliptic cross-sections should be $D_{e,t,short}$ = 0.5 mm based on Eq. (4.3) and the long diameter should be $D_{e,t,long}$ = 0.866 mm according to Eq. (4.4) where subscript *t* denotes the target value. A voxel element-based strut model can be generated layer by layer using these diameter values and a circular cross section of the strut with a diameter value of $D_{s,m}$ =0.5 mm can be obtained as shown in Figure 4.17(a). This resulting model verifies that Eq. (4.3) and Eq. (4.4) can be used to predict the diameter values of the elliptic cross sections of each layer in the fabricated strut with target diameter.

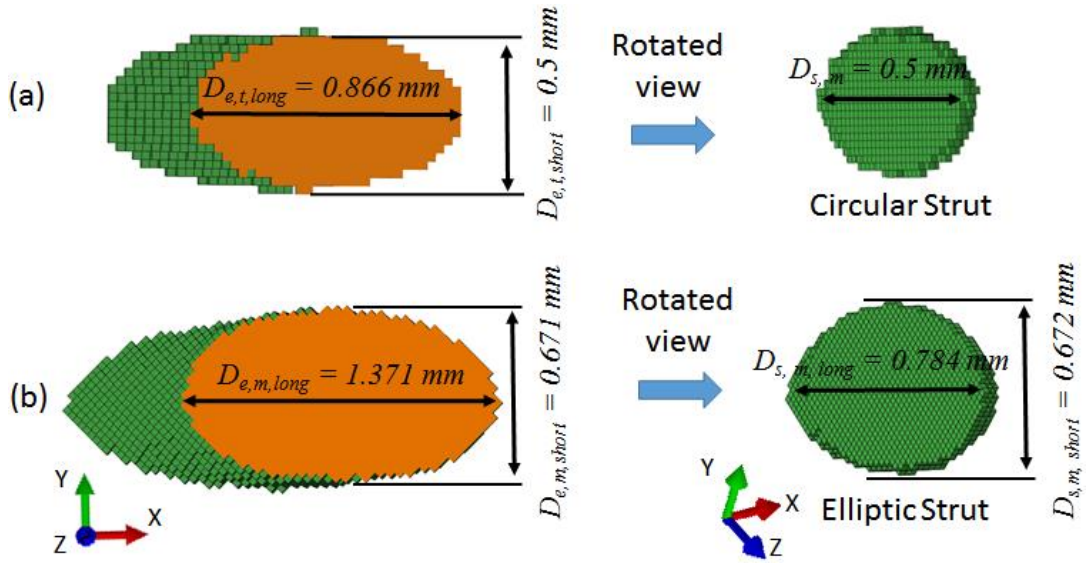

(a) Target elliptic cross-section that produces the circular strut (b) Fabricated elliptic cross-section obtained from the 3D reconstructed strut models

Figure 4.17. Elliptic cross-section of a reconstructed strut model

On the other hand, it is observed from the reconstructed 3D model of the SLM-fabricated lattice structure using the scanned images that the fabricated struts are not circular as can be seen on the right-hand side in Figure 4.17(b). Rather, two distinctive diameter values are measured in the directions perpendicular to each other as a long diameter and short diameter denoted by $D_{s,m,long}$ and $D_{s,m,short}$, respectively. In these notations, the subscript m denotes the reconstructed model measurements for the diameter values. The fabricated long strut diameter $D_{s,m,long}$ and short strut diameter $D_{s,m,short}$ were measured for 15 struts extracted from the reconstructed 3D models to quantify the uncertainties in the fabricated strut diameters. Diameter values were measured at different positions of the struts from bottom to top in its length direction to observe the variation throughout the strut length. 144 measurements were made from 15 struts in total. It was found from these measurements that the short diameter has an average value of $D_{s,m,short}$ = 0.672 mm while the long diameter has an average diameter of $D_{s,m,long}$ = 0.784 mm as shown on the right-hand side of Figure 4.17(b).

Since there exist two different diameters, we can consider an ellipsoid for the fabricated strut cross-sectional shape rather than circular. Then, the measured short and long dimeter values of the fabricated elliptic layers should match with the ones calculated by Eqs. (4.3) and (4.4), respectively. The short diameter of the elliptical cross-sections on each fabricated layer is calculated as $D_{e,m,short}$ = 0.672 mm by setting $D_s = D_{s,m,short}$ = 0.672 mm in Eq. (4.3). If the fabricated struts have elliptic cross-sections with these measured short and long diameters instead of the circular ones, then it is expected that the long diameter of the elliptic cross-section of each fabricated layer, $D_{e,m,long}$, can be calculated by Eq. (4.4) by setting $D_s = D_{s,m,long}$ = 0.784 mm. This assumption gives the result of $D_{e,m,long}$ = 1.358 mm from Eq. (4.4).

To justify these calculations when it is assumed that the strut cross-section is ellipsoid, measurements are also made on the elliptic diameters of each layer of the reconstructed models as shown on the left hand side in Figure 4.17(b) at different locations in the direction of the strut length. It was found from these measurements that the average value of the short ellipse diameter is $D_{e,m,short}$ = 0.671 mm, which is almost identical to $D_{s,m,short}$ value calculated by Eq. (4.3). This shows that the experimental measurements validate the use of Eq. (4.3) to calculate the short diameter. Moreover, the measurements of the long ellipse diameter on the fabricated strut has an average of $D_{e,m,long}$ =1.371 mm as shown on the left hand side ellipse geometry in Figure 4.17(b). This value has 0.9% difference from the $D_{e,m,long}$ value calculated from Eq. (4.4) as 1.358 mm, which shows a very close agreement to the value obtained from the model measurements. Thus, these results show that Eq. (4.4) can be used to calculate $D_{e,m,long}$, which justifies the assumption that the fabricated struts have an elliptic cross-section rather than a circular one.

The stair step shape is also clearly seen from the reconstructed strut models obtained from the fabricated struts in Figure 4.18(a). The stair step occurs because each layer is fabricated to satisfy pre-specified inclined angle of the strut as stated earlier. As indicated by Yan et al [207] with the image in Figure 4.18(b), during the fabrication process by SLM, additional melted particles are bonded on the direction of long diameter of the stair shape profile. The stair shape and the resulting partially or totally melted metal particles bonded on the layer during the fabrication process influence the surface quality of the SLM-fabricated parts greatly [208]. Hence, these bonded particles are the cause of the rough surfaces and corrugations observed on the lattice structures. This effect is mainly seen in the direction of the long diameter of the elliptic cross-section of each layer to ensure firm bonding of the layers since the short diameter direction does not have any inclined angle as can be seen in Figure 4.18(a). Hence, the reason of having a %0.9

difference with the calculated and measured long diameter values could be these bonded particles. These effects could also be the reason of the elliptic strut cross-section as well since the increase of the long diameter at each layer leads to a non-circular cross-sectional shape. To mitigate the effect of the stair step, a smaller layer thickness is preferred in the SLM process; but this also increases the time required to complete the fabrication [209].

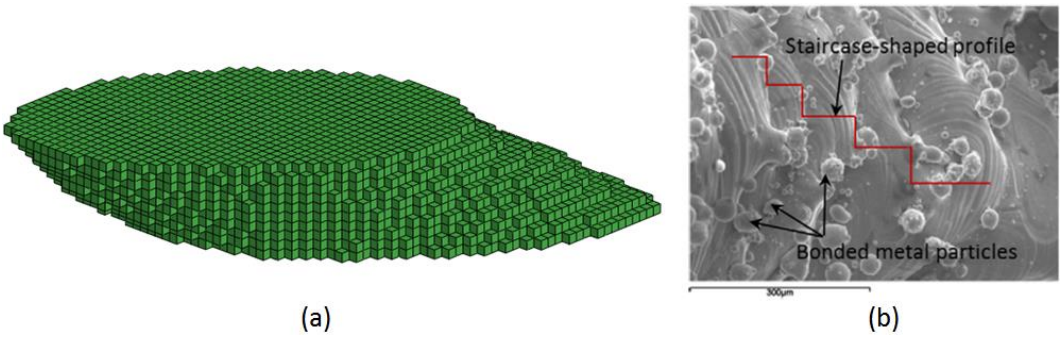

(a) stair shape profile in the reconstructed 3D model of fabricated strut by SLM, (b) High magnification picture of the strut [207] and

Figure 4.18. Stair shape profile on a fabricated strut.

Comparison of diameter values with experimental measurements

In addition to the diameter measurements made on the reconstructed models, the experimental strut dimeters of the SLM-fabricated struts were measured using a Vernier caliper for 50 different struts from the cellular lattice structure specimens. Only one measurement could be made for each strut since the length of the struts were small to distinguish the position of the caliper on the strut. It was found that the cross section of the strut has two distinctive diameter values similar to the reconstructed model measurements. These experimental measurements are given in Figure 4.19(a). The mean and standard deviation values of these experimental struts diameters were plotted in Figure 4.19(b) and compared with the measurements made from the reconstructed model.

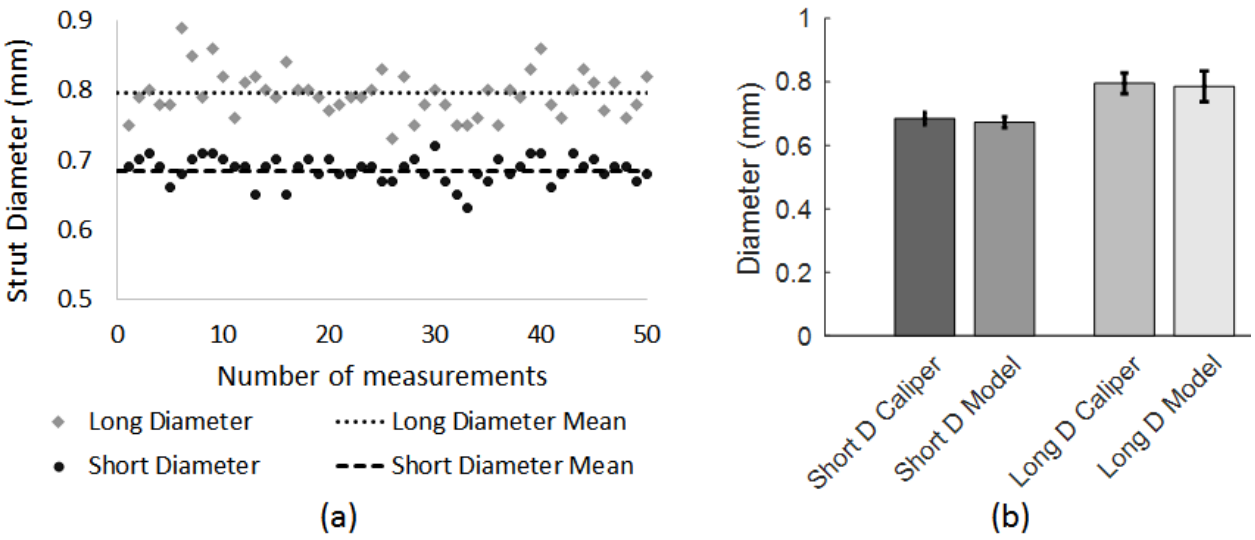

(a) Fabricated strut diameter measurements using Vernier caliper (b) Comparison of measured experimental diameters using a caliper and measured diameters from the reconstructed 3D model

Figure 4.19. Fabricated diameter measurements

These results in Figure 4.19(b) show very close agreement between the experimental and model measurements. It is seen that the experimentally measured values of both the short and long diameters are slightly greater than the ones measured from the reconstructed models. The reason of these slight differences could be the round-off errors during experimental measurements and errors because of the voxel-based reconstruction of the model. The average of the short dimeter of the strut was found to be $D_{s,exp,short}$ = 0.685 mm from the measurements made by Vernier caliper on 50 different struts in the structure. When compared to the model measurements of the short diameter, $D_{s,m,short}$, there is only 1.8% difference, The standard deviations from the experimental and model measurements were found to be 0.0186 and 0.0193, respectively, indicating that the standard deviation of the short diameter is very small in the SLM-fabricated struts.

The long diameter of the strut was also measured using the caliper from the specimens and the average diameter was found to be $D_{s,exp,long}$ = 0.795 mm, which was close to the model

measurement average calculated as $D_{s,m,long}$ = 0.784 mm. This means the measurements from the reconstructed model and from the experimental specimens have only a difference of 1.1%. This small difference indicates that the reconstructed models can accurately represent the test specimen geometry. The standard deviation of the experimental long diameter measurements was calculated to be 0.0327 mm, which was two times larger than the standard deviation of the small diameter. The reason of the larger deviation in long dimeter is again the stair step effect where additional particles are bonded in the direction of the long diameter to achieve the firm connection between layers. In addition, the standard deviation calculated for the long diameters from the model measurements was 0.0561. This value is larger than the standard deviation of the experimental measurements. This increase can be explained by the fact that the model measurements are also made at different locations in the direction of the strut length and that the long strut diameter has also additional variation depending on the spatial location on the struts. This spatial variation could not be captured by the caliper measurements since the strut length was not long enough to have different measurements in the length direction of the struts. Hence, since both experimental and model measurements agree well, the model measurements can be used in uncertainty quantification. Moreover, it can be concluded that the measurements made on the reconstructed voxel models should be preferred to be able to quantify the uncertainties accurately since the caliper measurements can only provide a rough variation estimate. Thus, the optimal distribution types and statistical parameters of the input variables that will be used in fine scale strut model generation are predicted using BIC method for the measured data from the reconstructed models.

BIC method for Uncertainty Quantification of Strut Diameter

The optimal distribution types and statistical parameters of the short and long diameters of the fabricated struts are determined using the BIC method by fitting normal, lognormal, gamma,

and generalized extreme value (GEV) distributions to the measured data from the reconstructed models as depicted in Figure 4.20. The BIC method indicates that a lognormal distribution gives the best fit to the measured data for both short diameter and long diameter. The resulting statistical parameters of the short and long diameter distributions are listed in Table 4.5.

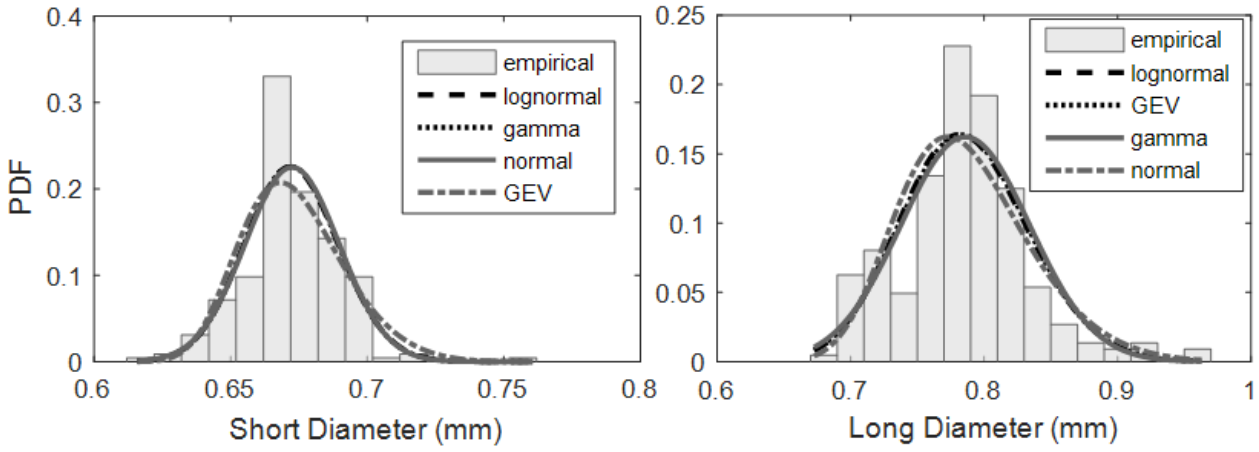

(a) (b)

Figure 4.20. Distributions of the short (a) and long (b) diameters of the strut cross section

Table 4.5. Distribution and statistic parameters for dimeter values in struts

Parameter	Distribution	Parameter *a*	Parameter *b*
Short Diameter	Lognormal	-0.3984	0.0277
Long Diameter	Lognormal	-0.2456	0.0704

Quantification of the difference of fabricated diameter from the target model diameter

When the lognormal distribution parameter values given in Table 4.5 are used, the mean value of the short diameter was calculated as 0.672 mm according to the lognormal distribution mean value formulation in Table 2.1. The difference between the target diameter (i.e. $D_{s,t}$ = 0.5mm) and

the obtained dimeter ($D_{s,m,short}$ = 0.672 mm) from the fabricated struts is calculated as $\delta_{s,short}$ = 0.172mm. As seen, there is an increase in the diameter value for the SLM-fabricated struts.

This observation about the increased strut diameter for the SLM-fabricated structures were made by several researchers, as well. Yan et al. [207] investigated gyroid structures fabricated by SLM with SS316L material and found about 0.08 mm constant increase in the thickness for different size of diameters compared to the fabricated diameters. Van Bael et al. [208] investigated the Ti6Al4V porous structures fabricated by SLM and found an increase of 0.112 mm compared to the designed value. Hollander et al. [210] found a 0.150 mm increase in the strut thickness when fabricated by SLM. Qiu et al. [211] show for struts fabricated by SLM using AlSi10Mg material that the thickness or diameter increase can show difference depending on the processing parameters used in the fabrication process. They found that the fabricated diameter can be two times larger than the target diameter depending on the processing parameter values used in the fabrication process. Based on these observations given in the literature, the increase of the diameter that was measured about 0.172mm in this study is reasonable and can be considered for any dimeter value used for designing the CLSs when constant processing parameter values are used. This difference can be added to the target diameter value for the voxel model generation of struts in the modeling process. Then parameters *a* and *b* are determined based on the formulations given in 0 for the lognormal distribution.

Similar to the short diameter, the mean value of the long diameter was calculated from 0 for lognormal distribution using the determined parameter values given in Table 4.5 as $D_{s,m,long}$ = 0.784 mm which gives a $\delta_{s,long}$ = 0.284 mm difference from the target diameter (i.e. $D_{s,t}$ = 0.5mm). This difference value will be added to the target diameter to calculate the long diameter of the elliptic layers ($D_{e,long}$) for voxel model generation. Thus, Eq. (4.3) and Eq. (4.4) are modified to find the

mean values of short and long elliptic diameters of each layer that will be used in the voxel model generation as

$$D_{e,short} = D_{s,t} + \delta_{s,short} \tag{4.5}$$

$$D_{e,long} = \frac{D_{s,t} + \delta_{s,long}}{\sin \alpha_s} \tag{4.6}$$

Similar to the assumption of constant diameter increase, the standard deviation of the strut diameter will be assumed to be constant for different strut sizes. Thus, the same standard deviation value calculated by the formulation in 0 using the Parameter *a* and *b* values in Table 4.5 for lognormal distribution can be used for any size of diameter in voxel-based strut model generation. The mean, standard deviation, and the diameter difference values for short and long diameters are listed in Table 4.6. Then, these parameters can easily be used in a sampling method to generate strut diameter values in the voxel model generation process using the underlying lognormal distribution. This process of generating strut models for different diameter values is used in Chapter 5 to develop a meta-model for the homogenized elastic modulus of the BCC lattice cell fabricated by SLM.

Table 4.6. Mean, standard deviation, and difference (δ_s) values of the diameters

Parameter	Mean ($D_{s,\mu}$)	$\delta_s = D_{s,\mu} - D_s$	Standard Deviation
Short Diameter	0.672 mm	0.172 mm	0.0193 mm
Long Diameter	0.784 mm	0.284 mm	0.0561 mm

Uncertainty Quantification of strut diameter for different strut angles

The relation between the diameter and the strut build angle is also needed to be quantified for voxel model generation. Since only one angle value is used in the fabricated BCC cells in this study, an assumption for the relation between the strut diameter and angle can be made based on the literature. Although the materials used in the literature are different from AlSi10Mg, the same SLM process is used for the fabrication of struts. Hence, a general opinion about the strut diameter change with the change of strut angle can be obtained from the literature. Van Bael et al. [208] indicates that fabricated vertical struts (i.e. 90^0 angle with respect to the horizontal build plane) have smaller diameter values than the struts fabricated in the BCC structure (i.e. with 35.264^0 angle with respect to the horizontal build plane). Besides, in both cases, the fabricated diameter was found to be larger than the target diameter. Shen [212] also finds 14% larger diameter values for 35^0 struts than the 90^0 struts when the largest diameter of the strut cross-section is measured for both angle values. Moreover, it was found in the literature that 90^0 struts have almost circular cross sections [213]. The increase in the diameter with the decrease of the strut angle is because of the stair-shape effect regardless of the material type in SLM process.

If 14% increase is also considered in our study, the long diameter of the 90^0 strut is calculated as 0.674mm (i.e. 84% of 0.784mm), which is very close to the value of the short diameter mean value given in 0. That means, with the assumption that a circular diameter is fabricated at 90^0 strut angle, the increase of strut diameter can be considered as the value found in our study (i.e. 0.172mm) for 90^0 strut angle. Moreover, it will be assumed that the fabricated strut diameter remains the same as the short diameter value, which is determined by Eq. (4.5) for any

degree of struts. Since the 90^0 strut will have a circular cross-section, $\delta_s = 0.172$ mm will be added to the target diameter to find the fabricated diameter.

For strut angles different from 90^0, the long diameter mean values can be assumed to be linearly increasing with the decrease of the angle up to 35.264^0 strut angle because of the increase of the stair shape effect. Hence, the difference in long diameter mean value, $\delta_{s,long}$ will be equivalent to the difference in short diameter mean value $\delta_{s,short} = 0.172$ at a strut angle of 90^0 and linearly increase to the value of $\delta_{s,long} = 0.284$, found for 35.264^0 in this study, when the angle is decreased up to 35.264^0. Thus, the difference value, $\delta_{s,long}$, for a strut angle (α_s) between 90^0 and 35.264^0 can be determined by using a linear interpolation process as follows

$$\delta_{s,long} = \frac{0.172 - 0.284}{90 - 35.264}(\alpha_s - 35.264) + 0.284 \tag{4.7}$$

Since a linear increase is assumed, the long diameter can be predicted for the angle values smaller than the 35.264^0, as well. On the other hand, SLM process requires support structure to build overhang section if its angle from the horizontal is less than a certain degree. Hence, the cellular structures with low strut angles from the horizontal (usually lower than 30^0) could not be built using the SLM process because overhanging struts led to the occurrence of serious deformation [214]. This limitation in the fabrication of CLSs have been investigated previously by a few researchers. Santorinaios et al [215] studied the manufacturability of cellular lattice structures with SLM process that only consist of vertical and diagonal cross struts since the SLM process cannot build horizontal struts. Hence, lattice unit cells that do not possess struts with small angles are preferred to design cellular lattice structures. Yan et al. [207], [214] investigated the

design and manufacturability of a unit cell type called “Schoen Gyroid” referred to as gyroid unit cell to enhance the geometrical capability of the SLM process. This unit cell has circular and smooth struts and a spherical core as different from the other lattice types with straight beam-like struts. The self-supported property of this unit cell types provides the capability of manufacturing the CLS without the need of support structure and without considering the strut angle in the SLM process. Mullen et al. [216] used BCC unit cell geometry, which includes straight circular beam-like struts because of its suitability for SLM fabrication process since it does not have any horizontal or low angle strands that are difficult to build. BCC seems to be the only symmetric lattice structure without horizontal or low angle struts, therefore, it is possible to fabricate BCC lattice structures in the SLM process without requiring support structure.

4.4.4.2. Uncertainty Quantification of Strut Angle

As stated in the beginning of Section 4.4, the surface roughness can be considered as a combination of the deviation of the diameter and deviation of each layer from the center based on the actual strut angle. Therefore, in addition to the quantification of the strut diameter uncertainties, the uncertainties in the strut angle of fabricated struts also need to be quantified from the reconstructed models to understand its effect on the strut surface irregularities.

Measurements of strut angle deviation from the reconstructed models

The models of the fabricated struts reveal that the strut angle deviation is large on the long diameter side because the build angle is determined on this side where the stair shape effect is seen. Hence, the measurements for the strut angle deviation are made in the long diameter direction. In the reconstructed voxel models of the fabricated struts, full ellipse cross-sections are not fabricated for some top and bottom layers to achieve the integrity of the strut as seen in Figure

4.21(a). The red regions of the strut in Figure 4.21(a) shows the layers that have partial elliptic cross-sections, while the green region have the full elliptic cross-sections. The deviation in the strut angle for each layer can be measured for the fully fabricated layers. Hence, the full elliptic cross-section portions of the struts are extracted to analyze the angle deviation.

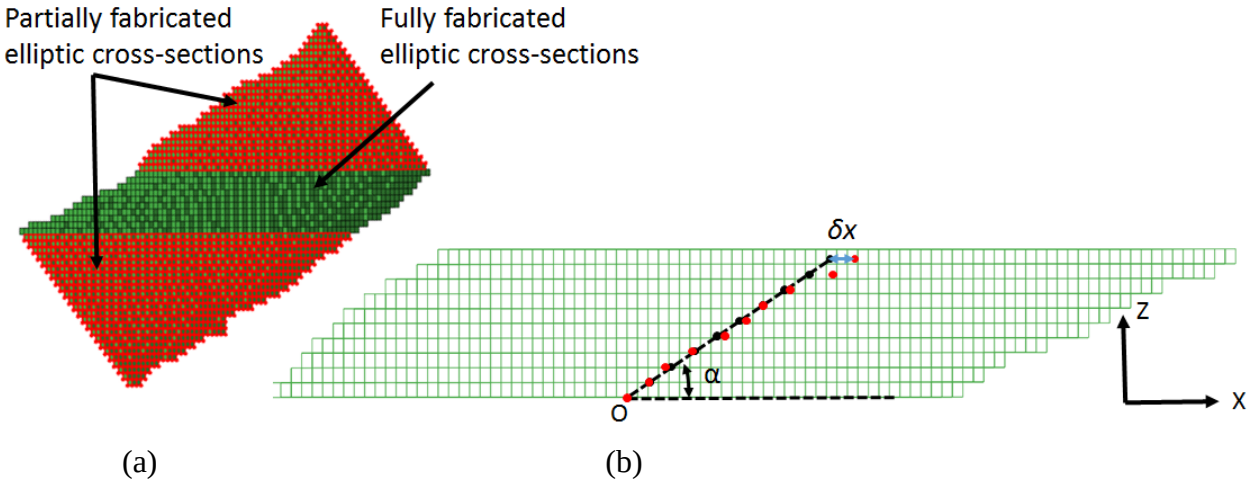

(a) (b)

(a) Elliptic section of the strut model (b) Calculation of the strut angle deviation of the fabricated elliptic cross section centers. Dashed line shows the actual center of the strut and the red dots are the centers of the elliptical cross-sectional layers fabricated in SLM

Figure 4.21. Elliptic section of the strut model.

Moreover, the deviation or the roughness on the surface of a strut is a combination of the angle deviation and the strut diameter deviation. To be able to differentiate these two deviations, the deviation of the angle should be determined as the deviation from the actual center points of the layers rather than the deviation on the edges as shown in Figure 4.21(b). In that regard, a deviation variable δx is defined to characterize the deviation of the angle. To calculate δx, first, each layer's target center coordinate value in the long diameter direction is calculated using the target strut angle (i.e. $\alpha_s = 35.264^0$) as depicted by the dashed line in Figure 4.21(b). Then, each fabricated

layer's center value is calculated from the reconstructed voxel model from the layer diameter, as depicted by the red dots in Figure 4.21(b). The difference between these two center values for each voxel layer is calculated as the deviation parameter, δx. Then, the build angle can be calculated with respect to the horizontal direction using the center coordinate values of each layer. The deviation, δx, values are depicted in Figure 4.22 for one strut. The deviations correspond to a mean value of δx_{mean} = 0.0177 mm as shown with the dashed line.

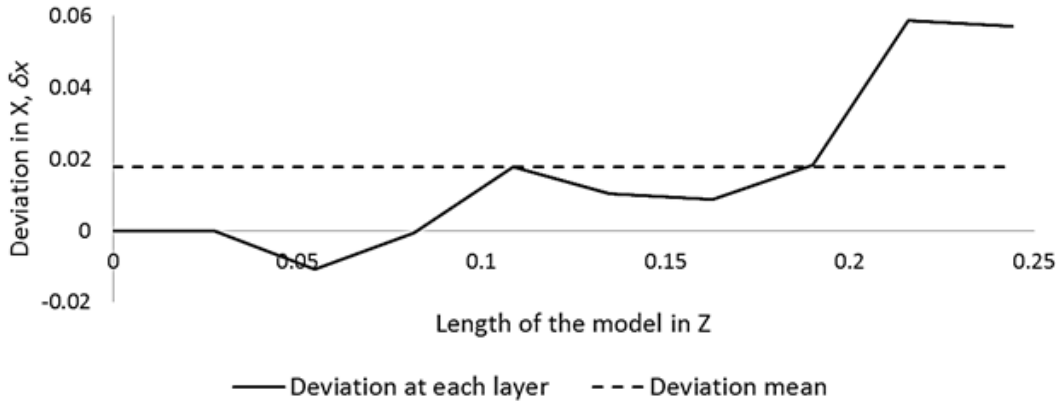

Figure 4.22. Angle deviation values for each voxel layer of a strut.

Uncertainty Quantification of the Strut Angle based on the measurements

The deviation parameter δx is calculated for 15 different struts using the aforementioned procedure. Then, for each layer, the fraction of the vertical length between the corresponding layer and the bottom layer to δx value is calculated. The inverse tangent of this fraction value gives the angle of the corresponding layer with respect to the build plane. The histogram of the angle of fabricated layers is depicted in Figure 4.23. Four different distribution types are fitted to the empirical data of the angle as seen in Figure 4.23. According to the BIC method, normal distribution is the best fit to the empirical data. The corresponding statistical parameters are listed in Table 4.7.

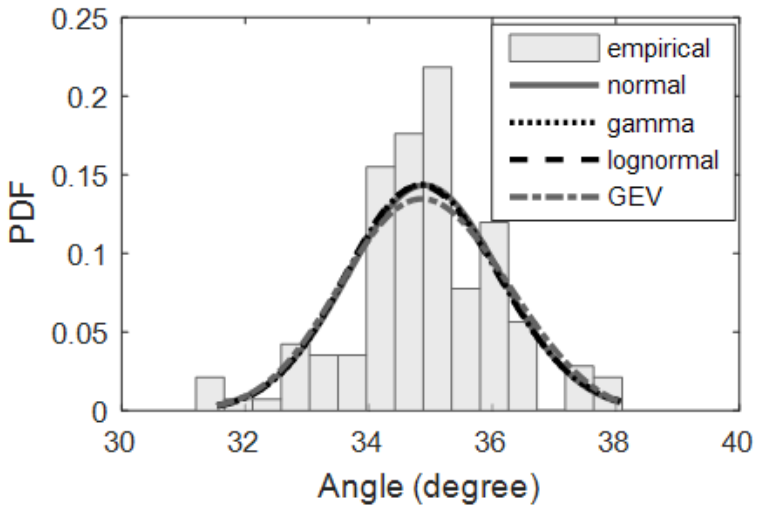

Figure 4.23. Distribution of the strut angle

Table 4.7. Distribution and statistic parameters for angle in struts

Parameter	Distribution	Parameter *a*	Parameter *b*
Strut Angle	Normal	34.898	1.2294

Since it follows a normal distribution, parameter *a* corresponds to the mean angle value, which is calculated as 34.898^0, while the parameter *b* corresponds to the standard deviation, which is 1.2294^0. Compared to the target diameter value of $\alpha_s = 35.264^0$, there is a difference of 1.04% with the mean angle value. This small difference shows that a good accuracy in respect of strut angle is achieved for the fabricated struts. Hence, the target strut angle can be used in the voxel model generation process as the mean value of the strut angle and the normal distribution is used to generate angle values for each generated layer.

Uncertainty for different strut angles

The assumptions made for uncertainties of different diameter values in the Section 4.4.4.1 can also be considered for the uncertainties of the angle, as well. In that regard, parameter *a* value for the angle that follows normal distribution is set equal to the target strut angle value. In addition, parameter *b* value given in Table 4.7 as 1.2294^0 is assumed to be the same for any strut angle. Then, these predicted parameters are used in the voxel model generation process to introduce the uncertainty in the strut angle at each layer. Thus, the roughness on the strut surface can be introduced to the voxel generation process as the uncertainty of the angle for each layer with parameters in Table 4.7 as well as the uncertainty of the diameter with parameters in Table 4.6.

Relationship of the geometrical irregularities with the process parameters

In this study, constant values of process parameters are used to fabricate the lattice structure specimens with the SLM process. Since the processing parameters are not the concern of this study, the quantification of the effects of the processing parameters on the diameter and porosity of the lattice structures are not studied and left as the future work. However, if necessary, the relation of the uncertain strut model parameters and the process parameters such as beam energy and laser power can be made based on the literature. For example, Van Bael et al. [208] found that the diameter obtained in the SLM process increases logarithmically with the increase of the beam energy parameter value up to a certain maximum diameter value. This maximum diameter is directly linked to the diameter of the melt pool, which, in turn is governed by the diameter of the melt isotherm that is produced by the beam. Qiu et al [211] indicates that the increase of laser power at a fixed laser scanning speed increased the diameter of the strut with a nearly linear

relationship. The authors also observed that the diameter of strut decreases with the increase of the laser scanning speed logarithmically at a fixed laser power.

4.4.4.3. Porosity and Pore Size Analysis

SLM process tends to produce defects in the material in the form of pores when melting layer by layer. Two porosity variables are defined and quantified: (1) Porosity, and (2) Pore Size Diameter. The mechanical properties and performance of the fabricated parts are strongly affected by the quantity and morphology of these pores in the material. The pores can come from either the atomization process to form the aluminum powder or the melting during the fabrication process. The CT-scan images obtained from this study and the 3D reconstructed models reveal that the pores are spherical in the struts as seen in Figure 4.14(e). It is seen in the reconstructed strut models at first sight that the range of pore sizes appears to be randomly distributed. More careful statistical analysis of such images are necessary to have a true quantification of the distribution of density and tendency of pores.

Porosity Distribution

The porosity can quantitatively be determined from the reconstructed strut models. The porosity of the structure is defined as the volume fraction of the pores in the structure. It can be measured by the ratio of the volume of the voxels that are void in the strut to the total volume of voxels in the reconstructed strut models. Thus, the porosity formulation can be given by

$$\rho = \frac{V_{pore}}{V_{solid} + V_{pore}} \tag{4.8}$$

where V_{pore} denotes the volume of the void voxel elements and V_{solid} denotes the volume of the solid voxel elements in the reconstructed model.

The porosity was first calculated for the entire CLS using Eq. (4.8). To calculate the total volume of the pores, two voxel models were reconstructed from the CT-scan images. First, the 3D model was reconstructed with the porosities. For this reconstruction process, the binary images were created such that the pixels corresponding to the void regions are represented by zeros while the solid pixels were represented by ones. Second, the 3D model was reconstructed through the binary images that do not include the porosities. For this latter case, the pixels with porosity (i.e. with zeros) in the binary images are found and replaced by solid (i.e. with ones) to eliminate the porosity inside the structure. Then, the difference of the total volume values of these two models (i.e. 209.66mm^3 for the first model and 211.24mm^3 for the second model) is calculated as the volume of the pores in the structure. This value is divided by the volume of the second model that does not have porosities to calculate the porosity value of the fabricated CLS. It was found that the entire structure has a porosity value of 0.75%.

This high resolution model cannot be used for detailed pore size diameter analysis due to its high demand of memory as mentioned previously. Hence, individual struts shown in are extracted from the reconstructed 3D model. The purpose of using separate struts is to have a better understanding of the distribution of the porosity and quantify the uncertainties that will be used in the fine scale model generation at strut level. The mean porosity value obtained from 90 different strut models is found to be 0.91% with a coefficient of variance (cov) value of 0.28. From the high resolution results, it can be seen that overall volume fraction of pores measured for the scanning process is low and less than 1%. The low value of porosity has a small effect on the elastic properties of the struts. However, it must be still considered to have accurate results. In addition,

for plastic and fatigue analysis it can have a crucial importance. The distribution of the porosity is given in Figure 4.24. BIC is implemented and found that the porosity distribution is better described with a gamma distribution with the given parameters in Table 4.8.

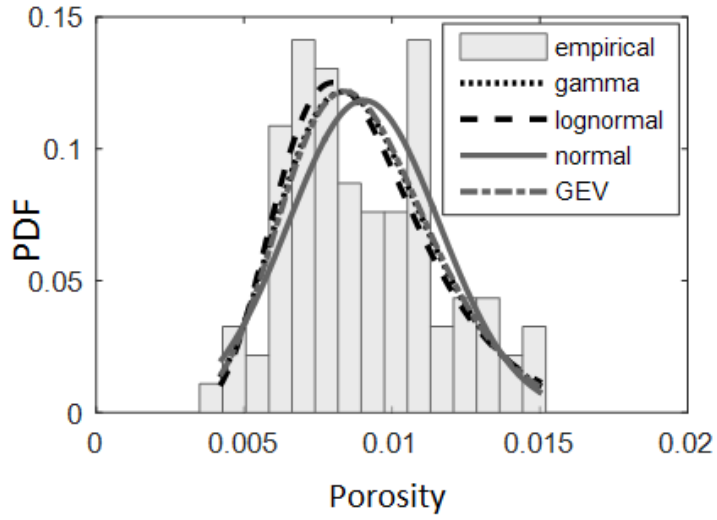

Figure 4.24. Porosity distribution in fabricated struts

Pore Size Diameter Distribution

The size of the pores is determined by calculating the corresponding equivalent spherical diameter of the pores. For this purpose, first, the number of voxel elements in each pore in each strut is collected from the 3D reconstructed strut models. The distribution of the number of voxels in each pore is shown for 19 strut models in Figure 4.25(a).

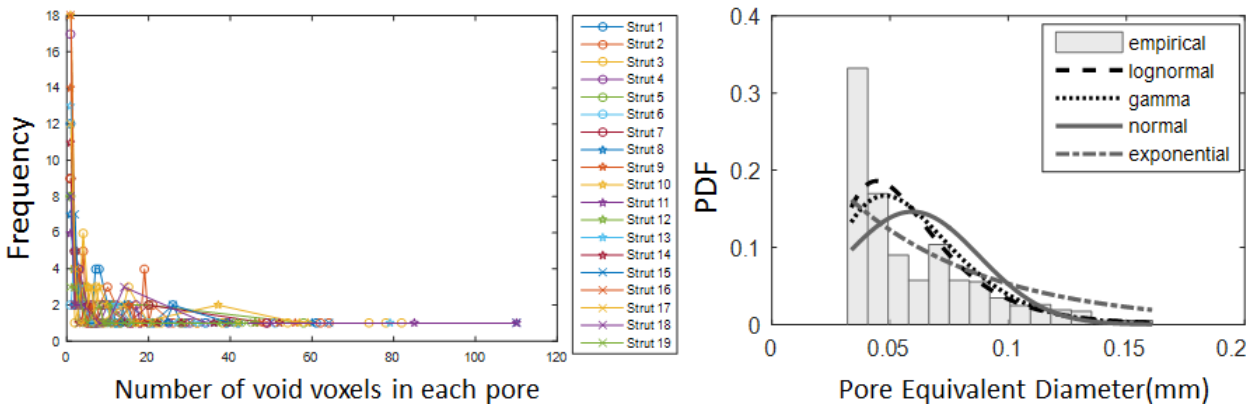

(a) (b)

(a) Distribution of the number of void voxels in each pore for each strut, (b) Distribution of pore diameter.

Figure 4.25. Pore size distribution

Then, the equivalent spherical diameter that gives the total volume of the void voxels in each pore is calculated and the equivalent diameter distribution for all of the samples is given in Figure 4.25(b). This combined distribution of all samples can be used to calculate the mean pore diameter. This study shows that the majority of the pore sizes can range from 0.03mm to 0.150mm with a mean pore diameter of D_p = 0.06mm and a few exist above 0.150 mm in size. In the measurements performed here, the pixel density value of the void within a pore was much less than that of solid aluminum background. Although this feature gives a good contrast, this can still be an issue for detecting small pores in the cross-sections. This is because when a defect is too small their morphology cannot be accurately represented as a pore equivalent to one voxel size will appear as a cube. Hence, the reconstructed model cannot detect very small pores (i.e. less than 27.06 μm in diameter). However, this would be expected to generate only a slight underestimate since such small pores contribute little to the overall volume. The large pores, on the other hand, have more importance for the mechanical responses of the structures, which have been identified by the current modeling resolution.

It is seen from Figure 4.25(b) that the pore size distribution is skewed to the left. The reason is that more than 30% of the pores correspond to the pores with only one voxel element which corresponds to an equivalent sphere diameter of 0.034 mm. Few pores are found to be larger than 0.12 mm (less than 5%). The pore diameter and distribution was found to be consistent with the literature [217], [218]. In addition to normal and lognormal and gamma distributions, an exponential distribution fit is also applied along with as the shape of the distribution looks exponential as seen in Figure 4.25(b).

The BIC results indicate that a lognormal distribution has a better fit than the normal and exponential distributions. On the other hand, the left side of the fitted lognormal distribution should not be considered since no porosity exist for a dimeter smaller than 0.034mm. Hence, a truncated lognormal distribution with the calculated parameters in Table 4.8 can be used as the distribution of the pore diameter. This information of the pore diameter distribution can be used for generating the porosity in the strut fine scale models. If the generated pore size is smaller than 0.034mm a new value is generated from the lognormal distribution until this value falls into the truncated region of the distribution.

Spatial Distribution of pores in the 3D space

The 3D reconstructed strut models show that the pores are found with proximity to the center of the struts. Moreover, it was seen that the pores are randomly distributed throughout the struts since the spherical porosity that exists in the initial powder cause the porosity in the structure during the forming process. Hence, we can assume a uniform distribution for the spatial distribution of the center position of the pores in the range of strut dimensions. To generate the pore centers in the voxel model generation process, first the element number in the voxel model

that will correspond to the center of the pore is randomly generated. Then the distance of the center of the element to the strut surfaces are measured based on the minimum and maximum parameters in 0 denoted by Parameter *a* and Parameter *b* for the pore center location. Since the pores are observed inside the strut (i.e. there is no partial pores on the strut surface), these bounds will allow to generate the pores inside the diameter. A small tolerance value of 0.05 was also added and subtracted from minimum and maximum bounds to guarantee that the generated pores will not concede with the strut surface. In the direction of strut length on the other hand there exist partial pores as seen in the strut models in Figure 4.14(e). Therefore, no limitations in the direction of strut length are set for the center location of the pores except to be inside the strut limits.

Table 4.8. Distribution and statistical parameters for porosity and pore size in struts

Parameter	Distribution	Parameter *a*	Parameter *b*
Porosity	Gamma	12.5925	0.0007184
Pore Diameter	Lognormal	-2.9242	0.4371
Pore Center Location	Uniform	$-D_s/2+D_p/2+0.05$	$D_s/2-D_p/2-.0.05$

Finally, it should be noted that the effect of process parameters on porosity was not considered in this study since only one set of process parameters were used to fabricate the lattice specimens. There exist several studies on the other hand investigating the process parameters effect on the porosity in the SLM-fabricated parts. These studies show that changing the machine settings can greatly change the distribution and density of pores [217], [219]. If necessary, the existing studies can be used to quantify the relationship between the pore parameters and the process parameters as this is left as a future study.

4.4.5. Strut Level Upscaling Step

A fine scale FE modeling technique that fills each deposited layer of the fabricated strut with voxel elements (i.e. 8-node brick elements) was used to accurately model the geometric and material uncertainties in the strut for mimicking the SLM fabrication process. The uncertainties quantified in Section 4.4.4 with BIC method for the strut level input variables were used with the corresponding distributions and statistical parameters given in Table 4.5, Table 4.6, Table 4.7, and Table 4.8 to generate the statistical samples of fine scale model. The fine scale model mesh size is set to 0.05412 mm at strut level due to the high computational time and memory requirements of the finer mesh sizes. The length of the strut that will be used in the upscaling method is modeled as l = 1 mm to further decrease the computational demand of fine scale model generation process. These simplifications have a very slight effect on the prediction accuracy, as will be shown in the strut level validation step. The mean of the Poisson's ratio and elastic modulus is set to v = 0.33 and E = 65GPa, respectively, with a coefficient of variation of 0.05 for AlSi10Mg material. The number of simulations is determined to be 200 after a convergence analysis of the mean and standard deviation of the reaction force (F) obtained from the fine scale model (Figure 4.26)

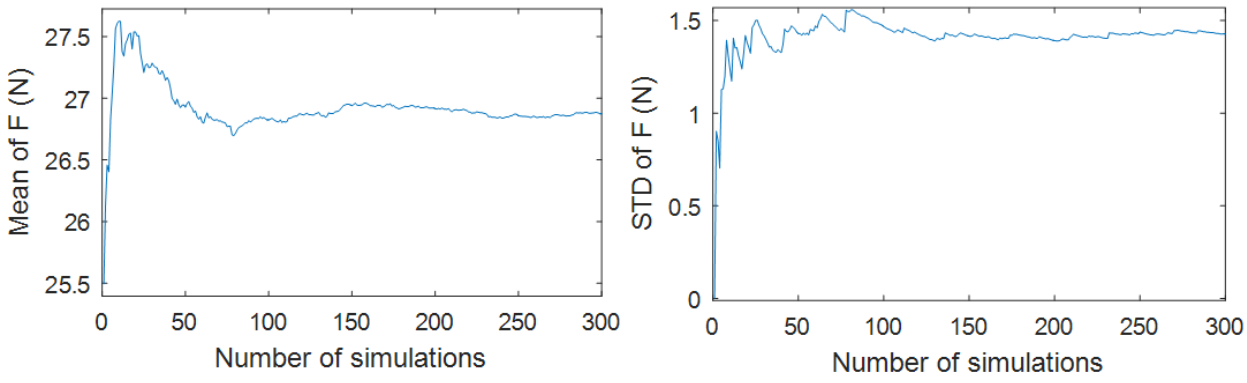

Figure 4.26. The convergence of mean value (left) and standard deviation (right) of the reaction force

In order to accurately model the effect of both the geometry and material uncertainties on the homogenized diameter and elastic modulus, the fine scale model generation process involves a two-step procedure as shown in Figure 4.27. In the first upscaling process, the fine scale model is generated by considering uncertainties only in the geometric parameters such as strut diameter and angle. This model is called *Strut Model 1* as shown in Figure 4.27. The material is assumed to be deterministic with the mean values of elastic modulus and Poisson's ratio at each sampling point. Then the reaction force on the top surface of the model is calculated as the fine scale output denoted by $y_{FM1,2}(j)$ in elastic FEA when a tensile strain of 0.1% is applied at each sampling point $j=1,2,\ldots,n$, where n is the total number of samples. These results are used in the upscaling process to find the uncertainties of the homogenized diameter, D_h. In the coarse scale model, known deterministic values of elastic material properties are used while the diameter of strut modeled by a beam element is the unknown parameter. Thus, only the effect of geometry uncertainties is propagated to the homogenized diameter while assuming that both the fine and coarse scale models have the same bulk material properties.

The generated fine scale strut models are retained for each sampling point and the uncertainties in the material properties, such as elastic modulus and porosity, are introduced to the strut model (i.e. *Strut Model 2* in Figure 4.27). It was observed from the reconstructed strut models that the pores are randomly distributed in the struts but there are no partial pores on the strut surface. Hence, the pore centers are randomly generated such that they can exist inside the strut models. A sampling method will be a useful tool to generate the porosity in the strut models. In the generation of the pores in *Strut Model 2*, at each sampling point, first a porosity value is generated from its distribution given in Table 4.8 using LHS. Then, a random number r_j in the

range of the number of elements in the generated strut model is initially used to generate the center coordinates of each spherical voids within the strut model. This is denoted by

$$r = (r_1, r_2, ..., r_n) \tag{4.9}$$

where r_j is the location (x_j, y_j, z_j) in the coordinate system for the jth pore in the strut, which will have n pores in total. The diameter value of the corresponding pore is also randomly generated from the pore diameter distribution given in Table 4.8. The pores are generated in the strut such that the total porosity value generated initially is met. For this purpose, the volume of the pore is calculated and summed to the existing volume of the pores after each trial. If the location of the center of the pore is out of the determined bounds, then a new number is generated. The random number generation process continues until eventually the total porosity reaches the target porosity value. The number of pores denoted by n is determined in the end of this random generation process.

Once *Strut Model 2* is generated, the reaction force on the top surface of the model is calculated in FEA as the fine scale outputs denoted by $y_{FM\,2,2}(j)$ under a tensile strain of 0.1%. The opposite plane is fixed in the loading direction as shown in Figure 4.27. Then, a second upscaling step is used for *Strut Model 2* with the results $Y_{FM\,2,2}$ obtained from the fine scale model. The coarse scale model is generated as a beam element with the homogenized diameter values from the first upscaling step while the unknown coarse scale model elastic modulus is determined. Thus, the effect of material uncertainties is propagated to the homogenized elastic modulus. The upscaling procedure is implemented for 200 samples considering a second order PCE for the representation of the homogenized variables. Once the homogenized diameter and elastic modulus

data are identified in the upscaling step, the validation of the homogenized model is performed as explained in Section 4.4.6.

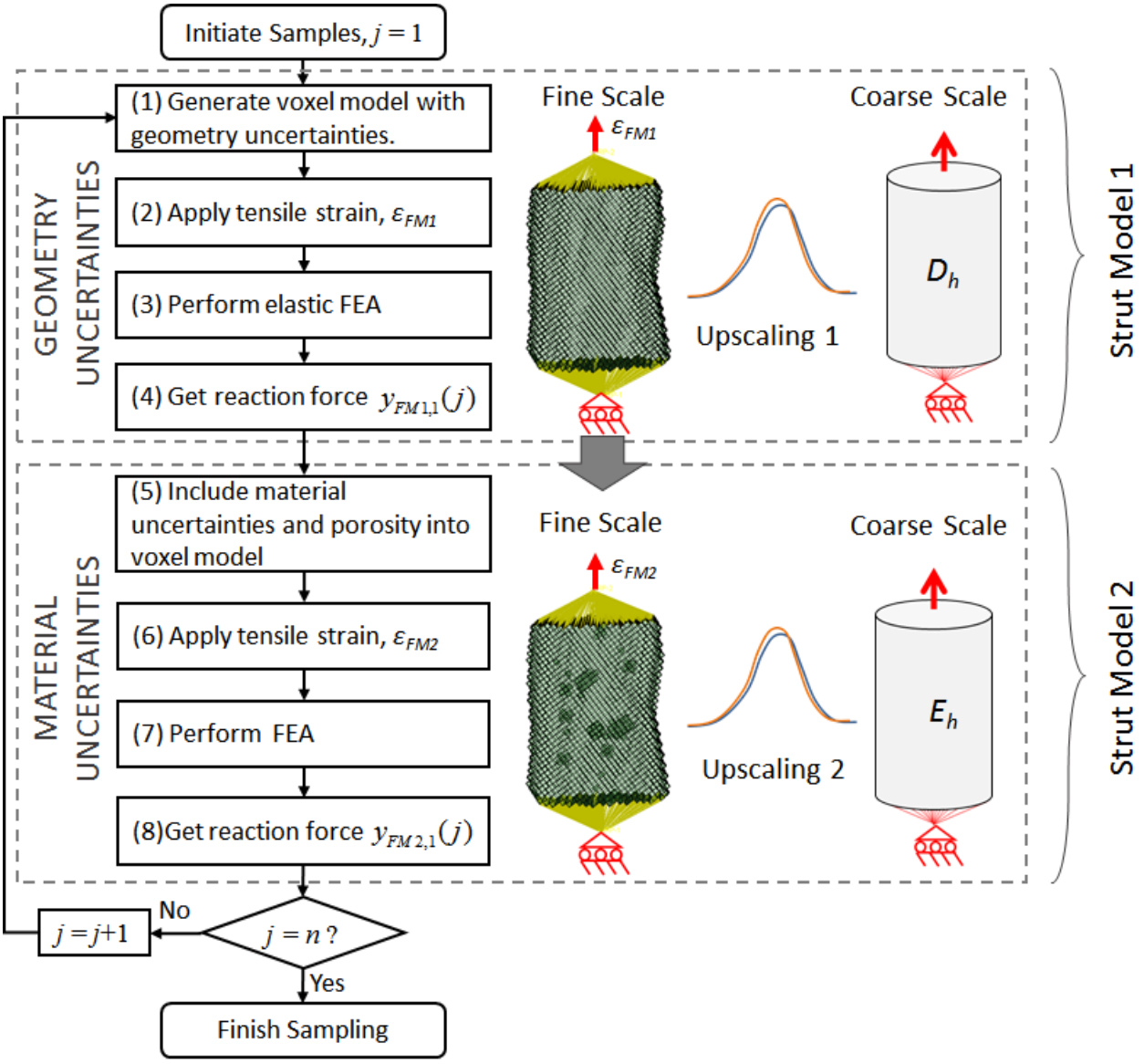

Figure 4.27. Strut level upscaling step.

4.4.6. Strut Level Validation Step

The goal of the strut level validation is to evaluate the accuracy of the predictions made by the coarse scale model at strut level with the homogenized diameter and elastic modulus against the results of these reconstructed models from CT-scan images. The FEA of 20 reconstructed strut models were carried out under a tensile strain of 0.1% and the reaction forces were obtained as the validation data. In these validation models, the lateral degrees of freedoms at the top and bottom surfaces of struts were also fixed in the FEA of struts. These reconstructed strut models have a length of 1.7 mm and a mesh size of 27.06 μm, which is finer than the mesh size of 54.12 μm used in the fine scale models in the upscaling method. Thus, the validation model will be different from the upscaling model to challenge the problem.

For validation, the corresponding coarse scale model of the struts with homogenized properties were created using beam elements and simulated under the tensile test boundary conditions described above. Before generating the coarse scale strut model in the validation step, the uncertainties of the homogenized properties were quantified using the BIC method. The distribution types and statistical parameters of the homogenized properties are listed in Table 4.9.

Table 4.9. Statistical parameters and distribution types for the homogenized strut properties

Homogenized Property	***Mean***	***Standard Deviation***	***Distribution***
Diameter (mm)	0.6375	0.00686	Normal
Elastic Modulus (GPa)	63.541	2.4415	Normal

These statistical parameters were used to generate the samples for the homogenized properties of the coarse scale strut model that is used in the validation step. The coarse scale model reaction force values are collected from 200 simulations to generate the prediction CDF using BIC method.

The proposed validation metric, along with u-pooling and the K-S test, were used to evaluate of the validity of the predictions made by the FE model. The *u* values of 20 reconstructed model results are computed using the prediction CDF. The ECDF of the *u* values are compared with the target distribution in Figure 4.28.

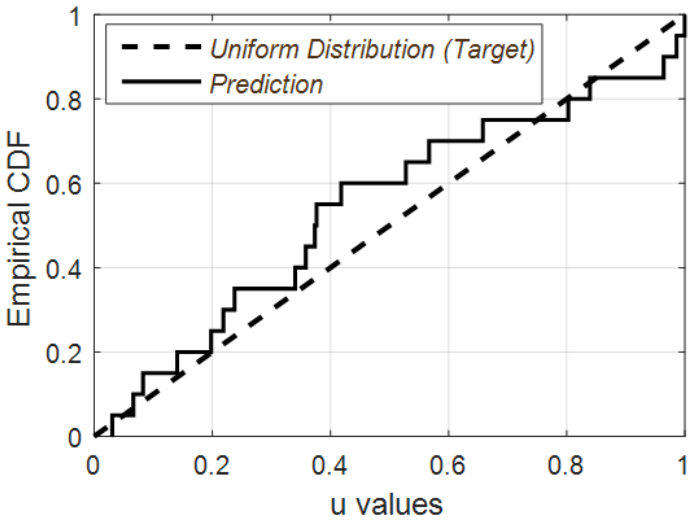

Figure 4.28. Strut level validation results with reconstructed models.

As seen in Figure 4.28, the u-pooling results agree well with the target SUD. The confidence level α was set to 0.05 and the maximum distance between the two distributions was found to be 0.1818, which produces a *p*-value of 0.4686. Since the *p*-value is greater than the α value, K-S test accepts the predictions. Thus, it is concluded according to the K-S test that the coarse scale strut model developed based on the quantified uncertainties has a good accuracy and can be used for developing the lattice level fine scale model.

4.4.7. Lattice Level Upscaling Step

At lattice level, the upscaling method is utilized again for the lattice cell model to find the homogenized coarse scale model properties $X_{CM,1}$. The uncertain parameters of the homogenized

diameter and elastic modulus are used to model the struts in the fine scale lattice model with smooth and constant cross-sections. At fine scale, three FE modeling approaches with quadratic tetrahedral elements are investigated to predict the effective elastic modulus of the fabricated CLS (Figure 4.29). It was observed that the fabricated specimens have missing struts on the corners of the structure that occur during the removal process of the specimen from the SLM machine (Figure 4.29(a)). To account for their effect on the overall elastic modulus of the fabricated CLS, the simulation of the lattice structure was carried out by removing the corner struts from the entire lattice structure FE model (Figure 4.29(b)). In addition, the FE model of the entire CLS (Figure 4.29(c)) is simulated for a comparison. However, these models are still computationally very expensive even if homogenized strut properties are used. Hence, a unit BCC cell (Figure 4.29(d)) is considered as the lattice level fine scale model.

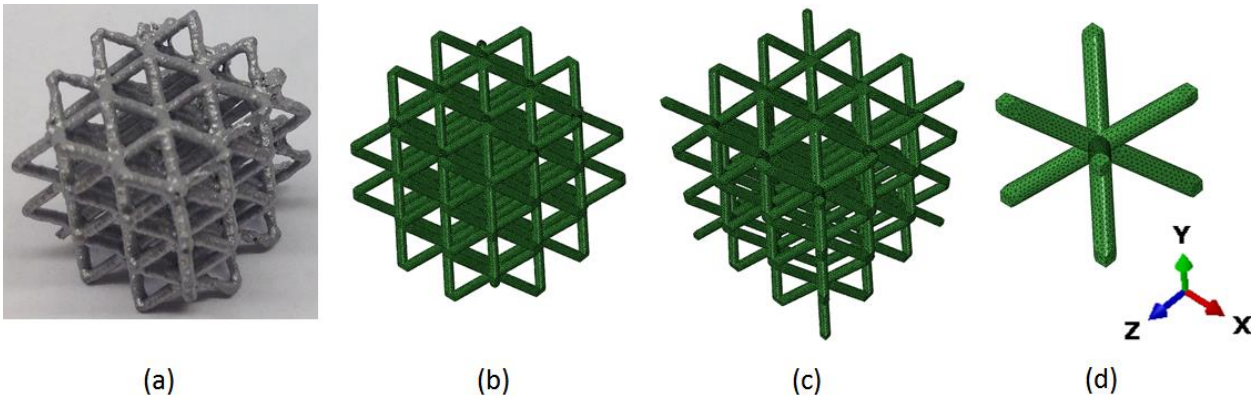

(a) Fabricated CLS using SLM. (b) Fine scale model of the CLS with missing corner struts to have a realistic modeling of the fabricated structure. (c) Fine scale model of the entire CLS that is represented by the unit cell model. (d) Fine scale model of the CLS using only one BCC cell to decrease the computational cost.

Figure 4.29. FE models of the CLS fabricated by SLM.

Periodic boundary conditions (PBCs) were applied on the unit cell FE model. A compression strain of 0.1% was applied in one direction to simulate the experimental procedure. The resulting reaction forces were obtained from the FE analyses. Quadratic tetrahedral elements were used to mesh the structure. A mesh convergence study was conducted to determine the optimal size of the mesh elements before using the fine scale model in the upscaling process. The deterministic values were used for the diameter and material properties in the mesh convergence study. It was found that a mesh size that was equivalent to a quarter of the diameter (i.e. 0.25xD) was appropriate based on the mesh convergence study.

A prediction accuracy study is needed to check if the unit cell model can produce accurate results when compared to the model of the entire CLS. The unit cell model and the lattice structure model were generated using the mean values of the homogenized diameter and elastic modulus of the struts given in Table 4.9. The resulting reaction forces were obtained from their deterministic FE analyses. At the coarse scale, each unit cell is represented with one hexahedral solid element with the same cell dimensions. This corresponding coarse scale model of the unit cell, which consists of only one hexahedral element with the BCC cell dimensions, was also simulated with PBCs. The elastic modulus value of this coarse scale model that enables the match between the coarse scale model reaction force and fine scale model reaction force was determined under a compression strain of 0.1%. Similarly, the coarse scale model of the entire lattice structure was generated by 3x3x3 hexahedral solid elements to determine the corresponding coarse scale model elastic modulus. The elastic modulus value of the corresponding coarse scale model (E_h) for each fine scale lattice model was normalized by dividing by the bulk material elastic modulus, E_0=65 GPa, and compared in Figure 4.30.

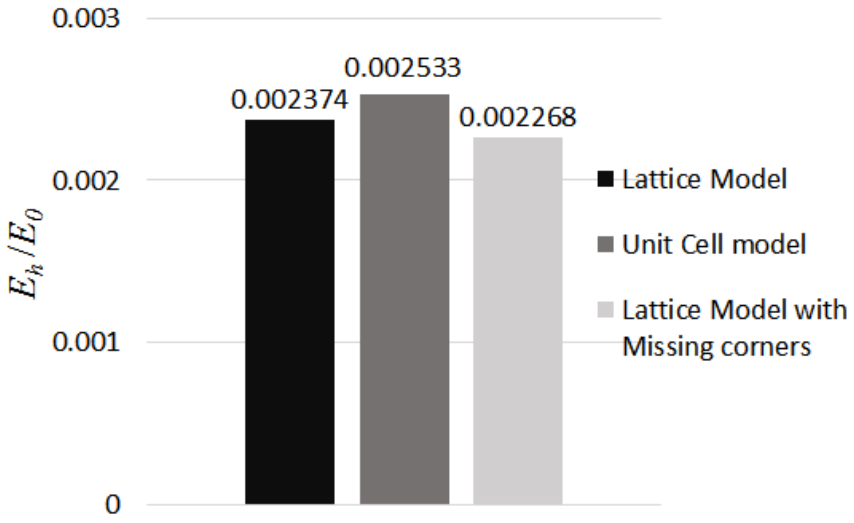

Figure 4.30. Normalized elastic modulus results obtained by three fine scale modeling approaches.

The results in Figure 4.30 show that the lattice structure model with missing corners, which is the model of the fabricated specimens, have the smallest elastic modulus value. The relative modeling error compared to the entire lattice model prediction was found to be 4.5%. It was also found that the unit cell model with PBCs produce an elastic modulus value greater than that of the entire lattice structure model. The relative error between the unit cell model and the lattice structure model was calculated as 6.3%. Furthermore, the relative error between the unit cell model and the lattice model with missing corner struts was 10.5%. That means at the lattice level, the homogenized statistical elastic modulus data of the CLS, which will be used in the validation step to compare with the experiments, can be found as 89.5% of the homogenized elastic modulus data found by upscaling method with the unit cell model. This modeling error between the unit cell model and the lattice model with missing struts will be accounted for the prediction of the realistic mechanical performance of the fabricated CLS under uncertainties.

Once the modeling error is determined deterministically, the stochastic upscaling method is implemented for the unit cell model to quantify the uncertainty of the homogenized elastic

modulus of the CLS specimen. The fine scale model of the CLS, which is the unit BCC cell with PBCs, is simulated for 200 samples generated for the homogenized strut properties using LHS. For each sample, the diameter and elastic modulus of each strut in the unit cell was assumed to be the same but changing with the sampling point depending on the distributions of the homogenized strut diameter and elastic modulus given in Table 4.9. The total reaction force value on one face of the unit cell is obtained as the fine scale response, $Y_{FM,1}$. A hexahedral brick element at the same size as one BCC cell is modeled with PBCs as the coarse scale model and the corresponding elastic modulus is projected onto a second order PCE. The unknown elastic modulus data of the coarse scale model is obtained from the PCE predicted using the upscaling process.

4.4.8. Lattice Level Validation Step

In order to identify the elastic properties of the BCC lattice structure specimens fabricated by SLM, a standard quasi-static uniaxial compression test was conducted. Experiments were carried out on as-fabricated lattice structure samples at room temperature using an Instron 5566 testing system. The force (F_{exp}) and change in gauge length (i.e. compressive strain) were recorded as the experimental results. Uniaxial compression engineering stress, σ, was calculated as the ratio of the force to one surface area, $A_{lattice}$ = 144 mm^3 of the specimen. Then, the effective elastic modulus ($E_{lattice}$) was calculated through the compression tests by

$$E_{lattice} = \frac{\sigma}{\varepsilon} = \frac{\sigma_b - \sigma_a}{\varepsilon_b - \varepsilon_a} \tag{4.10}$$

where ε is the compression engineering strain, σ_a is the stress at ε_a and σ_b is the stress at ε_b. Strains were taken as ε_a = 0.01 and ε_b = 0.025 from the linear region of the compression curves of four

lattice structure experiments shown in Figure 4.31. The mean and standard deviation of the experimental elastic modulus were calculated and compared in Table 4.10 with the ones calculated from the lattice level upscaling method that considers the modeling error. The mean value of the predicted data has only a 1.3% difference when compared to the experimental results, agreeing well with the experiments. For the elastic modulus data obtained from the lattice level upscaling method, the BIC method is used to predict the corresponding distribution type and the statistical parameters, as listed in Table 4.10.

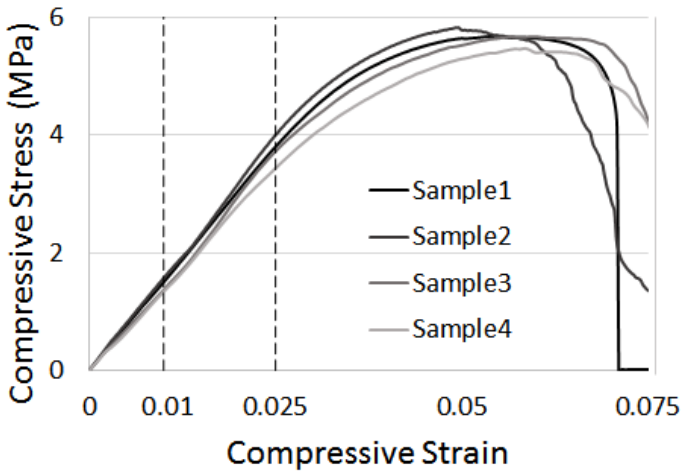

Figure 4.31. Compression test curves of four lattice structure specimens.

Table 4.10. Statistical parameters for the homogenized properties of BCC cell

Lattice Elastic Modulus (MPa)	*Mean*	*Standard Deviation*	*Distribution*	*Parameter a*	*Parameter b*
Experiment	153.0045	8.1848	-	-	-
Upscaling	154.1038	9.4339	Gamma	267.9302	0.575164

In order to evaluate the predictive capability of the coarse scale model of the lattice structure, the predicted responses from the compression simulation of the lattice structure must be compared to the experimental results rather than evaluating the predicted homogenized elastic modulus. For this purpose, a coarse scale model of the entire lattice structure specimen was generated, as illustrated at the top level of the validation pyramid in Figure 4.13. 200 samples were generated for the homogenized elastic modulus, and compression simulations were carried out for the coarse scale lattice model. A compression strain of 0.1% was applied in the simulations and the reaction force ($Y_{CM,1}^{(1)}$) was obtained from 200 simulations. The BIC method was used to predict the distribution model of the reaction force data. The experimental reaction force values for 0.1% strain were obtained from the compression curves of experiments. There exist n_e=4 experiments performed for one validation site (i.e. n_V=1), which gives n_T=4 experimental results in total. Then, the inverse CDF values of these four experimental reaction force values were calculated as the *u*-values from the predicted CDF of the reaction force. Empirical CDF of the *u*-values is calculated and compared with the SUD in Figure 4.32(a). The K-S test was implemented for the u-pooling results obtained from three different modeling approaches, i.e. entire lattice model, unit cell model, unit cell model by accounting for the modeling error. For the latter case 10.5% modeling error is taken into consideration for finding the homogenized elastic modulus of the lattice cell after the upscaling step. Then, the coarse scale model in the validation step is simulated using the predicted elastic modulus that accounts for the modeling error. The results for the K-S test are listed in Table 4.11 for each modeling approach.

The results in Figure 4.32(a) show that the ECDF predictions made by the unit cell model, shown by the dash-dot line, largely deviates from the target distribution if the modeling error is not considered. On the other hand, the CDFs of the full lattice model predictions and unit cell

model predictions with modeling error, tend to follow the target distribution, as shown by dotted line and solid line, respectively. According to the K-S test results in Table 4.11, the CDFs of all models are accepted as the corresponding *p*-values are smaller than the α value, which is set to 0.05. The reason is that the K-S test decision is made by accounting for the number of experiments. For a small number of experimental results, the K-S test enlarges the acceptance margin. Hence, for one validation site where there are only four experimental results, a large acceptance margin is calculated, which accept the predictions of all three models. In addition, the full lattice structure and unit cell models with modeling error have very close K-S statistic values (0.3157 and 0.3207, respectively), which are smaller than the value obtained for the unit cell model without the modeling error. This means that the former two models provide better predictions. However, since the K-S test statistic values are very close for these two, a comparison between them is not possible for one validation site. Thus, these observations suggest that using one validation site where only four experimental results exist may not be effective in prediction assessment. The number of experiments must be increased to have more reliable decisions; however, this will increase the experimental cost. A better method is to use multiple validation sites from the same experiments, i.e. to obtain experimental results for different strain values.

For this purpose, three validation sites are considered (i.e. $n_{VS} = 3$) to increase the number of experimental observations. The coarse scale model of the CLS specimen was simulated for three compression strain values, which are in the elastic region of the compressive curves obtained from the experiments: (1) A compression strain of $\varepsilon_{CM,1}^{(1)} = 0.001$ was applied and the reaction force data ($Y_{CM,1}^{(1)}$) was obtained from 200 simulations. (2) A compression strain of $\varepsilon_{CM,1}^{(2)} = 0.01$ was applied to obtain the reaction force data ($Y_{CM,1}^{(2)}$) as the second validation site. (3) A compression strain of

$\varepsilon_{CM,1}^{(3)} = 0.025$ was applied to compute the reaction force data ($Y_{CM,1}^{(3)}$) as the third validation site. These three strain values are considered because the first one was used in the upscaling process to predict the homogenized elastic modulus while the second and third ones were used to calculate the experimental elastic modulus value by Eq. (4.10). There exist four experimental reaction force values n_e = 4 for each validation site, which gives n_T = 12 experimental results in total. Then, the u-pooling method was used to find the ECDFs of all validation sites for three modeling approaches. Those results are compared with the SUD in Figure 4.32(b). Then, the K-S test was implemented and the decision results for three validation sites are listed in Table 4.12.

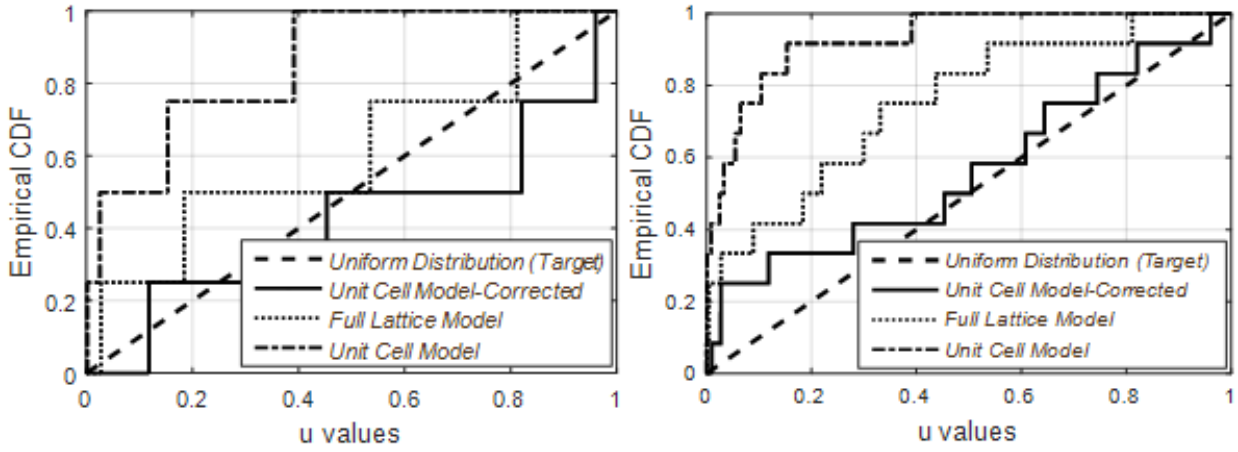

(a) ECDF results with only one validation site, i.e. $\varepsilon_{CM,1}^{(1)} = 0.001$. (b) ECDF results with three validation sites, i.e. $\varepsilon_{CM,1}^{(1)} = 0.001$, $\varepsilon_{CM,1}^{(2)} = 0.01$ and $\varepsilon_{CM,1}^{(3)} = 0.025$.

Figure 4.32. U-pooling results for the lattice structure models

Table 4.11. K-S test results for one validation site, i.e. $\varepsilon_{CM,1}^{(1)} = 0.001$

Model	***K-S Statistic***	***p-value***	***Decision***
Unit Cell	0.6087	0.0606	Accept
Full Lattice Structure	0.3157	0.7207	Accept
Unit Cell with Modeling Error	0.3207	0.7044	Accept

Table 4.12. K-S test results for three validation sites, i.e. $\varepsilon_{CM,1}^{(1)} = 0.001$, $\varepsilon_{CM,1}^{(2)} = 0.01$, **and** $\varepsilon_{CM,1}^{(3)} = 0.025$.

Model	***K-S Statistic***	***p value***	***Decision***
Unit Cell	0.7632	8.26E-4	Reject
Full Lattice Structure	0.4182	0.0204	Reject
Unit Cell and Modeling Error	0.2226	0.5211	Accept

As seen in Figure 4.32(b), similar to the one validation site results, the ECDF of the unit cell model predictions, shown by dot-dash line, also deviates largely from the target distribution for three validation sites. Unlike the case of one validation site, on the other hand, the ECDF of the full lattice model, shown by dotted line, also deviates from the SUD for three validation sites. Only the ECDF of the unit cell model that accounts for the modeling error, shown by the solid line, has the following trend with the SUD. Hence, the results given in Table 4.12 show that K-S test accepted only the predictions made by the unit cell model with the modeling error considered. The K-S statistic value is also the smallest for the unit cell model with the modeling error (i.e. 0.2226). The CDFs of the full lattice structure model predictions and unit cell model predictions for three validation sites are rejected as the calculated *p*-value is smaller than α=0.05 value. Thus, it is clear that the unit cell model that accounts for the modeling error can predict the reaction forces

accurately for three different strain values in the elastic region of the compression curve of the lattice structure, while the other models fail to make accurate predictions.

These results clearly show the advantage of the proposed validation approach that utilizes multiple validation sites and the K-S test: Having multiple validation sites was very effective in minimizing the experimental cost and distinguishing model predictions because there were twelve experimental results in this example, which narrowed down the acceptance margin of the K-S test, and also enabled a better representation of the CDFs even though only a few physical experiments are conducted. Thus, these results prove that the proposed methodology that utilizes the uncertainty quantification approach using the 3D strut models reconstructed by the CT scan images, the stochastic upscaling method, and the proposed validation approach used at multiple levels of scales provides an accurate prediction of the mechanical behavior of SLM-fabricated CLSs with minimal experimental cost.

4.5. Summary

Local geometric variations and uncertainties of the struts have considerable effect on the effective material properties of the CLSs. The realistic design of a CLS is therefore only possible when accurate material data is available. On the other hand, gathering accurate material data that is used in the design can be costly. To address this issue, a multi-level validation methodology is presented in this chapter. In Section 4.1, the multi-level validation framework that integrates the validation pyramid approach with the stochastic upscaling method is described. In Section 4.2, the proposed validation metric based on u-pooling method and K-S test is introduced. In Section 4.3, the flowchart of the validation step used at each scale level from bottom up is described. The efficacy of the presented validation framework has been shown on the material characterization of a simple

cubic (SC) – cellular lattice structure (CLS) specimen fabricated by material extrusion process in Section 4.4. In this example, the input uncertainties of the strut level fine scale model are assumed to be normally distributed. Two different strut level models and two different lattice level models are considered in the prediction of the homogenized material properties of the CLS to investigate the applicability.

The developed multiscale validation approach has shown that at the strut level, *Strut Model 2*, which includes both geometric and material imperfections of the fabricated struts, is the accepted strut model for the lattice structure. Both *Lattice Models 1* and *2* are accepted at macroscale level based on the validation experiments. Moreover, it was found that *Lattice Model 2*, in which the lattice is modeled using quadratic tetrahedral solid elements instead of the beam elements, provides better agreement with the target distribution. Thus, the applied procedure successfully identified the homogenized diameters and material properties while matching the responses between fine and coarse scale models accurately.

The SC-CLS example shows that the K-S test can provide an unbiased decision criterion since its statistic is calculated based on the number of experiments. It is shown that the area metric fails to make a correct decision when the number of experiments is small since the threshold for the decision criterion is chosen as a constant value by the designer. However, the area metric is preferred to provide a better comparison between different alternative models that are validated based on the K-S test. Thus, it is concluded based on these observations that the K-S test is very useful when making a decision for the validation of the computational models with minimized experimental cost, while the area metric can be used to determine the most accurate model if there is more than one accepted model based on the K-S test.

In Section 4.5, the proposed multi-level validation and upscaling approach is utilized for BCC lattice structure specimen fabricated by SLM process along with the strut level uncertainty quantification process using micro-CT scan images. To minimize the experimental cost, as a non-destructive experimental technique, the micro-CT scan was successfully applied to obtain cross-sectional images of lattice structures fabricated by the SLM process. The reconstructed 3D dataset from preprocessed 2D images were applied to characterize the uncertainties on the geometric variations on the strut surface and the pore structure in strut material. The uncertainties on the struts were identified based on the individual strut models reconstructed from the CLS specimens instead of the additionally fabricated individual strut specimens, which greatly decreased the experimental cost and effort to characterize the strut level properties. The corresponding uncertainties on the strut diameter, angle, and porosity are successfully quantified with parametric distribution models using the BIC method and used for fine scale FE model development of struts to achieve inherent relationships of pores and strut geometry. Thus, it became possible to generate and simulate a realistic 3D strut model of the fabricated structure using the statistical sampling method to minimize the experimental cost.

The applied upscaling procedure has successfully identified the homogenized diameters and elastic moduli at both strut level and lattice structure level while ensuring the accurate matching of the responses between the fine and coarse scale models. The simulated lattice structures with homogenized properties obtained from the upscaling process gave a good estimate with test data obtained for the fabricated CLS specimens when the modeling error is considered in computations. These observations show that a systematic validation approach that accounts for uncertainties with minimal experimental cost is critical for accurate predictions from the multi-level upscaling process of the CLSs. The use of multiple validation sites enables the evaluation of

the prediction capability of models with more experimental observations, even if the number of physical experiments is limited. The u-pooling method enabled the comparison of all of the validation sites with the target distributions at the same time, which greatly facilitated the validation process by minimizing the experimental cost. Although the presented CLS example is fabricated from the SLM process, the proposed approach can be applicable to the most AM processes and is not limited to specific materials. The presented upscaling method for uncertainty quantification and multi-level validation procedure have significant potential to effectively certify the additively manufactured CLSs while minimizing the experimental cost, thus enabling the efficient consideration of uncertainties in the design of the AM-fabricated parts for critical engineering applications.

CHAPTER 5. APPLICATION OF UPSCALING METHOD TO DESIGN CLS

5.1. Introduction

The objective in this chapter is to address the *Research Question 3*, which is posed to investigate the applicability of the proposed multi-level upscaling method for designing lattice structures. As stated in *Hypothesis 3*, the upscaling method can be utilized to develop a PCE-based meta-model of the homogenized material properties of the lattice structures with the quantified uncertainties. This stochastic meta-model can then be used to match the target modulus of an engineering structure as an application example to show the benefit of the proposed approach.

As AM offers a wide range of design possibilities, for better performance under the conflicting requirements, optimization methods are desirable to be able to design the optimal structure of CLSs. Hence, there has been some progress on using optimization to solve the CLS design problems as explained in Section 2.5. Topology optimization can be used to design optimal structures for particular purposes by minimizing a suitable objective on the topology without any constraint on the porosity.

Despite the advantages of AM techniques to fabricate the designed CLSs with complex geometry, the designed mechanical performance of the CLSs show difference compared to the AM-fabricated CLS performance. The reason is the variations on the geometry and imperfections in the materials due to the layer-by-layer manufacturing process. These effects not only produce a deterministic difference but also induce increased uncertainties on the performance of the fabricated CLSs. More specifically, when AM techniques are used for fabrication of these designs

with optimized lattice cells, although the lattice cell strut cross-sectional parameters such as diameter values are set deterministically in the CAD model, the material and geometry of the AM-fabricated struts will have uncertainty due to the layer by layer manufacturing process. Therefore, the details of the variations and imperfections have to be considered while developing the computational models used in the optimization processes to accurately predict the fabricated CLS performance. However, these details increase the computational burden and prohibits the design of CLSs using optimization methods especially when the uncertainties are involved.

The aim of this chapter is to show the applicability of the proposed multi-level upscaling framework for designing CLSs that does not require the computationally expensive optimization process while efficiently accounting for the uncertainties induced by the AM process. The theoretical foundations of the PCE-based meta-modeling approach is presented in Section 5.2. The effect of the unit cell size and the porosity on the homogenized elastic modulus of the CLS was investigated with the quantified uncertainties at multiple scale levels using the stochastic upscaling method to develop the meta-model in Section 5.3. The developed meta-model approach is utilized for the lightweight design of the fuselage structure of a micro-aerial vehicle (MAV) as an application example to match the target elastic modulus of an existing design in Section 5.4.

5.2. PCE-based Meta-Model Approach

Homogenized coarse scale input variables determined by the proposed stochastic upscaling method involves uncertainties represented by the PCE. Therefore, conventional meta-modeling techniques, which are trained by using deterministic input and response data are not applicable when the training data involves uncertainties. In order to overcome this problem, in this research, a PCE-based metamodeling approach, which was first introduced for RBDO problems by [142],

[143], is adapted for the prediction of the homogenized properties with uncertainties. In RBDO, the PCE-based meta-models substitute the actual expensive model in the reliability computation phase, and thus help in reducing the total cost of the calculation of the reliability of the response. Unlike the approach in [142]-[144] that use this PCE-based metamodeling approach to eliminate the expensive model evaluations while predicting the probability of failure of the response of the structure, our purpose is to eliminate the expensive model evaluations in the upscaling method to find the homogenized properties of the lattice cell for the optimal design with the quantified uncertainties in the fabricated strut members. This PCE-based meta-modeling technique is very suitable in our framework since the upscaling method quantifies the uncertainties of homogenized properties using PCE representations. Thus, with the PCE-based meta-models of the homogenized properties, the uncertainties can be propagated to the macroscale level FEA without requiring the expensive simulations of the computational models.

In the RBDO problems the stochastic structure response is dependent on some deterministic design variables denoted by X as described in Section 2.5.4.2. with Eq. (2.80). Similarly, in the context of designing CLSs, the uncertain homogenized properties (i.e. the coarse scale input variables), denoted by X_{CM}, which are estimated by the upscaling method, depend on some deterministic design variables, X, defined for the created CAD model of a CLS. Then, the PCE representation of a coarse scale homogenized input variable given by Eq. (3.17) in the upscaling method is rewritten as follows:

$$X_{CM}(X,\xi) = \sum_{k=0}^{P} b_k(X)\Phi_k(\xi) \tag{5.1}$$

where the coefficients (b) are found by the upscaling approach as explained in Section 3.1. To develop the PCE-based meta-modeling approach, first the PCE projection of the homogenized input variable X_{CM} is established for a set of design variables X in the design variable domain with the corresponding random variables ξ. Let the design variable sets in the variable domain is denoted by $X = \left\{X^{(i)}\right\}, i = 1,2,...,q$ where q is the total number of generated design variable sets. Then, the PCE models of the homogenized variable for the corresponding design variables are given by

$$X_{CM}(X^{(i)}, \xi^{(i)}) = \sum_{k=0}^{P} b_k(X^{(i)}) \Phi_k(\xi^{(i)}) \tag{5.2}$$

The random variable samples for each corresponding design variable set are denoted by $\xi^{(i)} = \left\{\xi_j^{(i)}\right\}, j = 1,2,...,n_s$ where n_s is the number of samples generated to represent uncertainties. In matrix form, this leads to:

$$\begin{Bmatrix} X_{CM}(X^{(1)}, \xi^{(1)}) \\ X_{CM}(X^{(2)}, \xi^{(2)}) \\ \vdots \\ X_{CM}(X^{(q)}, \xi^{(q)}) \end{Bmatrix} = \begin{bmatrix} \Phi_0(\xi^{(1)}) \; \Phi_1(\xi^{(1)}) \cdots \Phi_P(\xi^{(1)}) \\ \Phi_0(\xi^{(2)}) \; \Phi_2(\xi^{(2)}) \cdots \Phi_P(\xi^{(2)}) \\ \vdots \qquad \vdots \\ \Phi_0(\xi^{(q)}) \; \Phi_P(\xi^{(q)}) \cdots \Phi_P(\xi^{(q)}) \end{bmatrix} \times \begin{bmatrix} b_0(X^{(1)}) \; b_0(X^{(2)}) \cdots b_0(X^{(q)}) \\ b_1(X^{(1)}) \; b_1(X^{(2)}) \cdots b_1(X^{(q)}) \\ \vdots \qquad \vdots \qquad \vdots \\ b_P(X^{(1)}) \; b_P(X^{(2)}) \cdots b_P(X^{(q)}) \end{bmatrix} \tag{5.3}$$

or, in compact form:

$$X_{CM}(X, \boldsymbol{\xi}) = \boldsymbol{\Phi}(\boldsymbol{\xi}) \, b(X) \tag{5.4}$$

where $\boldsymbol{\xi}$ is the common set of random samples for each corresponding design variable set in all PCE developments. Once the PCEs are developed for each design variable set generated in the variable domain using the upscaling method, the PCE coefficients can be retrieved by

$$b(X) = \boldsymbol{\Xi}(\boldsymbol{\xi})\, X_{CM}(X, \boldsymbol{\xi}) \tag{5.5}$$

where $\boldsymbol{\Xi}$ is the mapping between the deterministic design variables X and the PCE coefficients b. This mapping can be built using various function approximation methods or meta-modeling methods (e.g. Kriging [142], moving least squares interpolation [143], spline interpolations [144], etc) based on the stored PCE coefficients and design variables. In this study, Piecewise Cubic Hermite Interpolating Polynomial (PCHIP) [223] is used due to its simplicity in one dimensional problems compared to the existing methods for function approximation. The functional relationship of each PCE coefficient can be represented by

$$\begin{Bmatrix} b_0 \\ b_1 \\ \vdots \\ b_P \end{Bmatrix} = \begin{bmatrix} f_0(X) \\ f_1(X) \\ \vdots \\ f_P(X) \end{bmatrix} \tag{5.6}$$

where $f_P(X)$ denotes the meta-model developed by PCHIP method for the k^{th} PCE coefficient in Eq. (5.2). In compact form, this is shown by

$$b = f(X) \tag{5.7}$$

Once the meta-models are developed for the PCE coefficients, the coefficient values at a given design point X^* can be estimated on-the-fly using Eq. (5.6) to reconstruct the PCE representation of the corresponding homogenized variable X_{CM}:

$$X_{CM}\left(X^{*},\xi\right)=b_0^{*}\Phi_0(\xi)+b_1^{*}\Phi_1(\xi)+\ldots=f_0(X^{*})\Phi_0(\xi)+f_1(X^{*})\Phi_1(\xi)+\ldots \quad (5.8)$$

This approach of using meta-models for PCE coefficient estimation at a design point is shown in Figure 5.1 for one dimensional input space. Thus, the computational cost can be mitigated by avoiding the expensive simulations for estimating the homogenized properties at the corresponding the design variable points.

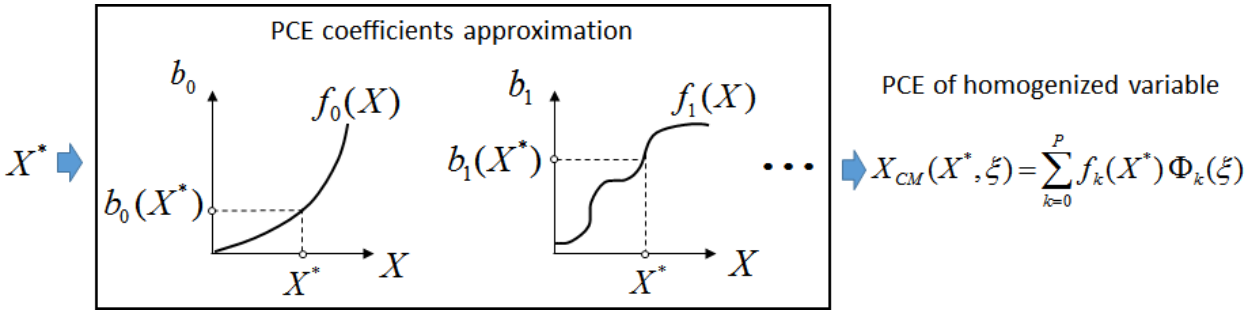

Figure 5.1. Approximation of the PCE coefficients of homogenized variable for a design point *X using PCE-based meta-modeling approach.**

5.3. PCE-based Meta-Model for BCC Lattice Cell

The BCC lattice cell fabricated by SLM is of the consideration of this chapter to develop the meta-model for its homogenized elastic modulus. Two deterministic design variables on the lattice cell CAD model are considered for CLS design: The lattice cell model density, ρ_M, and the lattice cell size, L_M. For the design of the BCC lattice cell, the diameter of each strut in the cell is assumed to be the same as the fabrication angle of the struts in BCC cell are all equivalent. Then, one diameter, D_M, can be calculated from the density of the unit cell, ρ_{FM} to generate the lattice cell model for the given cell length.

Since uncertainties induced by the AM process parameters exist on the strut geometry and material of the lattice cells, it is important to consider these uncertainties in the computer-aided

design stage to have accurate solutions. The stochastic upscaling method and the PCE-based meta-model approach described in Section 3.3 and Section 5.2, respectively are implemented as illustrated in the framework in Figure 5.2 to characterize the elastic modulus of the BCC lattice cell with uncertainties.

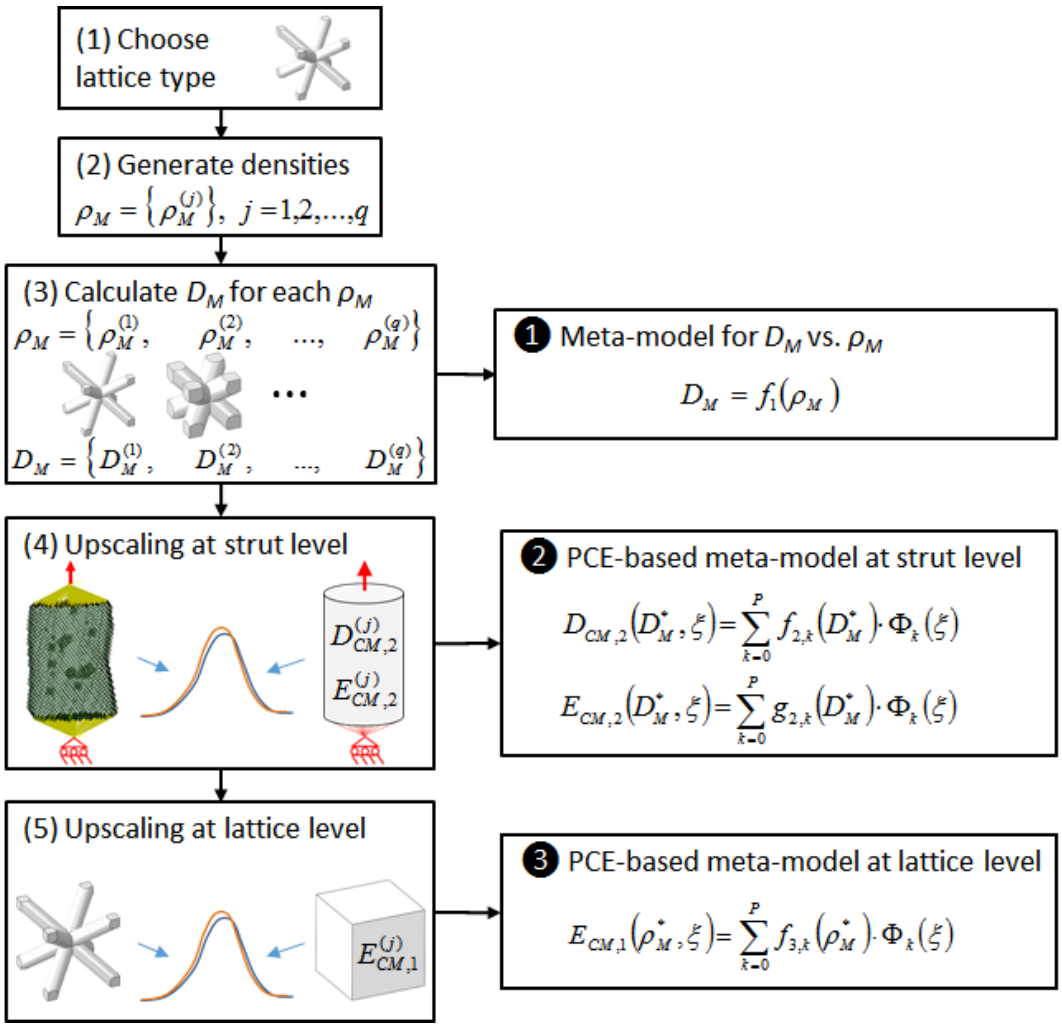

Figure 5.2. Multi-level PCE-based meta-model development framework.

The flowchart involves 7 steps to develop the PCE-based meta-models of the effective elastic modulus of the lattice cell with propagated uncertainties from the strut level:

Step (1). Choose the lattice type that will be used in the metamodeling approach: The BCC lattice cell described is used in this study.

Step (2). Generate a set of model density values, $\rho_M^{(j)}$, in the range of [0,1] for a given lattice cell length: The density values generated in this study are $\rho_M^{(j)}$={0, 0.05, 0.1, 0.2, 0.3, 0.4, 0.5, 0.6, 0.7, 0.8, 0.9, 0.99, 0.999, 1} for lattice cell length values L_M = {1, 2, 3, 4, 5, 7.5, 10}.

Step (3). Calculate the model diameter values, $D_M^{(j)}$, corresponding to each model density value $\rho_M^{(j)}$: The model diameter values are required to generate the CAD model of the lattice cell that will be used for FE analysis for the corresponding density value. To calculate the corresponding diameter for each density, first a function approximation process is performed. For this purpose, the lattice cell CAD model is generated with various diameter values. The corresponding lattice cell volume of each generated model is obtained from Abaqus software and divided by the total cubic cell volume to calculate the corresponding density. Then, the diameter values and corresponding density values are saved as a database. The diameter values, $D_M^{(j)}$ for the corresponding density values, $\rho_M^{(j)}$, generated in Step 2 are calculated by interpolating using PCHIP method [223] based on this database.

Step (4). Apply the stochastic upscaling method described in Section 3.1 at strut level for each model diameter value, $D_M^{(j)}$, calculated in Step (3): The upscaling method is utilized at strut level to predict the homogenized strut diameter $D_{CM,2}$, and strut elastic modulus, $E_{CM,2}$, (where subscripts *CM* and *2* stands for the coarse scale model and strut level, respectively) of a coarse scale model that can represent the fine scale strut model. The two step upscaling process described in Section 4.4.5 and shown in Figure 4.27 is used.

Then, the model diameter data D_M, calculated in Step (3), and the corresponding PCE coefficients obtained in strut level upscaling step are used to construct the meta-models. PCHIP method is used as the meta-model approach as stated in Section 5.2. The PCE-based meta-models are developed to predict the homogenized diameter, $D_{CM,2}$, and elastic modulus, $E_{CM,2}$, at strut level. These homogenized variables can be estimated for a given model diameter, D_M^*, using Eq. (5.8):

$$D_{CM,2}(D_M^*, \xi) = \sum_{k=0}^{P} f_{2,k}(D_M^*) \cdot \Phi_k(\xi) \tag{5.9}$$

$$E_{CM,2}(D_M^*, \xi) = \sum_{k=0}^{P} g_{2,k}(D_M^*) \cdot \Phi_k(\xi) \tag{5.10}$$

where $f_2(.)$ and $g_2(.)$ denote the meta-models for $D_{CM,2}$ and $E_{CM,2}$, respectively.

Step (5). Apply the stochastic upscaling method described in Section 3.3 at lattice level for each $D_M^{(j)}$ value calculated in Step (3): The upscaling method is utilized at lattice level to predict the homogenized elastic modulus, $E_{CM,1}$, (where subscripts *CM* and *1* stands for the coarse scale model and lattice level, respectively) of a coarse scale model that can represent the fine scale lattice cell model. The upscaling process produces the PCE representation of the homogenized elastic modulus $E_{CM,1}$ for each $D_M^{(j)}$ value at lattice level. This lattice-cell model is generated with the homogenized diameter and elastic modulus predicted at strut level for each $D_M^{(j)}$. The lattice level upscaling step for BCC cell fabricated by SLM is described in Section 4.4.

Then, the model density data ρ_M, determined in Step (2), and the corresponding PCE coefficients obtained in lattice level upscaling step are used to construct the PCE-based meta-model of the homogenized elastic modulus $E_{CM,1}$. PCHIP method is used as the meta-model

approach as stated in Section 5.2. The constructed meta-models for each PCE coefficient (Eq. (5.6)) are stored to formulate the PCE of the homogenized modulus for the desired model density, ρ_M^*, that will be used in the design of CLSs. These homogenized variables can be estimated for a given model density, ρ_M^*, using Eq. (5.8):

$$E_{CM,1}(\rho_M^*, \xi) = \sum_{k=0}^{P} f_{3,k}(\rho_M^*) \cdot \Phi_k(\xi) \tag{5.11}$$

where $f_3(.)$ is the meta-model for $E_{CM,1}$.

If necessary, these steps are repeated for various lattice cell sizes, L_M, and also for various lattice cell types that can be considered in the design of CLSs. In contrast to the deterministic relationships between the homogenized values and densities found in the existing studies [42], [77], the stochastic relationships are established with PCE expansions using the proposed approach. The corresponding three meta-models given on the right hand side of Figure 5.2 are explained in the following sub-sections.

5.3.1. Deterministic Relationship between the Model Density and Diameter

As stated in Step 3 of the proposed framework in Figure 5.2, to calculate the corresponding diameter, $D_M^{(i)}$, for each density, $\rho_M^{(i)}$, the solid CAD model of the lattice cell is used. The CAD model of the lattice cell generated for a diameter value can give the accurate volume as opposed to the analytical formulations, which are developed based on some assumptions to simplify the formulation. For instance, Gumruk et al. [86] formulated an analytical formulation of the relative density for BCC lattice cell

$$\rho = \pi \left(\frac{D}{L}\right)^2 \left[\sqrt{3} - 2\left(\frac{D}{L}\right)\tan\theta\left(1 - \frac{\tan^2\theta}{12}\right)\right] \tag{5.12}$$

where θ is the strut angle with respect to the lateral plane, which is 35.264^0 for the BCC cell. The curve obtained from this analytical equation that shows the change of density with the aspect ratio D/L is plotted in Figure 5.3.

This curve obtained by Eq. 6.12 is compared with the CAD model results. For this purpose, the lattice cell CAD model is generated with various diameter values, $D_M^{(j)}$, such that the density, will be in $\rho_M^{(j)} = [0,1]$ for the unit cell sizes in $L = [1,10]$. The corresponding lattice cell volume of each generated model is obtained from Abaqus software and divided by the total cubic cell volume to calculate the corresponding density. It was found that the aspect ratio D_M/L remains the same for different L values. Hence, the aspect ratio values and corresponding density values are saved as a database. PCHIP interpolation method can be used to calculate the aspect ratio value for a new density value. In Figure 5.3, the plotted curve obtained from the interpolation method agrees very well with the curve plotted using the CAD model predictions. The curve from the analytical equation (Eq. (5.12) give good predictions for density values less than 0.2, which was also shown by Gumruk et al. [86], but largely deviates from the CAD model curve when the density value is greater than 0.2. Hence, the PCHIP interpolation method is to be preferred predict the diameter value for a given density value and lattice cell size in Step 3 of the proposed meta-modeling approach.

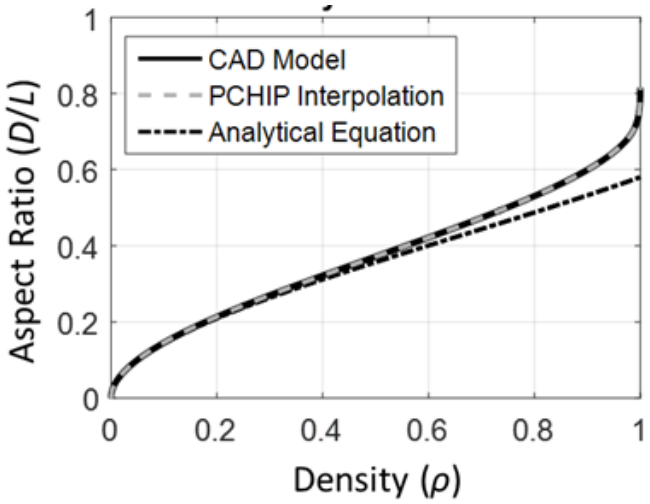

Figure 5.3. Comparison of the aspect ratio vs density curves obtained from CAD model, PCHIP interpolation method and analytical equation in Eq. (5.12).

5.3.2. Homogenized Properties without Uncertainties

Before implementing the proposed approach, a deterministic study is conducted to find the functional relationship between the design variables (i.e. the model density and lattice cell size) and the homogenized elastic modulus of the BCC lattice cell. This is the conventional way used in [42], [77], to eliminate the expensive FE simulations in designing CLSs where the AM effects such as uncertainty are not considered on estimating the homogenized elastic modulus of the lattice for a given density. For the model density values $\rho_M^{(j)}$ determined in Step 2 of Section 5.3, the strut diameter values are calculated from the PCHIP method in given Figure 5.3. The CAD model of the BCC unit cell for each corresponding diameter is generated in Abaqus. Then, the FEA of the unit cell model structure is carried out with PBCs and the corresponding deterministic effective elastic modulus is obtained for the coarse scale model. The response surface of the design variables, i.e. unit cell size and model density is depicted in Figure 5.4(a). The homogenized elastic

modulus E_h is normalized by the bulk material elastic modulus, E_0. (e.g. for AlSi10Mg material E_0 = 65 GPa).

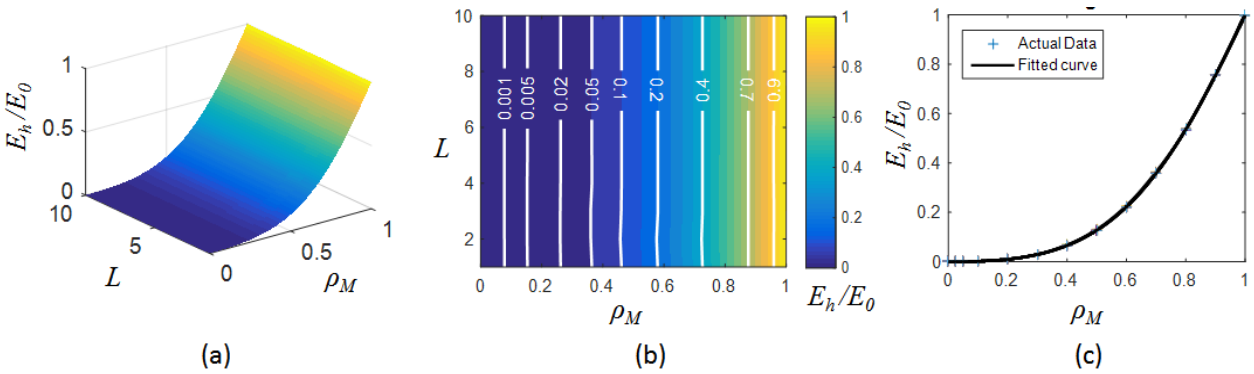

(a) The response surface of the normalized modulus. (b) The contour plot of the response surface. White lines denotes the contour lines of the normalized modulus. (c) The plot of model density vs. normalized modulus.

Figure 5.4. Functional relationship between the design variables and the homogenized elastic modulus normalized by E_0

It is seen from Figure 5.4(a) that the normalized homogenized modulus increases from 0 to 1 with the increase of the density as more material exist in the cell when the density increases. On the other hand, the unit cell size, L, appears to be making no change in the homogenized elastic modulus. This is more visible in the contour plot given in Figure 5.4(b), where the normalized modulus contours are straight lines for various density values. Therefore, a functional relationship between the density and normalized modulus of the lattice cell can be developed (Figure 5.4(c)) independent from the lattice cell length. The fitted curve is obtained by fitting the PCHIP method to the training data.

5.3.3. Homogenized Properties with Uncertainties

Although this deterministic process described in Section 5.3.2 is computationally very efficient to design CLSs as suggested previously in [42], [77], the fabricated structure modulus will differ

from the designed structure because the AM processes induce variations and uncertainties on the fabricated geometry and material properties. To overcome this issue, the proposed framework depicted in Figure 5.2 is utilized for developing the functional relationship between the design variables used for generating CAD models and the homogenized properties at strut level and lattice cell level. At the strut level, the quantified uncertainties of the fine scale model input variables in Section 4.4.4, given in Table 5.1, are used in generating the strut level fine scale model of the SLM-fabricated BCC lattice structures.

Table 5.1. Distributions and statistical parameters of input variables quantified at strut level using BIC

Parameter	Distribution	Mean	Standard Deviation
Short Diameter (mm)	Lognormal	$D_M^{(j)}$+0.172	0.0193
Long Diameter (mm)	Lognormal	$D_M^{(j)}$+0.284	0.0561
Strut Angle (^{0})	Normal	34.898	1.2294
Porosity	Gamma	0.0091	0.0025
Pore Diameter (mm)	Lognormal	0.0594	0.0283

As seen in Table 5.1, the short and long diameters that are used to generate the fine scale strut model have an increase of 0.172mm and 0.284mm, respectively. These increase values were obtained from uncertainty quantification process on the fabricated lattice structures with D_M = 0.5mm in Section 4.4.4. Existing studies [207], [208] that studied the increase of strut diameter in the SLM-fabricated lattice structures show that the increase is constant for different size of diameters for the same processing parameters. Hence, the increase values in Table 5.1 are used for any model dimeter value for the fine scale model generation of struts in the upscaling process as stated also in Section 4.4.4.1. The corresponding PCE coefficients of the homogenized diameter

and homogenized elastic modulus of the coarse scale strut models are determined using the upscaling method for each model diameter value, $D_M^{(j)}$. Then, the meta-models (i.e. PCHIP method) are developed to find the PCE coefficients of the homogenized strut level properties for a given value of the model diameter D_M^* (Eqs. (5.9) and (5.10)). The homogenized modulus is projected onto a second order PCE (i.e. P = 2), which represent the uncertainty with three chaos coefficients (i.e. b_0, b_1, and b_2) for each value of model diameter in the upscaling method. The corresponding meta-models for the PCE coefficients of the homogenized diameter and the normalized elastic modulus at strut level are illustrated in Figure 5.5.

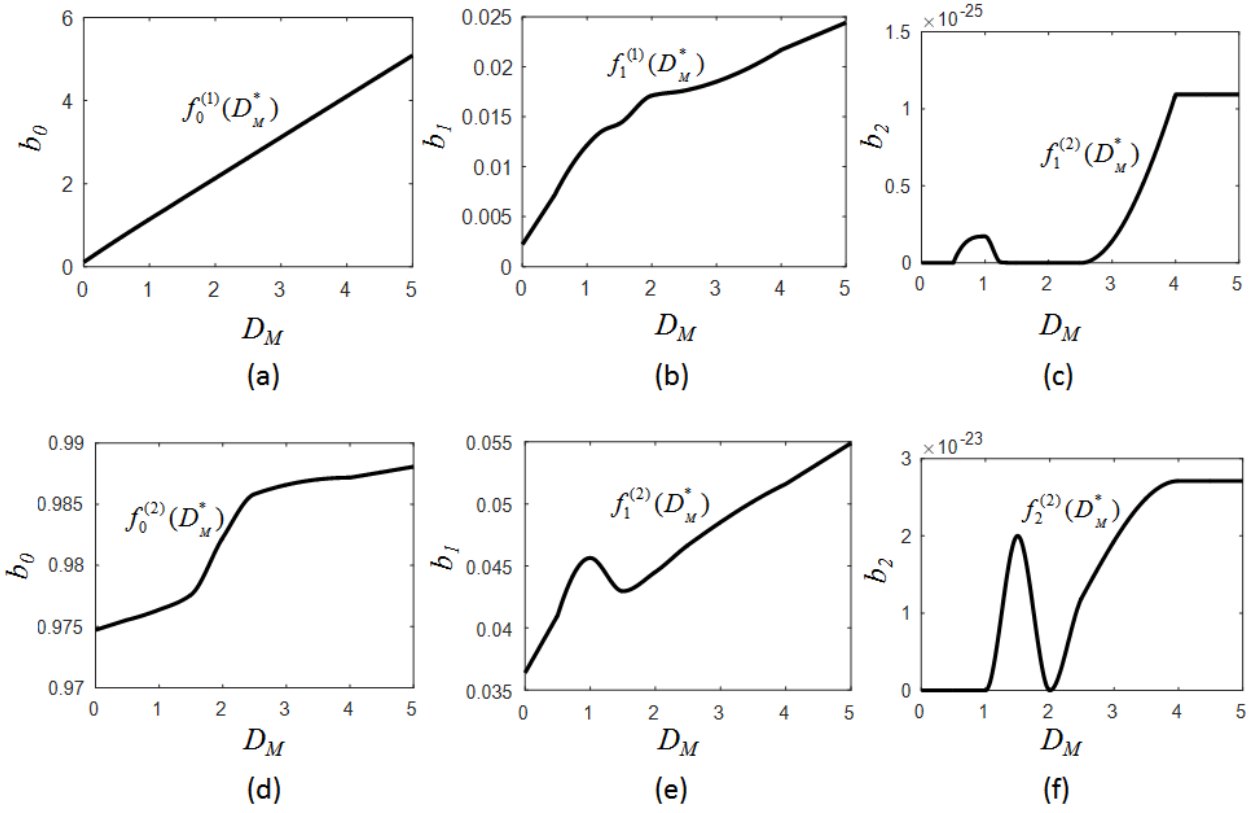

(a)-(c) Curves for homogenized diameter $D_{CM,2}$ (d)-(e) for normalized elastic modulus $E_{CM,2}$

Figure 5.5. Meta-models of PCE coefficients at strut level.

The mean and standard deviation of these homogenized properties can be determined from the PCE meta-models in Figure 5.5 using Eqs. (2.29) and (2.32) in Section 2.2.3, respectively. The last coefficient values in Figure 5.5(c) and Figure 5.5(f) are too small that those can be ignored in the PCE representation. Then the first coefficient gives the mean and the second coefficient gives the standard deviation of the homogenized properties at strut level.

Once the strut level meta-models are developed, those can be used to quantify the uncertainties of the input variables of the fine scale model at the lattice level in the upscaling process in Step 5 in Figure 5.2. The uncertain homogenized elastic modulus of the BCC lattice cell is projected on a second order PCE (i.e. $P = 2$ in Eq. (5.12)), which represents the uncertainty with three chaos coefficients (i.e. b_0, b_1, and b_2) for each value of the lattice cell model density $\rho_M^{(i)}$ and the cell size L in the upscaling method. The resulting PCEs obtained for all of the design variable values (i.e. model density and cell size) show that the last coefficient is either zero or very small. That means the uncertainty of the homogenized modulus can be represented by only using the first two chaos coefficients. Hence, the PCE-based meta-models are developed for coefficients b_0 and b_1. The contour plots of the normalized PCE coefficients by the bulk elastic modulus E_0 are illustrated in Figure 5.6.

For a one-dimensional PCE with Hermite polynomials used in this study, the mean and standard deviation of the normalized elastic modulus simplifies to $\mu_E = b_0$ and $\sigma_E = b_1$ from Eqs. (2.29) and (2.32), respectively. These results imply that the contour plots given in in Figure 5.6(a) and Figure 5.6(b) represents the mean and standard deviation of the normalized modulus of the fabricated BCC lattice structure, respectively. In this case, it is seen that the contours of the mean of the modulus in Figure 5.6(a) show differences when compared to the contour plot of the

modulus in Figure 5.4(b) where the uncertainties are not considered. The comparison of these figures indicates that the elastic modulus shows dependence to the lattice cell length when the homogenization process accounts for the uncertainties as opposed to the deterministic case in Figure 5.4(b) where no dependence is seen to the lattice cell length.

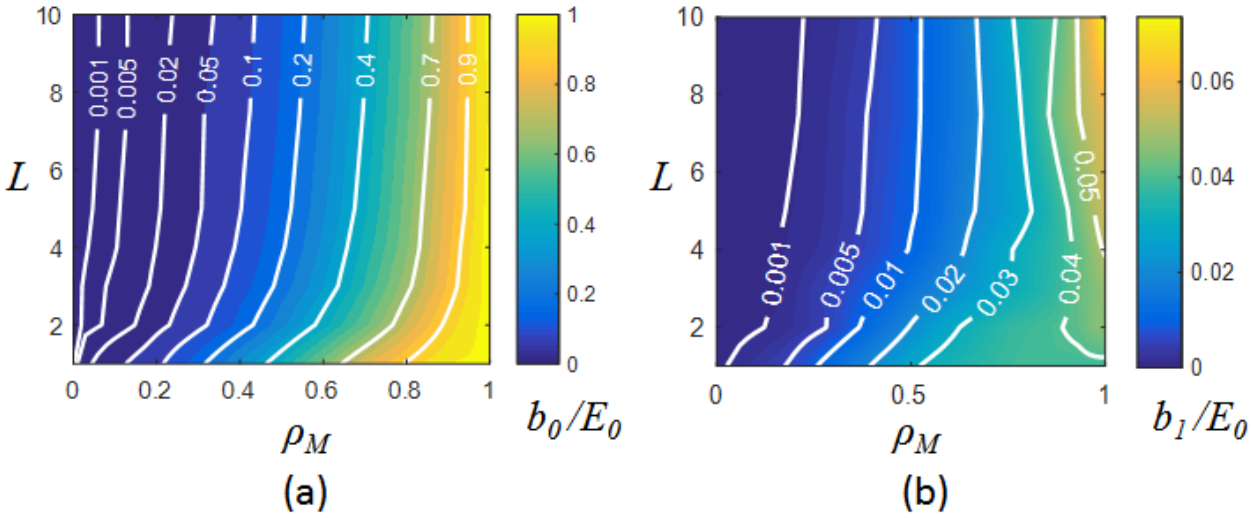

Figure 5.6. Contour plots of normalized PCE coefficients with respect to design variables (a) Contour plot for normalized b_0 (b) Contour plot for normalized b_1.

In addition, the comparison with the deterministic case in Figure 5.4(b) indicates that the homogenized modulus at the same model density value increases when the lattice length is decreased. In other words, we need to decrease the model density of the lattice cell if we decrease the lattice length to have the same elastic modulus. The decrease of the homogenized modulus is more discernable for smaller lattice cells (e.g. L < 5 mm) as can be seen in Figure 5.6(a). For instance, to have the same normalized modulus of 0.2, for L = 10 mm and 5mm lattice size values from the fabricated lattice structure, the model density ρ_M must be about 0.57 and 0.56, respectively. However, to obtain the same modulus for the fabricated lattice cell with L = 2mm, the model density must be about 0.42. These observations show that the modulus of the fabricated

lattice cell with L=2mm is 25% less than the modulus of fabricated lattice cell with L = 10mm; while the fabricated lattice cell with L = 5mm has 2% less modulus than that of L = 10mm. These observations from Figure 5.6(a) suggest that at the same density value the influence of the manufacturing process is greater for the smaller lattice cell size values. The reason of this observation can attributed to the following: As we reduce the lattice cell size the diameter of the struts also reduces to have the same density. However, the difference between the fabricated strut diameter and the model diameter remains the same although the strut dimeter decreases. That means the ratio of the fabricated strut diameter and the model diameter is larger in a smaller lattice cell size, which will increase the overall elastic modulus of the lattice cell.

A similar trend is also seen for the standard deviation of the modulus given in Figure 5.6(b). A changing trend occurs on the other hand in the region of density values closer to 1 for the standard deviation: As the lattice cell size decreases the standard deviation remains similar or decreases. The reason for that is the void region in the unit cell is getting too small which results in smaller geometric uncertainties leading to less changes in the deviation of the elastic modulus of the unit cell.

Finally, a general increase in the elastic modulus is observed for the case that accounts for the manufacturing uncertainties given in Figure 5.6(a) compared to the deterministic case in Figure 5.4(b). Hence, the results prove that the influence of the AM process must be considered in the material characterization of the designed CLSs.

5.4. Design of Micro-Aerial Vehicle (MAV) Fuselage

5.4.1. Problem Definition

Micro-aerial vehicles (MAVs) are critical in military operations for surveillance in hazardous areas. Their components such as the fuselage and the wings should be designed by lightweight and strong materials so that the MAVs can have high performance in endurance, landing, and take-off. The fuselage of an MAV is used as the example structure to show the applicability of the proposed meta-model approach in designing lattice structures without using any tedious simulations and optimization processes. The geometry of the fuselage is taken from [37], [38] and the important geometry parameters are shown in Figure 5.7.

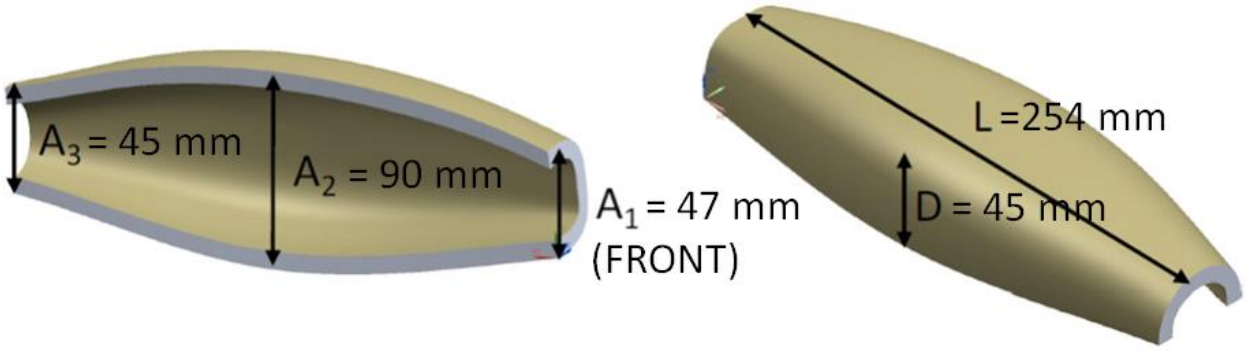

Figure 5.7. The geometry of the half of the MAV fuselage with its dimensions

The existing design of MAV fuselage is made of the lightweight ABS material which has an elastic modulus of 1960 MPa. Our goal in this study is to match this target modulus (E_t = 1960 MPa) by the BCC lattice cell fabricated by SLM for a periodic lattice structure design of the fuselage. The lattice design will be fabricated by an aluminum alloy, namely AlSi10Mg material which has an elastic modulus of E_0 = 65 GPa in SLM process. Aluminum alloy cellular structures are used for many applications in automotive, railway, and aerospace industries such as car body structures,

motorway sound insulation, heat exchangers, and lightweight conformal pressure tanks [220]. Ashby et al. [221] show that aluminum cellular structures offer much stiffer and lighter structural parts than the equivalent parts that are made of steel. Hence, recently, the aluminum alloy AlSi10Mg have been used in SLM process to fabricate CLSs and are the current interest [214], [219], [222]. For the MAV fuselage design, we assume that the design with aluminum material and periodic lattice structure instead of using solid plastic material will provide a better impact performance. We also expect the CLS design to be a lighter design than the solid fuselage design. Moreover, the proposed approach will provide a lattice-based design without requiring the expensive simulations and optimization processes.

For this purpose, the PCE-based meta-models, developed by PCHIP interpolation method to generate the contour plots in Figure 5.6, can be utilized in design of engineering structures with periodic CLSs to match a target modulus, E_t, by an appropriate choice of the model density and unit cell length. When we have a target modulus to match, first, the normalized target modulus is calculated by the ratio of the target modulus, E_t, and the modulus of bulk material, E_0. Then, at a desired unit cell size, the corresponding model density, ρ_M, of the lattice cell that corresponds to this normalized modulus value is read from Figure 5.6(a) (or from the meta-model of the first PCE coefficient, b_0). The standard deviation of the normalized modulus can also be predicted from Figure 5.6(b) (or from the meta-model of the second PCE coefficient, b_1) for the determined model density.

The diameter that will be used to generate the lattice cell model, D_M, should also be determined that corresponds to the calculated model density. For this purpose, the PCHIP function approximation developed to generate the curve of model density, ρ_M, vs. model aspect ratio, D_M/L, in Figure 5.3 is used. If the model diameter is greater than the minimum diameter that can be

fabricated by the AM process, then the design is accepted. Otherwise, the unit cell size is changed and the above-mentioned process is repeated. If the design is accepted, the corresponding mean value of the fabricated porosity of the designed lattice cell can also be estimated as follows: First, the model diameter, D_M is used in the meta-model developed to predict the first PCE coefficients of the homogenized diameter, $D_{CM,2}$, which produces the curve in Figure 5.5(a) at strut level. The predicted homogenized diameter can also be considered as the fabricated diameter, D_{fab}, since it is used in the lattice level upscaling process to predict the homogenized elastic modulus of the fabricated lattice cell. Then, the fabricated density, ρ_{fab}, that corresponds to this fabricated diameter value is estimated using again the developed PCHIP function of model density, ρ_M, vs. model aspect ratio, D_M/L, in Figure 5.3. Finally, the porosity of the fabricated CLS design can be estimated by $\gamma = (1- \rho_{fab})$.

This process of target modulus matching is implemented to design a micro-aerial vehicle fuselage with BCC lattice cells to demonstrate the applicability of the proposed approach.

5.4.2. Results for MAV Fuselage Design

When the lattice structure is considered to be fabricated using AlSi10Mg material, the normalized modulus to match with the target modulus of fuselage design will be $E_t/E_0 = 0.0302$. This normalized modulus value will be used in Figure 5.6 to find the density of the lattice structures that matches the target elastic modulus. Before implementing the proposed approach, it is important to choose a lattice cell size that can fit into the dimensions of the fuselage geometry before designing the lattice cell. First, a lattice cell size of L = 2mm is considered in the fuselage design because a small cell size allows for the lattice cells to conform to the structure's geometry without losing geometrical details. The model density of the BCC cell that matches the fabricated

elastic modulus of 1960 MPa was estimated to be ρ_M = 0.183 from the meta-model of the first PCE coefficient (b_0) for L = 2 mm given in Figure 5.6(a). This model density value produced a model diameter value of D_M = 0.405 mm when calculated from Figure 5.3. However, this design is not desired because the model diameter is less than the minimum diameter value of 0.5 mm that can be fabricated using the SLM process considered in this study.

Therefore, the length of the lattice cell was increased to have a model diameter that could be fabricated. Two different lattice cell sizes were considered for designing the fuselage: (1) If the unit cell size is desired to be L = 4 mm, the density of the lattice cell model that will match the target modulus is obtained as ρ_M = 0.236. (2) If the unit cell size is desired to be L= 8 mm, the model density to match the target modulus is obtained as ρ_M = 0.262. The corresponding results obtained by the proposed approach for both cases are listed in Table 5.2.

Table 5.2. Estimated results to match the target modulus of E_t =1960 MPa

	L = 4 mm		**L = 8 mm**	
	Proposed	**Deterministic**	**Proposed**	**Deterministic**
Target E_t (MPa)	1960	1960	1960	1960
Mean of Fabricated E_h (MPa)	1960	3578	1960	2900
Standard deviation of Fabricated E_h (MPa)	131.85	222.65	114.95	174.8
Model Density ρ_M	0.236	0.304	0.262	0.304
Model Diameter D_M (mm)	0.939	1.088	1.992	2.176
Fabricated porosity (1 - ρ_{fab})	0.698	0.628	0.708	0.665
Fabricated Diameter D_{fab} (mm)	1.084	1.231	2.123	2.305

As seen in Table 1, the diameters used to generate the lattice cell models, D_M, were estimated to be D_M = 0.939 mm, and D_M = 1.992 mm from the function approximation in Figure 5.3 for L = 4 mm and L = 8 mm, respectively. These values were found to be greater than the minimum diameter value of 0.5 mm that could be fabricated by the SLM process used in this study. Hence, both designs can be fabricated and the CAD models of the designed structures for both cell size values with BCC lattice cells are illustrated in Figure 5.8(a) and Figure 5.8(b), respectively. The corresponding STL files can be used to fabricate the designed fuselage structures by the SLM process using the AlSi10Mg material.

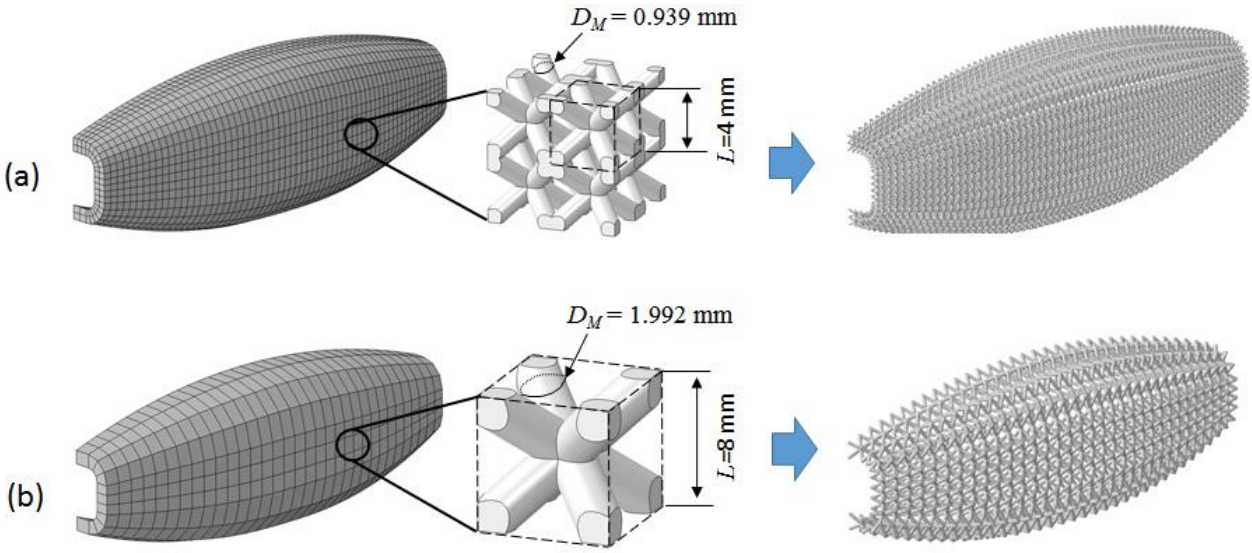

(a) Designed fuselage model with conformal BCC lattice cells with L = 4mm, (b) Designed fuselage model with conformal BCC lattice cells with L = 8mm.

Figure 5.8. Lattice-based design of MAV fuselage

The lattice-based fuselage designs that match the target modulus (i.e. 1960 MPa) were also done for the deterministic case where the influence of manufacturing uncertainties was not considered. The corresponding results are compared with the proposed approach in Table 1. The function approximations developed to generate the contour plot in Figure 5.4(b) were used in this

deterministic case to find the model density value that corresponds to the target modulus of 1960 MPa. As can be seen from Table 1, the predicted model density values are identical for both L=4mm and L=8mm, i.e. ρ_M = 0.304. Since the influence of the manufacturing process is not considered in the deterministic case, to have the same target modulus, the density of the lattice cell should be the same as explained in Section 5.3.2 and as shown in Figure 5.4(b).

Moreover, the fabricated structure moduli of these deterministic designs were estimated using the PCE-based meta-models as 3,578 MPa and 2,900 MPa for L=4 and L=8mm, respectively (Table 5.2). It is seen that if the deterministic design approach is used and the designed fuselage structure is fabricated by the SLM process, although the modulus of the CAD model matches the target, the fabricated structure modulus is different from the target modulus of 1960 MPa. Furthermore, the fabricated densities were estimated as ρ_{fab}=0.372 and ρ_{fab}=0.335 that produce porosity values of 62.8% and 66.5%, respectively. The proposed method, on the other hand, estimates the fabricated densities to be ρ_{fab} = 0.292 and ρ_{fab} = 0.302 for L = 4 mm and L = 8 mm (Table 5.2), which correspond to a fabricated porosity value of about 70% for both fuselage designs. Compared to the deterministic approach, these results prove that a lighter design is achieved while the target modulus is matched. Thus, accounting for the manufacturing uncertainties for matching the target modulus will help create a realistic design that satisfies the design targets in terms of modulus and porosity.

One question that should be addressed is whether one of these designs would be preferable over the other. A comparison on the standard deviations of the elastic modulus values, estimated for both designs as given in Table 1, reveals that the design with L= 8mm should be preferred because its standard deviation is smaller than that of the design with L = 4mm. The reason is that the diameter of the struts that are fabricated in SLM for the design with L = 8 mm is greater than

the diameter of the design with L = 4mm (Table 5.2). The increase of the diameter simply provides less variation in the fabricated struts by the SLM process so that a more robust design can be obtained if a larger diameter value is determined for design. Thus, when the design of the fuselage structure is repeatedly fabricated, less variation in overall elastic modulus can be obtained, which leads to a more consistent design that matches the target modulus.

5.4.3. Validation of Designed CLS performance

Once the lattice-based fuselage design with L = 8mm (Figure 2(b)) is determined as a better design option, we need to evaluate the validity of the predicted results by comparing its performance under the impact loadings with the target model, which is the solid model with the ABS material. In order to validate the performance of the designed fuselage structure, the simulation of the lattice design for L = 8mm can be performed under the loading and boundary conditions given in Figure 3 [37], [38]. The obtained results for these lattice designs can also be compared with the simulation results of the existing solid model with ABS material under the same loading and boundary conditions. The fuselage has two loadings: The weight of the motor in the front, F_{Motor} = 5.9 N and the weight of the tail in the rear, F_{Tail} = 2.7 N. These loads are the scaled loads by a factor of ten to model the impact loading on the fuselage. The contact area between the ground and the bottom of the fuselage is fixed in all directions as this is the impact zone. Since only half of the fuselage's geometry is modeled, symmetry boundary conditions were applied on the symmetry surface. The FE model of the target solid fuselage structure with ABS material was generated with a mesh size of 3mm using the hexahedral solid elements. For the lattice design, the fabricated diameter value, estimated by the proposed meta-modeling approach (Table 5.2), was used to generate the FE model used in the simulations to account for the SLM process uncertainties. The generated lattice model

is meshed using quadratic tetrahedral solid elements in Abaqus since those provide a better agreement with reality as discussed in Chapter 4 for the CLS examples compared to the beam element-based models.

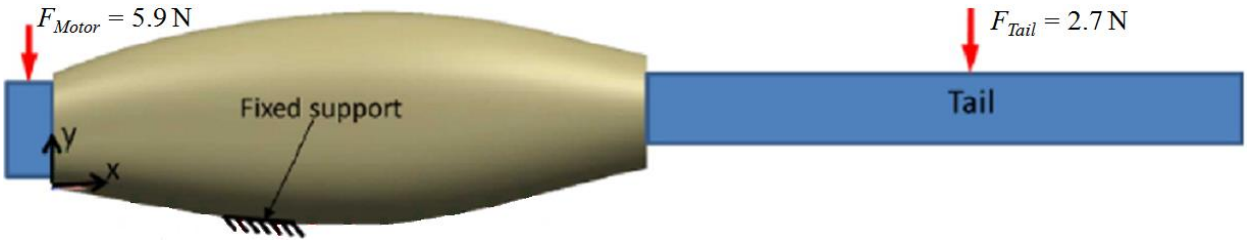

Figure 5.9. Loading and boundary conditions on the fuselage geometry [37]

Since the modulus of the target solid model is aimed to be matched for designing the lattice structure, it is expected that the lattice design obtained by the proposed approach should have a deflection behavior similar to the solid model. Hence, the maximum deflection values were obtained from simulations of the lattice design model and the target model, and are listed in Table 2 for comparison.

Table 5.3. Results of the simulations for MAV fuselage design

	Deflection (mm)	Weight (kg)
Solid - ABS	0.0211	0.305
Lattice – L = 8 mm	0.0173	0.158

5.4.4. Discussions

The maximum deflection result of the designed lattice model was found to be 0.0173 mm as seen in Table 2. This result was slightly smaller than the deflection result of the target solid model with

ABS material which was obtained as 0.0211 mm. Since our goal in designing the lattice structure was to match the target modulus of the solid model with ABS material, a similar deflection behavior would be expected from the lattice design. The slight decrease of the deflection in the lattice design can be attributed to two reasons. First, the solid element-based lattice model used to validate the performance of the designed lattice structure required a tremendous computational effort. Therefore, a coarse mesh was used, which results in slightly increased stiffness. Therefore, less deflection can be obtained from simulations. Although a coarse mesh was used, the simulation required 30Gb of memory to run as the model meshed with quadratic tetrahedral elements had about 1.7 million nodes. It took about 40 minutes to complete the simulation in Abaqus on an Intel i7 5960x processor when 4 cores were activated. The computational demand also shows that using such detailed simulations for the realistic design and analysis of the lattice structures would not be possible to design the lattice-based fuselage structure. Hence, it is validated in terms of computational cost from the solid element-based lattice model simulation results that the proposed method performs well to match the target modulus while eliminating these expensive simulations required to design lattice-based structure.

The second reason of having a smaller deflection result from the lattice design is that the lattice structure model generation process slightly increases the mass at the intersection points of the struts. Hence, a slight increase in the overall modulus of the structure is expected, which results in a slightly smaller deflection result as obtained in this example. Nevertheless, since this was an expected result, the comparison of the simulation results of the designed lattice structures with the target solid model validates that the approach of matching the target modulus produces an effective lattice-based design of the MAV fuselage. Moreover, it is seen from Table 5.3 that a significant reduction in weight was also obtained with the lattice design as the solid model has a weight of

0.305 kg while the weight of the lattice design fabricated by AlSi10Mg material using SLM was predicted to be 0.158 kg. These results show that the fabricated lattice-based design will have a weight of half of the existing design with ABS material, which provides a very lightweight design of the MAV fuselage. Hence, these results suggest that the lattice structure determined by the proposed approach can be used to replace the solid fuselage design with a lightweight but still strong structure.

In Section 5.4.2, it was found that the lattice design with the cell size of 8 mm was a more robust design compared to the lattice design with the cell size of 4mm since a larger diameter value is determined for the former lattice design to match the modulus. It should be noted, on the other hand, that this observation does not mean that a larger diameter is always a better solution. Because a larger lattice size will be required to have the same modulus when we increase the diameter value, after some point, the lattice cell size will not fit in the overall fuselage geometry. Moreover, the conformity of the geometry might be lost with the increase in the lattice cell size because for larger cell sizes the curvatures on the geometry cannot be modeled accurately due to the long straight strut members. In that regard, a smaller cell length (e.g. the design with L = 4mm) will provide a better conformity with the curved geometry than a larger cell length (e.g. the design with L=8mm) as can also be seen when Figure 5.8(a) compared with Figure 5.8(b). Although the geometry conformity was not an issue for this MAV fuselage example, this might impact the performance of the designed structure depending on the application. Nevertheless, for the fuselage example the lattice design with L = 8 mm was chosen as it provided a comparable performance with the target solid model.

Another issue that should be pointed out is that the conformal design of the lattice cell in the fuselage geometry may compromise the target elastic modulus of the designed lattice cell as

the homogenization is achieved for cubic cells. In other words, a better conformity could result in a better match of the target modulus for the conformal lattice structure. In the conformal design, the cubic geometry of the lattice is slightly skewed to conform the geometry, which may lead some difference in the predicted value of the elastic modulus. This could also be a reason that the lattice model has a slightly smaller deflection result than the target solid model although the same elastic modulus was targeted. Nevertheless, the conformity of the lattice cells enables the integrity of each unit cell in the designed structure as opposed to the non-conformal designs, which will have missing struts and partial unit cells in the geometry resulting in a worsening effect in the structure performance. Further study is necessary for the investigation of the effect of the conformal geometry on the elastic modulus along with the validation of the designed structures with experiments on the fabricated designs.

5.5. Summary

In this chapter, the application of the proposed multi-level upscaling and validation approach is presented for designing cellular lattice structures without using the computationally expensive simulation-based optimization processes while matching the realistic elastic modulus of the fabricated lattice structure with the target elastic modulus. In Section 5.2, the proposed PCE-based meta-modeling approach that considers the AM process effects on the fabricated CLSs by using the stochastic upscaling method is introduced. In Section 5.3 the flowchart to develop the meta-models is described and is utilized for BCC lattice cell. The effect of unit cell size and unit cell model density on the fabricated lattice cell elastic modulus that involves uncertainties has been examined, evaluated and compared with predicted results when uncertainties were not considered. A contour plot of the BCC lattice cell based on the PCE-based meta-models with varying cell

length and cell density is developed that gives the fabricated effective modulus as the output. This contour plot is used to find the desired effective modulus of the lattice cell to be used in the design of the lattice-based MAV fuselage design in Section 5.5. The design of the lattice structure is obtained without requiring the tedious optimization processes and FE simulations. The results demonstrated that the effects of the AM-process on the strut level are needed for a reliable evaluation and realistic design of the cellular lattice structures. Thus, the use of the proposed PCE-based meta-modeling approach has been proven to be a useful approach to design cellular lattice structures with desired realistic elastic properties under the uncertainties.

CHAPTER 6. CONCLUSIONS AND FUTURE WORK

In this chapter, the dissertation is concluded by summarizing the main points of the research. The contributions of the proposed research are summarized in Section 6.1. The limitations of the current work are discussed in Section 6.2. The possible future work to address the limitations and open new ways for research is suggested in Section 6.3.

6.1. Contributions

An extended summary of the main points and research questions in this dissertation are given in Section 6.1.1, and the contributions are summarized in Section 6.1.2.

6.1.1. Extended Summary

The main goal of this dissertation is to develop a computationally efficient modeling framework for uncertainty quantification and propagation in complex cellular lattice structures fabricated by AM. The framework is generalized to be applicable also to any complex engineering structures that require expensive simulations and experiments under uncertainties. There are increased uncertainties at small scales of complex engineering structures (e.g. in the strut members of cellular lattice structures when fabricated by AM techniques), which may greatly impact the accuracy and reliability of human scale structure predictions. Therefore, it is crucial that the small-scale uncertainties must be properly accounted for in the computational models used in analysis and design of engineering applications. However, considering these small scale uncertainties in direct modeling of the final structure to have accurate predictions is neither feasible nor efficient due to increased complexity.

Typically, the multiscale modeling approach is utilized to alleviate the complexity associated with the fine scale details and uncertainties. In multiscale modeling, instead of modeling all the details at once, upscaling/homogenization methods are used to model the fine scale details with continuum level constitutive laws that can explain how the material behaves with some homogenized properties. Then, the homogenized properties are used for a simplified model of the structure in engineering analysis and design. However, the multiscale modeling techniques usually focus on the homogenization at one scale level of the material structure, which can still be computationally infeasible when finer scale uncertainties are also considered in the modeling process. Even if the homogenization can be achieved at multiple scale levels, the existing homogenization methods used in multiscale modeling consist of complex linking mechanisms that link the fine and coarse scale domains. Furthermore, these methods usually penetrate the explicit formulations of the coarse scale domain (e.g. the explicit formulations of continuum level constitutive laws). Hence, there can be significant computational costs when these methods are used to account for uncertainties.

As a result, an effective framework for uncertainty quantification is required that can efficiently account for the fine scale uncertainties in predicting final structure to address these issues. This led us to pose the following ***Research Question 1***:

> ***Research Question 1*:** How can we efficiently quantify and propagate the fine scale uncertainties to predict the performance of human scale structures?

In the light of these constraints, a multi-level stochastic upscaling method through optimization was hypothesized to serve our purpose. This method treats the homogenization problem as an inverse optimization problem where the unknown homogenized input properties are

determined through probabilistic response matching of fine and coarse scale models. This way, black-box functions (e.g. FE modeling approach) can be used to develop both fine and coarse scale domain models, which eliminates the penetration of the explicit formulations. PCE was chosen as the dimension reduction method in the upscaling method because it can represent the uncertainty of a homogenized property with a few deterministic coefficients. PCE also allows for the representation of any distribution models when Hermite polynomials are used in its formulation, thus eliminating the issue of choosing an appropriate distribution model for the unknown homogenized input variable before the optimization. BIC method is integrated into the stochastic upscaling method for parametric modeling of the fine scale input uncertainties that will be used in fine scale response predictions. The exponential loss function is proposed to use in the optimization step of the upscaling method as the objective function since it can allow for the optimization algorithm to reach the optimal point quickly. Moreover, a hybrid optimization procedure of GA and SQP is utilized in the upscaling process to find the global optimal point quickly without being trapped at the local minima. This improved stochastic upscaling framework was introduced in Chapter 3 along with application examples at one level and multiple levels to demonstrate the benefits of the proposed improvements.

Current approaches for multiscale modeling under uncertainties include only the uncertainty from the homogenized properties. The homogenized model properties may not be an accurate representation of the structure as they ignore the effect of the discrepancy of the model from reality. Therefore, in a hierarchical multi-level upscaling process, a validation step should also be conducted at each level of interest to evaluate the accuracy of the predictions made by computational models where the homogenized properties are used. However, in a multi-level approach, the level of the available experiments may be different from the corresponding level of

the upscaling. The reason is that at small scale levels, the scale is too small and experiments are usually very limited and expensive. The experiments may be available only at the larger scale levels. Hence, along with developing an efficient stochastic upscaling technique, meaningful validation processes must be investigated to use the available experimental data in the most effective way for the prediction accuracy assessment at multiple levels. This led us to pose the following ***Research Question 2*:**

> ***Research Question 2:*** How can we improve the prediction accuracy of computational models used at multiple levels while minimizing the experimental cost?

The validation approaches are well established for complex engineering systems such as validation pyramid approach where the complex system can be divided into multiple simple sub-levels to increase the availability of the experiments. The validation pyramid approach starts with a calibration process at the bottom of the pyramid where the model input variables are estimated based on the experiments of simple models. Then the validation step is utilized for a different model from the calibration model using a validation metric to compare the model predictions with experimental observations. Additional validation steps can be done with the increased level of complexity of the models from bottom to up. We hypothesize in this research that this validation pyramid approach can be adapted to the multi-level upscaling approach. In that regard, at each scale level, the stochastic upscaling method is utilized to estimate the input homogenized properties of the coarse scale model at the bottom of the pyramid. Then, the validation step is achieved by comparing the experimental observations with the corresponding coarse scale model responses for a different model from the one used in the upscaling step with the experimental observations. As stated earlier, unlike the complex systems, where experiments are cheaper and available for simpler sub-level models, experiments at small scale levels are not available or

expensive in the multi-level modeling. To minimize the experimental cost, we hypothesize that a "pre-validation" step can be used at scale levels where the experiments are not available. The goal is to utilize the validation metric for the comparison of the responses obtained for a different fine scale model from the one used in the upscaling step with the responses of the corresponding coarse scale model with homogenized properties. Although the pre-validation step does not guarantee the validation at the corresponding scale level, it will be able to challenge the coarse scale model predictions. Thus, it will enable the increase of the confidence of accepting the predictions because the coarse scale model with the predicted homogenized properties is used for a different model. To be able to utilize this approach, on the other hand, the experiments must be available at least at the final scale level for validation with the real world. Thus, the requirement of the experiments can be decreased which can address the *Research Question 2*.

Moreover, we hypothesize that a validation metric that integrates the u-pooling method with K-S test can also enable the minimization of the experimental cost. The u-pooling method allows for the evaluation of the experimental observations made at multiple validation sites at one combined distribution. Thus, the number of samples in predictions assessment can be increased without requiring additional experiments. The K-S test accounts for the number of experiments when making a decision to accept/reject predictions based on the distribution obtained by the u-pooling method. Thus, it enables making trustable decisions in the predictive capability of the computational models even if there is a small number of experiments available.

In Chapter 4, the proposed validation approach was explained in detail and utilized for two lattice structure examples. The first example was for SC lattice structure fabricated by the material extrusion process with ABS material. The experimental data were available from the tensile test of the fabricated specimens. At strut level, the pre-validation step was utilized because individual

strut experiments were not available. The advantage of the validation metric that includes the u-pooling method and K-S test was shown by investigating the results for a different number of experiments. The second example was the BCC lattice structure fabricated by SLM process with AlSi10Mg material. For this example, the proposed multi-level upscaling and validation approach was implemented starting from the quantification of uncertainties at strut level using the reconstructed strut models from the CT-scan images. Experiments were available only for the lattice level specimens in this example. To minimize the experimental cost, the individual strut models were extracted from the reconstructed lattice specimen models. These strut models were used to quantify the input uncertainties. Furthermore, those were simulated to compare the responses with the coarse scale model with homogenized properties predicted by the upscaling method in the pre-validation step. Thus, the predictive capability of the upscaled model is investigated by experimentally generated strut models without requiring additional strut level experiments. Then, the lattice level coarse scale model predictions were evaluated by comparing with physical compression test results using the proposed validation metric. The advantage of using multiple validation sites in increasing the number of experimental observations in the predicted distribution with the same number of experiments using the u-pooling method was clearly demonstrated. Thus, it was proven that the proposed validation approach stated in *Hypothesis 2* could be employed for the validation of prediction accuracy in the multi-level upscaling framework with minimal cost.

Once the proposed multi-level uncertainty quantification with upscaling and validation framework was proven to produce good results in the application examples, the applicability of the upscaling method in the design process of cellular lattice structures was shown. For this purpose, we pose the following ***Research Question 3***:

***Research Question 3*:** How can the proposed uncertainty quantification approach be used for the realistic design of complex engineering structures?

We hypothesize that a PCE-based metamodeling technique developed based on the homogenized properties obtained by the upscaling process can be used in designing cellular lattice structures. In Chapter 5, the applicability of the developed approach was shown in designing an MAV fuselage with BCC lattice cell to match the target elastic modulus. Since the proposed multi-level upscaling approach is utilized beforehand, the uncertainties induced by the manufacturing process on the predicted homogenized elastic modulus of the lattice structure can be captured effectively. To develop the meta-model, the PCE coefficients of the homogenized elastic modulus were predicted by the upscaling method for various densities of the BCC lattice type. Then, the PCE coefficients of the homogenized elastic modulus that matches the target elastic modulus were estimated using the developed meta-model. The application examples demonstrated that the proposed method could provide a simulation-free design of cellular lattice structures with quantified uncertainties. For our specific purpose, we chose the design of an MAV fuselage as the example applications.

6.1.2. List of Contributions

In this dissertation, many critical challenges have been addressed in the area of uncertainty quantification and computational modeling of cellular lattice structures fabricated by AM techniques. The specific contributions and their respective explanations are listed below:

Uncertainty quantification at multiple scale levels using a simulation-based upscaling method: The main contribution of this research is that a comprehensive framework is proposed

and validated to quantify and propagate uncertainties at fine scales induced by AM process to accurately predict the statistical performance of the final structure. The reason of developing this framework is that the uncertainties existing at small scale levels complicate the computational modeling of the cellular lattice structures when considered for accurate predictions. Since the homogenization or upscaling methods available are usually based on complex, explicit equations, it would be an issue to implement them due to increased complexity. Moreover, the explicit constitutive laws at the continuum level are required to be determined for which the homogenized properties will be predicted. We propose to use a simulation-based upscaling method, where the user only needs to create the fine scale and coarse scale black-box functions to find the homogenized properties without penetrating the underlying governing equations. The use of black-box functions also allows for the implementation of the proposed upscaling method for uncertainty quantification and property characterization of any complex engineering structures.

For the lattice structure examples used in this dissertation, the fine scale model of the individual struts was represented by a simple beam element model as the coarse scale model at the strut level upscaling process. The fine scale lattice model at the lattice level was represented by a solid hexahedral element as the coarse scale model in the upscaling process. Thus, instead of penetrating the explicit governing equations of the coarse scale models, the responses obtained from the coarse scale FE models are used to predict the corresponding homogenized properties. This process also allows for the calibration of the homogenized properties that will be used at the subsequent level. For instance, the solid hexahedral elements are used to model the entire lattice structure at the macroscopic level, hence predicting the homogenized properties using a solid hexahedral element in the upscaling process will eliminate any modeling errors that could occur if

any other modeling strategy were utilized. The following contributions are also included to facilitate the computations in the stochastic upscaling method.

Parametric uncertainty representation of fine scale input variables using BIC method based on reconstructed strut models to minimize the experimental cost: The input uncertainties of the fine scale model are the most crucial part of the upscaling/homogenization process to have accurate predictions of the homogenized properties. Inadequate representation of these uncertainties may result in inaccurate predictions during multi-level upscaling when propagated across multiple scales. Hence, the input uncertainties must be characterized first based on experiments. For this purpose, in this study, the 3D individual strut models were reconstructed from the micro-CT scan of the fabricated lattice structure specimens rather than using the fabricated individual struts to decrease the experimental cost. It was observed that these reconstructed strut models provide sufficient accuracy when collecting the statistical data regarding the input variables of the strut at the fine scale such as diameter, angle, and porosity as shown in Chapter 4 for the SLM-fabricated lattice structure example.

Moreover, the BIC method is integrated into the upscaling method to use in parametric modeling of the available statistical data of the fine scale input variables. BIC is based on the MLE method, which utilizes a simple optimization process to find the optimal statistical parameters of a distribution model that can fit the statistical data. BIC also accounts for the number of statistical parameters and number of samples in the selection of the appropriate distribution model, which enables an accurate representation of the uncertainties. Thus the parametric distributions can be used in the generation of the fine scale model that is used for predicting the fine scale responses in the upscaling method.

Dimension reduction in the optimization step of the stochastic upscaling method using PCE: In deterministic upscaling method through optimization, only one unknown variable that represents the homogenized input is estimated by matching the fine and coarse scale model responses. When uncertainties are involved, on the other hand, the randomness of the unknown homogenized input is represented by samples that can produce the distribution of the input. Hence, the unknown samples must be estimated, which increases the computational cost of the optimization in the upscaling. The statistical parameters that can generate those unknown samples can be predicted for the homogenized input to reduce the dimensionality. We also need to know about the underlying distribution, from which the samples of the homogenized input are generated, to calculate the corresponding coarse scale model responses at each iteration in the optimization to compare with the known fine scale responses. This issue was eliminated in this study by projecting the homogenized input onto a PCE, where the randomness is represented by a few deterministic coefficients. The use of PCE in the stochastic upscaling method was inspired by the work in [98] for upscaling the uncertainties at one scale level.

One contribution included to the upscaling method is that the Hermite polynomials are used in the PCE representation to represent any distribution type. It is shown in Chapter 3 that this approach eliminates the necessity of determining the distribution model of the homogenized input during the optimization process. Moreover, the random samples required in the PCE representation of the homogenized input of the coarse scale model is proposed to be generated based on the known fine scale responses using Eq. (3.24) as opposed to the proposed PCE-based upscaling method in [98] where those samples are generated randomly. Thus, as shown by the examples in Chapter 3, the uncertainties of the fine scale model are propagated on the coarse scale model accurately.

Faster convergence of the optimization in upscaling using exponential loss function and a hybrid optimization algorithm of GA and SQP: It was hypothesized that the convergence of the optimization in the upscaling process could be increased by using an effective objective function used to compare the coarse and fine scale response. The results in Chapter 3 in the first example revealed that an exponential loss function penalizes the non-optimal points more severely than the existing objective functions. Thus the optimization algorithm can converge to the optimum point more quickly. Moreover, to eliminate the computational burden of the global optimization methods SQP is used after some iterations are done by GA. Since SQP is a gradient-based optimization approach, it has the issue of trapping the local minima although it is computationally faster than the global optimization methods. Therefore, using first the global optimization method of GA allows to approach the global minima, and SQP enables a more rapid convergence to the optimal point.

Validation metric with the u-pooling method and K-S test to minimize the experimental cost: The accuracy of the predicted results using the homogenization methods is still questionable because usually a simple deterministic comparison with the mean value of the effective properties obtained by experiments is performed. Since the number of experiments is limited, the experimental results do not provide an accurate mean value. Moreover, only a comparison between the predicted and experimentally obtained homogenized properties is made without investigating the applicability of the homogenized model in predicting the structure response. Available statistical validation metrics do not provide an acceptance/rejection criterion based on the number of experiments, and therefore a large number of experiments is required which increases the experimental cost. In the validation of model predictions, on the other hand, the goal should be to minimize the experimental cost. This goal can be achieved by finding ways

to use the available experiments in the most efficient way. The contribution of this study is the proposed validation metric that integrates u-pooling method with K-S test which can achieve accuracy assessment minimal experiments at each scale level of interest. The u-pooling method is a widely accepted procedure in the validation because it enables the pooling of the available experimental data into one combined distribution even if the experiments are done at multiple validation sites. Thus, the number of samples to generate the distribution can be increased even if the number of experiments is not sufficient, which eventually provide a better representation of the model predictions. The combined distribution must follow a standard uniform distribution according to the probability integral transformation method. Thus the discrepancy from the SUD will provide how much the predictions are accurate. Moreover, to minimize the experimental cost, we need to find ways that would not be affected by the change of the number of samples so that a reliable decision can be made even if a few experimental data are available. K-S test is promising in that sense because the decision is made by accounting for the number of samples. Hence, the integration of the u-pooling method with K-S test is proposed in this study to use as the validation metric to be able to use the available experimental data in the most efficient way.

Validation pyramid approach for a hierarchical validation at multiple levels: The validation pyramid approach that is introduced to enable validation of complex systems is adapted for the prediction assessment of the computational models used in the multilevel upscaling approach. The validation pyramid suggests finding the unknown input variables of the computational model with simplified models by a calibration process. Then, for a different model used in the calibration process is considered in a subsequent validation process to challenge the predicted input variables. This approach is also utilized in the multi-level upscaling approach for validation. In that regard, first, the homogenized input variables of the coarse scale model are

determined using the stochastic upscaling method, which corresponds to the calibration step in the validation pyramid. Once the homogenized input variables are estimated, the validation step can be implemented. For this purpose, a different model from the one in the upscaling process is determined at the same scale level, and the coarse scale model is developed with the predicted homogenized input variables. The validation is performed using this coarse scale model. The predicted coarse scale model responses are compared with the experimental data using the proposed validation metric. This approach enables a better evaluation of the prediction capability of the homogenized model since a different model from that utilized in the upscaling method is considered. Moreover, the corresponding response predictions are evaluated in the validation step as opposed to the existing multiscale modeling approaches where only a comparison is made between the predicted and experimentally obtained homogenized properties. Thus, the proposed validation approach evaluates the response predictions of the structure model rather than evaluating merely the homogenized property predictions.

Considering the uncertainty effects in the design of lattice structures using the developed PCE-based meta-model approach: The next step after validating the predictions made by the multi-level upscaling approach is to utilize these predictions in designing cellular lattice structures to have the effect of uncertainties in the fine structure performance. To show the applicability of the proposed approach in designing lattice structures, the PCE-based meta-model approach is suggested to predict uncertain homogenized properties in this research which is inspired by the work done by Coelho et al. [142], [143] for the reliability estimation in the optimization of engineering structures. In designing lattice structures, this approach allows for the prediction of the PCE coefficient values of the homogenized property at the macroscopic level,

thus eliminates the tedious simulations required to find the samples of the homogenized property in the traditional sampling-based approach.

To show the applicability of this PCE-based meta-model method in designing CLSs, it was implemented for the design of a micro-aerial vehicle fuselage. The goal was to match the target elastic modulus of an existing fuselage with that of BCC lattice cells for a lightweight design. The PCE-based meta-model for the BCC cell was developed based on the training data, which include the PCE coefficient predictions from the proposed multi-level upscaling and validation approach for various density values of the BCC lattice cell. Then, the lattice model density value that produces the target modulus is predicted using the PCE-based meta-model along with the corresponding uncertainties. Thus, when the CAD model of the designed CLS with the estimated model density value is used for fabricating the structure, this approach allows for the accurate prediction of the fabricated modulus of the designed CLS. This process eliminates the expensive simulation and optimization processes to match the target modulus since a predetermined meta-model is used in design, as well as enables the accurate prediction of the realistic homogenized properties since the uncertainties are propagated by the upscaling method.

In Section 6.2, the limitations of the current work are highlighted, and in Section 6.3 possible further work that can help address these limitations are suggested.

6.2. Limitations

The limitations of the work presented in this dissertation are discussed in this section.

Types of uncertainties considered: In this research, only the aleatory uncertainty was considered, where it is assumed that enough data is available to generate the probability density

functions (PDFs) of the random variables. Epistemic uncertainties, on the other hand, can also be available, which is ignored in the proposed framework.

The number of samples to generate the random responses: In all examples in this dissertation, a high number of samples (i.e. at least 200 samples) were considered to generate the random response from fine scale and coarse scale responses. Although effective methodologies are provided to quantify uncertainties, the number of samples can still impose increased complexity, especially for the fine scale model simulations due to the repetitions of the simulations for each sampling point.

PCE representation: In all examples considered in this dissertation, it was assumed that only one response is available from the computational models. The one-dimensional PCE are sufficient to represent the uncertainty of the homogenized properties when only one response is available. On the other hand, more than one response might exist in some applications, in which case a higher dimension of the PCE might be required for accurate representation of the homogenized properties. For example, when plastic deformation is considered the reaction force obtained from the fine scale simulation will differ at different strain values. In those cases, the one-dimensional PCE may result in a poor accuracy in the representation of the homogenized properties.

Anisotropic properties of lattice cells: In the provided examples, it was assumed that the lattice structure properties are isotropic, i.e. the properties are the same in all directions. This assumption would be reasonable for the AM processes such as FDM, SLS, or SLM as the variations are about 10% in both modulus and strength when the process parameters are chosen properly [33]. However, in some AM processes such as inkjet 3D printing, the effect of orientation

on the mechanical properties sometimes reach 30% which has been investigated in Stratasys Object500 Connex3 [224]. Besides, although the isotropic material properties can provide good accuracy in the former processes, the type of lattice cell as well as the uncertainties induced by AM process may still impose anisotropy in the predicted properties. Hence, the assumption of the isotropic properties can be a limitation of the proposed modeling approaches for accurate uncertainty quantification and characterization of the macroscopic level material properties.

Limitations of the Validation approach: The validation approach utilized in this research at multiple levels performs a comparison for the model of the test specimens. In reality, on the other hand, the designed structure will be different from the model of the test specimens used in the validation. For example, the design example of MAV fuselage was obtained using the upscaling method but the accuracy of the predicted results need to be evaluated by comparing with fabricated designs. Hence, additional validation steps are required with more complex models to be able to evaluate the accuracy of the predictions made by the coarse scale models with the homogenized properties obtained by the upscaling process.

Effect of process parameters and build direction on the uncertainties: In the examples used in this study, only one set of values of the AM process parameters were considered. Hence, the accurate predictions made by the upscaling approach are limited to only those process parameter values. When different parameter values are in consideration, those will change the quantified uncertainties and eventually the overall performance of the fabricated structures.

In Section 6.3, some suggestions are proposed to address these limitations and to improve the uncertainty quantification approach presented in this dissertation. Some areas are also suggested which can be investigated in the future related to the proposed approach.

6.3. Future Work

Many researchers have worked in the field of multiscale modeling by accounting for the uncertainties in the area of composite materials, but the research in the field of cellular lattice structures fabricated by AM techniques is still in its infancy. This dissertation aims to bridge that gap so that the uncertainties induced by AM processes can be quantified efficiently in the multi-level modeling of the cellular lattice structures to predict their mechanical performance. Besides, a generalized framework with decreased computational complexity is presented in this study so that it can be applicable for complex structures and materials other than the lattice structures. The following suggestions are provided in this section for future research so that the knowledge base for uncertainty quantification, multiscale modeling, and validation of models is advanced which will enable the efficient modeling and design of engineering applications.

Modeling the epistemic uncertainty: As stated in Section 6.2, the epistemic uncertainties are ignored in the current framework of the uncertainty quantification approach. On the other hand, uncertainties due to lack of knowledge can exist especially in the small scale levels, which may impact the final structure performance. For instance, the elastic modulus of the strut level fine scale models is taken from the literature in this study and assumed to have normal distribution to generate samples in simulating the fine scale strut models. In reality, the elastic modulus of the material deposited in AM machine to create the strut members of the lattice structure may vary depending on the material supplier of the AM machine, and therefore it may be an epistemic uncertainty. Hence, methodologies should be investigated and developed to quantify and model the epistemic uncertainty in the prediction of homogenized properties using the proposed multi-level upscaling approach.

A validation metric under epistemic uncertainty: When the epistemic uncertainties at fine scale levels are considered, then the influence of these uncertainties on the coarse scale model response that is used to predict the experiments at one scale level should also be investigated. In this case, the proposed validation metric should be improved to be able to account for the epistemic uncertainties in the quantitative assessment of the predictions. For example, if an interval-based modeling of the epistemic uncertainties at the fine scale is considered, the corresponding response of the coarse scale model will have a probability box (p-box), which represents the uncertainty by two probability distributions on the bounds of the interval [101]. In this case, the applicability of the K-S test should be extended to make a decision on a p-box. One way of achieving this could be to use the proposed approach in [225] where the K-S test is extended to make a comparison between two sampling data of interval values and the observed measurements.

Efficient sampling methods to decrease the number of required samples: The number of samples used to generate the distribution of a random variable is the most important computational bottleneck in the sampling based uncertainty propagation. Although the LHS approach provide a reduction in the number of samples for accurate representation of the uncertainty of a random variable compared to the MCS method, research is required to develop more efficient methods to decrease the number of samples further.

Non-linear Finite Element Analysis Methods: The current work focused on the uncertainty quantification of the linear elastic homogenized properties and linear static elastic analysis, in which only one or two properties are homogenized. In cases when the individual strut members of the lattice structures encounter to buckling, simple linear FEM modeling of the members is not accurate and geometrical nonlinearity should be considered. More investigation in this area should be conducted. The plastic behavior of lattice structures should also be investigated

under the quantified uncertainties to use the proposed upscaling method in applications where excessive deformation is seen such as impact simulations. In those cases, more than one homogenized variable is needed to be predicted for non-linear analysis to accurately capture both the elastic and plastic behavior of the lattice structures with a simplified coarse scale model. For instance, Ramberg-Osgood method given by the following equation requires four parameters to be predicted under the uncertainties:

$$E\varepsilon = S + \alpha\left(\frac{S}{S_y}\right)^{n-1} S \tag{6.1}$$

where S denotes the stress, ε denotes the strain. This coarse scale model has the corresponding four variables; E and S_y denote the elastic modulus and yield strength of the material, respectively and α and n are the plasticity constants. One issue when plastic behavior is considered is that the fine scale FEA will be solved at multiple strain levels to identify the stress-strain curve. Then, the one-dimensional PCE representation may not be sufficient to predict these homogenized variables because there will be more than one response on which the homogenized variables are dependent. One solution that can be considered as a future work would be to utilize a higher dimensional PCE in the upscaling process, in which the uncertainty is propagated from the fine scale responses at multiple strain levels. In that regard, the fine and coarse scale model responses can be compared at multiple strain levels, and the summation of the exponential loss function values at each strain level is used in the optimization step of the upscaling process to determine the homogenized input variables S_y, α, and n. Once the upscaling is completed, the proposed validation metric can pool the experimental measurements at the corresponding strain levels for a lattice specimen into one distribution to compare with the coarse scale model predictions. More investigation is required for

the application of the upscaling method in predicting the homogenized properties that can predict the plastic behavior of lattice structures.

Considering failure mechanisms in lattice structures: In this research, only the linear elastic behavior of the lattice structures was investigated assuming no failure mechanisms. The goal was to demonstrate the general procedure of uncertainty quantification of the lattice structures. Future work should be focused on incorporating different mechanical behavior phenomenon into the upscaling method such as fatigue, creep, crack propagation, etc. that can occur in the lattice structures based on the application type.

Predicting the anisotropy of the properties: The layer by layer fabrication process induces some dependency of the mechanical properties of the fabricated components on the build orientation as stated in Section 6.2. In order to have a better accuracy from the homogenized properties, research should be done to characterize the anisotropic properties at the macroscopic level. Moreover, efficient computational models are needed to model the material with the predicted anisotropic properties.

Design-specific validation: The proposed approach is used for validation by the experimental results of the fabricated test specimens at the lattice level. In the design process with the validated models using the proposed PCE-based metamodel approach, the realistic prediction of the properties is achieved with the quantified uncertainties. Although the use of predicted properties of the lattice structure used in Chapter 5 in design gives a good estimation of reality, simulations that account for the realistic loading through the surrounding would provide a complete picture. Moreover, additional design-specific validation of the designed structures should

be done to certify the final product performance. These detailed simulations of the designed part and the design-specific validation approach should be investigated as a future work.

Application of the proposed methodology for other material types: The proposed methodology is presented in this dissertation for uncertainty quantification of cellular lattice structures fabricated by AM. As this methodology generates material specific relationships between the fine and coarse scale models, there are numerous possibilities for the application of this method. It can also be used to predict the macroscopic level material properties of various types of other materials with complex microstructures (e.g. composite materials) as it requires only the black-box functions of the fine and coarse scale models. Moreover, as the proposed methodology utilizes the high-resolution 3D scan images of the material for uncertainty quantification at small scale levels, it can be extended to quantify uncertainties at the smaller scale levels than the strut level in AM-fabricated lattice structures where a highly heterogeneous nano- or micro- scale structure can exist by nature (e.g. with different phases of the material, with porosity, etc.).

Process-Structure-Property relationship: In this dissertation, only the quantification of the uncertainties in the material structure was conducted to identify its mechanical properties efficiently. This process corresponds to the structure-property (SP) relationship. On the other hand, the variations and uncertainties of the properties of an engineering material or structure occur because of the manufacturing process parameters. Hence, in addition to the SP relationship, the specific manufacturing processes used to form and shape the materials microstructure (i.e. process-structure (PS) relationship) need to be investigated in order to achieve the desired product performance. Future research should include developing novel computational tools that can be used to predict the effect that processing will have on the structure of the materials (i.e. PS

relationship) and developing the means to integrate these tools with the various SP models. Thus, the collection of process-structure (PS) and structure-property (SP) linkages data can be achieved especially for (but not limited to) the additively manufactured lattice structures. This research will also allow for the development of an integrated, stochastic multi-level modeling framework to predict the PSP linkages so that the risks in the design processes of structure topologies can be mitigated by quantifying and propagating uncertainties in various length scales.

Extending the design approach under uncertainties utilizing the upscaling method: The design procedure introduced in Chapter 5 is efficient to match the target elastic modulus without requiring any expensive optimization processes. Depending on the application, on the other hand, the design of the material layout based on the macroscopic boundary and loading conditions might be required. In those cases, the topology optimization is utilized, which is based on homogenization methods to estimate the homogenized elastic modulus of each continuum level element that corresponds to its density [42], [77]. When the fine scale uncertainties are considered, these deterministic relationships fail to provide accurate predictions. Hence, the proposed PCE-based meta-model approach that is developed based on the predictions made by the stochastic upscaling method is promising to be able to account for the uncertainties in the topology optimization process. A reliability-based topology optimization or robust topology optimization process can be developed by integrating the proposed meta-model approach into the topology optimization process as a future study. Thus, the applicability of the proposed method can be extended to the design of structures where the uncertainties are crucial in the design processes.

REFERENCES

[1]. McDowell, D.L., Panchal, J., Choi, H.J., Seepersad, C., Allen, J. and Mistree, F., 2009. *Integrated Design of Multiscale, Multifunctional Materials and Products*. Butterworth-Heinemann.

[2]. Choi, S.K., Grandhi, R. and Canfield, R.A., 2006. *Reliability-Based Structural Design*. Springer Science & Business Media.

[3]. Gibson, L.J. and Ashby, M.F., 1999. *Cellular Solids: Structure and Properties*. Cambridge University Press.

[4]. Evans, A.G., Hutchinson, J.W., Fleck, N.A., Ashby, M.F. and Wadley, H.N.G., 2001. The Topological Design of Multifunctional Cellular Metals. *Progress in Materials Science*, **46**(3), pp. 309-327.

[5]. Valdevit, L., Vermaak, N., Zok, F.W. and Evans, A.G., 2008. A Materials Selection Protocol for Lightweight Actively Cooled Panels. *Journal of Applied Mechanics*, **75**(6), pp.061022.

[6]. Deshpande, V.S., Fleck, N.A. and Ashby, M.F., 2001. Effective Properties of the Octet-Truss Lattice Material. *Journal of the Mechanics and Physics of Solids*, **49**(8), pp.1747-1769.

[7]. Hammetter, C.I., Rinaldi, R.G. and Zok, F.W., 2013. Pyramidal Lattice Structures for High Strength and Energy Absorption. *Journal of Applied Mechanics*, **80**(4), pp.041015.

[8]. Wadley, H.N., Fleck, N.A. and Evans, A.G., 2003. Fabrication and Structural Performance of Periodic Cellular Metal Sandwich Structures. *Composites Science and Technology*, **63**(16), pp.2331-2343.

[9]. Mines, R.A.W., 2008. On the Characterisation of Foam and Micro-Lattice Materials Used in Sandwich Construction. *Strain*, **44**(1), pp.71-83.

[10]. A. F2792-12a, 2012. Standard Terminology for Additive Manufacturing Technologies, West Conshohocken, PA.

[11]. Gibson, I., Rosen, D.W. and Stucker, B., 2010. *Additive Manufacturing Technologies*, New York: Springer.

[12]. Smith, M., Guan, Z. and Cantwell, W.J., 2013. Finite Element Modelling of the Compressive Response of Lattice Structures Manufactured Using the Selective Laser Melting Technique. *International Journal of Mechanical Sciences*, **67**, pp.28-41.

[13]. Rosen, D.W., 2007. Computer-Aided Design for Additive Manufacturing of Cellular Structures. *Computer-Aided Design and Applications*, **4**(5), pp.585-594.

[14]. Hopkinson, N., Hague, R. and Dickens, P. eds., 2006. *Rapid Manufacturing: An Industrial Revolution for the Digital Age*. John Wiley & Sons.

[15]. Heinl, P., Müller, L., Körner, C., Singer, R.F. and Müller, F.A., 2008. Cellular Ti–6Al–4V Structures with Interconnected Macro Porosity for Bone Implants Fabricated by Selective Electron Beam Melting. *Acta biomaterialia*, **4**(5), pp.1536-1544.

[16]. Murr, L.E., Gaytan, S.M., Medina, F., Lopez, H., Martinez, E., Machado, B.I., Hernandez, D.H., Martinez, L., Lopez, M.I., Wicker, R.B. and Bracke, J., 2010. Next-Generation Biomedical Implants Using Additive Manufacturing of Complex, Cellular and Functional Mesh Arrays. *Philosophical Transactions of the Royal Society of London A: Mathematical, Physical and Engineering Sciences*, **368**(1917), pp.1999-2032.

[17]. Hayes, A.M., Wang, A., Dempsey, B.M. and McDowell, D.L., 2004. Mechanics of Linear Cellular Alloys. *Mechanics of Materials*, **36**(8), pp.691-713.

[18]. Schaedler, T.A., Jacobsen, A.J., Torrents, A., Sorensen, A.E., Lian, J., Greer, J.R., Valdevit, L. and Carter, W.B., 2011. Ultralight Metallic Microlattices. *Science*, **334**(6058), pp.962-965.

[19]. Zheng, X., Lee, H., Weisgraber, T.H., Shusteff, M., DeOtte, J., Duoss, E.B., Kuntz, J.D., Biener, M.M., Ge, Q., Jackson, J.A. and Kucheyev, S.O., 2014. Ultralight, Ultrastiff Mechanical Metamaterials. *Science*, **344**(6190), pp.1373-1377.

[20]. Meza, L.R., Zelhofer, A.J., Clarke, N., Mateos, A.J., Kochmann, D.M. and Greer, J.R., 2015. Resilient 3D Hierarchical Architected Metamaterials. *Proceedings of the National Academy of Sciences*, **112**(37), pp.11502-11507.

[21]. Bauer, J., Schroer, A., Schwaiger, R. and Kraft, O., 2016. Approaching Theoretical Strength in Glassy Carbon Nanolattices. *Nature materials*, Vol. **15**, pp. 438-444.

[22]. Maass, R., Van Petegem, S., Ma, D., Zimmermann, J., Grolimund, D., Roters, F., Van Swygenhoven, H. and Raabe, D., 2009. Smaller is Stronger: The Effect of Strain Hardening. *Acta Materialia*, **57**(20), pp.5996-6005.

[23]. Bendsøe, M.P. and Sigmund, O., 2003. *Topology Optimization: Theory, Methods, and Applications*. Springer Verlag, New York.

[24]. Dorn, W., Gomory, R., and Greenberg, H., 1964. Automatic Design of Optimal Structures. *Journal de Mecanique.* Vol. **3**(6), pp. 25-52.

[25]. Rozvany, G. I. N., Bendose M. P., and Kirsch, U., 1995. Layout Optimization of Structures. *Applied Mechanics Reviews*, Vol. **48**, pp. 41-119.

[26]. Wang, H.V., and Rosen, D.W., 2006. An Automated Design Synthesis Method for Compliant Mechanisms with Application to Morphing Wings. *ASME 2006 International*

Design Engineering Technical Conferences and Computers and Information in Engineering Conference, pp. 231-239.

[27]. Seepersad, C.C., Dempsey, B., Allen, J.K., Mistree, F. and McDowell, D.L., 2004. Design of Multifunctional Honeycomb Materials. *AIAA Journal*, **42**(5), pp.1025-1033.

[28]. Chu, J., Engelbrecht, S., Graf, G. and Rosen, D.W., 2010. A Comparison of Synthesis Methods for Cellular Structures with Application to Additive Manufacturing. *Rapid Prototyping Journal*, **16**(4), pp.275-283.

[29]. Wieding, J., Wolf, A. and Bader, R., 2014. Numerical Optimization of Open-porous Bone Scaffold Structures to Match the Elastic Properties of Human Cortical Bone. *Journal of the Mechanical Behavior of Biomedical Materials*, **37**, pp.56-68.

[30]. Stanković, T., Mueller, J., Egan, P. and Shea, K., 2015. A Generalized Optimality Criteria Method for Optimization of Additively Manufactured Multimaterial Lattice Structures. *Journal of Mechanical Design*, **137**(11), p.111405.

[31]. Zhou, M. and Rozvany, G.I.N., 1992. DCOC: An Optimality Criteria Method for Large Systems Part I: Theory. *Structural Optimization*, **5**(1-2), pp.12-25.

[32]. Cansizoglu, O., Harrysson, O.L., West, H.A., Cormier, D.R. and Mahale, T., 2008. Applications of Structural Optimization in Direct Metal Fabrication. *Rapid Prototyping Journal*, **14**(2), pp.114-122.

[33]. Gorguluarslan, R.M., Gandhi, U.N., Mandapati, R. and Choi, S.K., 2016. Design and Fabrication of Periodic Lattice-based Cellular Structures. *Computer-Aided Design and Applications*, **13**(1), pp.50-62.

[34]. Patel, J. and Choi, S.K., 2012. Classification Approach for Reliability-based Topology Optimization Using Probabilistic Neural Networks. *Structural and Multidisciplinary Optimization*, **45**(4), pp.529-543.

[35]. Ruderman, A., Choi, S.K., Patel, J., Kumar, A. and Allen, J.K., 2010. Simulation-Based Robust Design of Multiscale Products. *Journal of Mechanical Design*, **132**(10), p.101003.

[36]. Chang, P.S., and Rosen, D.W., 2013. The Size Matching and Scaling Method: A Synthesis Method for the Design of Mesoscale Cellular Structures. *International Journal of Computer Integrated Manufacturing*, **26**(10), pp.907-927.

[37]. Nguyen, J., Park, S.I., and Rosen, D., 2013. Heuristic Optimization Method for Cellular Structure Design of Light Weight Components. *International Journal of Precision Engineering and Manufacturing*, **14**(6), pp.1071-1078.

[38]. Alzahrani, M., Choi, S.K., and Rosen, D.W., 2015. Design of Truss-like Cellular Structures Using Relative Density Mapping Method. *Materials & Design*, **85**, pp.349-360.

[39]. Brackett, D.J., Ashcroft, I.A., Wildman, R.D., and Hague, R.J.M., 2014. An Error Diffusion Based Method to Generate Functionally Graded Cellular Structures. *Computers & Structures*, **138**, pp.102-111.

[40]. Ning, X., and Pellegrino, S., 2012. Design of Lightweight Structural Components for Direct Digital Manufacturing. *53rd AIAA/ASME/ASCE/AHS/ASC Structures, Structural Dynamics and Materials Conference 20th AIAA/ASME/AHS Adaptive Structures Conference 14th AIAA*, pp. 1807.

[41]. Shea, K., and Smith, I.F., 2006. Improving Full-Scale Transmission Tower Design Through Topology and Shape Optimization. *Journal of Structural Engineering*, **132**(5), pp.781-790.

[42]. Bendsøe M.P., and Kikuchi N., 1998. Generating Optimal Topologies in Structural Design Using a Homogenization Method. *Computer Methods in Applied Mechanics and Engineering*, **71**(2), pp.197-224.

[43]. Eschenauer, H.A., and Olhoff, N., 2001. Topology Optimization of Continuum Structures: A Review*. *Applied Mechanics Reviews*, **54**(4), pp.331-390.

[44]. Horstemeyer, M.F., 2009. Multiscale Modeling: A Review. *Practical Aspects of Computational Chemistry*, Springer Netherlands, pp. 87-135.

[45]. Cheimarios, N., Kokkoris, G., and Boudouvis, A.G., 2010. Multiscale Modeling in Chemical Vapor Deposition Processes: Coupling Reactor Scale with Feature Scale Computations. *Chemical Engineering Science*, **65**(17), pp.5018-5028.

[46]. Rohan, E., and Cimrman, R., 2010. Two-Scale Modeling of Tissue Perfusion Problem Using Homogenization of Dual Porous Media. *International Journal for Multiscale Computational Engineering*, **8**(1), pp. 81-102.

[47]. Juanes, R., 2005. A Variational Multiscale Finite Element Method for Multiphase Flow in Porous Media. *Finite Elements in Analysis and Design*, **41**(7), pp.763-777.

[48]. Allen, J.K., Seepersad, C., Choi, H., and Mistree, F., 2006. Robust Design for Multiscale and Multidisciplinary Applications. *Journal of Mechanical Design*, **128**(4), pp.832-843.

[49]. Choi, H., McDowell, D.L., Allen, J.K., Rosen, D., and Mistree, F., 2008. An Inductive Design Exploration Method for Robust Multiscale Materials Design. *Journal of Mechanical Design*, **130**(3), p.031402.

[50]. Chen, W., Yin, X., Lee, S., and Liu, W.K., 2010. A Multiscale Design Methodology for Hierarchical Systems with Random Field Uncertainty. *Journal of Mechanical Design*, **132**(4), p.041006.

[51]. Ruderman, A., Choi, S.K., Patel, J., Kumar, A., and Allen, J.K., 2010. Simulation-Based Robust Design of Multiscale Products. *Journal of Mechanical Design*, **132**(10), p.101003.

[52]. Arbogast, T., 2004. Analysis of a Two-scale, Locally Conservative Subgrid Upscaling for Elliptic Problems. *SIAM Journal on Numerical Analysis*, **42**(2), pp.576-598.

[53]. Weinan, E., and Engquist, B., 2003. The Heterognous Multiscale Methods. *Communications in Mathematical Sciences*, **1**(1), pp.87-132.

[54]. Abdulle, A., Weinan, E., Engquist, B., and Vanden-Eijnden, E., 2012. The Heterogeneous Multiscale Method. *Acta Numerica*, **21**, pp.1-87.

[55]. Efendiev, Y., and Hou, T.Y., 2009. *Multiscale Finite Element Methods: Theory and Applications*, Springer Science & Business Media.

[56]. McVeigh, C., Vernerey, F., Liu, W.K., and Brinson, L.C., 2006. Multiresolution Analysis for Material Design. *Computer Methods in Applied Mechanics and Engineering*, **195**(37), pp.5053-5076.

[57]. Liu, W.K., and McVeigh, C., 2008. Predictive Multiscale Theory for Design of Heterogeneous Materials. *Computational Mechanics*, **42**(2), pp.147-170.

[58]. Farmer, C.L., 2002. Upscaling: A Review. *International Journal for Numerical Methods in Fluids*, **40**(1-2), pp.63-78.

[59]. Hao, S., Moran, B., Liu, W.K., and Olson, G.B., 2003. A Hierarchical Multi-Physics Model for Design of High Toughness Steels. *Journal of Computer-Aided Materials Design*, **10**(2), pp.99-142.

[60]. Qu, J., and Cherkaoui, M., 2006. *Fundamentals of Micromechanics of Solids*. John Wiley & Sons, New Jersey.

[61]. Eshelby, J.D., 1957. The Determination of the Elastic Field of an Ellipsoidal Inclusion, and Related Problems. *Proceedings of the Royal Society of London A: Mathematical, Physical and Engineering Sciences*, **241**(1226), pp. 376-396.

[62]. Mori, T., and Tanaka, K., 1973. Average Stress in Matrix and Average Elastic Energy of Materials with Misfitting Inclusions. *Acta Metallurgica*, **21**(5), pp.571-574.

[63]. Hill, R., 1965. A Self-Consistent Mechanics of Composite Materials. *Journal of the Mechanics and Physics of Solids*, **13**(4), pp.213-222.

[64]. Voigt, W., 1889. On The Relation Between the Elasticity Constants of Isotropic Bodies. *Annual Review of Physical Chemistry*, **274**, pp.573-587.

[65]. Reuss, A., 1929. Determination of the Yield Point of Polycrystals Based on the Yield Condition of Sigle Crystals. *Z. Angew. Mathematics and Mechanics*, **9**, pp.49-58.

[66]. Wang, A., and McDowell, D., 2004. In-Plane Stiffness and Yield Strength of Periodic Metal Honeycombs. *Journal of Engineering Materials and Technology*, **126**, pp. 137-56.

[67]. Wang A., and McDowell D., 2005. Yield Surfaces of Various Periodic Metal Honeycombs at Intermediate Relative Density. *International Journal of Plasticity*, **21**, pp. 285-320.

[68]. Yvonnet, J., Monteiro, E. and He, Q.C., 2013. Computational Homogenization Method and Reduced Database Model for Hyperelastic Heterogeneous Structures. *International Journal for Multiscale Computational Engineering*, **11**(3). pp. 201-225.

[69]. Terada, K., and Kikuchi, N., 1995. Computational Methods in Micromechanics. *ASME: San Francisco.* Vol. AMD-212/MD-62. Ghosh S, Ostoja-Starzewski M (eds)., CA, pp. 1-16.

[70]. Vigliotti, A. and Pasini, D., 2012. Stiffness and Strength of Tridimensional Periodic Lattices. *Computer Methods in Applied Mechanics and Engineering*, **229**, pp.27-43.

[71]. Oskay, C. and Fish, J., 2007. Eigendeformation-Based Reduced Order Homogenization for Failure Analysis of Heterogeneous Materials. *Computer Methods in Applied Mechanics and Engineering*, **196**(7), pp.1216-1243.

[72]. Dos Reis, F., and Ganghoffer, J., 2010. Discrete Homogenization of Architecture Materials: Implementation of the Method in a Simulation Tool for the Systematic Prediction of Their Effective Elastic Properties. *Technische Mechanik*, **30**, pp. 85-109.

[73]. Tollenaere, H., and Caillerie, D., 1998. Continuous Modeling of Lattice Structures by Homogenization. *Advances in Engineering Software*, **29**, pp. 699-705.

[74]. Hutchinson R., and Fleck, N., 2006. The Structural Performance of the Periodic Truss. *Journal of the Mechanics and Physics of Solids*, **54**, pp. 756-82.

[75]. Elsayed, M.S.A., and Pasini, D., 2010. Analysis of the Elasto Static Specific Stiffness of 2D Stretching-Dominated Lattice Materials. *Mechanics of Materials*, **42**, pp. 709-25.

[76]. Arabnejad, S., and Pasini, D., 2013. Mechanical Properties of Lattice Materials Via Asymptotic Homogenization and Comparison with Alternative Homogenization Methods. *International Journal of Mechanical Sciences*, **77**, pp. 249-262.

[77]. Khanoki, S. A., and Damiano, P., 2012. Multiscale Design and Multiobjective Optimization of Orthopedic Hip Implants with Functionally Graded Cellular Material. *Journal of Biomechanical Engineering*, **134**(3), pp. 031004.

[78]. Fish, J. and Wu, W., 2011. A Nonintrusive Stochastic Multiscale Solver. *International Journal for Numerical Methods in Engineering*, **88**(9), pp.862-879.

[79]. Cansizoglu, O., Harrysson, O., Cormier, D., West, H., and Mahale, T., 2008. Properties of Ti-6Al-4V Non-Stochastic Lattice Structures Fabricated via Electron Beam Melting. *Materials Science and Engineering A.*, Vol. 492, pp. 468-474.

[80]. Parthasarathy, J., Starly, B., Raman, S. and Christensen, A., 2010. Mechanical Evaluation of Porous Titanium (Ti6Al4V) Structures with Electron Beam Melting (EBM). *Journal of the Mechanical Behavior of Biomedical Materials.*, **3**(3), pp.249-259.

[81]. Harrysson, O.L., Cansizoglu, O., Marcellin-Little, D.J., Cormier, D.R. and West, H.A., 2008. Direct Metal Fabrication of Titanium Implants with Tailored Materials and Mechanical Properties Using Electron Beam Melting Technology. *Materials Science and Engineering: C*, **28**(3), pp.366-373.

[82]. Cahill, S., Lohfeld, S., and McHugh, P. E., 2009. Finite Element Predictions Compared to Experimental Results for the Effective Modulus of Bone Tissue Engineering Scaffolds Fabricated by Selective Laser Sintering. *Journal of Material Science: Materials in Medicine*, Vol. 20, pp. 1255-1262.

[83]. Campoli, G., Borleffs, M.S., Yavari, S.A., Wauthle, R., Weinans, and H. Zadpoor, A.A., 2013. Mechanical Properties of Open-cell Metallic Biomaterials Manufactured Using Additive Manufacturing. *Materials & Design*, **49**, pp. 957-965.

[84]. Ravari, M.K., Kadkhodaei, M., Badrossamay, M. and Rezaei, R., 2014. Numerical Investigation on Mechanical Properties of Cellular Lattice Structures Fabricated by Fused Deposition Modeling. *International Journal of Mechanical Sciences*, **88**, pp.154-161.

[85]. Tsopanos, S., Mines, R.A.W., McKown, S., Shen, Y., Cantwell, W.J., Brooks, W. and Sutcliffe, C.J., 2010. The Influence of Processing Parameters on the Mechanical Properties of Selectively Laser Melted Stainless Steel Microlattice Structures. *Journal of Manufacturing Science and Engineering*, **132**(4), p.041011.

[86]. Gümrük, R. and Mines, R.A.W., 2013. Compressive Behavior of Stainless Steel Micro-Lattice Structures. *International Journal of Mechanical Sciences*, **68**, pp. 125-139.

[87]. Doyle, H., Lohfeld, S. and McHugh, P., 2014. Predicting the Elastic Properties of Selective Laser Sintered PCL/β-TCP Bone Scaffold Materials Using Computational Modelling. *Annals of Biomedical Engineering*, **42**(3), pp.661-677.

[88]. Suard, M., Martin, G., Lhuissier, P., Dendievel, R., Vignat, F., Blandin, J.J. and Villeneuve, F., 2015. Mechanical Equivalent Diameter of Single Struts for the Stiffness Prediction of Lattice Structures Produced by Electron Beam Melting. *Additive Manufacturing*, **8**, pp.124-131.

[89]. Park, S-I, Rosen, D. W., Choi, S-K, and Duty, C. E., 2014. Effective Mechanical Properties of Lattice Material Fabricated by Material Extrusion Additive Manufacturing. *Additive Manufacturing*, Vol. 1, pp. 12-23.

[90]. Sriramula, S. and Chryssanthopoulos, M.K., 2009. Quantification of Uncertainty Modelling in Stochastic Analysis of FRP Composites. *Composites Part A: Applied Science and Manufacturing*, **40**(11), pp.1673-1684.

[91]. Xu, X.F., 2007. A Multiscale Stochastic Finite Element Method on Elliptic Problems Involving Uncertainties. *Computer Methods in Applied Mechanics and Engineering*, **196**(25), pp.2723-2736.

[92]. Asokan, B.V. and Zabaras, N., 2006. A Stochastic Variational Multiscale Method for Diffusion in Heterogeneous Random Media. *Journal of Computational Physics*, **218**(2), pp.654-676.

[93]. Xu, X.F. and Chen, X., 2009. Stochastic Homogenization of Random Elastic Multi-Phase Composites and Size Quantification of Representative Volume Element. *Mechanics of Materials*, **41**(2), pp.174-186.

[94]. Das, S. and Ghanem, R., 2011. Stochastic Upscaling for Inelastic Material Behavior from Limited Experimental Data. *Computational Methods for Microstructure-Property Relationships,* pp. 443-468.

[95]. He, X. and Jiang, L., 2013. An Upscaling Method Using Coefficient Splitting and its Applications to Elliptic PDEs. *Computers & Mathematics with Applications*, **65**(4), pp.712-730.

[96]. Arbogast, T., Minkoff, S.E., and Keenan, P.T., 1998. An Operator-Based Approach to Upscaling the Pressure Equation. *Computational Methods in Water Resources XII*, **1**, pp. 405-412.

[97]. Koutsourelakis, P.S., 2007. Stochastic Upscaling in Solid Mechanics: An Exercise in Machine Learning, *Journal of Computational Physics*, **226**(1), pp. 301-325.

[98]. Arnst, M. and Ghanem, R., 2008. Proabilistic Equivalence and Stochastic Model Reduction in Multiscale Analysis. *Computer Methods in Applied Mechanics and Engineering*, **197**(43), pp. 3584-3592.

[99]. Wiener, N., 1938. The Homogeneous Chaos. *American Journal of Mathematics*, **60**(4), pp.897-936.

[100]. Shokrieh, M.M. and Rafiee, R., 2010. Stochastic Multi-Scale Modeling of CNT/polymer Composites. *Computational Materials Science*, **50**(2), pp.437-446.

[101]. Oberkampf, W.L., C. Roy, 2010. Verification and Validation in Scientific Computing, *Cambridge University Press*, Cambridge, UK.

[102]. AIAA, 1998. *Guide for the Verification and Validation of Computational Fluid Dynamics Simulations, Tech Rep,* AIAA G-077-1998, American Institute of Aeronautics and Asronautics.

[103]. ASME Committee PTC-60 V&V 10, 2006. *Guide for Verification and Validation in Computational Solid Mechanics*, ASME.

[104]. Post D. E., *The Coming Crisis in Computational Sciences*, 2004. Technical Report Rep.LA-UR-03-88-2004, Los Alamos National Laboratory, Los Alamos, NM.

[105]. Babuška I., Nobile F., and Tempone R., 2007. Reliability of Computational Science. *Numerical Methods* for *Partial Differential Equations*, **23** (4), pp. 753-784.

[106]. Liu, Y., Chen, W., Arendt, P., and Huang, H. Z., 2011. Toward a Better Understanding of Model Validation Metrics. *Journal of Mechanical Design*,**133**(7), pp. 071005.

[107]. Ling, Y., and Mahadevan, S., 2013. Quantitative Model Validation Techniques: New Insights. *Reliability Engineering and System Safety*, Vol. 111, pp. 217-231.

[108]. Marden J., 2000. Hypothesis Testing: From p Values to Bayes Factors. *Journal of the American Statistical Association*, **95**(452), pp.1316-1320.

[109]. Haldar, A., and Mahadevan, S., 2000. *Probability, Reliability, and Statistical Methods in Engineering Design*, Wiley, New York.

[110]. Ferson S., Oberkampf W., and Ginzburg L., 2008. Model Validation and Predictive Capability for the Thermal Challenge Problem. *Computer Methods in Applied Mechanics and Engineering*, **197**(29-32), pp. 2408-30.

[111]. Li, W., Chen, W., Jiang, Z., Lu, Z., and Liu, Y., 2014. New Validation Metrics for Models with Multiple Correlated Responses. *Reliability Engineering & System Safety*, Vol. 127, pp. 1-11.

[112]. Farrell, K., and Oden, J.T., 2014. Calibration and Validation of Coarse-Grained Models of Atomic Systems: Application to Semiconductor Manufacturing. *Computational Mechanics*, **54**(1), pp. 3-19.

[113]. Oden, J.T., Ernesto E.P., and Paul T.B., 2013. Virtual Model Validation of Complex Multiscale Systems: Applications to Nonlinear Elastostatics. *Computer Methods in Applied Mechanics and Engineering*, **266**, pp. 162-184.

[114]. Oskay, C., and Fish, J., 2008. On Calibration and Validation of Eigendeformation-Based Multiscale Models for Failure Analysis of Heterogeneous Systems. *Computational Mechanics*, **42**(2), pp. 181-195.

[115]. Najm, H.N., 2009. Uncertainty Quantification and Polynomial Chaos Techniques in Computational Fluid Dynamics. *Annual Review of Fluid Mechanics*, **41**, pp.35-52.

[116]. Cramer, H., 1928. On the Composition of Elementary Errors. *Second Paper: Statistical Applications, Skand. Aktuarietidskrift*, **11**, pp. 13-74.

[117]. Anderson, T.W. and Darling, D.A., 1954. A Test of Goodness of Fit. *Journal of the American Statistical Association*, **49**(268), pp.765-769.

[118]. Marsaglia, G., Tsang, W.W., and Wang, J., 2003. Evaluating Kolmogorov`s Distribution. *Journal of Statistical Software*, **8**(18), pp. 1-4.

[119]. Cirrone, G.A.P., Donadio, S., Guatelli, S., Mantero, A., Mascialino, B., Parlati, S., Pia, M.G., Pfeiffer, A., Ribon, A. and Viarengo, P., 2004. A Goodness-of-fit Statistical Toolkit. *Nuclear Science, IEEE Transactions on*, **51**(5), pp.2056-2063.

[120]. D'Agostino, R. B., and Stephens, M. A., 1986. *Goodness-Of-Fit Techniques*, Marcel-Dekker, INC., New York, United States, ISBN: 0-8247-7487-6.

[121]. Donadio, S., Guatelli, S., Mantero, A., Mascialino, B., Parlati, S., Pia, M.G., Pfeiffer, A., Ribon, A. and Viarengo, P., 2004. A Goodness-of-fit Statistical Toolkit. *Nuclear Science, IEEE Transactions on*, **51**(5), pp.2056-2063.

[122]. Haldar, A., and Mahadevan, S., 2000. *Reliability Assessment Using Stochastic Finite Element Analysis*. John Wiley & Sons.

[123]. Myung, I.J., 2003. Tutorial on Maximum Likelihood Estimation. *Journal of Mathematical Psychology*, **47**, pp. 90-100.

[124]. Schwarz, G., 1978. Estimating the Dimension of a Model. *The Annals of Statistics*, **6**, pp. 461-464.

[125]. Beck, J.L. and Yuen, K.V., 2004. Model Selection Using Response Measurements: Bayesian Probabilistic Approach. *Journal of Engineering Mechanics*, **130**(2), pp.192-203.

[126]. Akaike, H., 1973. *Information Theory as an Extension of the Maximum Likelihood Principle*. In: Petrov, B.N., Csaki, F. (Eds.), Second International Symposium on Information Theory. Akademiai Kiado, Budapest, pp. 267-281.

[127]. Hurvich, C.M. and Tsai, C.L., 1989. Regression and Time Series Model Selection in Small Samples. *Biometrika*, **76**(2), pp.297-307.

[128]. Noh, Y., Choi, K.K. and Lee, I., 2010. Identification of Marginal and Joint CDFs Using Bayesian Method for RBDO. *Structural and Multidisciplinary Optimization*, **40**(1-6), pp.35-51.

[129]. Posada, D., and Buckley, T.R., 2004. Model Selection and Model Averaging in Phylogenetics: Advantages of Akaike Information Criterion and Bayesian Approaches over Likelihood Tests. *Systematic Biology*, **53**, pp. 793-808.

[130]. Beck, J.L. and Yuen, K.V., 2004. Model Selection Using Response Measurements: Bayesian Probabilistic Approach. *Journal of Engineering Mechanics*, **130**(2), pp.192-203.

[131]. Stark, P.B., and Tenorio, L., 2010. A Primer of Frequentist and Bayesian Inference in Inverse Problems, in: L. Biegler, G. Biros, O. Ghattas, M. Heinkenschloss, D. Keyes, B.

Mallick, L. Tenorio, B. van Bloemen Waanders, K. Willcox, Y. Marzouk (Eds.), *Computational Methods for Large Scale Inverse Problems and Uncertainty Quantification*, John Wiley & Sons, UK, pp. 9-32.

[132]. Huynh, D.B.P., Knezevic, D.J. and Patera, A.T., 2012. Certified Reduced Basis Model Validation: A Frequentistic Uncertainty Framework. *Computer Methods in Applied Mechanics and Engineering*, **201**, pp.13-24.

[133]. Ghanem, R.G., and Spanos, P.D., 1991. *Stochastic Finite Elements: A Spectral Approach*, Springer-Verlag, New York.

[134]. Desceliers, C., Ghanem, R. and Soize, C., 2006. Maximum Likelihood Estimation of Stochastic Chaos Representations from Experimental Data. *International Journal for Numerical Methods in Engineering*, **66**(6), pp.978-1001.

[135]. Rebba, R. and Cafeo, J., 2008. Probabilistic Analysis of a Static Frame Model. *Computer Methods in Applied Mechanics and Engineering*, **197**(29), pp.2561-2571.

[136]. Sobol, I.M., 1994. *A Primer for the Monte Carlo Method*, CRC Press, Boca Raton, Florida, USA.

[137]. McKay, M. D., Conover, W.J., and Beckman, R.J., 1979. A Comparison of Three Methods for Selecting Values of Input Variables in the Analysis of Output from a Computer Code. *Technometrics*, **21**, pp. 239-245.

[138]. Zein, S., Colson, B. and Glineur, F., 2013. An Efficient Sampling Method for Regression-Based Polynomial Chaos Expansion. *Communications in Computational Physics*, **13**(04), pp.1173-1188.

[139]. Tatang, M.A., 1995. *Direct Incorporation of Uncertainty in Chemical and Environmental Engineering Systems* (Doctoral dissertation, Massachusetts Institute of Technology).

[140]. Isukapalli, S.S., 1999. *Uncertainty Analysis of Transport-Transformation Models* (Doctoral dissertation, Rutgers, The State University of New Jersey).

[141]. Narayanan, V.A.B. and Zabaras, N., 2004. Stochastic Inverse Heat Conduction Using a Spectral Approach. *International Journal for Numerical Methods in Engineering*, **60**(9), pp.1569-1593.

[142]. Coelho, R.F. and Bouillard, P., 2011. Multi-Objective Reliability-Based Optimization with Stochastic Metamodels. *Evolutionary Computation*, **19**(4), pp.525-560.

[143]. Coelho, R.F., Lebon, J. and Bouillard, P., 2011. Hierarchical Stochastic Metamodels Based on Moving Least Squares and Polynomial Chaos Expansion. *Structural and Multidisciplinary Optimization*, **43**(5), pp.707-729.

[144]. Suryawanshi, A. and Ghosh, D., 2016. Reliability Based Optimization in Aeroelastic Stability Problems Using Polynomial Chaos Based Metamodels. *Structural and Multidisciplinary Optimization*, **53**(5), pp.1069-1080.

[145]. Capdeville, Y., Guillot, L. and Marigo, J.J., 2010. 2-d Non-Periodic Homogenization to Upscale Elastic Media for p–sv Waves. *Geophysical Journal International*, **182**(2), pp.903-922.

[146]. Suquet, P., 1987. Elements of Homogenization Theory for Inelastic Solid Mechanics. *In: E Sanchez-Palencia, Zaoui, A., (eds): Homogenization techniques for composite media*, pp. 194-278. Berlin, Heidelberg, Springer, New York.

[147]. Li, S., Sauer, R.A., and Wang, G., 2005. A Circular Inclusions in a Finite Domain I. The Dirichlet-Eshelby Problem. *Acta Mech*, **179,** pp. 67-90.

[148]. Doghri, I. and Tinel, L., 2006. Micromechanics of Inelastic Composites with Misaligned Inclusions: Numerical Treatment of Orientation. *Computer Methods in Applied Mechanics and Engineering*, **195**(13), pp.1387-1406.

[149]. Gusev, A. A., 1997. Representative Volume Element Size for Elastic Composites: A Numerical Study, *Journal of the Mechanics and Physics of Solids*, **45**, pp. 1449-1459.

[150]. Hazanov, S. and Amieur, M., 1995. On Overall Properties for Elastic Heterogeneous Bodies Smaller than the Representative Volume, *International Journal of Engineering Science*, **33**(9), pp. 1289-1301.

[151]. Pindera, M. J., Aboudi, J., and Arnold, S. M., 1995. Limitations of the Uncoupled, RVE-Based Micromechanical Approach in the Analysis of Functionally Graded Composites, *Mechanics of Materials*, **20**, pp. 77-94.

[152]. Hill, R., 1963. Elastic Properties of Reinforced Solids: Some Theoretical Principles. *Journal of the Mechanics and Physics of Solids*, **11**, pp. 357-372.

[153]. Ostoja-Starzewski, M., 2006. Material Spatial Randomness: From Statistical to Representative Volume Element. *Probabilistic Engineering Mechanics*, 21(2), pp. 112-132.

[154]. Hollister, S.J., and Kikuchi, N., 1992. A Comparison of Homogenization and Standard Mechanics Analyses for Periodic Porous Composites. *Computational Mechanics*, **10**, pp.73-95.

[155]. Hazanov, S., 1998. Hill Condition and Overall Properties of Composites. *Archive of Applied Mechanics*, **68**(6), pp.385-394.

[156]. Van der Sluis, O., Schreurs, P.J.G., Brekelmans, W.A.M. , and Meijer,v H.E.H., 2000. Overall Behavior of Heterogeneous Elastoviscoplastic Materials: Effect of Microstructural Modeling, *Mechanics of Materials*, **32**, pp. 449-462.

[157]. Anthoine, A., 1995. Derivation of the In-plane Elastic Characteristics of Masonry Through Homogenization Theory. *International Journal of Solids and Structures*, **32**(2), pp.137-163.

[158]. Wienecke, H.A., Brockenbrough, J.R. and Romanko, A.D., 1995. A Three-dimensional Unit Cell Model with Application Toward Particulate composites. *Journal of Applied Mechanics*, **62**(1), pp.136-140.

[159]. Xia, Z., Zhou, C., Yong, Q. and Wang, X., 2006. On Selection of Repeated Unit Cell Model and Application of Unified Periodic Boundary Conditions in Micro-Mechanical Analysis of Composites. *International Journal of Solids and Structures*, **43**(2), pp.266-278.

[160]. Terada, K., Hori, M., Kyoya, T. and Kikuchi, N., 2000. Simulation of the Multi-Scale Convergence in Computational Homogenization Approaches. *International Journal of Solids and Structures*, **37**(16), pp.2285-2311.

[161]. Bensoussan, A., Lions, J.L. and Papanicolaou, G., 1978. *Asymptotic Analysis for Periodic Structures*, North-Holland, Amsterdam.

[162]. Roache, P. 1998. *Verification and Validation in Computational Science and Engineering. Albuquerque*, N.Mex.: Hermosa Publishers.

[163]. Babuska, I. 2004. Verification and Validation in Computational Engineering and Science: Basic Concepts. *Computer Methods in Applied Mechanics and Engineering*, **193**, pp. 4057-4066.

[164]. Veluri, S. P., Roy, C. J., Ahmed, A., Rifki, R., Worley, J. C., and Recktenwald, B., 2009. Joint Computational/Experimental Aerodynamic Study of a Simplified Tractor/Trailer Geometry, *Journal of Fluids Engineering*, **131**(8).

[165]. Oberkampf W.L., Barone M.F., 2006. Measures of Agreement Between Computation and Experiment: Validation Metrics. *Journal of Computational Physics*, Vol. **217**, pp. 5-36.

[166]. Chen W., Baghdasaryan L., Buranathiti T., Cao J., 2004. Model Validation via Uncertainty Propagation. *AIAA Journal*, Vol. **42**, pp. 1406-1415.

[167]. Zhang R, and Mahadevan S., 2003. Bayesian Methodology for Reliability Model Acceptance. *Journal of Reliable Engineering Systems Safety*, Vol. **80**(1), pp. 95-103.

[168]. Sankararaman, S., and Mahadevan, S., 2015. Integration of Model Verification, Validation, and Calibration for Uncertainty Quantification in Engineering Systems. *Reliability Engineering & System Safety*, Vol. **138**, pp. 194-209.

[169]. Rebba, R., and Mahadevan, S., 2008. Computational Methods for Model Reliability Assessment. *Reliability Engineering & System Safety*, Vol. **93**(8), pp. 1197-1207.

[170]. Oberkampf, W. L., Trucano, T. G., and Hirsch, C., 2004. Verification, Validation, and Predictive Capability in Computational Engineering and Physics. *Applied Mechanics Reviews*, **57**(3), pp. 345-384.

[171]. Thacker, B. H., Paez, T. L., 2014. A Simple Probabilistic Validation Metric for the Comparison of Uncertain Model and Test Results. *16th AIAA Non-Deterministic Approaches Conference*.

[172]. Seghouane, A., Bekara, M., and Fleury, G., 2005. A Criterion for Model Selection in the Presence of Incomplete Data Based on Kullback's Symmetric Divergence. *Signal Processing*, Vol. **85**(7), pp.1405-1417.

[173]. Angus, J.E., 1994. The Probability Integral Transform and Related Results. *SIAM Review*, **36**(4), pp.652-654.

[174]. Rao, S.S., 2009. *Engineering Optimization*, Wiley & Sons Inc.

[175]. Brackett, D., Ashcroft, I. and Hague, R., 2011. Topology Optimization for Additive Manufacturing. *Proceedings of the Solid Freeform Fabrication Symposium, Austin, TX*, pp. 348-362.

[176]. Dorn, W., Gomory, R., and Greenberg, H., 1964. Automatic Design of Optimal Structures. *Journal de Mecanique*, **3**, pp. 25-52.

[177]. Cheng, K.T. and Olhoff, N., 1981. An Investigation Concerning Optimal Design of Solid Elastic Plates. *International Journal of Solids and Structures*, **17**(3), pp.305-323.

[178]. Haftka, R.T. and Grandhi, R.V., 1986. Structural Shape Optimization—A Survey. *Computer Methods in Applied Mechanics and Engineering*, **57**(1), pp.91-106.

[179]. Bendsøe, M.P., 1989. Optimal Shape Design as a Material Distribution Problem. *Structural Optimization*, **1**(4), pp.193-202.

[180]. Sigmund, O., 2001. A 99-line Topology Optimization Code Written in Matlab. *Structural and Multidisciplinary Optimization*, **21**(2), pp.120-127.

[181]. Zhou, M. and Rozvany, G.I.N., 1991. The COC Algorithm, Part II: Topological, Geometrical and Generalized Shape Optimization. *Computer Methods in Applied Mechanics and Engineering*, **89**(1-3), pp.309-336.

[182]. Mlejnek, H.P., 1992. Some Aspects of the Genesis of Structures. *Structural Optimization*, **5**(1-2), pp.64-69.

[183]. Bendsøe, M.P. and Sigmund, O., 1999. Material Interpolation Schemes in Topology Optimization. *Archive of Applied Mechanics*, **69**(9-10), pp.635-654.

[184]. Suzuki, K. and Kikuchi, N., 1991. A Homogenization Method for Shape and Topology Optimization. *Computer Methods in Applied Mechanics and Engineering*, **93**(3), pp.291-318.

[185]. Tsui, K.L., 1992. An Overview of Taguchi Method and Newly Developed Statistical Methods for Robust Design. *IIE Transactions*, **24**(5), pp. 44-57.

[186]. Dunning, P.D. and Kim, H.A., 2013. Robust Topology Optimization: Minimization of Expected and Variance of Compliance. *AIAA journal*, **51**(11), pp.2656-2664.

[187]. Kharmanda, G., Olhoff, N., Mohamad, A., and Lemaire, M., 2004. Reliability-Based Topology Optimization. *Structural and Multidisciplinary Optimization*, **26**(5), pp. 295-307.

[188]. Kim, S.R., Park, J.Y., Lee, W.G., Yu, J.S., and Han, S.Y., 2008. Reliability-Based Topology Optimization Based on Evolutionary Structural Optimization. *International Journal of Mechanical Systems Engineering*, **1**, pp. 135-9.

[189]. Luo, Y., Zhou, M., Wang, M.Y. and Deng, Z., 2014. Reliability Based Topology Optimization for Continuum Structures with Local Failure Constraints. *Computers & Structures*, **143**, pp.73-84.

[190]. Tootkaboni, M., Asadpoure, A. and Guest, J.K., 2012. Topology Optimization of Continuum Structures Under Uncertainty–a Polynomial Chaos Approach. *Computer Methods in Applied Mechanics and Engineering*, **201**, pp.263-275.

[191]. Torii, A.J., Novotny, A.A. and Santos, R.B., 2016. Robust Compliance Topology Optimization Based on the Topological Derivative Concept. *International Journal for Numerical Methods in Engineering*.

[192]. Theocaris, P.S., and Stavroulakis, G.E., 1999. Optimal Material Design in Composites: An Iterative Approach Based on Homogenized Cells. *Computer Methods in Applied Mechanics and Engineering*, **169**(1), pp.31-42.

[193]. Rodrigues, H., Guedes, J.M., and Bendsoe, M.P., 2002. Hierarchical Optimization of Material and Structure. *Structural and Multidisciplinary Optimization*, **24**(1), pp.1-10.

[194]. Coelho, P.G., Fernandes, P.R., Guedes, J.M., and Rodrigues, H.C., 2008. A Hierarchical Model for Concurrent Material and Topology Optimisation of Three-Dimensional Structures. *Structural and Multidisciplinary Optimization*, **35**(2), pp.107-115.

[195]. Xia, L. and Breitkopf, P., 2014. Concurrent Topology Optimization Design of Material and Structure within Nonlinear Multiscale Analysis Framework. *Computer Methods in Applied Mechanics and Engineering*, **278**, pp.524-542.

[196]. Liu, L., Yan, J. and Cheng, G., 2008. Optimum Structure with Homogeneous Optimum Truss-like Material. *Computers & Structures*, **86**(13), pp.1417-1425.

[197]. Andreasen, C.S. and Sigmund, O., 2012. Multiscale Modeling and Topology Optimization of Poroelastic Actuators. *Smart Materials and Structures*, **21**(6), p.065005.

[198]. Xia, L. and Breitkopf, P., 2016. Recent Advances on Topology Optimization of Multiscale Nonlinear Structures. *Archives of Computational Methods in Engineering*, pp.1-23.

[199]. Guo, X., Zhao, X., Zhang, W., Yan, J. and Sun, G., 2015. Multi-Scale Robust Design and Optimization Considering Load Uncertainties. *Computer Methods in Applied Mechanics and Engineering*, **283**, pp.994-1009.

[200]. Gogarty, E. and Pasini, D., 2015. Hierarchical Topology Optimization for Bone Tissue Scaffold: Preliminary Results on the Design of a Fracture Fixation Plate. *Engineering and Applied Sciences Optimization*, pp. 311-340.

[201]. Zabaras, N. and Ganapathysubramanian, B., 2008. A Scalable Framework for the Solution of Stochastic Inverse Problems Using a Sparse Grid Collocation Approach. *Journal of Computational Physics*, **227**(9), pp. 4697-4735.

[202]. Shell, M.S., 2008. The Relative Entropy is Fundamental to Multiscale and Inverse Thermodynamic Problems, *The Journal of Chemical Physics*, **129**, pp. 144108.

[203]. Zhang, H., Dai, H., Beer, M., Wang, W., 2013. Structural Reliability Analysis on the Basis of Small Samples: An Interval Quasi-Monte Carlo Method. *Mechanical Systems and Signal Processing*, Vol. **37**, pp. 137-151.

[204]. Van Weeren, R., Agarwala, M., Jamalabad, V. R., Bandyophadyay, A., Vaidyanathan, R., Langrana, N., Safari, A., Whalen, P., Danforth, S. C., and Ballard, C., 1995. Quality of Parts Processed by Fused Deposition. *Proceedings of the Solid Freeform Fabrication Symposium*, Vol. **6**, pp. 314-21.

[205]. B. H., Abdullah, J., and Khan, Z. A., 2005. Optimization of Rapid Prototyping Parameters for Production of Flexible ABS Object. *Journal of Materials Processing Technology*, Vol. **169**, pp. 54-61.

[206]. Otsu, N., 1979. A Threshold Selection Method from Gray-Level Histograms. *IEEE Transactions on Systems, Man, and Cybernetics*, Vol. **9**, No. 1, pp. 62-66.

[207]. Yan, C., Hao, L., Hussein, A., Young, P. and Raymont, D., 2014. Advanced Lightweight 316L Stainless Steel Cellular Lattice Structures Fabricated via Selective Laser Melting. *Materials & Design*, **55**, pp.533-541.

[208]. Van Bael, S., Kerckhofs, G., Moesen, M., Pyka, G., Schrooten, J. and Kruth, J.P., 2011. Micro-CT-Based Improvement of Geometrical and Mechanical Controllability of Selective Laser Melted Ti6Al4V Porous Structures. *Materials Science and Engineering: A*, **528**(24), pp.7423-7431.

[209]. Ahn, D., Kim, H. and Lee, S., 2009. Surface Roughness Prediction Using Measured Data and Interpolation in Layered Manufacturing. *Journal of Materials Processing Technology*, **209**(2), pp.664-671.

[210]. Hollander, D.A., Von Walter, M., Wirtz, T., Sellei, R., Schmidt-Rohlfing, B., Paar, O. and Erli, H.J., 2006. Structural, Mechanical and in Vitro Characterization of Individually Structured Ti–6Al–4V Produced by Direct Laser Forming. *Biomaterials*, **27**(7), pp.955-963.

[211]. Qiu, C., Yue, S., Adkins, N.J., Ward, M., Hassanin, H., Lee, P.D., Withers, P.J. and Attallah, M.M., 2015. Influence of Processing Conditions on Strut Structure and Compressive Properties of Cellular Lattice Structures Fabricated by Selective Laser Melting. *Materials Science and Engineering: A*, **628**, pp.188-197.

[212]. Shen, Y. 2009. *High Performance Sandwich Structures Based on Novel Metal Cores*. Thesis PhD. University of Liverpool, UK.

[213]. Hasan, R., 2013. *Progressive Collapse of Titanium Alloy Micro-Lattice Structures Manufactured Using Selective Laser Melting.* Thesis PhD. University of Liverpool, UK.

[214]. Yan, C., Hao, L., Hussein, A. and Raymont, D., 2012. Evaluations of Cellular Lattice Structures Manufactured Using Selective Laser Melting. *International Journal of Machine Tools and Manufacture*, **62**, pp.32-38.

[215]. Santorinaios, M., Brooks, W., Sutcliffe, C.J. and Mines, R.A.W., 2006. Crush Behaviour of Open Cellular Lattice Structures Manufactured Using Selective Laser Melting. *WIT Transactions on the Built Environment*, **85**, pp.481-490.

[216]. Mullen, L., Stamp, R.C., Brooks, W.K., Jones, E. and Sutcliffe, C.J., 2009. Selective Laser Melting: A Regular Unit Cell Approach for the Manufacture of Porous, Titanium, Bone in-Growth Constructs, Suitable for Orthopedic Applications. *Journal of Biomedical Materials Research Part B: Applied Biomaterials*, **89**(2), pp.325-334.

[217]. Tammas-Williams, S., Zhao, H., Léonard, F., Derguti, F., Todd, I. and Prangnell, P.B., 2015. XCT Analysis of the Influence of Melt Strategies on Defect Population in Ti–6Al–4V

Components Manufactured by Selective Electron Beam Melting. *Materials Characterization*, **102**, pp.47-61.

[218]. Lin, C.L. and Miller, J.D., 2000. Pore Structure and Network Analysis of Filter Cake. *Chemical Engineering Journal*, **80**(1), pp.221-231.

[219]. Yan, C., Hao, L., Hussein, A., Young, P., Huang, J. and Zhu, W., 2015. Microstructure and Mechanical Properties of Aluminium Alloy Cellular Lattice Structures Manufactured by Direct Metal Laser Sintering. *Materials Science and Engineering: A*, **628**, pp.238-246.

[220]. Wang, Z., Ma, H., Zhao, L. and Yang, G., 2006. Studies on the Dynamic Compressive Properties of Open-Cell Aluminum Alloy Foams. *Scripta Materialia*, **54**(1), pp.83-87.

[221]. Ashby, M.F., Evans, A., Fleck, N.A., Gibson, L.J., Hutchinson, J.W. and Wadley, H.N., 2000. *Metal Foams: A Design Guide*, Butterworth-Heinemann, Boston, MA.

[222]. Yan, C., Hao, L., Hussein, A., Bubb, S.L., Young, P. and Raymont, D., 2014. Evaluation of Light-Weight AlSi10Mg Periodic Cellular Lattice Structures Fabricated via Direct Metal Laser Sintering. *Journal of Materials Processing Technology*, **214**(4), pp.856-864.

[223]. Fritsch, F. N. and R. E. Carlson, Monotone Piecewise Cubic Interpolation, 1980. *SIAM J. Numerical Analysis*, Vol. **17**, pp.238-246.

[224]. Mueller, J., Shea, K. and Daraio, C., 2015. Mechanical Properties of Parts Fabricated with Inkjet 3D Printing Through Efficient Experimental Design. *Materials & Design*, **86**, pp.902-912.

[225]. Destercke, S. and Strauss, O., 2014. Kolmogorov-Smirnov Test for Interval Data. *International Conference on Information Processing and Management of Uncertainty in Knowledge-Based Systems*, pp. 416-425.